UNIVERSITÀ DI GENOVA

Università
di Genova

PHD PROGRAM IN Mechanical, energy and management engineering

Development of a Hydrogel-Based 3D Printed Scaffold for Full Meniscus Replacement

Martina Meazzo

Thesis submitted for the degree of Doctor of Philosophy (37° cycle)

25 June 2026

Main supervisor: Peter Dubruel

Supervisor: Catherine Van Der Straeten

Supervisor: Fabrizio Barberis

Head of PhD program: Giovanni Berselli

Acknowledgements

I would like to express my sincere gratitude to my supervisors, Prof. Peter Dubruel, Prof. Catherine Van der Straeten, and Prof. Fabrizio Barberis, for their guidance, support, and valuable expertise throughout the course of this PhD.

First and foremost, I would like to thank Prof. Peter Dubruel for the opportunity to carry out this research within the Polymer Chemistry and Biomaterials Group. I am grateful for his trust, his scientific guidance, and for providing an inspiring research environment in which I could develop both personally and professionally.

I would also like to sincerely thank Prof. Catherine Van der Straeten for her support, encouragement, and insightful feedback throughout this project. Her expertise and perspective have been highly valuable, particularly in maintaining the clinical relevance of this work and in strengthening its broader context.

My sincere thanks also go to Prof. Fabrizio Barberis for his support, advice, and contribution to this joint PhD trajectory. I greatly appreciate his involvement, his guidance, and the opportunity to carry out this work within an international and collaborative framework.

I am deeply thankful to all three supervisors for their time, patience, and commitment to this project. Their complementary expertise and continued support have been essential to the completion of this thesis.

I would also like to thank my colleagues, and especially Manon and Lobke. Thank you for all the fun moments, the conversations, and, above all, the constant support you have given me throughout this journey. Your help, both inside and outside the lab, has meant so much to me, and I truly cannot thank you enough for it. Having people like

you around made even the most stressful and difficult moments lighter and more manageable.

A special thank you goes to my family: my father Massimo, my mother Silvia, and my sister Carolina. You have been my anchor throughout this entire journey, even from 1,080 kilometres away. Every phone call, every visit, every "dai che ce la fai" reminded me where I come from and why I keep going. I know this PhD wasn't always easy to understand from the outside, honestly, it wasn't always easy to understand from the inside either, but you never once stopped believing in me, and that made all the difference. I carry your love with me in everything I do.

And finally, to Giulio: I don't think you'll ever fully realize how much you held together while I was falling apart over failed prints, impossible deadlines, and reviewer comments that made me want to scream. You sat through my rants, celebrated my small victories, and never once made me feel like my stress was too much. You gave me a home to come back to when the lab felt like a battlefield. This thesis has both our names on it, mine on the cover, yours in every page I managed to finish. Thank you, for everything.

Martina Meazzo

25th June 2026

Table of Contents

Acknowledgements 1

Table of Contents 3

List of Abbreviations 8

List of Figures 12

List of Tables 25

Nederlandse samenvatting 27

English Summary 37

Chapter 1: 46

An introduction to biomaterials and 3D printing techniques for the fabrication of meniscal tissue engineering scaffolds 46

1.1 Problem statement 47

1.2 Anatomy of the meniscus 49

1.3 Meniscus biochemical content 52

1.4 Biomechanics of the Menisci 53

1.4.1 Mechanical properties of the Meniscus 56

1.5 Meniscal lesions 77

1.6 The role of tissue engineering in meniscus repair and replacement 80

1.7 Polymer application in Meniscus Tissue Engineering 83

1.7.1 Hydrogels 85

1.7.2 Synthetic polymers 88

1.7.3 Natural polymers 97

1.8 Additive manufacturing technologies 99

1.8.1 Extrusion-based systems 101
1.8.2 Vat polymerization 106
1.8.3 Indirect rapid prototyping 110
1.9 Outline of the PhD 114
Chapter 2: 119
Customizable 3D-Printed Scaffolds for Meniscal Replacement: Mechanical Insights into Urethane-Based Poly(Ethylene Glycol) polymer 119
2.1 Introduction 120
2.2 Materials and methods 124
2.2.1. Materials 124
2.2.2 Methods 124
2.3 Results and discussion 137
2.3.1 Hydrogel building block synthesis 137
2.3.2 Gel fraction, swelling capacity and degree of crosslinking of AUP4K DA 140
2.3.3 Tensile testing of AUP4K DA 141
2.3.4 Structural characterization of AUP4K DA scaffolds 145
2.3.5 Gel fraction and swelling degree of AUP4K DA scaffolds 154
2.3.6 Static compression measurements of AUP4K DA scaffolds 156
2.3.7 Dynamic mechanical analysis of AUP4K DA scaffolds . 162
2.3.8 Fatigue testing of AUP4K DA scaffolds 166
2.4 Conclusion 169

Chapter 3: 171

PEG-based Hydrogels for Meniscus Replacement: Advancing Scaffold Fabrication Flexibility through a Customized Injection Moulding Setup 171

3.1 Introduction 172

3.2 Materials and methods 176

3.2.1 Materials 176

3.2.2 Methods 176

3.3. Results and discussion 185

3.3.1 Hydrogel building block synthesis and structural characterisation 185

3.3.2 Melting temperature and viscosity determination 187

3.3.3 Development of injection-based indirect 3D printing set-up 189

3.3.4 Development of AUP scaffolds through injection-based indirect 3D printing 193

3.3.5 PLA sacrificial mould removal 194

3.3.6 AUP scaffold characterization 196

3.4 Conclusions 209

Chapter 4: 211

Synthetic PEG-based Hydrogel Scaffolds for Meniscus Replacement via Digital Light Processing 211

4.1 Introduction 212

4.2 Materials and Methods 215

4.2.1 Materials 215

4.2.2 Methods 215
4.3. Results and discussion 227
4.3.1 Hydrogel building block synthesis and structural characterisation 227
4.3.2 Evaluation of the hydrogel building block properties via (photo)-rheology 230
4.3.3 Development of AUP scaffolds through DLP 234
4.3.4 Thermal properties of uncrosslinked AUP and crosslinked AUP scaffolds 240
4.3.5 Physico-chemical characterization of printed AUP scaffolds 243
4.3.6 Assessment of the *in vitro* cytotoxicity of 3D printed scaffolds 253
4.4. Conclusions 256
Chapter 5: 258
Influence of Drying Techniques on the Structural and Mechanical Properties of Urethane-Based Poly(ethylene glycol) Scaffolds 258
5.1 Introduction 259
5.2 Materials and Methods 263
5.2.1 Materials 263
5.2.2 Methods 263
5.3 Results and Discussion 267
5.3.1 Hydrogel building block synthesis 267
5.3.2 Structural characterization of AUP4K DA scaffolds 268
5.3.3 Comparative SEM Visualization: The Impact of Drying on Scaffold Architecture. 269

5.3.4 Gel fraction and swelling degree of dried AUP4K DA scaffolds 271

5.3.5 Static compression measurements of AUP4K DA scaffolds 273

5.4 Conclusion 279

Chapter 6: 280

General conclusion and future perspectives 280

Appendix: Curriculum Vitae 293

References 295

List of Abbreviations

ε	tensile strain
σ	tensile stress
2D	two dimensional
3D	three dimensional
AM	additive manufacturing
APM	arthroscopic partial meniscectomy
AUP	acrylate end-capped urethane-based polymer or synonymously used in this PhD with acrylate end-capped urethane-based PEG macromer
AUPx DA	AUP with a molar mass of x [g mol^{-1}], containing the oligo-ethylene glycol (n = 6) acrylate endcap
AUPx HA	AUP with a molar mass of x [g mol^{-1}], containing the EPPETA endcap
BHT	butylated hydroxy toluene
CAD	computer-aided design
CAM	computer-aided manufacturing
$CDCl_3$	deuterated chloroform
CT	computed tomography
DA	di-acrylate
DMA	dynamic modulus analysis

DSC	differential scanning calorimetry
ECM	extracellular matrix
EO	ethylene oxide
EPPETA	ethoxylated and propoxylated pentaerythritol tri-acrylate
ET	Elastic Tensile Modulus
FDA	U.S. Food and Drug Administration
FDM	fused deposition modelling
FTIR	Fourier transform infrared spectroscopy
G’	storage modulus
G’’	loss modulus
GAGs	Glycosaminoglycans
Gel	gelatin
Gel-MA	gelatin methacrylamide
HR-MAS	high resolution magic-angle spinning
IPDI	isophorone diisocyanate
iRP	indirect rapid prototyping
LAP	lithium phenyl-2,4,6-trimethylbenzoyl phosphinate
M_n	number average molar mass
MAT	meniscal allograft transplantation
MM	molar mass

MQ	ultra-pure type I water (Milli-Q; MilliPore)
MSCs	mesenchymal stem cells
M_w	weight average molar mass
NMR	nuclear magnetic resonance spectroscopy (proton NMR, ^{1}H-NMR)
NSF	National Science Foundation
OA	osteoarthritis
PB	photo-blocker
PBS	phosphate buffered saline
PCL	poly-ε-caprolactone
PCU	polycarbonate-urethane
PDMS	Polydimethylsiloxane
PEG	polyethylene glycol (MM < 20,000 g mol^{-1}), is synonymous with
PEO	polyethylene oxide (MM > 20,000 g mol^{-1})
PET	Polyethylene terephthalate
PGA	poly(glycolic acid)
PI	photo-initiator
PLA	polylactic acid
PLLA	poly-(L)-lactic acid
PLGA	poly-(lactic-co-glycolic acid)
PPF	Poly(propylene fumarate)

PTZ	phenothiazine
PVA	poly-vinyl alcohol
PU	polyurethane
RP	rapid prototyping
RT	room temperature
SFF	solid freeform fabrication
SLA	stereolithography
T_c	crystallization temperature
TCP	tissue culture plate
TE	tissue engineering
T_g	glass transition temperature
TGA	Thermogravimetric analysis
T_m	melting temperature
TPP	triphenylphosphite
UV	ultraviolet
UV-A	ultraviolet A (λ = 315 – 400 nm)
UHMWPE	ultra-high molecular weight polyethylene
VIDP	vacuum-based indirect 3D printing

List of Figures

Figure 1.1: Meniscal Anatomy from a Superior Tibial Plateau Perspective. 50

Figure 1.2: Regional Differences in Meniscal Vascularization and Cellular Composition. Left: At birth, the meniscus is entirely supplied by blood vessels, but this vascular network diminishes with age. In adults, the majority of vascularization is confined to the peripheral red-red zone. Right: The outer portion of the meniscus, which retains vascular supply (red-red zone), contains elongated cells with visible processes, resembling fibroblasts. In contrast, the middle (white-red) and inner (white-white) regions host cells that are more like chondrocytes, although they differ from true chondrocytes in phenotype. 51

Figure 1.3: Representation of Collagen Fibre Ultrastructure in the Meniscus. 52

Figure 1.4: Free body diagram of stress acting on the knee meniscus during loading. Under normal loading conditions, the meniscus is compressed by the downward stress exerted by the femur. This compression causes the meniscus to deform radially, while its anterior and posterior horns (Fant and Fpost) anchor it in place. During this process, tensile, compressive, and shear stress are generated. Radial deformation leads to a tensile hoop stress (Fcir), while vertical and horizontal stress (Fv and Fh) arise from the femur compressing the curved superior surface of the meniscus. A radial reaction stress (Frad) counteracts the femoral horizontal stress (Fh). 55

Figure 1.5: Illustration of the most common types of meniscus tears. 78

Figure 1.6: Overview of the “TE triad”: cells, scaffolds, and regulatory signals. Cells are the primary agents responsible for tissue generation. Porous scaffolds, made from biomaterials, provide a habitat for these cells. The behavior of the cells is influenced by different factors, which include the chemical, physical, and biological variables and substances present in the culture system. Created with BioRender.com 81

Figure 1.7: Key characteristics required for a TE scaffold. Created with BioRender.com 82

Figure 1.8: Schematic Representation of a Polymerization - This figure illustrates the process of polymerization, where monomers (small molecules) are linked together to form a polymer (large macromolecule). Created with BioRender.com 84

Figure 1.9: Commonly used synthetic polymer in the meniscal tissue engineering field. 89

Figure 1.10: General (top panel) and specific (bottom panel) chemical structure of a PEG-derived AUP polymer. Created with BioRender.com 92

Figure 1.11: Illustration of the hot material extrusion 3D printing technique. On the left, the apparatus is shown, where the filament is fed into the extruder and melted. The material is deposited layer by layer through the nozzle to create the printed object. On the right, the extrusion head of the hot material extrusion apparatus is depicted. The filament is pulled by two gears through the heat unit and nozzle, where it is melted and forms the object. 103

Figure 1.12: Schematic of the different extrusion-based bioprinting system: Pneumatic-drive, piston-driven and screw-driven. 104

Figure 1.13: Schematics of the Stereolithography (SLA) 3D Printing Mechanism. In this additive manufacturing technique, a UV laser is used to selectively harden liquid photopolymer resin layer by layer. After each layer is cured, the build platform descends incrementally, enabling the object to take shape in successive layers. This method is particularly well-suited for producing intricate geometries and components with fine detail and smooth surface quality. 107

Figure 1.14: Schematics of DLP-Based 3D Printing. A) Bottom-up approach, the printed object forms in an inverted orientation, with each layer cured from beneath the resin vat and the build platform gradually rising. B) Top-down method constructs the object upright, with layers polymerized from above the vat as the build platform lowers. 108

Figure 1.15: Indirect rapid prototyping process. Flow work of iRP process, from CAD design to realization. 112

Figure 2.1: Dimensions (in mm) of the ring specimens in the swollen condition as full part (left) and sectional view (right). 134

Figure 2.2: A) The metal cylinder on which the ring specimens were placed and B) the relevant parts of the dynamic testing machine with the test chamber. 136

Figure 2.3: Chemical structure, FTIR and NMR spectra of AUP4K DA hydrogel precursor. A) The general (top) and the detailed (bottom) chemical structures of the developed AUP4K DA. B) FTIR spectrum of AUP4K DA. The characteristic IR peaks of the AUP4K DA are indicated. C) 1H-NMR spectrum of AUP4K DA. Peak annotation is performed through the applied colour code in parts A and C of the figure. 138

Figure 2.4: Swelling degree, gel fraction and absolute acrylate conversion of AUP4K DA discs. A) Effect of PI on the swelling degree

and the gel fraction of AUP4K DA in water. B) The HR-MAS 1H NMR spectrum of AUP4K DA with and without PI. The table shows the values of the absolute degree of crosslinking, while the red box highlights the peaks corresponding to the acrylate protons. Statistical significance between groups was assessed by the paired Student's t-test (n = 6). 141

Figure 2.5: Effect of PI on the stress-strain behaviour of water-swollen AUP4K DA dogbones at a tensile speed of 10 mm.min-1, a preload speed of 1 mm.min-1 and a preload of 0.2 N. A) Stress-strain curves for AUP4K DA without PI, B) Stress-strain curves for AUP4K DA + 2 mol% PI, C) Young modulus, D) ultimate strength and E) ultimate strain as determined from the tensile curves in parts A and B. The asterisk indicates p values <0.05. Statistical significance between groups was assessed by the paired Student's t-test (n = 6). 143

Figure 2.6: Schematic representation of the different printing patterns applied in this study. A) 0°/45°, B) 0°/90° and C) 0°/45°/90°/135° printing pattern. 147

Figure 2.7: Optical microscopy images (5X magnification) of AUP4K DA scaffolds printed using the Bioscaffolder device in a 0°/45° (A), 0°/90° (B) and 0°/45°/90°/135° (C) pattern. For all scaffolds, the strut diameter and the pore size are respectively 370 µm (± 20 µm) and 300 µm (± 20 µm). The scale bars are indicated on each figure. 149

Figure 2.8: Optical microscopy images (5X magnification) of AUP4K DA scaffolds printed using the Bioscaffolder device in a 0°/90° pattern with different strut diameter and pore size. A) Scaffold with strut diameter of 370 µm (± 20 µm) and pores size of 250 µm (± 20 µm); B) Scaffold with strut diameter of 400 µm (± 20 µm) and pores size of 250 µm (± 20 µm); C) Scaffold with strut diameter of 450 µm (± 20 µm) and pores size of 250 µm (± 20 µm); D) Scaffold with strut diameter of 450

µm (± 20 µm) and pores size of 200 µm (± 20 µm). The scale bars are indicated on each figure. 150

Figure 2.9: Optical microscopy images (5X magnification) of AUP4K DA scaffolds printed using the Bioscaffolder device in a 0°/90° pattern with different strut diameter and pore size. A) Scaffold with strut diameter of 350 µm (± 20 µm) and pores size of 350 µm (± 20 µm); B) Scaffold with strut diameter of 290 µm (± 20 µm) and pores size of 390 µm (± 20 µm); C) Scaffold with strut diameter of 240 µm (± 20 µm) and pores size of 390 µm (± 20 µm). The scale bars are indicated on each figure. 152

Figure 2.10: Swelling degree (SD) and gel fraction (GF) of various AUP4K DA scaffolds. A) Effect of printing pattern on SD and GF, B) Effect of pore size and strut diameter on SD and GF. C) Effect of scaffold shape (cylinder versus ring-shaped) on SD and GF. All scaffolds were printed in the presence of 2 mol% PI. The scaffolds analysed in parts A and C have strut sizes of 370 µm (± 20 µm) and pore sizes of 300 µm (± 20 µm). Scaffolds analysed in parts B and C were obtained using a 0°/90° printing pattern. The asterisk indicates that the $p < 0.05$. Statistical significance between groups was assessed by the paired Student's t-test (n = 3). 155

Figure 2.11: Effect of printing pattern on stress-strain compressive properties of AUP scaffolds. The cylindrical water-swollen scaffolds were compressed at a speed of 2 mm.min-1, and a preload speed of 0.5 mm.min-1. Panels A) to C) represent the obtained curves for respectively the 0°/45°, 0°/90° and 0°/45°/90°/135° printing patterns. The data in panels D) to F) represent the Young's moduli, the ultimate strength and the ultimate strain values of the same printing patterns. These values are calculated starting from the obtained stress-strain curves. The Young modulus is calculated as the slope of the curve between 10-20% strain. The asterisk(s) indicate(s) that the p values <

0.05. Statistical significance between groups was assessed by the paired Student's t-test. (n=4). 158

Figure 2.12: Effect of pore size (P) and strut diameter (S) on the stress-strain compressive properties of AUP scaffolds printed in the presence of 2 mol% PI. A) Young's modulus, B) ultimate strength and C) ultimate strain. The Young's modulus is calculated as the value of the slope of the curve between 10-20% of the strain. The asterisks indicates that the p values < 0.05. Statistical significance between groups was assessed by the paired Student's t-test and indicated with an asterisk (n=3). 161

Figure 2.13: Effect of printing pattern on the scaffold storage (panels A-C) and loss modulus (panels D-F) as studied using DMA in the 2 - 100 Hz frequency range. Panels A & D, B & E and C & F represent the data of respectively the 0°/45°, 0°/90° and 0°/45°/90°/135° printing patterns. Panels G and H represent the average storage moduli and the average loss moduli as derived from the data in panels A-F. All AUP4K DA scaffolds were printed in the presence of 2 mol% Irgacure and revealed strut and pore sizes of respectively of 370 µm (± 20 µm) and of 300 µm (± 20 µm). Statistical significance between groups was assessed by the paired Student's t-test (n=4). The asterisk indicates p < 0.05. 164

Figure 2.14: Exemplary force curves over time for A) the material testing machine and B) the dynamic testing machine. 167

Figure 3.1: Reaction scheme for the AUP4K DA and HA synthesis. 177

Figure 3.2: Overview of AUP4K chemical structure and the obtained infrared and NMR spectra. A) Chemical structure of the developed AUP (top: di-acrylated AUP, AUP4K DA); bottom: hexa-acrylated AUP, AUP4K HA). B) FTIR spectrum of both AUP4K. The characteristic IR

peaks of the AUP4K are indicated. C) 1H-NMR spectrum of both AUP4K. Peak annotation is performed through the applied colour code in parts A and C of the figure. 186

Figure 3.3: A) Differential scanning calorimetry thermograms of AUP4K DA and AUP4K HA. B) Effect of the AUP concentration and end-cap on the dynamic viscosity as measured by rheology. 188

Figure 3.4: Injection moulding set-up applied for AUP injection-based indirect 3D printing. A) Overview of all the components of the designed non-assembled set-up, B) top view of the upper runner system, C) view of the designed assembled set-up, and D) image of the fabricated assembled set- up. 191

Figure 3.5: Visualisation of the different steps of the production process of the 80 wt% AUP4K DA and AUP4K HA scaffolds using optical microscopy. Panels A-D and E-H represent respectively vertical and lateral views of the scaffolds A&E) PLA sacrificial mould, B&F) PLA sacrificial mould after AUP4K DA injection and crosslinking; C&G) AUP4K DA 80 wt% scaffold after PLA removal D&H) AUP4K HA 80 wt% scaffold after PLA removal. The scale bars are indicated on each figure (5X magnification). Vertical views (top row) are taken along the build direction, perpendicular to the printing plane. Lateral views (bottom row) are taken perpendicular to the build direction, showing the scaffold cross-section. 194

Figure 3.6: Application of TGA to assess the removal of the PLA sacrificial mould after AUP4K crosslinking. A) & B) Thermal degradation curves of PLA, a dried 80 wt% AUP4K with PLA mould and a dried 80 wt% AUP4K scaffold after removal of the PLA mould; C) & D) Peaks of the first derivative of the weight loss as a function of temperature of respectively panels A and B. 196

Figure 3.7: Effect of AUP concentration and endcap on the scaffold microstructure after injection-based indirect 3D printing, as visualized using optical microscopy. From top to bottom, images represent vertical and lateral porosities for both AUP4K types at one concentration. Panels A to G represent scaffolds at different concentrations (from 30-90 wt %). The scale bars are indicated on each figure (5X magnification). 197

Figure 3.8: SEM images of 90 wt % AUP4K DA (panel A) and AUP4K HA (panel B) scaffolds. The scale bars are indicated on each figure. The images were acquired with the viewing direction perpendicular to the strut surface / perpendicular to the printing plane 198

Figure 3.9: Swelling degree (SD) and gel fraction (GF) of AUP scaffolds. A) Effect of AUP concentration and endcap on the SD and the GF. B) Images of the swollen AUP4K DA scaffolds. The swollen scaffolds from left to right are those with an increasing AUP4K DA concentration (from 30-90 wt %). 200

Figure 3.10: Effect of the AUP concentration and - endcap on the compressive properties of equilibrium water-swollen scaffolds. The scaffolds were compressed at a speed of 2 mm.min-1. Panels A and B represent the obtained test curves for respectively AUP4K DA and AUP4K HA. Panels C to E represent respectively the Young moduli, the ultimate strength and the ultimate strain values for AUP4K DA and AUP4K HA, as derived from panels A and B. 202

Figure 3.11: Effect of the AUP endcap on the compressive properties of non- porous equilibrium water-swollen scaffolds at a 90 wt % AUP concentration. The scaffolds were compressed at a speed of 2 mm.min-1. Panels A and B represent the obtained test curves for respectively AUP4K DA and AUP4K HA (n = 4). 205

Figure 3.12: Effect of the AUP concentration and endcap on the hardness of equilibrium water-swollen scaffolds as studied using texturometry. 207

Figure 4.1: Schematic overview of the digital light processing (DLP) workflow for the fabrication and evaluation of acrylate-terminated urethane-PEG (AUP) scaffolds. The process includes (1) AUP synthesis and resin formulation, (2) DLP printing and architectural design, and (3) post-processing and physico- chemical, mechanical, and biological characterization. 214

Figure 4.2: Developed test setup to simultaneously induce a compression and a stretching in two fatigue-ring specimens. 221

Figure 4.3: Test station with the fatigue-ring specimen (sectional view) receiving a compression as well as a stretching. 222

Figure 4.4: Minimum and maximum load acting on the test setup for each load level of 50.000 cycles (locati test). 223

Figure 4.5: Overview of AUP chemical structure and obtained infrared and NMR spectra. A) The chemical structure of the synthesized AUPs. B) The FTIR spectrum of AUP2K DA and 4K DA, highlighting its characteristic IR peaks. C) The 1H-NMR spectrum of AUP2K DA and 4K DA, with peak annotations indicated using the color code applied in parts A and C of the figure. 229

Figure 4.6: Effect of AUP concentration and - molar mass on dynamic viscosity, measured by rheology at 35 °C. The green line marks the printability threshold, defining the viscosity range considered compatible with the LumenX system's operating capabilities. 231

Figure 4.7: Effect of AUP type and - concentration on the crosslinking behaviour as determined by photo-rheological analysis of AUP solutions: A) AUP2K DA at a concentration of 30 wt% to 80 wt%; B)

AUP4K DA at a concentration of 30 wt% to 70 wt%. All solutions contain 5 mol% Li-TPO-L and 0.5 mol% Tartrazine as respectively photo-initiator and photo-absorber. 232

Figure 4.8: Computer-aided design (CAD) model of the porous scaffolds (10*10*5 mm) used for digital light processing (DLP) printing. The design features a regular cubic lattice with uniform pore geometry and a nominal pore size of 400 µm. The left image shows the oblique view of the scaffold, while the right image depicts the top view. 235

Figure 4.9: Effect of AUP concentration and - molar mass on the scaffold microstructure, as visualized using optical microscopy. Images represent vertical porosities for both AUP2K DA and AUP4K DA at different concentrations (30 wt% to 80 wt% for AUP2K DA and 30 wt% to 70 wt% for AUP4K DA). At the bottom right, the CAD model of the porous scaffold is shown. The scale bars are indicated on each figure (5X magnification). 239

Figure 4.10: Optical microscopy images of AUP scaffolds cross-section showing a side-view (viewing direction perpendicular to the build direction) indicating the vertical porosity in the scaffolds. A) AUP2K DA 80 wt%, B) AUP4K DA 70 wt%. 240

Figure 4.11: Effect of crosslinking on the thermal properties of AUP2K DA and AUP4K DA. A) TGA curve of AUP2K DA (uncrosslinked) and the crosslinked scaffold printed at 80 wt% with 5 mol% Li-TPOL and 0.5 mol% Tartrazine, B) TGA curve of AUP4K DA (uncrosslinked) and the crosslinked scaffold printed at 70 wt% with 5 mol% Li-TPOL and 0.5 mol% Tartrazine; C) and D) DSC thermograms of (un)crosslinked AUP2K DA (panel C) and (un)crosslinked AUP4K DA (panel D.). 242

Figure 4.12: Effect of AUP concentration and molar mass on: (A) gel fraction and (B) swelling degree of AUP scaffolds. Data are presented

as mean ± SD. Letters indicate significant differences between concentrations within the same material type; bars sharing at least one common letter are not significantly different ($p > 0.05$) according to one-way ANOVA followed by Tukey's HSD post-hoc test ($n = 4$). Non-asterisked and asterisked letters denote separate comparison groups (i.e., different material types) and should not be compared directly. 244

Figure 4.13: Effect of AUP concentration and molar mass on the compressive properties of AUP scaffolds. Scaffolds were compressed at a crosshead speed of 2 mm/min. Panels A and B show the compression curves of AUP2K DA and AUP4K DA, respectively. Panels C–E present the Young's modulus, ultimate strength, and ultimate strain of AUP2K DA and AUP4K DA scaffolds at different concentrations. Data are presented as mean ± SD. Letters indicate significant differences between concentrations within the same material type; bars sharing at least one common letter are not significantly different ($p > 0.05$) according to one-way ANOVA followed by Tukey's HSD post-hoc test ($n = 4$). Non-asterisked and asterisked letters denote separate comparison groups (different material types) and should not be compared directly. 246

Figure 4.14: Fatigue performance of printed fatigue-ring specimens. A) Representative images of fatigue-ring specimens at failure after cyclic loading. B) Number of cycles to failure obtained from the fatigue test (bars represent mean ± SD). 250

Figure 4.15: Indirect cell viability tests of DLP-printed AUP materials using HFF cells after 1, 3 and 7 days of leaching in cell culture medium. The metabolic activity as assessed by the MTS assay is represented in panel (A). Cellular viability of HFF cells after 1,3 and 7 days of incubation is quantified in panel (B) and qualitatively presented in panel (C). HFF cells exposed for 1 day to non-treated cell culture medium

were used as a positive control. According to the ISO 10993-5 standard, a viability above 70 % (dotted line in panels A and B) is required. The scale bars represent 200 µm. (*p ≤ 0.05; **p ≤ 0.01). 255

Figure 5.1: Optical microscopy images (5X magnification) of AUP4K DA scaffolds printed using the Bioscaffolder device. For all scaffolds, the strut diameter and the pore size are respectively 400 µm (± 20 µm) and 250 µm (± 20 µm). The scale bars are indicated on each figure. 268

Figure 5.2: Scanning electron microscopy (SEM) images of AUP4K DA scaffold struts after dehydration using different drying protocols: (A) freeze-drying, (B) desiccator drying, (C) ventilated oven drying, and (D) vacuum oven drying. Distinct differences in surface morphology and strut integrity are observed depending on the drying method, highlighting the strong influence of dehydration strategy on the final scaffold microarchitecture. 270

Figure 5.3: Swelling degree (SD) and gel fraction (GF) of AUP4K DA scaffolds dried using different drying methods (n = 4). Data are presented as mean ± SD. Different letters indicate significant differences between groups; bars sharing at least one common letter are not significantly different (p > 0.05) according to one-way ANOVA followed by Tukey's HSD post-hoc test. 272

Figure 5.4: Compressive mechanical behaviour of AUP4K DA scaffolds after dehydration using different drying protocols and subsequent rehydration in double-distilled water for 24 h. The water-swollen scaffolds were compressed at a speed of 2 mm.min-1, and a preload speed of 0.5 mm.min-1. A) Freeze- dried, B) desiccator-dried, C) ventilated oven-dried, and D) vacuum oven-dried scaffolds. The data in panels E) to G) represent the Young's moduli, the ultimate

strength and the ultimate strain values. These values are calculated starting from the obtained stress-strain curves. The Young modulus is calculated as the slope of the curve between 10-20% strain (n=3) Different letters indicate significant differences between groups; bars sharing at least one common letter are not significantly different ($p > 0.05$) according to one- way ANOVA followed by Tukey's HSD post-hoc test.

List of Tables

Table 1.1: Comparative Analysis of Tensile Properties of the Human Meniscus from Various Studies. 57

Table 1.2: Comparative Analysis of Compressive Moduli of the Human Meniscus from Various Studies. 67

Table 1.3: Dynamic properties of human menisci. 72

Table 2.1: Summary of printing parameters utilized for scaffold fabrication: an overview of the specific printing parameters used in the fabrication of scaffolds, including but not limited to, printing temperature, print speed, layer thickness, and strand distance. These parameters were optimized to ensure structural integrity and desired porosity of the scaffolds. 131

Table 2.2: Summary of printing parameters used for scaffold fabrication. The table provides an overview of the specific printing conditions applied during scaffold production, including the printing temperature, the extrusion speed, the layer height, and the strand spacing. These parameters were optimized to achieve consistent structural integrity and the targeted porosity. 151

Table 2.3: Results of the fatigue tests using the material testing machine and the dynamic testing machine. 167

Table 3.1: Comparison of compressive Young Modulus (MPa) for porous and non-porous scaffolds. The table presents Young modulus values for two types of scaffolds, AUP4K DA and AUP4K HA, in both porous and non-porous forms. 205

Table 4.1: Effect of AUP type and - concentration on the storage modulus (G′) and loss modulus (G″). 233

Table 4.2: Effect of AUP concentration and - molar mass on DLP printing parameters. 237

Table 4.3: Effect of crosslinking on the thermal stability and transition temperatures of AUP as studied using TGA and DSC analyses. 242

Table 5.1: Overview of the printing conditions employed for scaffold fabrication, including key parameters such as printing temperature, deposition speed, layer height, and strand spacing. These parameters were systematically optimized to achieve the targeted scaffold architecture, ensuring adequate structural stability and controlled porosity. 265

Nederlandse samenvatting

Meniscusletsels behoren tot de meest voorkomende aandoeningen van het kniegewricht en vormen een belangrijke klinische en biomechanische uitdaging. De meniscus speelt een essentiële rol in de knie door bij te dragen aan de verdeling van belastingen, schokdemping, gewrichtsstabiliteit, congruentie tussen femur en tibia, en bescherming van het gewrichtskraakbeen. Wanneer de meniscus beschadigd is, en in het bijzonder wanneer het letsel zich in de avasculaire binnenzone bevindt, is het intrinsieke herstelvermogen beperkt. Hierdoor is herstel vaak moeilijk en wordt in ernstige gevallen nog steeds een partiële of totale meniscectomie uitgevoerd. Hoewel deze ingreep op korte termijn de symptomen kan verlichten, leidt het verlies van functioneel meniscusweefsel tot een gewijzigde belastingsverdeling in het gewricht en verhoogt het op lange termijn het risico op degeneratieve veranderingen en osteoartrose. Tegen deze achtergrond is er een duidelijke behoefte aan alternatieve strategieën die kunnen leiden tot een functionele vervanging van de meniscus.

Het doel van dit proefschrift was de ontwikkeling van een op hydrogel gebaseerd, 3D-geprint scaffold voor volledige meniscusvervanging. Hiervoor werden acrylaat-‘endcapped’ urethaan-gebaseerde poly(ethyleenglycol)-macromeren (AUP's) gebruikt als hydrogel bouwstenen. AUP's zijn synthetische, foto-crosslinkbare polymeren bestaande uit een poly(ethyleenglycol) (PEG) backbone met een gedefinieerde molaire massa, verbonden via urethaanbindingen met acrylaat-eindgroepen die UV- of zichtbaar-licht-geïnduceerde crosslinking tot een stabiel hydrogelnetwerk mogelijk maken. De nomenclatuur die doorheen dit proefschrift wordt gehanteerd, weerspiegelt de belangrijkste ontwerpvariabelen: AUP2K en AUP4K verwijzen naar precursoren met PEG-backbone-molaire massa's van

respectievelijk 2 000 en 4 000 g/mol, terwijl de suffixen DA (di-acrylaat) en HA (hexa-acrylaat) het aantal crosslinkbare acrylaat-eindgroepen per ketenuiteinde aanduiden - één in het geval van DA en drie in het geval van HA. Dit modulaire ontwerp maakt het mogelijk om zowel de chemische samenstelling als de resulterende mechanische en fysicochemische eigenschappen van het materiaal systematisch af te stemmen. De centrale hypothese van dit werk was dat, door de combinatie van goed controleerbare polymeerchemie, een op maat ontworpen poreuze scaffold-architectuur en geschikte additive manufacturing (AM) technieken, scaffolds kunnen worden ontwikkeld die de eigenschappen van de natieve meniscus benaderen en tegelijkertijd voldoende reproduceerbaar, verwerkbaar en potentieel klinisch vertaalbaar zijn. Om deze hypothese te toetsen werden de volgende specifieke doelstellingen nagestreefd: (i) het vaststellen van structuur–verwerking–eigenschaprelaties voor AUP-hydrogelen als functie van PEG-molaire massa, eindgroepfunctionaliteit en polymeerconcentratie; (ii) het aantonen van scaffold-produceerbaarheid via drie complementaire fabricageroutes - extrusie-gebaseerd 3D-printen, indirect rapid prototyping via injection moulding, en digital light processing (DLP); (iii) het uitvoeren van een uitgebreide mechanische karakterisering onder belastingscondities relevant voor de meniscus, inclusief statische, dynamische en cyclische fatigue-testen; (iv) het evalueren van het effect van nabehandeling (dehydratatie) op de scaffold-eigenschappen met het oog op klinische vertaling; en (v) het uitvoeren van een eerste biocompatibiliteitsscreening.

Hoofdstuk 1 presenteerde de algemene context van meniscusweefsel en meniscusvervanging. Dit hoofdstuk behandelde niet alleen de anatomie, samenstelling en biomechanische functie van de meniscus, maar ook de beperkingen van de huidige klinische behandelingsopties.

Daarnaast werd een overzicht gegeven van materialen en fabricagestrategieën die reeds onderzocht zijn voor meniscus tissue engineering, met bijzondere aandacht voor hydrogelen en additive manufacturing technieken. Deze literatuurstudie toonde duidelijk aan dat een succesvolle meniscusvervanger niet alleen biocompatibel moet zijn, maar ook een hoog watergehalte, geschikte porositeit, voldoende mechanische ondersteuning en langdurige weerstand tegen repetitieve belasting moet combineren. Deze bevinding vormde het uitgangspunt voor de experimentele hoofdstukken van dit proefschrift.

In Hoofdstuk 2 werd de geschiktheid van AUP4K DA — de di-acrylaat-'endcapped' precursor met een PEG-backbone-molaire massa van 4 000 g/mol — als materiaalplatform voor de fabricage van meniscus-scaffolds onderzocht. Een belangrijk onderdeel van dit hoofdstuk was het aantonen dat het materiaal stabiele netwerken kan vormen met een hoge mate van crosslinking. Daarnaast werd duidelijk dat niet alleen de chemische samenstelling van de hydrogel, maar ook de architectuur van het scaffold een beslissende rol speelt in het uiteindelijke gedrag. Met behulp van extrusie-gebaseerd 3D-printen werden verschillende scaffold-configuraties geproduceerd waarin het printpatroon, de poriegrootte en de strutdiameter systematisch werden gevarieerd. De resultaten toonden aan dat deze parameters een uitgesproken effect hebben op de mechanische eigenschappen onder druk. Meer isotrope printpatronen en een geschikte combinatie van kleinere poriën en dikkere struts resulteerden in stijvere constructen met een hogere druksterkte. Dit toonde aan dat architecturale optimalisatie een krachtig instrument is om mechanische eigenschappen af te stemmen, zelfs wanneer hetzelfde basismateriaal wordt gebruikt.

Naast statische druktesten werden in Hoofdstuk 2 ook dynamisch-mechanische analyses en fatigue-testen uitgevoerd. Deze analyses bevestigden dat de scaffolds een uitgesproken viscoelastisch gedrag vertonen, wat relevant is voor toepassingen in een dynamisch belast gewricht zoals de knie. Tegelijkertijd werd echter ook een belangrijke beperking duidelijk: hoewel de drukeigenschappen binnen of nabij de onderste gerapporteerde waarden voor meniscusweefsel konden worden gebracht, bleef de weerstand tegen langdurige cyclische belasting onvoldoende. De fatigue-testen maakten duidelijk dat de fatigue-weerstand één van de belangrijkste uitdagingen blijft bij de verdere ontwikkeling van een klinisch toepasbaar meniscus-scaffold. Dit hoofdstuk leverde daarom niet alleen bewijs voor het potentieel van AUP4K DA, maar ook een duidelijke richting voor verdere optimalisatie.

Hoofdstuk 3 ontwikkelde een alternatieve fabricagestrategie om architecturale kenmerken te realiseren die moeilijk te bereiken zijn met conventionele directe extrusie-printtechnieken. Er werd een innovatieve injection-moulding-opstelling ontworpen, waarbij stijdelijke structuren (sacrificial moulds) werden gefabriceerd uit polylactide (PLA) met behulp van hot extrusion. De AUP-precursoroplossing werd vervolgens in de poreuze PLA-mal geïnjecteerd en gecrosslinkt, waarna de mal selectief werd opgelost in chloroform om het uiteindelijke hydrogel-scaffold te bekomen. Deze indirecte benadering - die, voor zover wij weten, niet eerder was toegepast op AUP-gebaseerde hydrogelsystemen - maakte de fabricage mogelijk van scaffolds met laterale porositeit, dat wil zeggen onderling verbonden poriekanalen georiënteerd parallel aan de laterale vlakken van de scaffold. Dit architecturaal kenmerk is ontoegankelijk via conventioneel laag-per-laag direct printen en is van bijzonder belang voor meniscus tissue engineering, waar nutriënttransport van de gevasculariseerde

buitenzone naar de avasculaire binnenzone porieconnectiviteit in de laterale richting vereist. In dit hoofdstuk werden twee verwante materialen onderzocht: AUP4K DA en AUP4K HA, waarbij het laatste drie acrylaat-groepen per ketenuiteinde bevat in plaats van één, wat resulteert in een verhoogde crosslinking-dichtheid. Beide materialen werden bestudeerd over een breed concentratiebereik (30–90 wt%), wat een systematische evaluatie mogelijk maakte van de invloed van functionaliteit en concentratie op de scaffold-eigenschappen.

De resulterende scaffolds werden gekarakteriseerd met optische microscopie en scanning-elektronenmicroscopie (SEM), met de focus op morfologie, poriestructuur en succesvolle verwijdering van de mal. Daarnaast werden de gelfractie en de zwellingsgraad bepaald om inzicht te verkrijgen in de netwerkvorming en het wateropnamevermogen van de verschillende formuleringen. De mechanische karakterisering toonde aan dat een toenemende polymeerconcentratie leidde tot stijvere scaffolds en een hogere druksterkte, terwijl de vervormbaarheid afnam. Er werd ook vastgesteld dat de hogere functionaliteit van AUP4K HA aanleiding gaf tot een stijver netwerk in vergelijking met AUP4K DA, wat in overeenstemming is met de verwachting dat meer reactieve groepen leiden tot een hogere crosslinking-dichtheid. Hoofdstuk 3 bevestigde aldus dat niet alleen architectuur, maar ook subtiele variaties in chemische samenstelling doelgericht kunnen worden ingezet om de scaffold-prestaties af te stemmen. Bovendien toonde dit hoofdstuk aan dat indirecte fabricage een waardevolle aanvulling vormt op direct 3D-printen binnen het bredere kader van meniscus-scaffold-ontwikkeling.

In Hoofdstuk 4 werd de AUP-technologie verder uitgebreid naar digital light processing (DLP), een vat-fotopolymerisatietechniek waarbij een volledige laag fotocurable hars selectief wordt belicht en gecrosslinkt in één enkele projectiestap met behulp van een digital micromirror

device. In tegenstelling tot extrusie-gebaseerde fabricage, waar de architectuur wordt bepaald door de sequentiële afzetting van individuele filamenten, maakt DLP de productie mogelijk van complexere, geometrisch preciezere en zeer regelmatige scaffold-architecturen met verbeterde resolutie en reproduceerbaarheid. Dit hoofdstuk vertegenwoordigde de eerste demonstratie van DLP-printen van AUP-gebaseerde hydrogelmaterialen. Twee AUP-systemen met verschillende PEG-molaire massa's werden onderzocht: AUP2K DA (PEG-molaire massa van 2 000 g/mol) en AUP4K DA (4 000 g/mol). De onderliggende rationale was dat een lagere molaire massa, en dus een hogere dichtheid aan reactieve eindgroepen per massaeenheid, zou leiden tot een stijver en dichter netwerk na crosslinking, waardoor een breder bereik van haalbare mechanische eigenschappen kon worden verkend.

Om DLP-printen van AUP-harsen mogelijk te maken, werden zichtbaar-licht-uithardbare formuleringen ontwikkeld met lithiumfenyl-2,4,6-trimethylbenzoylphosphinaat (Li-TPO-L) als wateroplosbare photo-initiator en tartrazine als biocompatibele photoabsorber — een combinatie die niet eerder was gerapporteerd voor AUP-systemen. Reologische en fotoreologische analyses werden gebruikt om te bepalen welke formuleringen voldoende verwerkbaar waren en tegelijkertijd een snelle en efficiënte netwerkvorming tijdens belichting mogelijk maakten. Vervolgens werden scaffolds met een regelmatige architectuur en verticale porositeit geproduceerd, en werden printparameters zoals belichtingstijd en projectorvermogen geoptimaliseerd om een goede overeenstemming tussen het CAD-ontwerp en de geprinte structuur te verkrijgen. De resultaten toonden aan dat DLP inderdaad een veelbelovende techniek is voor de fabricage van AUP-gebaseerde scaffolds met hoge reproduceerbaarheid en goede poriegetrouwheid.

Na fabricage werden de geprinte scaffolds onderworpen aan een uitgebreide karakterisering. Thermische analyse door middel van TGA en DSC verschafte aanvullende informatie over de materiaaleigenschappen voor en na crosslinking. Gelfractie- en zwellingsmetingen bevestigden een efficiënte netwerkvorming en toonden aan dat de wateropname, zoals verwacht, afnam met toenemende crosslinking-dichtheid. De mechanische testen maakten duidelijk dat de molaire massa van het PEG-segment een belangrijke invloed heeft op het drukgedrag: scaffolds op basis van AUP2K vertoonden over het algemeen hogere drukmoduli dan scaffolds op basis van AUP4K bij vergelijkbare concentraties. Voor beide materiaaltypen resulteerde een toenemende concentratie in stijvere scaffolds, terwijl de ultieme rek afnam. Een eerste evaluatie onder cyclische belasting werd eveneens uitgevoerd met behulp van ringvormige proefstukken, zodat niet alleen statische maar ook dynamische prestaties in rekening werden gebracht. Ten slotte werd een voorlopige indirecte cytocompatibiliteitsscreening uitgevoerd door middel van MTS- en live/dead-assays. Deze resultaten ondersteunden de verdere ontwikkeling van DLP-geprinte AUP-scaffolds als een veelbelovend platform voor meniscustoepassingen.

Waar de voorgaande hoofdstukken zich voornamelijk richtten op materiaalontwikkeling en scaffold-fabricage, behandelde Hoofdstuk 5 een kwestie die cruciaal is voor de praktische en klinische vertaling van op hydrogel gebaseerde constructen, namelijk de invloed van dehydratatie op de uiteindelijke scaffold-prestaties. Aangezien hydrogelen over het algemeen een hoog watergehalte bezitten, is het vaak noodzakelijk om een droogstap in te voeren voor opslag, transport of hantering. Deze stap is echter zeer belangrijk, omdat de verwijdering van water gepaard kan gaan met structurele veranderingen in het netwerk en bijgevolg ook in het mechanische

gedrag na rehydratatie. In dit hoofdstuk werden daarom vier verschillende droogmethoden vergeleken: vriesdrogen, desiccatordrogen, drogen in een geventileerde oven en drogen in een vacuümoven.

De resultaten toonden duidelijk aan dat de droogmethode een uitgesproken effect heeft op de scaffold-morfologie. Vriesdrogen leidde tot een verbeterde poreuze microstructuur en resulteerde in een hoge zwellingscapaciteit na rehydratatie. De ovengebaseerde methoden daarentegen resulteerden in drukeigenschappen die vergelijkbaar met of hoger waren dan die van de gevriesdroogde scaffold. Het zwellingsgedrag werd eveneens beïnvloed door de geselecteerde droogmethode. Deze resultaten zijn van groot belang omdat ze aantonen dat dehydratatie niet louter als een praktische nabewerkingsstap moet worden beschouwd, maar als een bijkomende procesparameter die het mogelijk maakt om de uiteindelijke balans tussen porositeit, wateropname, mechanische sterkte en hanteerbaarheid verder af te stemmen. Dit hoofdstuk voegde daarom een belangrijke translationele dimensie toe aan het proefschrift.

Wanneer de resultaten van alle experimentele hoofdstukken samen worden beschouwd, ontstaat een samenhangend beeld van AUP-gebaseerde hydrogelen als een veelzijdig platform voor de ontwikkeling van 3D-geprinte meniscus-scaffolds. Een eerste belangrijke conclusie is dat de materiaaleigenschappen sterk kunnen worden gestuurd via chemische parameters zoals molaire massa, functionaliteit en polymeerconcentratie. Een tweede belangrijke conclusie is dat de scaffold-architectuur minstens even bepalend is als de materiaalchemie. Printpatroon, poriegrootte, strutdiameter en oriëntatie beïnvloeden rechtstreeks de wijze waarop belastingen doorheen het construct worden verdeeld en bepalen daarom in sterke mate de drukrespons. Een derde belangrijke conclusie is dat de

gekozen fabricageroute niet louter een technische productiestap is, maar ook bepaalt welke architecturen haalbaar zijn en welke eigenschappen uiteindelijk kunnen worden bereikt. Extrusie-printen, indirecte injection-moulding-fabricage en DLP-printen hebben elk hun eigen voor- en nadelen, maar samen tonen ze aan dat AUP-hydrogelen compatibel zijn met meerdere verwerkingsstrategieën. Opmerkelijk is dat verschillende aspecten van dit werk originele bijdragen aan het vakgebied vertegenwoordigen: de eerste uitgebreide multimodale mechanische karakterisering van AUP-hydrogel-scaffolds — inclusief fatigue-testen, die cyclische duurzaamheid identificeerden als het voornaamste translationele knelpunt; de ontwikkeling van een nieuwe indirecte fabricageroute die laterale scaffold-porositeit mogelijk maakt; en de eerste vertaling van AUP-materialen naar DLP-gebaseerde additive manufacturing.

Tegelijkertijd maakte dit proefschrift ook duidelijk dat het ontwikkelen van een functionele meniscusvervanger veel complexer is dan enkel het benaderen van een statische drukmodulus. De meniscus is een anisotroop, viscoelastisch en cyclisch belast weefsel, en een succesvolle vervanger moet daarom niet alleen initieel voldoende sterk zijn, maar moet ook zijn prestaties behouden in de tijd onder repetitieve belasting. De fatigue-resultaten tonen in het bijzonder aan dat deze eigenschap momenteel de belangrijkste beperking vormt voor verdere klinische vertaling. Hoewel de statische mechanische eigenschappen in meerdere gevallen reeds gerapporteerde waarden voor humane menisci benaderen, blijft het noodzakelijk om de weerstand tegen scheurvorming, schadeaccumulatie en structureel falen onder langdurige belasting verder te verbeteren.

Op basis van de bevindingen in dit proefschrift kunnen verschillende richtingen voor toekomstig onderzoek worden geformuleerd. Een eerste duidelijke piste is de verdere optimalisatie van de

hydrogelchemie, bijvoorbeeld door aanpassing van de molaire massa, verhoging van de functionaliteit, of introductie van alternatieve of secundaire crosslinking-mechanismen die resulteren in een taaier netwerk. Een tweede piste is de verdere verfijning van de scaffold-architectuur, met bijzondere aandacht voor anisotrope of gradiëntontwerpen die de natieve meniscus beter nabootsen. Een derde piste ligt in het combineren van de hydrogelmatrix met bijkomende versterkende componenten, zoals vezels of textielstructuren, om de weerstand tegen circumferentiële spanningen en langdurige cyclische belasting te verhogen. Daarnaast blijft verdere biologische evaluatie noodzakelijk, zowel *in vitro* met relevante celtypes als, op langere termijn, in meer fysiologisch relevante modellen.

Samenvattend toont dit proefschrift aan dat AUP-gebaseerde synthetische hydrogelen een sterk en veelzijdig uitgangspunt vormen voor de ontwikkeling van een 3D-geprint scaffold voor volledige meniscusvervanging. Door een combinatie van materiaalontwikkeling, architecturale optimalisatie, meerdere fabricageroutes en evaluatie van nabehandelingsstrategieën werd een brede basis gelegd voor verdere vooruitgang in dit onderzoeksdomein. De verkregen resultaten bevestigen dat het mogelijk is om poreuze, reproduceerbare en mechanisch afstembare hydrogelstructuren te ontwikkelen die veelbelovend zijn voor meniscustoepassingen. Tegelijkertijd maken ze duidelijk dat verdere optimalisatie, in het bijzonder wat betreft fatigue-weerstand en langdurige functionele prestaties, essentieel blijft. Desalniettemin biedt dit werk een solide basis voor de volgende ontwikkelingsstappen richting een klinisch relevant synthetisch scaffold voor volledige meniscusvervanging.

English Summary

Meniscal injuries are among the most common disorders of the knee joint and represent an important clinical and biomechanical challenge. The meniscus plays an essential role in the knee by contributing to load distribution, shock absorption, joint stability, congruency between femur and tibia, and protection of articular cartilage. When the meniscus is damaged, and particularly when the injury is in the avascular inner zone, the intrinsic healing capacity is limited. As a result, repair is often difficult, and, in severe cases, partial or total meniscectomy is still performed. Although this procedure may relieve symptoms in the short term, the loss of functional meniscal tissue leads to altered load distribution in the joint and increases the risk of degenerative changes and osteoarthritis in the long term. Against this background, there is a clear need for alternative strategies that can lead to a functional replacement of the meniscus.

The aim of this thesis was the development of a hydrogel-based, 3D-printed scaffold for full meniscus replacement. For this purpose, acrylate-endcapped urethane-based poly(ethylene glycol) macromers (AUPs) were used as hydrogel building blocks. AUPs are synthetic, photo-crosslinkable polymers consisting of a poly(ethylene glycol) (PEG) backbone of defined molar mass, connected via urethane linkages to acrylate end groups that enable UV- or visible-light-induced crosslinking into a stable hydrogel network. The nomenclature used throughout this thesis reflects the key design variables: AUP2K and AUP4K refer to precursors with PEG backbone molar masses of 2 000 and 4 000 g/mol respectively, while the suffixes DA (di-acrylate) and HA (hexa-acrylate) denote the number of crosslinkable acrylate end groups per chain end — one in the case of DA and three in the case of HA. This modular design allows both the chemical composition and the resulting mechanical and physicochemical properties of the material to

be systematically tuned. The central hypothesis of this work was that, through the combination of well-controllable polymer chemistry, a tailored porous scaffold architecture, and suitable additive manufacturing (AM) techniques, scaffolds can be developed that approach the properties of the native meniscus while also being sufficiently reproducible, processable, and potentially translatable. To test this hypothesis, the following specific objectives were pursued: (i) to establish structure–processing–property relationships for AUP hydrogels as a function of PEG molar mass, end-group functionality, and polymer concentration; (ii) to demonstrate scaffold manufacturability via three complementary fabrication routes, extrusion-based 3D printing, indirect rapid prototyping via injection moulding, and digital light processing (DLP); (iii) to perform a comprehensive mechanical characterization under loading conditions relevant to the meniscus, including static, dynamic, and cyclic fatigue testing; (iv) to evaluate the effect of post-processing (dehydration) on scaffold properties for clinical translation; and (v) to provide initial biocompatibility screening.

Chapter 1 presented the general context of meniscal tissue and meniscus replacement. This chapter discussed not only the anatomy, composition, and biomechanical function of the meniscus, but also the limitations of current clinical treatment options. In addition, an overview was given of materials and fabrication strategies that have already been investigated for meniscus tissue engineering, with particular attention to hydrogels and additive manufacturing techniques. This literature study clearly showed that a successful meniscus substitute should not only be biocompatible, but should also combine high water content, suitable porosity, sufficient mechanical support, and long-term resistance to repetitive loading. This finding formed the starting point for the experimental chapters of this thesis.

In Chapter 2, the suitability of AUP4K DA, the di-acrylate-endcapped precursor with a PEG backbone molar mass of 4 000 g/mol, as a material platform for meniscus scaffold fabrication was investigated. An important part of this chapter was demonstrating that the material could form stable networks with a high degree of crosslinking. In addition, it became clear that not only the chemical composition of the hydrogel, but also the architecture of the scaffold plays a decisive role in the final behavior. Using extrusion-based 3D printing, different scaffold configurations were produced in which printing pattern, pore size, and strut diameter were systematically varied. The results showed that these parameters have a pronounced effect on compressive mechanical properties. More isotropic printing patterns and an appropriate combination of smaller pores and thicker struts resulted in stiffer constructs with higher compressive strength. This demonstrated that architectural optimization is a powerful tool for tuning mechanical properties, even when the same base material is used.

In addition to static compression tests, dynamic mechanical analyses and fatigue tests were also performed in Chapter 2. These analyses confirmed that the scaffolds exhibit a pronounced viscoelastic behavior, which is relevant for applications in a dynamically loaded joint such as the knee. At the same time, however, an important limitation was also revealed: although the compressive properties could be brought within or close to the lower reported values for meniscal tissue, resistance to prolonged cyclic loading remained insufficient. The fatigue tests made it clear that fatigue resistance remains one of the most important challenges in the further development of a clinically applicable meniscus scaffold. This chapter therefore provided not only evidence for the potential of AUP4K DA, but also a clear direction for further optimization.

Chapter 3 developed an alternative fabrication strategy to realize architectural features that are difficult to achieve with conventional direct extrusion printing. An innovative injection-moulding setup was designed, in which sacrificial moulds were fabricated from poly(lactic acid) (PLA) using hot extrusion technique. The AUP precursor solution was then injected into the porous PLA mould and crosslinked, after which the mould was selectively dissolved in chloroform to reveal the final hydrogel scaffold. This indirect approach, which, to the best of our knowledge, had not been previously applied to AUP-based hydrogel systems, enabled the fabrication of scaffolds with lateral porosity, meaning interconnected pore channels oriented parallel to the scaffold's lateral faces. This architectural feature is inaccessible via conventional layer-by-layer direct printing and is of particular relevance for meniscus tissue engineering, where nutrient transport from the vascularized outer zone toward the avascular inner region requires pore connectivity in the lateral direction. In this chapter, two related materials were investigated: AUP4K DA and AUP4K HA, the latter containing three acrylate groups per chain end instead of one, thereby providing an increased crosslinking density. Both materials were studied over a broad concentration range (30–90 wt%), enabling a systematic evaluation of the influence of functionality and concentration on scaffold properties.

The resulting scaffolds were characterized by optical microscopy and scanning electron microscopy (SEM), with the focus on morphology, pore structure, and successful removal of the mould. In addition, gel fraction and swelling degree were determined to gain insight into network formation and water uptake capacity of the different formulations. The mechanical characterization showed that increasing the polymer concentration led to stiffer scaffolds and a higher compressive strength, while deformability decreased. It was also found

that the higher functionality of AUP4K HA gave rise to a stiffer network compared with AUP4K DA, which is in line with the expectation that more reactive groups lead to a higher crosslinking density. Chapter 3 thus confirmed that not only architecture, but also subtle variations in chemical composition can be used to purposefully tune scaffold performance. Moreover, this chapter demonstrated that indirect fabrication is a valuable complement to direct 3D printing within the broader framework of meniscus scaffold development.

In Chapter 4, the AUP technology was further extended to digital light processing (DLP), a vat photopolymerization technique in which an entire layer of photocurable resin is selectively exposed and crosslinked in a single projection step using a digital micromirror device. In contrast to extrusion-based fabrication, where the architecture is determined by the sequential deposition of individual filaments, DLP enables the production of more complex, geometrically precise, and highly regular scaffold architectures with improved resolution and reproducibility. This chapter represented one of the first demonstration of DLP printing of AUP-based hydrogel materials. Two AUP systems with different PEG molar masses were investigated: AUP2K DA (PEG molar mass of 2 000 g/mol) and AUP4K DA (4 000 g/mol). The underlying rationale was that a lower molar mass, and thus a higher density of reactive end groups per unit mass, would lead to a stiffer and denser network after crosslinking, enabling the exploration of a broader range of achievable mechanical properties.

To enable DLP printing of AUP resins, visible-light-curable formulations were developed using lithium phenyl-2,4,6-trimethylbenzoylphosphinate (Li-TPO-L) as a water-soluble photoinitiator and tartrazine as a biocompatible photoabsorber, a combination that had not been previously reported for AUP systems. Rheological and photorheological analyses were used to determine

which formulations were sufficiently processable while at the same time allowing rapid and efficient network formation during exposure. Subsequently, scaffolds with a regular architecture and vertical porosity were produced, and printing parameters such as exposure time and projector power were optimized to obtain a good correspondence between the CAD design and the printed structure. The results showed that DLP is indeed a promising technique for fabricating AUP-based scaffolds with high reproducibility and good pore fidelity.

After fabrication, the printed scaffolds were subjected to extensive characterization. Thermal analysis by TGA and DSC provided additional information about the material properties before and after crosslinking. Gel fraction and swelling measurements confirmed efficient network formation and showed that water uptake, as expected, decreased with increasing crosslinking density. The mechanical tests made clear that the molar mass of the PEG segment has an important influence on the compressive behavior: scaffolds based on AUP2K generally exhibited higher compressive moduli than scaffolds based on AUP4K at comparable concentrations. For both material types, increasing concentration resulted in stiffer scaffolds, while the ultimate strain decreased. A first evaluation under cyclic loading was also performed using ring specimens, so that not only static but also dynamic performance was taken into account. Finally, a preliminary indirect cytocompatibility screening was carried out by means of MTS and live/dead assays. These results supported the further development of DLP-printed AUP scaffolds as a promising platform for meniscus applications.

Whereas the previous chapters mainly focused on material development and scaffold fabrication, Chapter 5 addressed an issue that is crucial for the practical and clinical translation of hydrogel-based

constructs, namely the influence of dehydration on final scaffold performance. Since hydrogels generally possess a high water content, it is often necessary to introduce a drying step for storage, transport, or handling. However, this step is very important, because the removal of water can be accompanied by structural changes in the network and consequently also in the mechanical behavior after rehydration. In this chapter, four different drying methods were therefore compared: freeze-drying, desiccator drying, drying in a ventilated oven, and drying in a vacuum oven.

The results clearly showed that the drying method has a pronounced effect on scaffold morphology. Freeze-drying led to an enhanced porous microstructure and resulted in a high swelling capacity after rehydration. In contrast, the oven-based result into closer or higher compressive responses compared to the freeze-dried scaffold.. Swelling behavior were also affected by the selected drying method. These results are of great importance because they demonstrate that dehydration should not merely be considered as a practical post-processing step, but as an additional process parameter that allows the final balance between porosity, water uptake, mechanical strength, and handling to be further tailored. This chapter therefore added an important translational dimension to the thesis.

When the results of all experimental chapters are considered together, a coherent picture emerges of AUP-based hydrogels as a versatile platform for the development of 3D-printed meniscus scaffolds. A first important conclusion is that the material properties can be strongly controlled through chemical parameters such as molar mass, functionality, and polymer concentration. A second important conclusion is that scaffold architecture is at least as determining as material chemistry. Printing pattern, pore size, strut diameter, and orientation directly influence the way in which loads are distributed

throughout the construct and therefore strongly determine the compressive response. A third important conclusion is that the selected fabrication route is not merely a technical production step, but also determines which architectures are feasible and which properties can ultimately be achieved. Extrusion printing, indirect injection-moulding fabrication, and DLP printing each have their own advantages and limitations, but together they demonstrate that AUP hydrogels are compatible with multiple processing strategies. Notably, several aspects of this work represent original contributions to the field: the first comprehensive multi-modal mechanical characterization of AUP hydrogel scaffolds, including fatigue testing, which identified cyclic durability as the dominant translational bottleneck; the development of a novel indirect fabrication route enabling lateral scaffold porosity; and the first translation of AUP materials to DLP-based additive manufacturing.

At the same time, this thesis also made clear that developing a functional meniscus substitute is far more complex than simply approaching a static compressive modulus. The meniscus is an anisotropic, viscoelastic, and cyclically loaded tissue, and a successful substitute must therefore not only be sufficiently strong initially, but must also retain its performance over time under repetitive loading. The fatigue results in particular show that this property currently forms the most important limitation for further clinical translation. While the static mechanical properties in several cases already approach reported values for human menisci, it remains necessary to further improve resistance to crack formation, damage accumulation, and structural failure under prolonged loading.

Based on the findings in this thesis, several directions for future research can be formulated. A first clear avenue is further optimization of the hydrogel chemistry, for example by modifying the molar mass,

increasing the functionality, or introducing alternative or secondary crosslinking mechanisms that result in a tougher network. A second avenue is further refinement of the scaffold architecture, with particular attention to anisotropic or gradient designs that better mimic the native meniscus. A third avenue lies in combining the hydrogel matrix with additional reinforcing components, such as fibers or textile structures, in order to increase resistance to circumferential stresses and prolonged cyclic loading. In addition, further biological evaluation remains necessary, both *in vitro* with relevant cell types and, in the longer term, in more physiologically relevant models.

In summary, this thesis demonstrates that AUP-based synthetic hydrogels form a strong and versatile starting point for the development of a 3D-printed scaffold for full meniscus replacement. Through a combination of material development, architectural optimization, multiple fabrication routes, and evaluation of post-processing strategies, a broad foundation was established for further progress in this research field. The obtained results confirm that it is possible to develop porous, reproducible, and mechanically tunable hydrogel structures that are promising for meniscus applications. At the same time, they make clear that further optimization, particularly about fatigue resistance and long-term functional performance, remains essential. Nevertheless, this work provides a solid foundation for the next development steps toward a clinically relevant synthetic scaffold for full meniscus replacement.

Chapter 1:

An introduction to biomaterials and 3D printing techniques for the fabrication of meniscal tissue engineering scaffolds

This chapter introduces the main concepts related to meniscus tissue engineering. It discusses the structure and function of the native meniscus, the current challenges associated with meniscal injuries, and the potential of biomaterials and additive manufacturing for scaffold development. Finally, an overview is given of the polymer systems and 3D printing techniques relevant to this thesis.

1.1 Problem statement

Meniscus injuries are some of the most frequent injuries and can lead to significant functional impairment in the knee [1]. Current clinical interventions, such as partial meniscectomy (removal of the damaged meniscal tissue) or meniscal repair, often fall short due to incomplete healing, loss of meniscal function, and the potential for long-term joint degeneration [2]. These limitations underscore the urgent need for innovative approaches in meniscus tissue engineering (TE) to restore the native function and biomechanics of the meniscus.

More recently, the promising TE approach where cells, growth factors and scaffolds are elegantly combined for the development of new more performing biomedical implants has been investigated in the field of meniscus regeneration [3]. The primary objective is to develop a TE meniscus that closely mimics the native meniscus in terms of its structural, functional, and biomechanical properties [4]. The choice of the scaffold material for this approach is crucial. The material should facilitate integration with the surrounding knee tissue, support cell viability and proliferation, and withstand the mechanical stresses encountered during daily activities and athletic endeavours [5]. As versatile materials, hydrogels have gained significant attention in the TE field. Their properties can be adjusted to resemble native extracellular matrices, creating an appropriate microenvironment. Similar to the meniscus nature, hydrogels consist of fluid, due to their hydrophilicity, and a solid component, which allows them to mimic the structure of meniscal tissue. These intrinsic characteristics position hydrogels as a potential solution for therapeutic strategies in the repair and regeneration of the meniscus [6]. Hydrogels are viewed as one of the most suitable materials for creating a scaffold to substitute the menisci [7].

Among the various scaffold manufacturing techniques, additive manufacturing (AM) technologies enable the reproducible fabrication of scaffolds with different properties. More specifically, the properties of the scaffolds can vary significantly depending on the 3D printing techniques employed. Different printing methods can influence the mechanical properties, the porosity, and the overall structural integrity of the scaffold [8]. This variability allows for the customization of scaffolds to better mimic the meniscus native tissue, enhancing their potential for successful TE applications.

The objective of this PhD project is to develop novel photo-crosslinkable hydrogel precursors that could be utilized with various printing techniques (bioplotting, digital light processing, injection moulding) to fabricate a hydrogel scaffold. Indeed, depending on the properties of the precursors used - such as melting point, viscosity, thermal stability, etc. - only certain printing techniques may be applicable. The developed scaffold will subsequently be subjected to an in-depth mechanical evaluation, including tensile, compression, dynamic mechanical analysis (DMA), and fatigue tests, to replicate the properties of the native meniscus. This comprehensive assessment will offer unprecedented opportunities for advancements in meniscus tissue engineering.

A detailed description of the sub-objectives is given in paragraph 1.9 of this chapter.

1.2 Anatomy of the meniscus

The meniscus is a crescent-shaped fibrocartilaginous structure found in several joints, most notably in the knee [9]. Each knee joint contains two menisci: the medial meniscus and the lateral meniscus (Figure 1.1). The medial meniscus is situated on the inner (medial) side of the knee. It is firmly attached to the joint capsule, which limits its mobility and makes it more susceptible to injury when the knee twists or turns. In contrast, the lateral meniscus is located on the outer (lateral) side of the knee. It has a more circular shape and is not as tightly bound to the capsule, allowing for greater mobility. This increased flexibility makes the lateral meniscus less prone to tears compared to the medial meniscus [10,11].

Although the menisci are distinct structures, they function as an extension of the tibial plateau, enhancing the relative depth of the tibial articular surface. Positioned on the peripheral rim of the tibial condyles, the menisci extend into the centre of the joint. They are triangular in cross-section, featuring a thicker, more convex peripheral region that gradually tapers to a thin, free edge centrally [12,13].

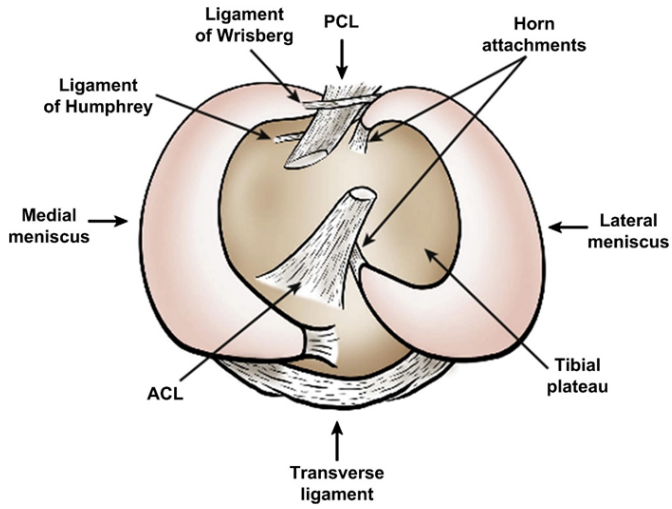

Figure 1.1: Meniscal Anatomy from a Superior Tibial Plateau Perspective [14].

The vascularization of the meniscus is a critical aspect of its anatomy and healing capacity. The menisci of an adult knee are relatively avascular structures, meaning they have limited blood supply. This vascular pattern is strongly related to their ability to heal. In its structure, three zones can be distinguished based on its vascularization (Figure1.2) [15].

- Red-Red Zone: The outermost one-third of the meniscus, which has an abundant blood supply. This zone has the highest potential for healing due to its rich vascularization.
- Red-White Zone: The middle one-third of the meniscus, which has a moderate blood supply. The healing potential in this zone is limited compared to the red-red zone.
- White-White Zone: The innermost one-third of the meniscus, which is avascular (lacking blood supply). This zone has the least potential for healing [16].

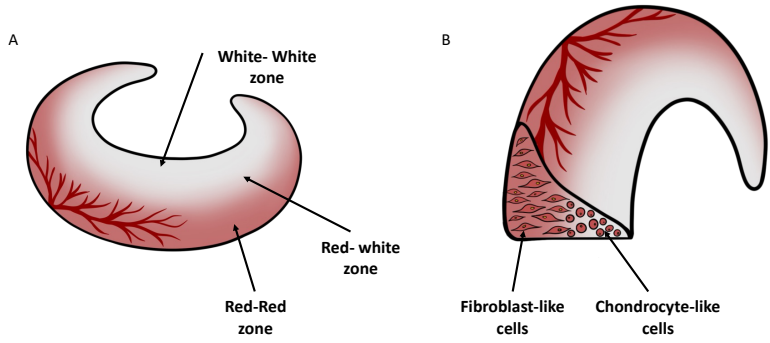

Figure 1.2: Regional Differences in Meniscal Vascularization and Cellular Composition. Left: At birth, the meniscus is entirely supplied by blood vessels, but this vascular network diminishes with age. In adults, the majority of vascularization is confined to the peripheral red-red zone. Right: The outer portion of the meniscus, which retains vascular supply (red-red zone), contains elongated cells with visible processes, resembling fibroblasts. In contrast, the middle (white-red) and inner (white-white) regions host cells that are more like chondrocytes, although they differ from true chondrocytes in phenotype [17].

The blood supply to the menisci comes from branches of the medial and lateral geniculate arteries, which form a perimeniscal capillary plexus in the synovium and joint capsule, supplying the peripheral portion of the meniscus [16,18].

This specific distribution of the vascular network is associated with a distinct biochemical composition. The inner part predominantly consists of cartilaginous-like tissue, mainly composed of type II collagen. In contrast, the outer part is primarily made up of fibrous-like tissue, which is rich in type I collagen. Due to this unique collagen composition, the mechanical properties and healing capacity of the meniscus vary by zone: the avascular zone offers higher resistance to compression but has a reduced healing capacity, while the vascular zone provides greater resistance to tension and better healing potential [19].

Understanding the vascularization of the meniscus is essential for developing effective treatment strategies for meniscal injuries, as the healing potential varies significantly across different zones.

1.3 Meniscus biochemical content

The meniscus is predominantly hydrated, consisting of approximately 72% water. The remaining 28% is composed of organic matter, primarily extracellular matrix (ECM) and cells. Typically, collagens constitute about 75% of this organic matter, while glycosaminoglycans (GAGs) make up around 17%, DNA accounts for 2%, and adhesion glycoproteins and elastin each constitute less than 1%. These proportions can vary depending on factors such as age, injuries, and other pathological conditions [14].

Due to the presence of collagen fibres in the meniscus structure, it is possible to distinguish different layers (Figure 1.3) [20].

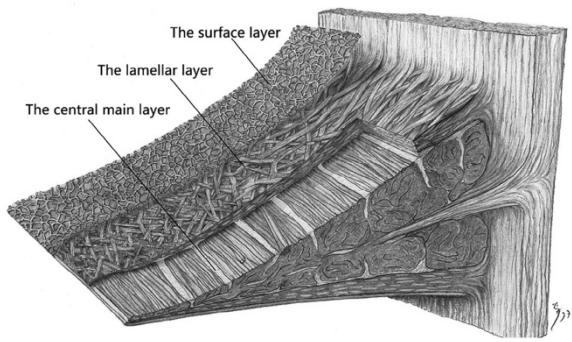

Figure 1.3: Representation of Collagen Fibre Ultrastructure in the Meniscus [20].

The orientation of collagen fibres is related to the mechanical properties of the menisci and their tearing patterns. Histological evaluation of meniscal sections reveals three distinct layers. The superficial layer, present on both the tibial and femoral surfaces, is composed of a thin collagen fibre network. Beneath this reticular layer lies the lamellar layer, also present on both the femoral and tibial sides. In the lamellar layer, collagen fibres are radially oriented at the outer parts of the anterior and

posterior horns, while at the inner parts, they intersect at various angles. The main part of meniscal tissue is situated between the two lamellar layers, where the collagen fibres are circumferentially oriented throughout the menisci. Additionally, a few radial fibres connect the circumferential collagen fibres to each other [20–22].

The literature does not provide a uniform classification for meniscal cells. Histological examination of the inner white zone of the menisci reveals rounded cells that behave similarly to fibrochondrocytes or chondrocyte-like cells. In contrast, the cells in the outer red zone are oval or fusiform in shape and can be classified as fibroblasts. Additionally, a third cell population has been identified in the superficial zone of the meniscus. These cells are flattened and fusiform, lacking extensions. While their exact purpose is still unknown, it has been suggested that they might be progenitor cells that confer regenerative capacity to the structure [23,24].

1.4 Biomechanics of the Menisci

Understanding the biomechanical properties of meniscal tissue *ex vivo* is essential, especially for developing effective meniscus replacements or therapeutic strategies that mimic the natural mechanical characteristics of the meniscus [25].

When a load is applied to the knee joint, it generates a compression stress on the menisci. This stress is counteracted by the elastic properties of the collagen fibres and the matrix. Initially, the load is resisted by these elastic components, but over time, the fluid within the meniscus is extruded, and the tissue begins to deform, a process known as creep [26,27].

As the menisci are compressed and held, the required load to maintain this compression decreases due to tissue relaxation, a process

referred to as stress relaxation. Both creep and stress relaxation are characteristics of viscoelastic materials [27].

When the knee joint is subjected to compressive stresses, such as during walking, running, or jumping, the meniscus experiences an outward radial force. This force tends to push the meniscus radially away from the center of the joint towards the outer edges.

To counteract the radial stress, the circumferentially arranged collagen fibres generate tension, known as *hoop stress*. These hoop stresses create a compressive force that acts inward, towards the center of the meniscus. This inward compressive force prevents the meniscus from being extruded or displaced from the joint space. The compression stress across the knee, transmitted from the femur through the meniscus to the tibia, generates tension along the circumferential collagen fibres within the meniscal tissues (Figure 1.4) [28,29].

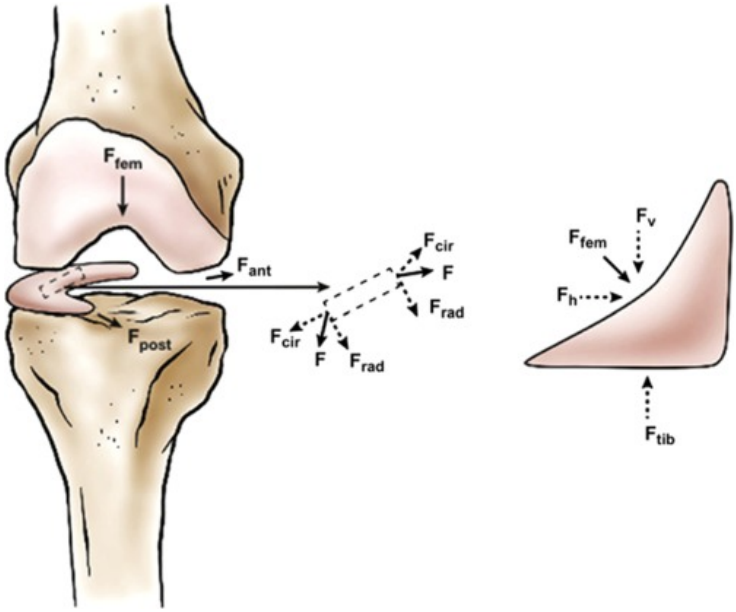

Figure 1.4: Free body diagram of stress acting on the knee meniscus during loading. Under normal loading conditions, the meniscus is compressed by the downward stress exerted by the femur. This compression causes the meniscus to deform radially, while its anterior and posterior horns (F_{ant} and F_{post}) anchor it in place. During this process, tensile, compressive, and shear stress are generated. Radial deformation leads to a tensile hoop stress (F_{cir}), while vertical and horizontal stress (F_v and F_h) arise from the femur compressing the curved superior surface of the meniscus. A radial reaction stress (F_{rad}) counteracts the femoral horizontal stress (F_h) [14].

Numerous studies have shown that when the meniscus is intact, the load and the dynamic stresses during walking, running etc. are well-distributed across the knee joint. However, its removal leads to a significant decrease in the contact area of the femoral condyle and a substantial increase in contact stress [30]. Research has indicated that a total lateral meniscectomy can result in a 40-50% reduction in contact area and a 200-300% increase in contact stress in the lateral compartment. This significant rise in load per unit area may contribute to accelerated damage and degeneration of the articular cartilage [11,31,32].

1.4.1 Mechanical properties of the Meniscus

The menisci possess unique properties attributed to their complex structure, tissue composition, and geometry. Gaining a deep understanding of their mechanobiology could provide valuable insights for developing innovative meniscal implants [33,34].

Various approaches have been employed over the years to assess the properties of the meniscus. The meniscus displays a non-linear stress-strain relationship, particularly in the toe region, which complicates the prediction of its in-situ mechanical responses [33,35]. The tensile elastic modulus, the compressive modulus, the peak strain and the peak stress have been investigated in various studies. Although these properties are useful, defining the appropriate range for calculating the elastic modulus is challenging due to the anisotropic nature of the meniscus. Most studies have focused on explanted menisci under different conditions (e.g., hydrated versus non-hydrated, sliced versus intact, natural versus decellularized), and the results of these tests are highly dependent on these conditions. Consequently, and very unfortunately, the results are often difficult to compare. In this thesis, literature searches were exclusively focused on human meniscus-related research, deliberately excluding any studies involving animal models. The selected time frame for this review spans from 1995 to 2023, ensuring a comprehensive examination of the advancements in this area over nearly three decades.

The studies highlighted in Table 1.1, indicate how the anisotropy of the tissue influences the test results. Both the portion of the tissue from which the samples are taken and the orientation of the collagen fibres are key factors in understanding the differences in the obtained results. The data summarized in Table 1.1 represent the outcomes of several studies on the tensile properties of human menisci.

Table 1.1: Comparative Analysis of Tensile Properties of the Human Meniscus from Various Studies.

	Specimen		Test Parameters					Results
Reference	**Lateral / Medial**	**Location of Sample**	**Shape**	**Method of layering**	**Method of cutting / punching**	**Thickness (mm)**	**Direction of Loading**	**Elastic Tensile Modulus ET (in MPa)**
Henderson et al. [36]	Medial	P, M	DB	Deli slicer	Custom punch	0.90	Cir	MA+MP= 101.7 ± 71.60
								MA+MP= 47.5 ± 12
Yin et al. [37]	Medial	C	R	-	-	-	Cir	AH: 0.18 ± 0.08
								PI: 0.23 ± 0.09
								PH: 0.11 ± 0.04
Nesbitt et al. [38]	Lateral	P, M	DB	Deli slicer	Custom punch	0.73 (0.09)	Cir	MA+MP= 109.9 ± 40.8

						0.70 (0.15)		MA+MP= 97.2 ± 33.8
						0.80 (0.15)	Axial	MA+MP= 1.67 ± 0.67
						0.81 (0.14)		MA+MP= 1.05 ± 0.96
Ahmad et al. [39]	Lateral	P	ENTIRE	-	-	6.69 (1.35)	Cir	Entire: 85.26 ± 43.43
						7.43 (0.40)		Entire: 54.17 ± 19.54
	Medial					7.83 (0.60)	Cir	Entire: 88.72 ± 44.74
						7.72 (1.70)		Entire: 69.17 ± 35.55
Yan et al. [40]	Medial	I	ENTIRE	-	-	-	Cir	Entire: 15.09 ± 11.27
		I-M						Entire: 29.01 ± 17.79
		P-M						Entire: 46.05 ± 20.67
		P						Entire: 46.04 ± 25.51
Freutel et al. [41]	Lateral	C	DB	Microtome	Custom punch	1.00 (0.20)	Cir	AH-ARA: 62.35 ± 35.18 PH- PRA: 47.43 ± 22.59

	Medial							AH-ARA: 59.36 ± 28.37 PH- PRA: 67.56 ± 36.44
	Lateral	T						AH-ARA: 73.87 ± 39.05 PH- PRA: 89.31 ± 73.06
	Medial							AH-ARA: 92.47 ± 69.11 PH- PRA: 107.41 ± 73.96
Tanaka et al. [42]	Medial	C	ENTIRE	Cryostat microtome	Cryostat microtome	1.00 (-)	Cir	Entire: 97.7 ± 21.8
Quiroga et al. [43]	Medial	F, C, T	R	Cryostat microtome	Cryostat microtome	0.1-1.0	Cir	MA: 27.6 ± 1.26 MP: 18.38 ± 1.04
Abraham et al. [44]	Lateral	-	R	-	Custom drop-cutter	-	Rad	ARA:1.21 ± 0.46 PRA:1.21 ± 0.56
	Medial							ARA: 1.35 ± 0.76 PRA:6.42 ± 0.78
Hauch et al. [45]	Lateral	-	-	N.a.	N.a.	-	Cir	Entire: 139.93 ± 109.3

	Medial							Entire: 179.67 ± 131.68
Bursac et al. [46]	Lateral	P	ENTIRE	Scalpel	Scalpel	3.70 (0.30)	Cir	Entire: 80.9 ± 24.6
	Medial							Entire: 65.5 ± 18.2
Lechner et al. [47]	Medial	P, M	DB	Sledge microtome (frozen)	Custom punch	0.50 (-)	Cir	AH: 141.2 ± 56.7 PI: 116.4 ± 47.5 PH: 108.4 ± 42.9
						1.50 (-)		AH: 104.6 ± 63.8 PI: 93.9 ± 49.1 PH: 60.7 ± 40.6
						3.00 (-)		AH: 72 ± 95.2 PI: 43.4 ± 26.8 PH: 67.1 ± 75.7
		P				0.50 (-)		AH+PI+PH: 116.9 ± 58.2
						1.50 (-)		AH+PI+PH: 73.5 ± 49.9
						3.00 (-)		AH+PI+PH: 52.5 ± 44.5
		M				0.50 (-)		AH+PI+PH: 120.3 ± 27.4
						1.50 (-)		AH+PI+PH: 93.8 ± 25.2

						3.00 (-)		AH+PI+PH: 42.9 ± 25.6
Tissakht and Ahmed [48]	Lateral	F	R	Scalpel	Scalpel (using a rectangular guide & optical microscope)	1.50 - 2.00	Cir	AH: 124.58 ± 39.51 PI: 91.37 ± 23.04 PH: 143.24 ± 55.04
		C						AH: 88.01 ± 31.47 PI: 67.68 ± 10.7 PH: 95.8 ± 46.83
		T						AH: 112.23 ± 29.77 PI: 151.8 ± 44.78 PH: 130.24 ± 32.65
	Medial	F						AH: 106.21 ± 47.53 PI: 77.95 ± 25.09 PH: 82.36 ± 22.23
		C						AH: 79.86 ± 24.90

								PI: 57.97 ± 19.08 PH: 80.72 ± 23.95
		T						AH: 87.61 ± 10.12 PI: 94.54 ± 19.48 PH: 80.35 ± 27.16
	Lateral	F				0.80 - 2.00	Rad	AH: 10 ± 4.29 PI: 14.17 ± 5.88 PH: 14.62 ± 9.62
		C						AH: 4.07 ± 1.86 PI: 10.14 ± 5.88 PH: 4.21 ± 1.26
		T						AH: 13.01 ± 8.76 PI: 13.24 ± 6.96 PH: 21.24 ± 6.3
	Medial	F						AH: 6.75 ± 5.15 PI: 9.31 ± 7.46 PH: 13.53 ± 8.44
		C						AH: 3.59 ± 1.43 PI: 5.6 ± 2.23 PH: 2.03 ± 0.54
		T						AH: 9.50 ± 6.35

								PI: 16.51 ± 9 PH: 22.62 ± 7.18
Fithian et al. [49]	Lateral	P, M	DB	Sledge microtome	Special cutting die	0.40 (-)	Cir	AH: 159.58 ± 26.20 PI: 93.18 ± 52.4 PH: 110.23 ± 40.7
	Medial							AH: 159.07 ± 47.4 PI: 228.79 ± 54.4 PH: 294.14 ± 9.4
Bullough et al. [50]	Mixed	F, T	R	Cryostat microtome	Cryostat microtome	0.09 -0.2	Cir	AH: 8.06 ± 3.93 PI: 4.22 ± 2.17 PH: 5.42 ± 2.79
							Rad	AH: 0.8 ± 0.17 PI: 1.47 ± 1.22 PH: 1.13 ± 0.68
Warnecke et al. [51]	Lateral	P	DB	-	Custom punch	-	Cir	*

Jacquet et al. [52]	Lateral	F, T	ENTIRE	-	-	-	Cir	ENTIRE: 11.66 ± 0.97 ENTIRE: 19.97 ± 1.37 ENTIRE: 45.25 ± 1.39
Fischenich et al. [53]	Lateral Medial	P, M	DB	Custom drop-cutter	Custom punch	1.00 (-)	Cir	*

Where * means graphical data available, ARA means anterior root attachment, AH means anterior horn, PI means pars intermedia, PH means posterior horn, PRA means posterior root attachment, ARA-AH means transition zone between ARA and AH, PRA-PH means transition zone between PRA and PH, MA means mid-anterior zone, MP means mid-posterior zone, F means femoral layer (axial plane), C means central layer (axial plane), T means tibial layer (axial plane), P means peripheral layer (radial plane), M means middle layer (radial plane), I means inner layer (radial plane), DB means dumbbell shaped specimen, R means rectangular shaped specimen, Cir means circumferential, Rad means radial, Cr means cryopreservation, and N.a. means not applicable.

The data reveals several key trends in the elastic tensile modulus (ET) of the human meniscus, highlighting variability based on anatomical location, loading direction, conservation method, and sample thickness. The medial meniscus generally exhibits a higher variability in ET values compared to the lateral meniscus, as demonstrated by Henderson et al. and Nesbitt et al. [36,38]. Circumferential loading tends to produce more consistent ET values than radial loading, with Ahmad et al. showing more stable medial meniscus results under circumferential conditions [39]. Conservation methods also significantly influence ET values, with deep-frozen samples generally displaying lower ET values compared to frozen samples. Furthermore, thicker samples are associated with higher ET values, reinforcing the findings of Ahmad et al. who reported increased ET values for thicker medial meniscus samples [39].

A second mechanical property that has been frequently studied is the compressive modulus. Table 1.2 shows the results of compressive tests on human menisci. The reported compressive elastic modulus

(EC) in the axial direction of both the lateral and medial meniscus was significantly influenced by the level of applied load, the thickness and the geometry of the samples, the conservation and the strain at the point of evaluation.

Table 1.2: Comparative Analysis of Compressive Moduli of the Human Meniscus from Various Studies.

Study detail	Specimen		Testing protocol				Results
Reference	**Lateral / medial**	**Location of Sample**	**Shape**	**Direction of loading**	**Load / strain level**		**Elastic compressive modulus EC (in MPa)**
					Applied	**Evaluation**	
Truhn et al. [54]	Lateral	C	Cylindrical	Axial	100% strain	20% strain	AH + Pi + PH: 17.30 ± 11.20
						80% strain	AH + Pi + PH: 299.6 ± 70.8
Jacquet et al. [52]	Lateral	-	Cuboidal	Axial	50 N	-	PI: 28.86 ± 0.77
							PI: 37.26 ± 1.08
							PI: 37.26 ± 1.08
Fischenich et al. [53]	Lateral	F	-	Axial	12%	-	*
	Medial						
Seitz et al. [55]	Lateral	F	-	Axial	0.5 mm	-	*
	Medial						
Berni et al. [56]	Lateral	C	Cuboidal	Axial	2, 4, 6, 8, 10% strain	-	*
				Cir			
				Rad			

Pordzik et al. [57]	Mixed	F	-	Axial	0.5 mm	-	PH: 0.13 ± 0.07 **
Nebelung et al. [58]	Lateral	C	Cylindrical	Axial	100% strain	20% strain	PI: 16.5 ± 7.71
						80% strain	PI: 349. 4 ± 49.97
Chia and Hull. [59]	Medial	C	Cuboidal	Axial	3% strain	12% strain	AH: 0.14 ± 0.22 PI: 0.06 ± 0.06 PH: 0.04 ± 0.61
					6% strain		AH: 0.28 ± 0.44 PI: 0.13 ± 0.14 PH: 0.08 ± 0.16
					9% strain		AH: 0.57 ± 0.88 PI: 0.30 ± 0.37 PH: 0.18 ± 0.38
					12% strain		AH: 1.13 ± 1.64 PI: 0.67 ± 0.80 PH: 0.36 ± 0.74
				Radial	3% strain		AH: 0.1 ± 0.12 PI: 0.05 ± 0.04 PH: 0.08 ± 0.09
					6% strain		AH: 0.2 ± 0.23 PI: 0.11 ± 0.08 PH: 0.11 ± 0.13
					9% strain		AH: 0.45 ± 0.5 PI: 0.24 ± 0.2 PH: 0.18 ± 0.19

					12% strain		AH: 0.97 ± 1.01 PI: 0.55 ± 0.51 PH: 0.3 ± 0.31
Leslie et al. [60]	Mixed	C	Cuboidal	Cir	1500 N	20%	MA+MP: 10.00
						80%	MA+MP: 288.00
				Rad		20%	MA+MP: 13.00
						80%	MA+MP: 287.00
				Axial		20%	MA+MP: 19.00
						80%	MA+MP: 299.00
Sweigart et al. [61]	Medial	F	-	Axial	0.02-0.04 N	-	**AH: 150 ± 30 **PI: 100 ± 30 **PH: 110 ± 20
		T					**AH: 160 ± 50 **PI: 110 ± 40 **PH: 90 ± 30

Where * means graphical data available, ** means Aggregate modulus Ha, ARA means anterior root attachment, AH means anterior horn, PI means pars intermedia, PH means posterior horn, PRA means posterior root attachment, MA means mid-anterior zone, MP means mid-posterior zone, F means femoral layer (axial plane), C means central layer (axial plane), T means tibial layer (axial plane), OA means osteoarthritis, UC means unconfined compression, CC means confined compression, I means indentation, SR means stress relaxation, CR means creep, Cir means circumferential, Rad means radial.

The mechanical properties of soft tissues exhibit significant variability influenced by strain levels, anatomical regions, conservation methods, and testing protocols. A nonlinear increase in stiffness was observed across studies, with the elastic modulus escalating from 17.3 ± 11.2 MPa at 20% strain to 299.6 ± 70.8 MPa at 80% strain (Truhn et al.). Axial loading consistently yielded higher stiffness compared to radial and circumferential directions, reflecting directional dependence of tissue structure (Chia and Hull). Preservation techniques, such as deep freezing, enhanced stiffness compared to cryopreservation, with values increasing from 28.86 ± 0.77 MPa to 37.26 ± 1.08 MPa for the pars intermedia (Jacquet et al.) that refers to the middle third of the meniscus, situated between anterior horn and the posterior horn. Regional variability was evident, with aggregate moduli ranging from 90 ± 30 MPa to 160 ± 50 MPa across different zones of the tibial and femoral layers (Sweigart et al.). These findings underscore the complex interplay between biomechanical properties and experimental conditions, highlighting the need for standardized protocols to ensure reproducibility and accurate modeling of tissue mechanics.

As indicated higher (§ 1.4) the meniscus exhibits viscoelastic behaviour [62] and several studies assessed the determination of the

storage modulus (E') and the loss modulus (E''). The elastic storage modulus (E') is the ratio of the elastic stress and strain, which indicates the ability of a material to store energy elastically [63]. The loss modulus is a measure of the energy dissipated or lost per cycle of sinusoidal deformation [64]. An overview of the obtained dynamic properties of human menisci are summarized in Table 1.3.

Table 1.3: Dynamic properties of human menisci

Study detail	Specimen		Testing protocol				Results		
Reference	**Lateral / medial**	**Location of Sample**	**Shape**	**Direction of loading**	**Rate/ Frequency (in Hz)**	**Strain level**	**Storage modulus (in MPa)**	**Loss modulus (in MPa)**	**Dynamic Modulus (in MPa)**
Ala-Myllymäki et al. [65]	Mixed	F	-	Axial	1	20 ± 2% (C ± C)	-	-	AH+PI+PH: 0.8 ± 0.13
Nordberg et al. [66]	Mixed	M	Cylindrical	Axial	Mixed (0.1, 1, 10)	10 ± 1% (C ± C)	-	-	AH+PI+PH: 0.41 ± 0.35
						20 ± 1% (C ± C)			AH+PI+PH: 0.75 ± 0.66
Gaugler et al. [67,68]	Mixed	I	-	Axial	0.1	-	-	-	AH+PI+PH: 0.37 ± 0.37
		M			0.1				AH+PI+PH: 0.29 ± 0.23
		P			0.1				AH+PI+PH: 0.17 ± 0.11

Danso et al. [68,69]	Lateral	F	-	Axial	0.10	20 ± 2% (C ± C)	-	-	AH: 0.63 ± 0.57 PI: 0.6 ± 0.36 PH: 0.57 ± 0.32
					1.00				AH: 0.69 ± 0.63 PI: 0.65 ± 0.38 PH: 0.64 ± 0.33
	Medial				0.10				AH: 1.18 ± 0.78 PI: 0.48 ± 0.28 PH: 0.74 ± 0.37
					1.00				AH: 1.3 ± 0.73 PI: 0.42 ± 0.23 PH: 0.69 ± 0.32
Pereira et al. [68,70]	Lateral	-	Cylindrical	Axial	0.10	0.05 mm (C)	AH: 0.46 ± 0.90 PI: 0.47 ± 0.68 PH: 0.71 ± 0.91	AH: 0.07 ± 0.12 PI: 0.07 ± 0.09 PH: 0.11 ± 0.14	-
					1.00		AH: 0.48 ± 0.93 PI: 0.48 ± 0.7 PH: 0.75 ± 0.95	AH: 0.06 ± 0.09 PI: 0.05 ± 0.07 PH: 0.09 ± 0.11	
					10.00		AH: 0.51 ± 1.0	AH: 0.07 ± 0.12	

							PI: 0.52 ± 0.75 PH: 0.80 ± 1.02	PI: 0.07 ± 0.09 PH: 0.11 ± 0.14	
	Medial				0.10		AH: 0.28 ± 0.46 PI: 0.82 ± 1.43 PH: 0.57 ± 1.16	AH: 0.05 ± 0.08 PI: 0.12 ± 0.20 PH: 0.10 ± 0.21	
					1.00		AH: 0.30 ± 0.48 PI: 0.88 ± 1.51 PH: 0.61 ± 1.27	AH: 0.04 ± 0.03 PI: 0.10 ± 0.16 PH: 0.09 ± 0.18	
					10.00		AH: 0.32 ± 0.52 PI: 0.92 ± 1.61 PH: 0.66 ± 1.37	AH: 0.06 ± 0.09 PI: 0.13 ± 0.20 PH: 0.11 ± 0.21	
Pillai et al.[71]	Mixed	-	Cuboidal	Axial	0.1	1% (S)	AH+PI+PH: 1.03 ± 0.75	AH+PI+PH: 0.22 ± 0.25	-

					1		AH+PI+PH: 1.37 ± 0.88	AH+PI+PH: 0.24 ± 0.26	
					10		AH+PI+PH: 9.97 ± 8.67	AH+PI+PH: 0.26 ± 0.09	
Bursac et al. [68,72]	Lateral	M	Cylindrical	Axial	1	20 ± 0.2% (C ± C)	AH: 0.83 ± 0.15 PI: 0.96 ± 0.15 PH: 1.21 ± 0.17	-	-
							AH: 1.3 ± 0.73 PI: 0.42 ± 0.23 PH: 0.69 ± 0.32		-
	Medial				0.1		-		AH+PI+PH: 0.92 ± 0.68
	Mixed				1		-		AH+PI+PH: 1.04 ± 0.44

Where * means graphical data available, AH means anterior horn, PI means pars intermedia, PH means posterior horn, M means middle layer (axial/radial plane), F means femoral layer (axial plane), I means inner layer (radial plane), P means peripheral layer (radial plane), C means compression, S means shear, and DMA means dynamic mechanical analysis.

Dynamic mechanical analysis of soft tissues reveals frequency- and strain-dependent behavior, alongside significant regional and layer-specific variability. The storage modulus, a measure of tissue stiffness, increases markedly with loading frequency, ranging from 1.03 MPa at 0.1 Hz to 9.97 MPa at 10 Hz, as reported by Pillai et al [71]. This trend indicates enhanced resistance to deformation under faster cyclic loading. Similarly, the dynamic modulus increases with strain, reflecting strain-dependent stiffening, as observed by Nordberg et al., where the modulus rose from 0.41 MPa at 10% strain to 0.75 MPa at 20% strain [66]. Regional variability is evident, with medial samples exhibiting higher moduli compared to lateral samples. Danso et al. reported medial anterior horn values of 1.18 MPa compared to 0.63 MPa in lateral samples at 0.1 Hz and 20% strain [69]. Additionally, stiffness varies across tissue layers, with inner layers exhibiting higher moduli than peripheral layers. While the loss modulus shows minor increases with frequency, it remains consistently lower than the storage modulus, underscoring the viscoelastic nature of tissues with energy storage dominating over dissipation.

The values represented in Tables 1.1-1.3 clearly illustrate the differences between various studies and the diverse values obtained from different tests. Despite these variations, the findings from numerous studies are crucial for a better understanding of the biomechanical properties of a healthy meniscus and provide a rationale for developing new meniscus replacement devices.

1.5 Meniscal lesions

Meniscus injury is the most frequent orthopaedic injury. Indeed, these injuries include 50% of all knee surgeries with 1.7 million meniscus surgeries performed annually in the EU and USA [2,73]. In 2021, the global market for meniscus repair systems was valued at $458.6 million. It is projected to grow at a compound annual growth rate (CAGR) of 8.6%, reaching $1,046.6 million by 2031 [74].

Mechanical failure of the meniscal tissue is the most common type of meniscal injury, typically resulting from chronic degeneration or acute trauma, which leads to a meniscus tear. Traumatic injuries cause acute tears due to forced movements. Conversely, degenerative meniscal lesions often occur due to eventual decompensation following minor trauma or even without any traumatic event due to aging of the tissue. These lesions are characterized by macroscopic and microscopic alterations known as myxoid degeneration [75–77].

There are different classification systems for meniscal injuries (Figure 1.5), each focusing on specific features of the meniscus structure, such as its morphology, vascularization, injury pattern, and anatomical site. Regarding tear types and orientations, distinctions can be made between vertical/longitudinal, flap, oblique, radial/transverse, and degenerative tears [78].

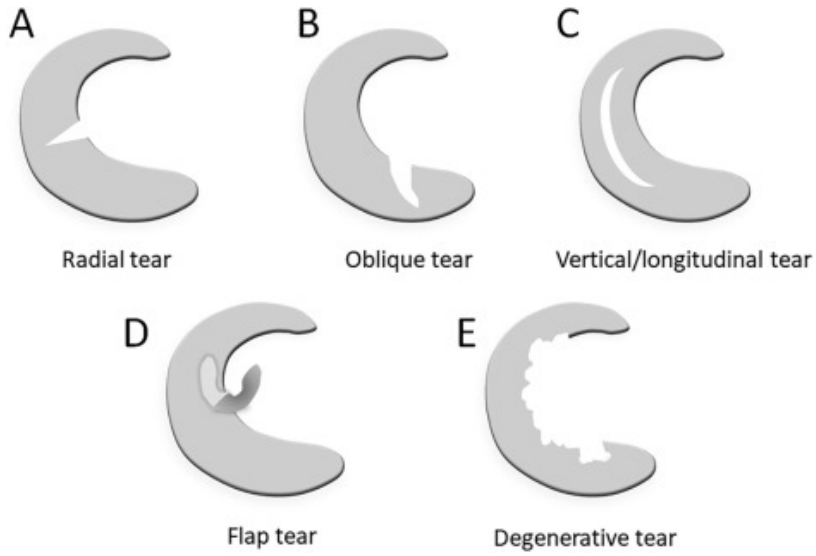

Figure 1.5: Illustration of the most common types of meniscus tears [79].

The biomechanical significance of the meniscus as a stabilizer and shock absorber in the knee joint has been well-documented by numerous studies. When the meniscus is partially or completely injured, an inflammatory response can be observed in the joint. A damaged meniscus may lead to cartilage overload and/or damage leading to chronic joint degeneration resulting in osteoarthritis (OA). Research has shown that even a small loss of meniscal tissue, such as 16-34%, can result in a 350% increase in contact stress during load transfer. This highlights the importance of maintaining an intact and functional meniscus [80,81].

The meniscus tissue was previously thought to be a redundant, vestigial structure that could be removed with minimal consideration [82]. Although total meniscectomy was once a common practice, it has largely been abandoned due to disappointing long-term results associated with acceleration of knee osteoarthritis. Major meniscectomy has been associated with adverse effects, including the degradation of underlying articular cartilage and the subsequent

development of early osteoarthritis [34,83]. Nowadays, unless painful locking and hydrops of the knee occur too frequently, conservative management is recommended for tears in the highly vascular areas of the meniscus, specifically the red/red zone or the outer 30% of the medial meniscus and 25% of the lateral meniscus [84].

In recent years, to mitigate the inevitable joint degeneration following meniscectomy, experimental and clinical studies have been focused on finding a safe substitute for an irreparably torn meniscus. Consequently, various approaches have been developed and adapted for meniscus repair and regeneration. However, arthroscopic partial meniscectomy (APM) is currently the most commonly performed orthopedic procedure worldwide. Recent studies have demonstrated that the outcomes of APM are not surpassing those of sham or placebo surgeries [84,85].

In addition to the aforementioned surgical repair, other options are being explored, including:

- Gene therapy and growth factor addition [86];
- Intra-articular cell delivery [87];
- Meniscal replacement: allograft/autograft transplantation [88–90]. Studies have shown that MAT provides good short-term clinical outcomes, particularly in patients with intact articular cartilage, as it helps restore load distribution and knee stability. However, the procedure remains scarce due to the limited availability of suitable donor grafts, strict size-matching requirements, and the need for a well-equipped surgical center for proper graft preservation and implantation [88,89,91].
- Tissue engineering: meniscal scaffold/implant [5,6,90,92,93].

More recently, the use of tissue engineering, which employs either natural or synthetic matrices as a three-dimensional scaffold to direct

tissue repair or regeneration, shows considerable promise potential for the regeneration of the meniscus and will hence be discussed in the next paragraph.

1.6 The role of tissue engineering in meniscus repair and replacement

Over the past few decades, tissue engineering (TE) has developed as a promising alternative to address the challenges related to organ and tissue transplantation [94]. The term "tissue engineering" was officially defined in a National Science Foundation (NSF) workshop (United States) in 1988 as "*the application of principles and methods of engineering and life sciences toward fundamental understanding of structure-function relationships in normal and mammalian tissues and the development of biological substitutes to restore, maintain or improve tissue function*" [95].

One of the first milestones toward modern tissue engineering was the first successful bone graft implantation by the Dutch surgeon Job van Meekeren in the 17th century. More specifically, he performed a heterologous graft surgery by inserting a fragment of dog skull into the skull of an injured soldier. The surgery was successful but after some time the soldier asked the surgeon to remove the fragment because he was excommunicated from the church due to the fact that he had received an animal graft. Therefore, the fragment was removed, and it was possible to observe the success of the operation because it was completely incorporated into the skull [96].

The first significant attempt at tissue engineering is often credited to Joseph Vacanti and Robert Langer in the late 1980s. They developed a technique to create a biodegradable scaffold seeded with cells, which was implanted under the skin of a mouse. This experiment, famously

known as the "Vacanti mouse," involved growing a human ear on the back of a mouse.

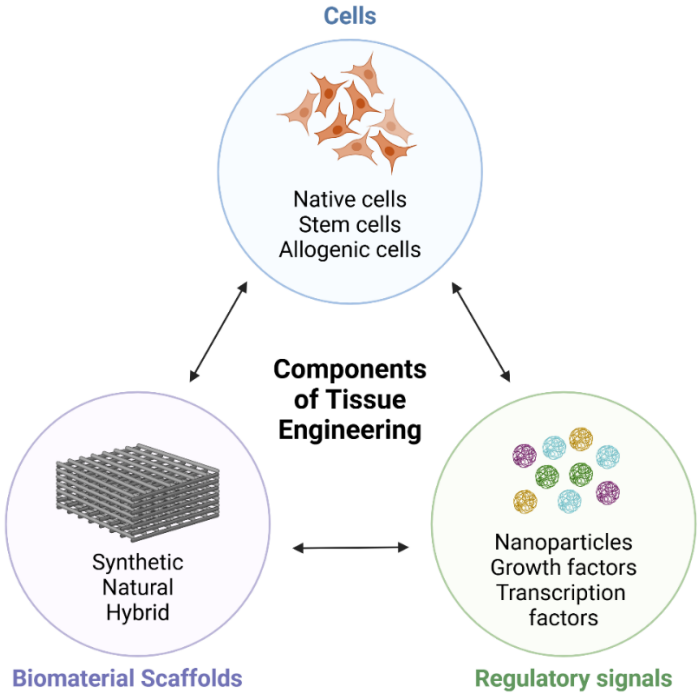

Figure 1.6: Overview of the "TE triad": cells, scaffolds, and regulatory signals. Cells are the primary agents responsible for tissue generation. Porous scaffolds, made from biomaterials, provide a habitat for these cells. The behavior of the cells is influenced by different factors, which include the chemical, physical, and biological variables and substances present in the culture system. Created with BioRender.com

This pioneering work laid the foundation for modern tissue engineering, demonstrating the potential to grow biological tissues and organs using scaffolds and cells [97]. Indeed, cells, scaffolds, and regulatory signals are collectively known as the tissue engineering triad, which are the essential elements of engineered tissues. Scaffolds, frequently composed of polymeric biomaterials, offer the structural framework necessary for cell attachment and the subsequent development of tissue (**Error! Reference source not found.**) [98].

Scaffolds are three-dimensional microporous biomaterials engineered to replicate many functions of the extracellular matrix (ECM) that constitutes tissues. Scaffolds should be biocompatible, excluding among others toxic reaction and immunogenic reaction. They must maintain a biodegradability rate that allows the scaffold to be replaced by new tissue without collapsing the construct. Additionally, they should possess mechanical properties that mimic the surrounding *in vivo* environment and have an architecture that supports cellular processes such as migration, adhesion, spreading on the scaffolds, proliferation and differentiation, vascularization, and enable nutrition supply and waste removal. Finally, the scaffolds should be in reach through an efficient and economical manufacturing (**Error! Reference source not found.**) [6,99] .

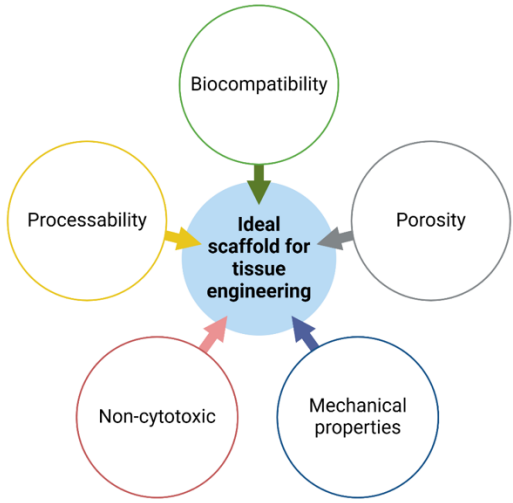

Figure 1.7: Key characteristics required for a TE scaffold. Created with BioRender.com

In the meniscus field, TE aims at reproducing the anisotropic meniscal architecture by using a specific spatial distribution of different cell types. A 3D printed scaffold with different zonal growth factors

supplementation, different microarchitecture and/or cell disposition offers more chances of regenerating a fully active meniscus due to the anisotropic nature that allows different cell types to differentiate and to proliferate [93,100]. The principal aim is to construct a meniscal implant or a scaffold for meniscal TE in order to relieve symptoms after (partial) meniscectomy, improve functional properties and, in the long term, prevent the development of osteoarthritis [80].

Notably, meniscus TE presents a unique set of challenges due to the complex structure and function of the meniscus. The meniscus must withstand significant mechanical loads, including compressive, tensile, and shear stress, which makes replicating its biomechanical properties difficult. Additionally, the meniscus has limited blood supply, particularly in the inner regions, which complicates its natural healing process and poses a challenge for engineered tissues. Sourcing appropriate cells is another hurdle, as meniscus cells are heterogeneous and lack specific markers for isolation. Ensuring biocompatibility and seamless integration with the host tissue without triggering an immune response is crucial. Moreover, developing efficient and economical manufacturing processes for scalable production remains a significant challenge [6,101,102].

The selection of biomaterial(s) to construct the meniscus TE scaffolds plays a crucial role on the quality of the engineered tissue *in vivo or in vitro* [4]. Various polymer materials have been tested, and meniscal scaffolds can be categorized into synthetic and biological types.

1.7 Polymer application in Meniscus Tissue Engineering

A polymer is a macromolecule made up of numerous repeating subunits. The term “polymer” comes from the ancient Greek words “polýs” (meaning “many” or “much”) and “meros” (meaning “parts”, Figure 1.8) [103]. In essence, polymers are large, high molar mass

molecules, formed by linking together numerous small molecules called monomers. The process of joining monomers to create a polymer is referred to as polymerization. Generally, this reaction involves joining two or more molecules, either with or without the elimination of byproducts resulting in a high molecular mass molecule [104] (Figure 1.8).

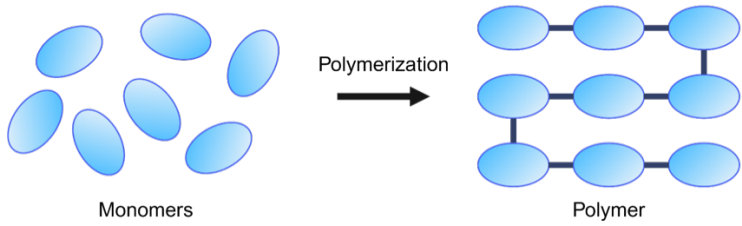

Figure 1.8: Schematic Representation of a Polymerization - This figure illustrates the process of polymerization, where monomers (small molecules) are linked together to form a polymer (large macromolecule). Created with BioRender.com

Polymeric materials possess several valuable properties, including high strength or modulus-to-weight ratios (making them lightweight yet stiff and strong), toughness, resilience, and resistance to corrosion. They also exhibit low thermal and electrical conductivity, come in various colors, can be transparent, are easy to process, and are cost-effective. Many of these advantageous properties are unique to polymers and stem from their long-chain molecular structure [105].

Their versatility allows them to possess specific properties tailored to meet the demands of TE, such as porosity, biocompatibility, biodegradability and mechanical characteristics [105,106].

In the following section, the primary scaffolds that have demonstrated promising results in meniscal tissue engineering will be discussed in detail. These scaffolds have been evaluated based on their mechanical properties, biocompatibility, and ability to promote cell proliferation and - differentiation. The advancements in scaffold fabrication techniques

and materials will be highlighted, providing a comprehensive overview of the current state of meniscal tissue engineering.

1.7.1 Hydrogels

Among the plethora of biomaterials, polymeric hydrogels stand out as promising candidates due to their generally high cell biocompatibility and adjustable properties, which allow for the controlled release of bioactive molecules or cells. Hydrogels are three-dimensional crosslinked materials composed of a network of polymer chains. Due to their highly hydrophilic nature, hydrogels can retain large amounts of water. The crosslinked or entangled structure of these chains prevents hydrogels from dissolving in aqueous environments under normal conditions [6]. Hydrogels, with their hydrophilic nature, exhibit both fluid and solid characteristics, enabling them to replicate the structure of meniscal tissue. Their biomechanical properties can be customized to closely match the regional characteristics of the native meniscal tissue. These inherent properties make hydrogels a promising option for therapeutic strategies aimed at meniscus repair and regeneration [5,6].

There are various types of hydrogels and applications in extrinsic substance delivery, meniscus rehabilitation, and regeneration [107,108].

Alginate is the most commonly used hydrogel matrix for immobilizing cells such as meniscal fibrochondrocytes, chondrocytes, and mesenchymal stem cells (MSCs). Studies have shown increased proteoglycan synthesis and cell numbers when human meniscal fibrochondrocytes are encapsulated in alginate spheres. Verdonk et al. found that meniscal cells embedded in non- biomedical-grade alginate exhibited a more fibrochondrocyte-like phenotype compared to monolayer culture. Recent research highlights the importance of the 3-D microenvironment in maintaining the phenotype of human meniscal

fibrochondrocytes. Among various alginates, only biomedical-grade medium viscosity and high mannuronic acid content (BioMVM) alginate spheres effectively produced and retained significant amounts of proteoglycans [5,24,109].

In recent years, tissue-derived ECM biomaterials have garnered significant attention as a treatment for meniscus injuries. These matrix-based biomaterials, obtained through the decellularization of native tissues, contain complex matrix components that closely mimic natural tissue [5]. Studies have shown that hydrogels derived from juvenile bovine menisci [110], porcine meniscus-derived matrix (MDM) [111], and equine cartilage can promote meniscus repair and influence cell differentiation [92].

Significant efforts have been made to identify materials capable of replacing lost or damaged knee meniscal tissue. Synthetic polymers are promising candidates for creating artificial menisci, as they can be tailored to mimic the mechanical properties of native meniscal tissue, thus avoiding the issues associated with allografts. PVA hydrogelsare promising biomaterials due to their high biocompatibility and viscoelastic properties that are comparable to those of meniscal tissue [112,113].

Implantation of PVA hydrogels as artificial lateral meniscus implants in rabbits has shown normal articular cartilage conditions at 1-, 1.5-, and 2-years post-surgery [5,114,115]. Limited joint degradation and wear were observed compared to meniscectomy knees, which exhibited osteoarthritis after one year in these rabbits [115]. However, rabbits are not fully comparable to humans due to differences in joint loading, biomechanics, and cartilage regeneration capacity, which may limit the direct translation of these findings to clinical applications. To enhance the mechanical properties of PVA hydrogels, fibre reinforcement with

ultrahigh molecular weight polyethylene (UHMWPE) has been used, increasing tensile modulus and interfacial adhesion. Additionally, modifying PVA hydrogels with salts like sodium sulfate has improved crystallinity and storage modulus, resulting in load-bearing systems with mechanical properties similar to the native meniscus [6,116–118].

Another synthetic polymer used in meniscal TE is Polyethylene Glycol (PEG). PEG is a widely used biomaterial in TE and drug delivery applications because of its biocompatibility, versatility, hydrophilicity and resistance to fouling [119]. PEG diacrylate (PEGDA) is an excellent choice for quick and easy injection, as it rapidly undergoes photo-crosslinking to form biocompatible hydrogels. This characteristic makes PEGDA highly advantageous for delivering cells and other compounds to aid in meniscus repair [120,121].

Gelatin methacrylamidate (GelMA) is a promising material in meniscus TE due to its biocompatibility, tunable physical properties, and ability to mimic the natural extracellular matrix (ECM) [122]. In meniscus TE, GelMA provides a three-dimensional micro-environment that can be customized to match the mechanical properties of the meniscal tissue. Once cured, GelMA hydrogel no longer undergoes sol-gel transitions due to temperature changes. This characteristic makes GelMA precursors ideal for delivering cells into meniscus defects, as the cells can be anchored in the defect sites through the curing process, promoting tissue repair. Additionally, cell-laden GelMA can be incorporated into 3D-printed scaffolds to create meniscus scaffolds for regeneration. Studies have shown that human fibrochondrocytes in GelMA hydrogels exhibit high levels of COL I mRNA, indicating that GelMA supports the adoption of a fibrotic phenotype [6,123,124].

Although the high water content of hydrogels is one of their main advantages for tissue engineering applications, it also introduces practical challenges for storage, transport, sterilization, handling, and

long-term stability. Hydrogel scaffolds are often fabricated and characterized in a hydrated state, but clinical or industrial translation may require a dehydration step before use. However, removing water from a hydrogel network can alter its microstructure, pore morphology, swelling behaviour, and mechanical properties after rehydration. Therefore, dehydration should not be considered only as a practical post-processing step, but also as a parameter that may influence final scaffold performance. This is particularly relevant for meniscus scaffold development, where structural integrity and mechanical response after rehydration are essential. For this reason, the influence of different dehydration strategies on AUP scaffold morphology and compressive behaviour was investigated later in this thesis.

1.7.2 Synthetic polymers

Synthetic scaffolds offer the clear advantage of being manufactured to specific shapes and sizes, with precise control over porosity, dimensions and biomechanical properties [125]. The most commonly used polymers to date include poly-(L)-lactic acid (PLLA), poly-glycolic acid (PGA), poly-(lactic-co-glycolic acid) (PLGA), polycarbonate-urethane (PCU), and poly-ε-caprolactone (PCL).

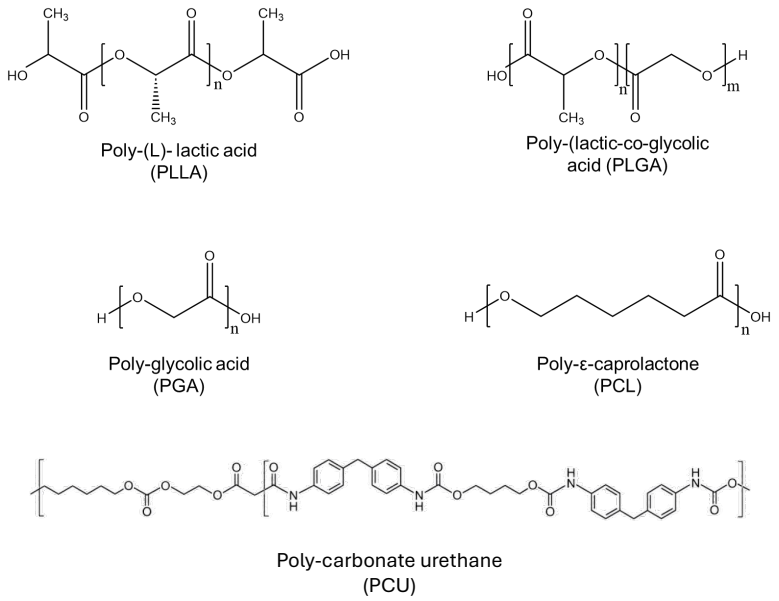

Figure 1.9: Commonly used synthetic polymer in the meniscal tissue engineering field.

One of the earliest studies on synthetic resorbable polymers for meniscal scaffolds was conducted by Veth et al. in 1986. This study utilized a graft made of polyurethane-PLLA (PU-PLLA) reinforced with carbon fibres to repair large wedge-shaped meniscus lesions in 14 dogs. Four- and eight-weeks post-operation, the implants were excised. In 10 subjects, the reconstructed area was covered by fibrous tissue and, in some parts, by repair-simulating hyaline cartilage, with no signs of infection [126]. Subsequent studies revealed that PLLA fibres slowed down both the degradation process and the ingrowth of fibrocartilaginous tissue. Additionally, there was no evidence of increased cell proliferation adjacent to the implant [127]. Recently, another *in vivo* study concluded that the bioresorbable scaffold facilitated tissue ingrowth and induced fibrocartilage formation after 12 weeks. A meniscal replica was developed, indicating that this material has significant potential as a meniscal prosthesis [128].

In the literature, the terms scaffold, implant, and prosthesis are sometimes used inconsistently. In this thesis, “implant” is used as a broad term for any device surgically placed in the body. The term “scaffold” refers to porous structures designed to support tissue ingrowth, regeneration, or gradual replacement by newly formed tissue. In contrast, “prosthesis” is used for devices that primarily aim to replace the mechanical function of the meniscus, without necessarily acting as a regenerative template. Based on this distinction, porous and tissue-integrative systems are referred to as meniscal scaffolds or scaffold implants, whereas PCU-based replacement devices such as NUSurface® and Artimis® are referred to as meniscal prostheses or synthetic meniscal replacement implants.

The study of Murakami et al. focuses on the development and evaluation of a novel meniscal scaffold made from polyglycolic acid (PGA) coated with polylactic acid/caprolactone (PLA/CL). This scaffold aims to treat irreparable meniscal tears by promoting new tissue growth. The research includes biomechanical testing and a clinical trial involving six patients who underwent arthroscopic implantation of the scaffold. Results showed improved knee function and pain relief, with meniscal-like tissue regeneration observed in five patients [129].

Various studies have shown that PCU is an attractive material for meniscal implant applications due to its durability, bio-stability, and excellent mechanical and tribological properties. PCU demonstrated a chondroprotective role in the knee, showing minimal to no short-term damage to various compartments post-meniscectomy, although some joint degeneration was observed on the longer term [130,131].

Since 2008, NUsurface® has been available in Europe. It is made of flexible PCU and is circumferentially reinforced with ultra-high molecular weight polyethylene (UHMWPE) fibres. Its wedge-shaped geometry, applied to the entire circumference including the lateral side,

allows it to be self-centering. However, due to the lack of fixation, an intact peripheral meniscus rim of at least 2 mm is required to prevent dislocation. Clinical studies have indicated that it suffers from a high failure rate (16.9%) and does not prevent knee osteoarthritis to develop [132].

Koller et al. enhanced the biological activity of polymeric scaffolds by adding PET to PCL scaffolds, which increased collagen II mRNA production and glycosaminoglycan secretion. Histological analysis showed meniscal cell colonization, proliferation, differentiation, and attachment [133]. Fisher et al. modified the orientation of scaffold nanofibres composed of poly(ε-caprolactone) to better mimic the native meniscus cellular orientation. Various multi-layer groups were cultured for 6 weeks under conditions promoting fibrocartilaginous tissue formation [134].

A more recent scaffold is composed of a synthetic polyurethane-based material, consisting of 80% poly(ε-caprolactone) and 20% urethane segments (Actifit; Orteq Sports Medicine, London, UK). This scaffold is highly porous and slowly biodegradable, with an estimated degradation time of 4 to 6 years [135]. The Actifit implant showed good integration and patient satisfaction, with stable functional scores and cartilage status over five years, despite a high failure rate (18%) and some abnormal MRI appearances [132,133,135–138].

Another very recent prosthesis is the Trammpolin®, now known as Artimis®, developed by ATRO Medical and composed of a polycarbonate urethane (PCU).

In 2024, the Artimis® meniscus prosthesis received the FDA's Breakthrough Device Designation, underscoring its potential to significantly improve outcomes for patients with persistent knee pain

post-meniscectomy. Clinical studies are underway to evaluate the safety and performance of the Artimis® prosthesis [137].

Synthetic polymers are more prone to complications such as poor cell adhesion and the potential for foreign body reactions or aseptic inflammation. These issues can alter joint architecture and subsequently worsen functional outcomes [138].

1.7.2.1 Acrylate-endcapped urethane-based hydrogel precursors (AUP)

Hydrogels made from synthetic polymers exhibit less batch-to-batch variability compared to natural polymers and are more easily customizable, allowing for tailored mechanical and swelling properties [139,140]. In this context, acrylate-endcapped urethane-based precursors (AUP) present a promising option as synthetic building blocks for meniscal TE application [141]. These polymers, patented by the PBM research group in collaboration with Allnex, of which the general structure is shown in Figure 1.10, demonstrate excellent solid-state crosslinking capabilities upon UV irradiation and have shown outstanding biocompatibility in previous studies. At room temperature, most AUP form a semi-crystalline solid comprising crystalline zones primarily made of PEG and amorphous zones mainly consisting of the acrylate functionalities. The solid-state reactivity is due to a small spacer that separates the polymer backbone from the acrylate end group, allowing mobility for crosslinking under UV [142,143].

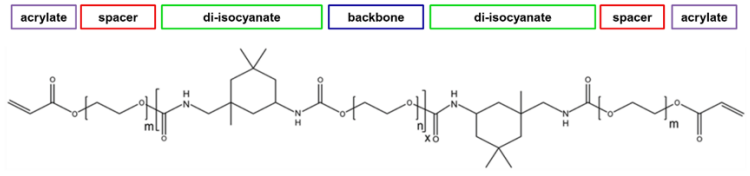

Figure 1.10: General (top panel) and specific (bottom panel) chemical structure of a PEG-derived AUP polymer. Created with BioRender.com

AUP hydrogel precursors can be derived from various polymer backbones, such as poly(ethylene glycol), poly(propylene glycol), or poly(ε-caprolactone). PEG-based AUP materials are particularly effective at absorbing large amounts of water, making them ideal for mimicking the natural extracellular matrix and mimicking the environment of the natural meniscus [142,144]. Their exceptional solid-state reactivity is especially valuable for polymer processing techniques in hydrogel applications, especially in additive manufacturing techniques, including the indirect 3D printing, fused deposition modeling, and digital light processing [141,145–147].

Since their initial development within the PBM research group in collaboration with Allnex, AUP-based materials have been explored across a growing range of tissue engineering and biomedical applications, demonstrating the versatility of this polymer platform. Early work focused on the systematic characterization of AUP hydrogels with varying PEG backbone molar masses (ranging from 1 000 to 8 000 g/mol), establishing the fundamental structure–property relationships that underpin the tunability of these materials. [140,148,149]

These studies showed that by varying the backbone molar mass and the number of reactive acrylate end groups, the resulting crosslinked networks could be tailored over a broad range of swelling capacities (4–11 g water per g polymer) and mechanical properties (Young's modulus 0.1–0.6 MPa), while consistently achieving gel fractions approaching or exceeding 95% [150]

A particularly active line of research has focused on the application of AUP hydrogels in the field of wound healing. Ionescu et al. processed AUP materials with PEG backbones into films and electrospun mats for wound dressings, demonstrating superior exudate uptake capacity compared to commercial dressings (Aquacel®Ag, Exufiber®, and Help®). An *in vivo* study on an acute wound model in rats showed

significantly improved wound contraction and tissue regeneration compared to both positive and negative controls, confirming the clinical potential of AUP-based wound care materials [148]. Building on this, Minsart et al. further explored the influence of endcap chemistry on exudate management performance, developing AUP-based hydrogel wound dressings with PEG backbone molar masses of 10 000 and 20 000 g/mol that combined mechanical strength with high absorption capacities, outperforming several commercial benchmarks [141].

More recently, the AUP platform has been extended toward vascular tissue engineering. Pien et al. exploited the DLP-printability of AUP polymers — using both PEG and PPG backbones with di-acrylate and hexa-acrylate functionalities — to fabricate tubular constructs with precise dimensions and morphology for use as *in vitro* vascular wall models [151]. Furthermore, ongoing research within the group has explored the incorporation of Laponite nanoclay into AUP networks to enhance cell-interactive properties and improve printability for extrusion-based applications [150,152], as well as the use of graphene to introduce porosity into otherwise non-porous AUP networks [153]. The development of AUP formulations for frontal sinus wound care in the context of post-surgical chronic rhinosinusitis is also currently under investigation within the group.

Collectively, these studies establish AUPs as a well-characterized and increasingly validated polymer platform with demonstrated potential across soft tissue engineering, wound healing, and bioprinting applications. However, it should be noted that the majority of these prior studies have targeted tissues with relatively moderate mechanical demands. The application of AUP hydrogels to meniscus replacement, as pursued in this thesis, introduces a fundamentally different and more demanding set of scientific challenges.

1.7.2.1.1 Scientific challenges for AUP-based meniscus scaffolds

The meniscus operates in one of the most mechanically demanding environments in the human body, and this imposes stringent requirements on any candidate scaffold material. Several key scientific challenges must be addressed when developing AUP-based hydrogels for this specific application.

First, the native meniscus exhibits complex anisotropic mechanical behaviour resulting from the highly organized arrangement of circumferential collagen fibres, which carry the primary tensile loads, embedded in a matrix that provides compressive resistance. A homogeneous, isotropic hydrogel network, as produced by conventional AUP crosslinking, does not inherently replicate this directional mechanical response. Approaching the compressive properties of the meniscus, while necessary, is therefore insufficient on its own — the tensile properties and the anisotropic stiffness profile must also be considered.

Second, and perhaps most critically, the meniscus is subjected to continuous cyclic loading during daily activities such as walking, running, and climbing. It has been estimated that the knee joint undergoes approximately one million loading cycles per year. This places exceptional demands on the fatigue resistance and long-term mechanical stability of any replacement material. While many hydrogel systems, including AUPs, can be designed to achieve adequate static mechanical properties, resistance to crack initiation, damage accumulation, and structural failure under prolonged repetitive loading remains a major unresolved challenge for synthetic hydrogel-based scaffolds.

Third, the high water content that makes hydrogels attractive as tissue mimics simultaneously introduces practical challenges for clinical translation. Hydrated scaffolds are difficult to store, sterilize, transport, and handle in a surgical setting. A dehydration step is therefore often necessary, but the removal and subsequent rehydration prior use of water can lead to structural changes in the polymer network, altered pore morphology, and shifts in mechanical behaviour after rehydration. Understanding and controlling this dehydration–rehydration behaviour is essential for developing a clinically viable scaffold.

Fourth, the porous architecture of the scaffold plays a critical role not only in determining the mechanical response, but also in facilitating nutrient transport, waste removal, and potential cell infiltration. The meniscus requires an interconnected pore network that allows for adequate mass transport while maintaining structural integrity under load. Achieving such architectures through additive manufacturing requires careful optimization of printing parameters and, in some cases, the development of alternative fabrication strategies beyond conventional direct extrusion printing.

Finally, the biocompatibility requirements for a meniscus scaffold extend beyond basic cytocompatibility. Although AUP materials have consistently demonstrated non-cytotoxic behaviour in *in vitro* assays [141,149,154,155], the long-term *in vivo* response, including potential inflammatory reactions, integration with surrounding tissue, and the capacity to support or promote the formation of functional meniscus-like tissue, remains to be fully evaluated. This represents an important area of future investigation that goes beyond the scope of the present thesis but is essential for eventual clinical translation.

These challenges collectively define the scientific landscape within which the experimental work of this thesis is situated, and they provide the rationale for the systematic approach to material optimization, architectural design, and fabrication strategy development pursued in the following chapters.

1.7.3 Natural polymers

To enhance the biocompatibility and the biodegradability of polymeric scaffolds, biopolymers like silk fibrous protein can be used. Silks are fibrous proteins and show modular units that are linked together to form a high molar mass biopolymer. These modular units have a precise amino acid sequence that provides specific functions [81]. The process to have it is versatile, but it is necessary to work on the initial mechanical proprieties because they have to be modified in order to obtain a comparable value range to the native human meniscus. Indeed, silk fibroin typically exhibits superior properties compared to collagen, which is a key component of the meniscus. Different studies showed how this material is promising in the meniscus TE application [51,156–159]. Fibrofix™, a silk-derived meniscus scaffold, has shown promise in protecting cartilage in a sheep model of partial meniscus replacement [158]. This implant, developed by Orthox Limited, is still under clinical investigation and has not yet been fully commercialized. The compressive properties were similar to meniscal tissue, and there were no significant short-term differences in cartilage degeneration compared to the sham group in the sheep study. However, the scaffold's fixation was sometimes unstable, leading to cracking or loss of the implant in some cases. Therefore, improving the fixation technique is necessary for better integration with host tissue [160].

Bodin et al proposed a gel of bacterial cellulose (BC). Cellulose is an organic polysaccharide consisting of a linear chain of several hundred

to over ten thousand linked glucose units. They found that the compression modulus of BC was five times higher than that of collagen, although it was still lower than the compression modulus of the native pig meniscus [161].

Other studied materials are collagen and proteoglycans. Collagen is a naturally occurring matrix polymer which is highly conserved across species while proteoglycans are a group of molecules that possess a protein core and sugars as side chains (glycosaminoglycans, or GAGs) and they are naturally found in the ECM of the meniscus [162]. These two biomaterials are excellent candidates for meniscal engineering due to their high biocompatibility and ability to modify the porosity, the texture, and the size to adapt to the patient's original meniscus [81]. However, they have poor biomechanical characteristics and degrade more rapidly than other materials, which could interfere with complete host tissue replacement [163].

Rodkey et al. conducted a controlled randomized trial using a collagen scaffold in subjects with chronic and acute meniscal tears. One-year post-implant, biopsies showed good scaffold integration and functional outcomes in the chronic group compared to the control group. Histological evaluations indicated that the implant supported the production and integration of meniscus-like matrix. However, subjects with acute lesions did not show a difference in outcomes [164,165].

Another conducted study with a minimum follow-up of 10 years showed significant improvements in pain, activity level, and radiologic outcomes with the medial collagen meniscus implant compared to partial medial meniscectomy alone. They recommend longer follow-up and larger patient populations in randomized controlled trials to confirm the effectiveness of collagen-based meniscal scaffolds [165,166].

A meniscal scaffold made by natural polymer available on the market is the CMI®. The CMI® was developed in the early 1990s and is composed of fibrillar type I collagen sourced from bovine Achilles tendons. Initial clinical trials of the CMI® revealed no adverse effects on the human knee, along with the formation of new tissue and improved clinical scores 36 months post-implantation. Although these early trials did not have appropriate controls to compare the CMI® to standard treatments, recent results from a prospective randomized clinical trial have been published. After an average follow-up period of five years, the findings indicated that the CMI® improved clinical outcomes for chronic medial meniscal defect patients but did not provide benefits for those with acute injuries. Despite generally improved clinical scores, MRI studies of the CMI® indicate consistent findings: the implant size reduces over time, and its signal intensity differs from the native meniscus, even after more than ten years. MRI images suggest that the regenerated tissue is not fibrocartilage, leaving the CMI®'s mechanism of action still unclear [167,168].

1.8 Additive manufacturing technologies

There are numerous traditional techniques for fabricating TE scaffolds, such as fibre bonding, solvent casting, gas foaming, fibre meshes, phase separation, emulsion freeze-drying, freeze casting, and electrospinning [169]. However, these methods struggle to precisely control pore size, geometry, spatial distribution, and internal channels. Solvent-casting particulate-leaching methods cannot ensure pore interconnection, as it depends on adjacent salt particle contact. Skin layers form during evaporation, and salt particle agglomeration complicates pore size control. Only thin scaffold cross-sections are possible due to difficulties in removing deeper located salt particles. Gas foaming achieves only 10-30% pore interconnection [170,171].

Recently, rapid prototyping (RP) techniques have emerged as an alternative to traditional scaffold fabrication methods in TE. RP encompasses various advanced manufacturing techniques that utilize an additive process to build complex structures layer by layer, guided by computer programs [171].

In the past twenty years, over 20 rapid prototyping (RP) systems have been developed and brought to market. These systems can be categorized into three main types: liquid-based, solid-based, and powder-based. Liquid-based technologies include stereolithography and two-photon polymerization, while fused deposition modeling represents a solid-based system. The materials used in these processes include various polymers, ceramics, and metals [172].

The ability of rapid prototyping (RP) techniques to reproducibly manufacture objects with fine features, from micro to nanometers, has created significant opportunities in the field of TE. These techniques allow for the production of scaffolds with precisely controlled geometries, enabling the creation of custom constructs with specific mechanical properties and cellular functions. Additionally, RP technologies can produce personalized scaffolds tailored to individual patients' needs by utilizing data from medical scans of the targeted site [172,173].

In the context of meniscus scaffold fabrication, the selection of a 3D printing technique is not only determined by material compatibility, but also by technical parameters such as spatial resolution, layer thickness, strand diameter, pore fidelity, and printing accuracy. These parameters strongly influence the final scaffold architecture, including pore size, strut geometry, interconnectivity, and surface morphology. Since scaffold architecture directly affects swelling behaviour, mechanical performance, nutrient diffusion, and potential tissue

ingrowth, differences in printing resolution and layer-by-layer control can have a substantial impact on scaffold quality.

A key motivation for employing AM technologies in meniscus tissue engineering, beyond the general advantages of geometric control and patient-specific customization, lies in the potential to direct material deposition in patterns that replicate the native meniscus fibre organization. The native meniscus possesses a highly organized collagen architecture, with circumferentially oriented fibres in the deep zone providing tensile hoop stresses that resist extrusion of the meniscus itself under compressive loading, and radially oriented tie fibres near the surface that provide structural cohesion between the circumferential bundles. This fibre arrangement, with predominantly circumferentially oriented bundles in the deep zone providing tensile hoop stress resistance, and radially oriented tie fibres near the surface ensuring structural cohesion, is directly responsible for the unique mechanical behaviour of the meniscus, including its nonlinear tension–compression response and its ability to convert axial compressive loads into circumferential tensile stresses. Conventional scaffold fabrication methods such as solvent casting, gas foaming, or freeze-drying cannot reproduce this directional organization. [1,2] In contrast, AM techniques offer the possibility, at least in principle, to align material deposition trajectories, control pore orientation, and create architectures that guide cell alignment and extracellular matrix organization along biomechanically relevant directions. [1] The extent to which each AM technology can achieve this, however, varies considerably and represents a central consideration in the selection of fabrication strategies for meniscus scaffolds.

1.8.1 Extrusion-based systems

Extrusion bioprinting operates on the principle of material extrusion or dispensing to create a 3D structure layer by layer. A typical extrusion

bioprinting system comprises four main components: a dispensing head that holds a bioink-laden syringe or cartridge with temperature control, a positioning system that moves the dispensing head in x, y, and z directions, a printing stage with adjustable position and temperature, and a computer that allows the user to set deposition parameters, control the position of the dispensing head and/or printing stage, and regulate the temperature of both [174]. It offers several advantages for producing TE scaffolds, such as being cell-friendly and enabling the creation of multi-component constructs [175].

The simplest extrusion-based technique is fused deposition modelling (FDM) or hot material extrusion. This method involves feeding a thermoplastic polymer filament through rollers into a heated nozzle, which melts the polymer material just before it is deposited [7]. During deposition, the heat from the freshly deposited polymer softens the previous layer, promoting interlayer attachment. Hot material extrusion can produce structures with strut diameters in the range of several hundred micrometers, primarily controlled by the nozzle diameter and extrusion rate (Figure 1.11) [176]. The range of materials suitable for hot material extrusion is limited because they must be thermoplastic, exhibit appropriate viscoelasticity and melting/solidification properties, and be pre-processed into polymer filaments [177]. This technique has shown great promise in the fabrication of 3D scaffolds with the use of polymers such as PCL, PLA, PMMA and PLGA [178].

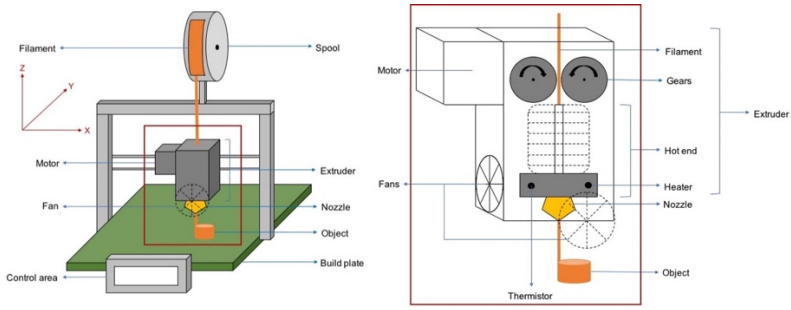

Figure 1.11: Illustration of the hot material extrusion 3D printing technique. On the left, the apparatus is shown, where the filament is fed into the extruder and melted. The material is deposited layer by layer through the nozzle to create the printed object. On the right, the extrusion head of the hot material extrusion apparatus is depicted. The filament is pulled by two gears through the heat unit and nozzle, where it is melted and forms the object [177].

In addition to hot material extrusion, 3D bioplotting provides a versatile method for constructing objects from hydrogel building blocks, pastes, dispersions, and thermoplastic polymers, allowing the extrusion of biofunctional materials and hydrogel building blocks to integrate aqueous biosystems or living cells into 3D scaffolds [172,179].

3D bioplotting allows for the plotting of various biomaterials, including PEG, PVA, PLA, PCL, and PLGA, as well as biopolymer solutions like agar, fibrin and gelatin [180]. This technique is particularly beneficial for processing materials with low viscosities due to buoyancy compensation. Given its versatility, 3D bioplotting presents new and attractive opportunities for biofunctional rapid prototyping in TE. Unlike other rapid prototyping technologies, 3D bioplotting can design and fabricate hydrogels with complex architectures and internal substructures [175].

Extrusion bioprinting fabricates structures using bioinks extruded from one or more nozzles. Generally, three different extrusion-based bioprinting systems can be identified [181] (Figure 1.12):

1. **Pneumatic-Driven Extrusion**: This system uses pressurized air to push the bioink through the nozzle. The air pressure can be precisely controlled to achieve the desired flow rate and droplet size. It's commonly used for its simplicity and ability to handle a wide range of bioink viscosities [182];

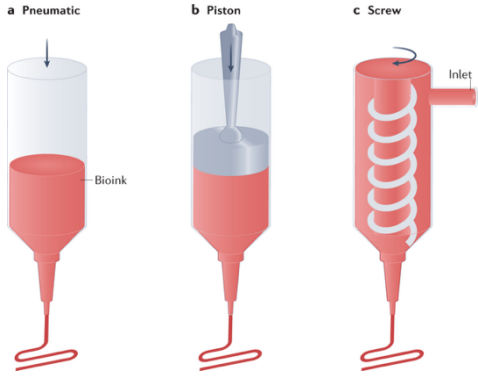

Figure 1.12: Schematic of the different extrusion-based bioprinting system: Pneumatic-drive, piston-driven and screw-driven [173].

2. **Piston-Driven Extrusion**: In this system, a piston mechanically pushes the bioink through the nozzle. The piston is typically connected to an electric motor that converts rotational motion into linear motion. This method provides precise control over the extrusion process and is suitable for high-viscosity bioinks [183];
3. **Screw-Driven Extrusion:** This system uses a screw mechanism to move the bioink through the nozzle. The screw rotates, creating a helical motion that pushes the bioink forward. It's particularly effective for continuous and consistent extrusion, making it ideal for large-scale bioprinting applications [184].

The achievable resolution of extrusion-based printing is strongly dependent on nozzle diameter, polymer viscosity, printing speed, extrusion pressure, and the ability of the deposited filament to retain its shape after extrusion. As a result, the final strut diameter and pore size

may deviate from the original CAD design, particularly when soft or highly hydrated hydrogel systems are processed.

However, a major challenge for all systems is the high shear stress near the nozzle walls, which can impact cell viability, particularly with high-viscosity bioinks. High-resolution bioprinting requires small-diameter nozzles, limiting bioink flow rate and throughput. Printable shear-thinning biomaterials can help, but suitable materials are not always available. Other challenges include finding stable in situ crosslinking methods for non-shear-thinning bioinks, low printing resolution compared to other methods, and difficulties in fabricating free-standing constructs [185].

Extrusion-based techniques have been the most widely explored AM approach for meniscus scaffold fabrication to date. Several groups have demonstrated the feasibility of extrusion printing anatomically shaped meniscal constructs using polycaprolactone (PCL) as the primary structural material. Zhang et al. fabricated 3D-printed PCL scaffolds augmented with mesenchymal stem cells for total meniscal substitution and demonstrated biocompatibility and chondroprotective effects in a 12- and 24-week rabbit model [186]. Building on this, the same group developed an orchestrated approach combining biomechanical, structural, and biochemical stimuli in 3D-printed anisotropic meniscus constructs using PCL scaffolds with circumferentially patterned deposition [187]. A particularly relevant development has been the use of dual-extrusion bioprinting, in which one nozzle deposits a structural polymer (e.g. PCL or polyurethane) while a second deposits a cell-laden bioink within the porous framework, enabling the fabrication of multi-component constructs that combine mechanical strength with biological functionality. Other groups have explored cryo-printing of polyurethane scaffolds with controlled pore sizes mimicking native meniscus geometry, with surface modification using collagen I and

fibronectin to promote mesenchymal stem cell adhesion and chondrogenic differentiation [188].

1.8.2 Vat polymerization

Vat photopolymerization (VP) is one of the pioneering and most widely utilized 3D printing techniques, significantly influencing numerous industries. This process works by selectively curing a resin, layer by layer, using controlled light exposure. This method allows for the precise creation of three-dimensional objects with high resolution and intricate geometries [189,190]. A solution of the material is placed in a vat and exposed to a UV light source. The primary requirement for these technologies is that the material (bioink) must be photo-crosslinkable. When UV light strikes the photo-crosslinkable material, it creates covalent bonds between the reactive sites, enabling crosslinking [190].

Stereolithography (SLA) is the oldest of the rapid prototyping techniques, it was introduced in 1986 [191]; a liquid resin placed in a vat, and a platform is lowered into it. A computer-guided laser, typically in the UV-A range, scans the first layer of the CAD construct in the x,y-plane. The laser photopolymerizes the scanned area, creating the first layer. The platform then moves in the z-direction to define the layer thickness, allowing consecutive layers to be scanned and cured, building up the 3D construct as shown in Figure 1.13 [192].

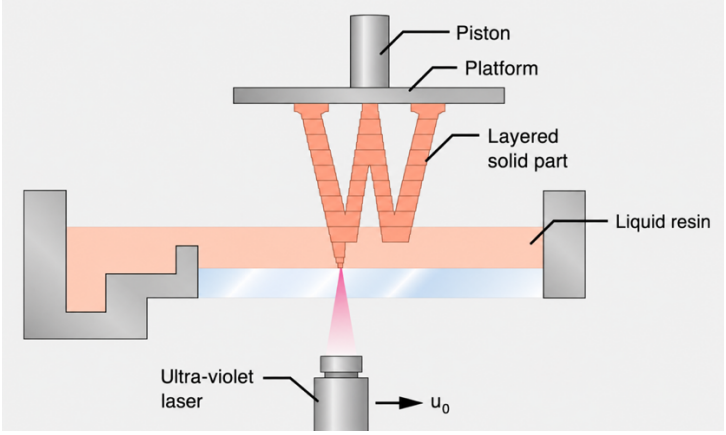

Figure 1.13: Schematics of the Stereolithography (SLA) 3D Printing Mechanism. In this additive manufacturing technique, a UV laser is used to selectively harden liquid photopolymer resin layer by layer. After each layer is cured, the build platform descends incrementally, enabling the object to take shape in successive layers. This method is particularly well-suited for producing intricate geometries and components with fine detail and smooth surface quality [193].

One of the major advantages of SLA is its rapid fabrication speed. Indeed, to achieve high print speeds, galvanometric mirrors are used to deflect the laser's focus. Once a layer is completed, the build plate lowers by the thickness of the layer, and the next layer is printed on top. This process is repeated until the final shape is formed [189]. SLA is also cost-effective, as it uses maskless lithography and only consumes material when cured. Due to its ability to produce high-resolution structures, SLA has been utilized in constructing scaffolds for TE, fabricating microvascular stamps, and studying cell-to-cell interactions. The SLA printer's spatial resolution varies between 25 to 50 μm in the XY plane and 50 to 100 μm in the Z direction. The XY resolution is constrained by the printer's optical diffraction, while the Z resolution is influenced by the absorbance, thickness, and formulation of the print layer [194]. Micron and nanoscale features influence cell behavior, including cell proliferation and differentiation. While SLA can fabricate structures in the micron range using UV wavelengths, researchers are

exploring other technologies for nanoscale fabrication and wavelengths that are less toxic to cells [195].

Digital Light Processing (DLP) is a variant of SLA. DLP uses a projected light source to cure an entire layer of photopolymer material simultaneously, making it an efficient and rapid 3D printing process [196].

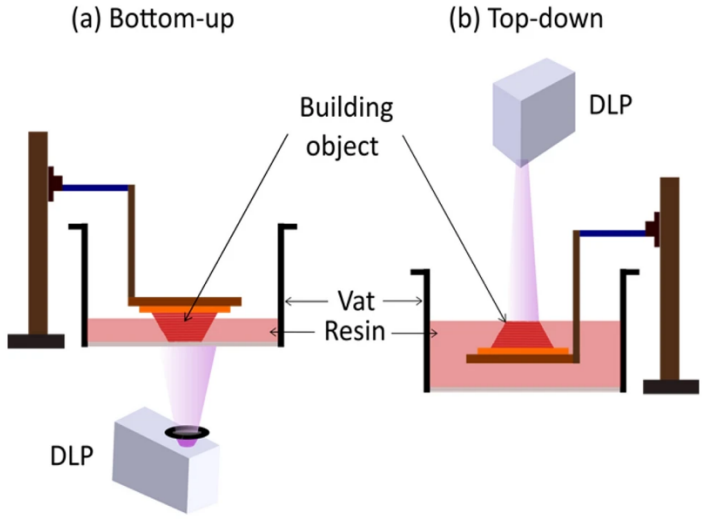

Figure 1.14: Schematics of DLP-Based 3D Printing. A) Bottom-up approach, the printed object forms in an inverted orientation, with each layer cured from beneath the resin vat and the build platform gradually rising. B) Top-down method constructs the object upright, with layers polymerized from above the vat as the build platform lowers [186].

Digital Light Processing (DLP) typically uses two geometric configurations: bottom-up and top-down [197] (**Error! Reference source not found.**). In the bottom-up configuration, the build head is dipped into the resin container (vat) to a height equal to the desired layer thickness. The transparent vat bottom allows UV light to pass through and project the image onto the thin layer of liquid resin between the vat base and the build head. This resin layer is polymerized and remains attached to the build head after exposure. The build head then moves

upward, separating the polymerized layer from the vat base and, if necessary for large printing refilling the vat with fresh resin.

In a top-down configuration of DLP printing, the build platform is positioned above the resin vat and gradually lowers as each layer is cured. This setup involves the digital light projector or an LCD screen that is placed above the resin vat, projecting light patterns onto the resin to solidify each layer. The process begins with the build platform in a raised position, moving downward incrementally to allow the light to cure the photopolymer resin layer by layer. This method enables the precise and high-resolution fabrication of three-dimensional objects, as the cured layers accumulate from top to bottom [196,197].

For constructing TE scaffolds, functionalized polymeric resins allow the creation of biocompatible structures with controlled physical properties, such as strength and degradation rate. Among the commonly used polymeric precursors in lithography-based processes are polyethers (e.g. PEG) and polyesters (e.g. PLA, PCL) with photo-crosslinkable groups [198].

Compared with extrusion-based printing, SLA and DLP generally allow improved spatial resolution and finer layer thickness because the scaffold geometry is defined by light-induced polymerization rather than by the physical deposition of individual filaments. This can improve pore fidelity and surface smoothness, although the final resolution still depends on light scattering, resin composition, photo-initiator concentration, photoabsorber content, exposure time, and layer thickness.

The application of vat photopolymerization techniques to meniscus scaffold fabrication has received increasing attention in recent years, driven by the improved spatial resolution these methods offer compared to extrusion-based systems. Grogan et al. were among the

first to demonstrate the use of projection stereolithography for the fabrication of micropatterned methacrylated gelatin (GelMA) scaffolds designed to emulate the circumferential alignment of cells in native meniscus tissue. Human meniscus cells seeded on these scaffolds aligned along the patterned strands and promoted a fibrocartilage-like phenotype, with scaffold integration confirmed in an explant organ culture model [199]. More recently, DLP printing has been explored for the fabrication of meniscal scaffolds from dual-crosslinked GelMA hydrogels, demonstrating the ability to produce patient-specific geometries with tunable mechanical properties directly from CAD models derived from clinical imaging data. A particularly innovative approach was demonstrated by Yang et al., who used electrically assisted DLP-based stereolithography to align carbon nanotube fillers within a photocurable resin, creating biomimetic anisotropic reinforcement architectures that mimic the circumferential and radial fibre alignment of the human meniscus [200]. This study demonstrated that controlled filler alignment significantly improved the tensile modulus compared to random orientations, representing a promising strategy for reproducing the anisotropic mechanical behaviour of the native tissue. Despite these developments, the application of SLA/DLP techniques to meniscal scaffolds remains in an early stage, and several challenges must be addressed. These include the limited availability of photo-crosslinkable hydrogel formulations that combine printability with adequate mechanical performance, the difficulty of fabricating large-volume meniscal constructs without overcuring or geometric distortion, and the need for biocompatible photoinitiator and photoabsorber systems that do not compromise cell viability.

1.8.3 Indirect rapid prototyping

Indirect rapid prototyping (iRP) offers several advantages over other fabrication methods for tissue engineered scaffolds [145]. Indeed, this

technique allows to address the limitations of conventional solid freeform fabrication techniques, such as limited material selection, brittleness, the necessity for post-treatment, low resolution (usually around 100 to 250 micrometers), and lengthy optimization processes for new materials [177,201,202]. This method utilizes a construct created through a 3D printing technique as a temporary (negative) mold or template for the final product. Consequently, this method is known as the 'lost-mold technique,' indirect solid freeform fabrication (iSFF), indirect rapid prototyping, indirect additive manufacturing, or indirect 3D printing [203–206]. Utilizing high-resolution techniques for template fabrication, such as SLA or DLP, allows for the creation of scaffolds with pore and strut sizes as small as 50 and 65 µm, respectively. This is particularly beneficial for materials that are not suitable for direct fabrication using high-resolution manufacturing methods [207]. As a result, well-defined 3D scaffolds can be easily produced from materials that were previously considered 'unprintable' due to their thermomechanical properties, which do not meet the stringent temperature and pressure requirements of direct rapid prototyping [146,202,206,208,209].

A particularly relevant advantage of indirect fabrication in the context of meniscus tissue engineering is the ability to produce scaffolds with lateral porosity — that is, interconnected pore channels oriented parallel to the printing plane. In direct extrusion-based printing, porosity is primarily generated in the vertical build direction through the stacking of filament layers, and achieving well-defined lateral interconnectivity is inherently difficult. However, for a meniscal scaffold, lateral porosity is important because it facilitates nutrient diffusion, waste removal, and cellular infiltration from the peripheral rim of the meniscus toward the avascular inner zone — a direction that is critical for promoting tissue integration and regeneration across the full scaffold volume. Indirect

fabrication methods overcome this limitation because the pore architecture is defined by the sacrificial mould rather than by the printing trajectory, allowing porosity to be designed in any spatial direction.

IRP consists generally out of three steps as shown in Figure 1.15:

1. Creation of the mold
2. Casting of the material in the mold
3. Removal of the mold

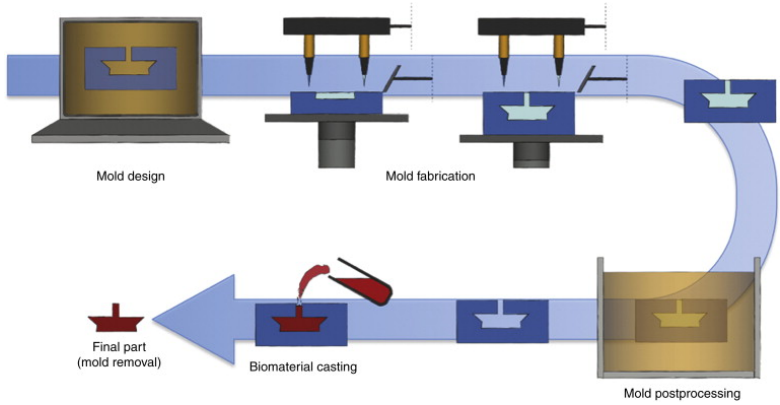

Figure 1.15: Indirect rapid prototyping process. Flow work of iRP process, from CAD design to realization [208].

The primary challenge in the molding step is ensuring that all voids within the mold are filled. To achieve this, researchers have proposed various techniques, which can be broadly classified into vacuum-based and injection-based indirect 3D printing methods [146].

In vacuum-based indirect 3D printing (VIDP), the mold is typically submerged in a hydrogel precursor solution, and the entire container is vacuumed to remove air and fill the mold's voids with the hydrogel precursors. In the second approach, the template is placed inside another mold that encases its outer surface, and the hydrogel

precursor is injected into this mold using a cylinder, which can be operated manually or automatically by a pneumatic system and then subsequently the mold is removed through a solvent [210].

A variety of indirect scaffold materials have been documented in the literature, including biopolymers (collagen, silk fibroin, gelatin), synthetic polymers (PLLA, PCL, PPF), ceramics, and composites [146].

Indirect rapid prototyping approaches have also been explored for meniscal scaffold fabrication, although to a considerably lesser extent than direct printing techniques. Sathish et al. designed a 3D-printed PLA negative mould with meniscus geometry using FDM and subsequently filled it with an optimized gelatin–carboxymethylcellulose–alginate (GCA) composite bioink, demonstrating the feasibility of indirect fabrication for producing anatomically shaped meniscal scaffolds from hydrogel materials [211]. This approach also allowed the encapsulation of live cells within the hydrogel during the casting step. More recently, hybrid strategies combining indirect fabrication with reinforcing polymer networks have been reported. For instance, circumferential and three-dimensional PCL reinforcement networks have been incorporated into hydrogel scaffolds via SLA-printed moulds, improving compressive stiffness, stress relaxation behaviour, and load-bearing capacity compared to non-reinforced hydrogel scaffolds alone [212]. Despite these initial demonstrations, indirect fabrication methods remain underexplored for meniscus applications. A key advantage of indirect approaches is their ability to process low-viscosity hydrogel precursor solutions that cannot be directly extruded or that lack the photoreactivity required for DLP-based processing. This is particularly relevant for synthetic hydrogel systems, such as the AUP-based materials investigated in this thesis, which can be processed as aqueous solutions of varying concentrations and crosslinked within a sacrificial mould framework.

Additionally, indirect prototyping can generate scaffolds with lateral porosity, that is, interconnected pore channels oriented parallel to the peripheral rim of the meniscus, which is difficult to achieve through conventional direct layer-by-layer printing but is essential for facilitating nutrient diffusion and cell infiltration from the vascularized outer zone toward the avascular inner region of the tissue. This specific advantage is explored in detail in Chapter 3 of this thesis.

1.9 Outline of the PhD

The overall objective of this PhD was to develop a tunable, synthetic, hydrogel-based scaffold platform for full meniscus replacement using photo-crosslinkable acrylate-endcapped urethane-based PEG macromers, referred to as AUPs. The central hypothesis of this thesis was that the combination of controllable polymer network chemistry, tailored scaffold microarchitecture, and suitable fabrication strategies would enable the production of hydrogel scaffolds with reproducible porosity and mechanical properties within, or approaching, the range reported for native meniscal tissue. More specifically, this work investigated how AUP molar mass, end-group functionality, polymer concentration, scaffold architecture, and processing route influence network formation, swelling behaviour, mechanical performance, and practical translation.

To address this hypothesis, the thesis was structured around the following objectives:

1) To develop and characterize photo-crosslinkable AUP hydrogel networks suitable for meniscus-oriented scaffold fabrication.
2) To evaluate how scaffold architecture, including printing pattern, pore size, and strut diameter, influences the

physicochemical and mechanical behaviour of extrusion-printed AUP4K DA scaffolds.

3) To improve scaffold performance by modifying AUP chemistry, first by increasing precursor functionality from di-acrylated AUP4K DA to hexa-acrylated AUP4K HA, and subsequently by decreasing PEG backbone molar mass from AUP4K DA to AUP2K DA.
4) To investigate different fabrication strategies, including direct extrusion-based 3D printing, injection-based indirect 3D printing, and DLP printing, and to assess how each method affects scaffold architecture, reproducibility, and mechanical response.
5) To benchmark the obtained scaffold properties against literature values for native meniscal tissue, with particular attention to compressive behaviour, viscoelastic response, and fatigue resistance.
6) To evaluate the effect of dehydration and rehydration as relevant post-processing steps for practical handling, storage, and potential translation of hydrogel-based meniscus scaffolds.
7) To perform preliminary cytocompatibility screening of selected printed AUP scaffolds and identify future optimization steps required for biological and translational development.

The individual chapters were designed to address these objectives in a stepwise manner. Chapter 1 provides the general background of the thesis, including meniscus anatomy, composition, biomechanical function, current treatment limitations, and the role of biomaterials and additive manufacturing in meniscus tissue engineering.

Chapter 2 will focus on the mechanical characterization of a AUP4K DA, both in 2D and 3D shapes, to match the meniscus native mechanical properties. Initially, the study will examine the intrinsic mechanical properties of the AUP in a 2D format, followed by the 3D level by fabricating scaffolds using extrusion-based 3D printing. More specifically, ^{1}HR-MAS, along with swelling degree and gel fraction experiments, will be performed on 2D samples. This initial step will be crucial in confirming that the bulk material is chemically compliant with previous synthesized AUP and can be effectively crosslinked. Following these tests, the experiments will then be conducted on 3D scaffold levels to validate the findings and ensure consistency for the final application. The mechanical performance of these 3D-printed scaffolds will beevaluated through compression testing, Dynamic Mechanical Analysis (DMA) and fatigue testing. Compression tests will measure the scaffolds' ability to withstand mechanical loads, while DMA while provides insights into their viscoelastic properties by analyzing their response to stress and strain over time. Finally, the fatigue test will evaluate the ability of the synthesized scaffold to endure various load cycles, mimicking the conditions experienced by the human meniscus during normal activities.

Chapter 3 will present the development of an innovative injection-moulding setup, designed to be printed using a commercial hot material extrusion printer. This setup should enable the creation of scaffolds with two different types of AUP (AUP4K DA and AUP4K HA). The use of this technique should allow us to obtain scaffolds with lateral porosity, essential for effective meniscus implants that are difficult to obtain by classic hot material extrusion printers. By employing the injection-moulding setup, we aim to achieve consistent and reproducible scaffolds with controlled porosity, which is critical for nutrient diffusion and cellular infiltration. With this set-up, we will aim to

fabricate multiple scaffolds with varying AUP concentrations (ranging from 30wt% to 90wt%) for both AUP types. The fabricated scaffolds will be analysed using optical microscopy and SEM to ensure their integrity and successful mould removal. The swelling degree and gel fraction will also be evaluated, with comparisons made between different concentrations of both types of AUP. Finally, the mechanical properties will be assessed through two tests: the static compression test and the TPA test, to investigate whether the obtained values fall within the range of the human meniscus mechanical properties.

Chapter 4 will describe the fabrication of AUP hydrogel scaffolds for meniscus replacement using DLP printing. Two formulations with different PEG molar masses (AUP2K DA and AUP4K DA) will be synthesized and then we will aim to formulate these into visible-light-curable resins (photoinitiator and photoabsorber) and screened for printability using (photo-)rheology to guide the selection of suitable concentrations.

We will aim to print a regular 400 μm scaffold design with vertical porosity using DLP. Printing parameters—particularly exposure time and projector power—will be tuned with the goal of achieving good pore fidelity and reproducible scaffold geometries, which will be evaluated by optical microscopy and SEM. The resulting printed scaffolds will then be characterized by thermal analysis (TGA/DSC), gel fraction, and swelling measurements to assess network formation and water uptake. Finally, we will aim to evaluate their mechanical performance through static compression and cyclic loading (fatigue/ring specimens), and to perform a preliminary cytocompatibility screening via indirect assays (MTS and live/dead) to guide future meniscus-oriented optimization.

Chapter 5 will evaluate how different dehydration strategies influence the final structure and performance of urethane-based PEG (AUP4K

DA) scaffolds intended for meniscus implants. Specifically, we will compare four drying protocols—desiccation, lyophilization (freeze-drying), ventilated oven drying, and vacuum oven drying—and investigate how each method affects scaffold pore morphology (via SEM), as well as key physicochemical readouts such as gel fraction and swelling behavior after rehydration.

To link drying-induced structural changes to functional performance, we will then aim to assess the compressive mechanical response of the scaffolds in the swollen state following rehydration, using static compression testing. Overall, this chapter will seek to identify a dehydration approach that best preserves scaffold architecture and meniscus-relevant mechanical properties.

Chapter 6 integrates the main findings of the thesis and discusses how AUP chemistry, scaffold architecture, fabrication route, and post-processing influence the final properties of hydrogel-based meniscus scaffolds. It also identifies the remaining limitations, particularly fatigue resistance and long-term functional performance, and outlines future research directions toward more clinically relevant meniscus scaffold development.

Chapter 2:

Customizable 3D-Printed Scaffolds for Meniscal Replacement: Mechanical Insights into Urethane-Based Poly(Ethylene Glycol) polymer

This chapter describes the fabrication of a 3D-printed hydrogel scaffolds for meniscal tissue engineering application. Most of the work described in this chapter was performed by M. Meazzo. S. Schröder performed the fatigue testing. This chapter has been published as:

Martina Meazzo; Stefan Schroeder; Jan Philippe Kretzer; Fabrizio Barberis; Catherine Van Der Straeten, Peter Dubruel. Customizable 3D-Printed Scaffolds for Meniscal Replacement: Mechanical Insights into Urethane-Based Poly(Ethylene Glycol) polymer, *European Polymer Journal*, Volume 242, Article Number: EPJ_114451.

DOI: https://doi.org/10.1016/j.eurpolymj.2025.114451.

2.1 Introduction

As already discussed in Chapter 1, meniscus injury is the most common orthopaedic injury, accounting for half of all knee surgeries, with 1.7 million procedures performed annually in the EU and the USA. Meniscectomy remains the standard treatment for severe damage, but its well-documented link to knee osteoarthritis—a chronic and debilitating condition affecting a significant portion of the population—raises concerns about long-term joint health [2,73,213].

Over the years, researchers have investigated different implant materials of which most are polymer-based: resorbable natural polymers, resorbable synthetic polymers, non-resorbable synthetic polymers and decellularized ECM. [71,80,214]. Commercial meniscus implants used today include CMI (Stryker, collagen type I), Actifit® (Orteq, anchored polyurethane) and NUSurface® Meniscus Implant (flexible PCU, a non-anchored polycarbonate-urethane material reinforced with ultra-high molar mass polyethylene (UHMWPE) fibres). CMI and Actifit® implants have shown to be associated with limited regeneration of host meniscal tissue whilst osteoarthritis progression, cartilage loss and a high failure rate were reported. [100] NUSurface® implants can redistribute loads in a similar fashion to the natural meniscus under static axial conditions but they also suffer from a high failure rate and other complications. [130,132]

Elastic modulus, maximum strain, and stress have been widely studied, mostly in explanted menisci under varying conditions (e.g., hydration, slicing, decellularization). Results vary significantly due to these factors, as well as testing parameters like load, speed, strain rate, and the model used to calculate the Young's modulus, as described in Chapter 1. [68] Due to this, the results are often difficult to compare.

In addition to the testing conditions and parameters, the anisotropy of the native tissue also influences the results. [47–50] Consequently, reported mechanical values should not be interpreted as a single fixed target, but rather as broad reference ranges for evaluating scaffold performance. Reported Elastic Tensile Modulus (ET) values range from 0.11 MPa to 294.14 MPa reflecting differences in testing parameters, experimental conditions, conservation methods, sample size, and thickness (see Table 1.1). [68] On the other hand, the reported Elastic Compressive Modulus (EC) values range from 0.05 MPa to 349.4 MPa (see Table 1.2). [68]

As the meniscus exhibits viscoelastic behaviour [62], several studies assessed the storage modulus (E'), the ability of the material to store energy elastically [63], and the loss modulus (E''), the measure of the energy dissipated or lost per cycle [64], through Dynamic Mechanical Analysis (DMA), a non-destructive technique. For the storage modulus, the values range from a minimum of 0.17 MPa to a maximum of 9.97 MPa at a frequency of 10 Hz. The loss modulus values range from 0.22 MPa to 0.26 MPa at frequencies of 0.1 Hz and 10 Hz (typical frequency range of human movements), respectively (see Table 1.3). [68]

As described in Chapter 1, hydrogels are emerging as promising biomaterials in meniscal implant due to their versatility and ability to be fine-tuned. They can be easily modified and are capable of delivering exogenous drugs, cells, proteins, and cytokines. There are various types of hydrogels used in meniscus rehabilitation, implant and regeneration, that are engineered to provide tunable mechanics, controlled release, and cell-instructive microenvironments that support tissue repair. [6,107]

In the context of hydrogels for meniscus regeneration, acrylate-endcapped urethane-based polymer precursors (the so-called AUP

family) are very promising due to their ability to cross-link in the solid state through UV irradiation and the capacity to take up very large amounts of water. Variations that can be implemented in the polymer series include the (1) type and the length (molar mass) of the polymer backbone, (2) the type and (3) the number of end groups. This polymer family thus exhibits a tuneable mechanical strength while being biocompatible as indicated in our first paper on AUP. [143] In that work, polyethyleneglycol (PEG) with a molar mass of 2000 g/mol was the applied polymer backbone. The general chemical structure is shown in Chapter 1, Figure 1.10.

Since their development, AUP-based hydrogels have been systematically explored across a range of tissue engineering and biomedical applications, establishing a broad evidence base for their versatility and biocompatibility. Early studies within the PBM research group characterized AUP hydrogels with PEG backbone molar masses ranging from 1 000 to 8 000 g/mol, demonstrating that the swelling capacity, crosslinking density, and mechanical properties of the resulting networks can be systematically tuned by varying the backbone molar mass and end-group chemistry [141,143,148]. Applications of AUP in tissue engineering have been extensively discussed in Chapter 1, including their use in wound dressings, tendon repair, vascular applications, and other regenerative medicine strategies. A preliminary study from our group identified AUP4K DA, an AUP with a PEG backbone molar mass of 4 000 g/mol, as a candidate meniscal substitute based on initial compressive mechanical testing [140]. While this early work provided an encouraging starting point, several critical knowledge gaps remained. First, the mechanical characterization was limited to basic compression; a full understanding of the material's performance under the diverse loading conditions experienced by the meniscus, including tension, dynamic loading, and fatigue, was

lacking. Second, the relationship between scaffold architecture (printing pattern, pore size, strut diameter) and the resulting mechanical properties had not been established for AUP-based scaffolds, despite this being a crucial design parameter for any 3D-printed implant. Third, the fatigue resistance of AUP4K DA under cyclic loading, arguably the most demanding mechanical requirement for a meniscal substitute, given that the knee joint undergoes approximately one million loading cycles per year, had not been assessed. Finally, although AUP materials had demonstrated non-cytotoxicity in prior studies on other AUP types, this had not been verified for the specific AUP4K DA formulation and scaffold format intended for meniscus application.

2.2 Materials and methods

2.2.1. Materials

Poly(ethylene glycol) (PEG, molar mass of 4000 g/mol), phosphoric acid, isophorone diisocyanate (IPDI), phenothiazine (PTZ) and triphenylphosphite (TPP) were purchased from Merck. Bismuth neodecanoate (Valikat BI 2021) was purchased from Shepherd. Butylated hydroxytoluene was bought from Innochem GmbH and Bisomer PEA-6 from Geo Specialty Chemicals. Irgacure 2959 was obtained from BASF. Deuterated chloroform (CDCl3) was purchased from Euriso-Top. Printing needles (25 gauge and 27 gauge) were purchased from DL technology. All materials were used as received.

2.2.2 Methods

2.2.2.1 Synthesis of acrylate-endcapped urethane-based poly(ethylene glycol) precursors

The AUP-PEG4K-6EO-DA (AUP4K DA) was synthesized as described in literature [143,148,150]. Firstly, PEG was weighed and placed into a three-neck flask and molten at 90°C. Since PEG is slightly basic, phosphoric acid (178 ppm according to titration) was added under magnetic stirring once the material was completely molten. Next, butylated hydroxytoluene (BHT) was added (500 ppm) as radical scavenger. The PEG was dried under vacuum (< 30 mbar) and under Argon sparge for at least 3 hours.

Subsequently, the temperature was decreased to 65°C before the addition of IPDI and the catalyst. The decrease in temperature was necessary since the reaction between PEG and IPDI is exothermic. The magnetic stirring bar was substituted by a mechanical stirrer (set at 225-250 rpm) due to the increase in viscosity after the addition of the catalyst. The flask was kept in a nitrogen environment. After 2

hours, the post-stabilizers TPP (500 ppm with respect to the final product) and PTZ (500 ppm with respect to the final product) were added to the solution and mixed until complete dissolution. The addition of post-stabilizers is necessary to prevent premature crosslinking.

Finally, two equivalents of Bisomer PEA6 were added dropwise, followed by a second addition of the catalyst. The temperature was then increased up to 80°C and the reaction continued for another 2 hours in air atmosphere. The isocyanate (NCO) content could be determined qualitatively via Fourier transform infrared (FTIR) spectroscopy. The reaction was proceeded until no absorption band was observed at 2270 cm^{-1}, indicating that the NCO groups of IPDI had completely reacted.

2.2.2.2 Chemical structure of AUP hydrogel building blocks via FTIR spectroscopy

The PerkinElmer Frontier FTIR mid-IR, in conjunction with an MKII Golden Gate setup that includes a diamond crystal from Specac, was used to examine the molecular structures of the fabricated AUPs through Fourier transform infrared (FTIR) spectroscopy. The apparatus functioned in the attenuated total reflection (ATR) mode. The spectra for PEG, the initial reaction step's intermediate product (PEG-IPDI), and the end products (AUPs) were captured over eight scans within the 800-4000 cm-1 range.

2.2.2.3 AUP acrylate content determination via ^{1}H-NMR spectroscopy

The acrylate content and the molar mass of the AUP4K DA were measured using ^{1}H-NMR spectroscopy (Bruker Avance II Ultrashield 400 MHz), with deuterated chloroform serving as the solvent. The spectral data were processed using the MestReNova software.

Acrylate quantity was determined by utilizing dimethyl terephthalate (DMT) as an internal standard and comparing the integration of the aromatic ring protons signal in DMT (δ 8 ppm) with the integration of the acrylate protons peaks (δ 5.8, 6.2, and 6.4 ppm) using Equation (2.1):

$$C_{acr} = \frac{I_{\delta=5.8ppm}+I_{\delta=6.1ppm}+I_{\delta=6.4ppm}}{I_{\delta=8ppm}} \times \frac{N_{H,\delta=8ppm}}{N_{\delta=5.8ppm}+N_{\delta=6.1ppm}+N_{\delta=6.4ppm}} \times \frac{W_{DMT}}{MW_{DMT}} \times \frac{1000}{W_p} \quad (2.1)$$

Where, C_{acr} is the concentration of acrylates in the precursors (mmol acrylate per g precursor), (I_{δ}=5.8ppm + I_{δ}=6.1ppm + I_{δ}=6.4ppm) is the sum of the integrals of the signals of the acrylate protons (δ=5.8, 6.1 and 6.4 ppm), I_{δ}=8ppm is the integral of the signal of the protons from the aromatic ring in DMT (δ=8ppm), (N_{δ}=5.8ppm + Nδ=$_6$.1ppm + N_{δ}=6.4ppm) is the number of protons in one acrylate end group, $N_{H,\delta}$=8ppm is the number of protons in the benzene ring of DMT, MW_{DMT} is the molar mass of DMT (g mol-1), W_{DMT} and W_p are the weights of DMT (g) and the weight of the precursors (g) that were present in the NMR solution, respectively [142].

The molar mass of the AUP could be determined using Equation (2.2)

$$M_{AUP} = 2 * M_{Bisomer-PEA6} + M_{IPDI} + X * (M_{IPDI} + M_{PEG}) \quad (2.2)$$

in which $M_{Bisomer-PEA6}$, M_{IPDI} and M_{PEG} correspond to the molar mass of Bisomer-PEA6 (336.0 g mol^{-1}), the molar mass of IPDI (222.3 g mol^{-1}) and the molar mass of the PEG backbone used during the synthesis, respectively (4000 g mol^{-1}). The amount of repeating units (X) in the AUP molecules was determined using Equation (2.3)

$$X = \frac{\left(\left(N_{acrylate} * \frac{I_{\delta=3.4-4.0\ ppm}}{I_{\delta=5.83\ ppm}+I_{\delta=6.12\ ppm}+I_{\delta=6.40\ ppm}} * \frac{3}{4}\right) - N_{SEO}\right)}{\frac{M_{PEG}}{M_{EO}}} \quad (2.3)$$

Where $N_{acrylate}$ indicates the quantity of acrylate functionalities in the AUP molecule, which is assumed to be 2 for Bisomer PEA-6. The term $I_{\delta=3.4-4.0\ ppm}$ represents the intensity of the signal in the range of 3.4 to 4.0 ppm. This signal corresponds to the methylene units within the PEG backbone and the methylene units in the endcap. Additionally, the fraction 3/4 serves as a correction factor for the number of protons in one acrylate group (which is 3) compared to the number of protons in one EO unit (which is 4). N_{SEO} indicates the amount of EO repeating units in the spacers within the AUP molecule (which equals 12). Lastly, M_{PEG} refers to the molar mass of the PEG backbone used in the synthesis, while M_{EO} represents the molar mass of one EO unit (44 g mol^{-1}). [150]

2.2.2.4 Degree of crosslinking of AUP using High Resolution Magic Angle Spinning NMR spectroscopy

The crosslinking degree was assessed using high resolution magic angle spinning (HR-MAS) 1H NMR spectroscopy on a Bruker 700 MHz Avance II spectrometer. This instrument is fitted with a HR-MAS probe that includes a 1H, 13C, 119Sn, and gradient channel. The spinning speed was established at 6 kHz.

The degree of crosslinking was calculated using Equation (2.4):

$$\text{Degree of crosslinking (\%)}: \frac{\left(\frac{I}{R_I}-\frac{X}{R_X}\right)}{\frac{I}{R_I}} * 100\% \quad (2.4)$$

In which I = integral of the acrylate protons before crosslinking, R_I= integral of the PEG backbone before crosslinking, X = integral of the acrylates protons after crosslinking and R_x = integral of the PEG backbone after crosslinking.

2.2.2.5 Formation of AUP hydrogel networks via UV-induced free radical polymerization

To cast thin AUP films, AUP4K DA was melted at 60 °C. Two types of films were prepared: one without any photoinitiator, where the molten polymer was simply poured between two glass plates covered with Teflon foil and separated by a 1 mm silicone spacer; and a second in which 2 mol% of Irgacure was incorporated into the melted polymer under mechanical stirring prior to casting. Both samples were then placed in a UV-A device for 30 minutes (lamp intensity: 10 mW/cm², top and bottom) to initiate crosslinking where applicable. In addition, mirrors were present around the lamps and the samples to enhance light reflection and uniform distribution of UV intensity across the exposed surface, thereby promoting consistent crosslinking across all regions of the scaffold.

For crosslinking 3D printed scaffolds, the same UV setup was applied.

2.2.2.6 Material physical characterization

The geometric factor is one crucial parameter that influences the final properties of the product [215]. For this reason, the experimental campaign focused firstly on the evaluation of the material without any geometric effects (i.e. 2D level). Therefore, the first tests were conducted on 2D film (disk and dogbone) and subsequently on the 3D level (printed scaffold).

2.2.2.7 Swelling capacity and gel fraction on 2D AUP film

The characterization of AUP4K DA was performed on 2D disks obtained from an AUP4K DA film. AUP4K DA film was casted, crosslinked as described in the previous paragraph and six cylindrical samples (0.8 cm of diameter) were pouched out with a cylindrical plunger and their weights recorded.

These samples were then place into double distilled water for 72 hours as internal protocol. Every 24 hours, the medium was refreshed to promote the leaching of the uncrosslinked part and permit a complete swelling. The samples were placed inside a homemade incubator at constant temperature of 19° C that is considered an adequate temperature for the polymer since the T_g is assessed to be approximately of 28° C. After the recording of swollen weight, the samples were placed inside desiccator, filled with silica gel, and placed inside a drying chambers (FD 23, Binder) at 40°C overnight. Lastly, the samples were weighed again.

The swelling degree was calculated through the Equation (2.5) and the gel fraction through the Equation (2.6).

Swelling degree (%) = $\frac{Ws-Wdes}{Wdes} * 100$ (2.5)

Gel fraction (%) = $\frac{Wdes}{Wd} * 100$ (2.6)

In which: W_d is initial weight, W_s is weight in swollen condition and W_{des} is weight after drying.

2.2.2.8 Tensile measurements of 2D AUP dogbones

Following established in-house protocols, tensile tests were performed on dogbone-shaped samples (50 mm long, 1 mm thickness and 4 mm wideness) punched out from a AUP4K DA casted film as described in the previous paragraph. The samples were then placed into double distilled water for 72 hours at 19°C refreshing the medium every 24 hours in order to remove the un-crosslinked part of the material.

Tests were executed on a Tinius Olsen 5ST with a load cell of 500 N. Preload was set at 0.2 N, preload speed was set at 1 mm/min and deformation speed was set at 10 mm/min. All the tests were performed on swollen samples at room temperature.

2.2.2.9 Extrusion-based 3D printing

The data collecting of 2D samples were crucial to move from 2D to 3D and to project the scaffold creation. The photo-initiator Irgacure 2959 (2 mol% relative to the acrylate concentration) was added in the AUP material before the printing process.

Porous AUP cylindrical scaffolds (dry specimen size: 5 mm of highness, 10 mm of diameter) and specific fatigue-ring scaffolds described in §2.2.2.14 were produced using a Bioscaffolder® device (Sys-Eng, Germany). The use of this device has been described in literature. [216–218] The device melts the material in a dispense head and extrudes it in the form of a filament. The filament size depends on the diameter of the needle. Subsequently, the filament is deposited on a builder plate and the scaffold is made layer by layer.

PrimCam (Sys-Eng, Germany) was the software used to design the structure of the scaffolds and modify different printing parameters (i.e. speed, temperature, pression, printing pattern, strand distance etc…). [216] The software enables the user to digitally visualize the scaffold geometry after the setting of the various parameters and before the printing process.

Table 2.1 presents a summary of the printing parameters employed for generating AUP4K DA scaffolds with various printing patterns.

Table 2.1: Summary of printing parameters utilized for scaffold fabrication: an overview of the specific printing parameters used in the fabrication of scaffolds, including but not limited to, printing temperature, print speed, layer thickness, and strand distance. These parameters were optimized to ensure structural integrity and desired porosity of the scaffolds.

Parameters	**0°/90°**	**0°/45°**	**0°/45°/90°/135°**
Needle type	27 gauge	27 gauge	27 gauge
Temperature	57 C°	57° C	57° C
Layer thickness	0.12 mm	0.12 mm	0.12 mm
Strand distance	0.67 mm	0.67 mm	0.67 mm
Plotting speed	300 mm/min	280 mm/min	280 mm/min
Screw spindle speed (S)	250 rpm	270 rpm	270 rpm
Dispensing pressure	4 bar	4 bar	4 bar

The printed AUP4K DA scaffolds were subsequently crosslinked under UV-A for 30 minutes (lamp intensity top and bottom of 10 mW/cm^2).

2.2.2.10 Gel fraction and swelling capacity of AUP scaffolds

The characterization of AUP4K DA was performed both in 2D and then in 3D (scaffold level).

The procedure to calculate the gel fraction and swelling capacity is described before in the § 2.2.2.7. Therefore, the scaffolds were crosslinked, weighted, placed in double distilled water for 72 hours and

the medium was refreshed after every 24 hours, following the same procedure of the 2D. Before the drying, the swollen weights were recorded. After desiccation, the scaffolds were weighed again.

2.2.2.11 Static compression test of AUP scaffolds

Static compression tests were performed on the aforementioned AUP4K DA cylindrical-shape scaffolds in swollen condition. Once the scaffolds were printed, they were crosslinked for 30 minutes (lamp intensity 10mW/cm2) and subsequently were then place into double distilled water for 72 hours at 19°C to remove the un-crosslinked part (refreshing the medium after every 24 hours) and then immediately tested.

In the 3D level, it is necessary to evaluate the geometric effects. In the extrusion-based printing techniques, the printing pattern is extremely important. Therefore, it was decided to investigate three different printing patterns (i.e. 0°/90°, 0°/45° and 0°/45°/90°/135°) to assess the eventual mechanical behaviour differences between them. Subsequently, also the effect of varying the pores size and struts size on the mechanical properties was investigated.

Tests were executed on a Tinius Olsen 5ST with a load cell of 500 N. The speed was set relatively low (2 mm/s) since the viscoelastic nature of the polymer. The preload was set following the internal lab protocol at 0.3 N.

2.2.2.12 Dynamic modulus analysis of AUP scaffolds

The samples were prepared as described above in § 2.4.2 and were always tested in swollen condition.

Dynamic mechanical analysis (DMA) was performed using an home-made set-up already described in previous research. [219]

DMA was performed on scaffolds with different printing patterns (0°/90°, 0°/45° and 0°/45°/90°/135°) to evaluate differences in mechanical properties and to investigate any potential resonance peaks. Indeed, every physical structure possesses natural frequencies. These frequencies correspond to the rates at which the structure is inclined to resonate when exposed to specific external forces. These frequencies are dependent on the way mass and stiffness are distributed within the structure. The phenomenon of the resonance occurs when a dynamic force drives a structure to vibrate at its natural frequency. In a state of resonance, even a minor force can result in a substantial vibrational reaction. [220] The presence of the mechanical resonances can cause performance degradation, motion problems and undesired response from the materials itself. Therefore, identifying them is crucial for any potential applications. [221]

2.2.2.13 Fatigue tests of AUP scaffolds

To investigate if the printed AUP4K DA material may be suitable for cyclically loaded applications, such as meniscus implants, fatigue tests needed to be performed. Therefore, simplified meniscus specimens of AUP4K DA material were printed, crosslinked and dried using a desiccation process and soaked again in double distilled water until the specimens were saturated. The simplified specimens were symmetric rings. The ring specimens in the swollen condition have an outer diameter of 35 mm, an inner diameter of 25 mm and a maximum height at the outer rim of 7 mm. A rounding with a radius of 30 mm at the outer rim results in a height of the inner rim of the swollen ring specimens of approximately 4.1 mm. A schematic of the applied design is provided in Figure 2.1.

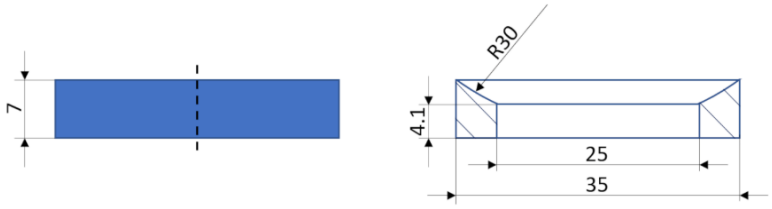

Figure 2.1: Dimensions (in mm) of the ring specimens in the swollen condition as full part (left) and sectional view (right).

Figure 2.1 shows the simplified specimens being symmetric rings. In the swollen state, the rings had an outer diameter of 35 mm, an inner diameter of 25 mm, and a maximum height of 7 mm at the outer rim. Due to a 30 mm rounding radius at the outer edge, the height at the inner rim was reduced to approximately 4.1 mm.

A test chamber was developed in which the ring specimens were placed on a metal cylinder. The metal cylinder contains a hole in the middle with a bulging edge. The ring specimens were placed around the bulging edge, to prevent the rings from slipping, without inducing any force on the specimens. The metal cylinder was placed on the baseplate of the test chamber and could move freely on the baseplate. The test chamber was filled with double distilled water. A polished hemisphere made of cobalt-chromium-molybdenum with a radius of 24 mm was used as counterpart. The hemisphere was fixated at the testing machines, which pressed the hemisphere cyclically on the ring specimens to induce a compression as well as a shearing/elongation of the ring specimens. Using this approach, a maximum compression of the ring specimens of at least 80% was applicable.

Two devices were applied for the fatigue testing: a material testing device and a dynamic testing device.
The first fatigue compression tests were performed using the material testing machine Zwick Z005 (ZwickRoell GmbH & Co. KG, Ulm, Germany). The testing machine was operated in displacement control

and a compression of approximately 75% of the specimen height (inner ring height) was set as target parameter. This corresponds to 3 mm of compressive motion from the starting position. The starting position corresponds to the position, when inducing a preload of 0.5 N to the specimens. The velocity of the compression was set to 13 mm/s. Thereby, the maximum force is reached fast (approximately 0.3 s) and then held for a short time period (approximately 0.9 s). This enables the scaffolds to release the contained fluid at the maximum force while limited fluid release is possible between the unloaded and the loaded state. After that, the device returns to its starting position with a similar speed as for the compression within a total time of approximately 0.3 s. To conclude one cycle, the device stays for more than one second in the starting position until the next compression cycle begins. This device thus realizes 7 load cycles in 20 seconds. As maximum test duration 200.000 cycles was chosen as long as the samples did not fail earlier.

The second test was based on a dynamic load application (Testing machine: TP 10kN, DYNA-MESS Prüfsysteme GmbH, Stolberg, Germany), which applied a sinusoidal compression to the specimens. In contrast to the tests using the material testing machine a cyclic compression from 5% to 80% of the specimen height (inner ring height) was set as target parameter. This corresponds to 3 mm of compressive motion, similar to the material testing machine. However, the absolute maximum compression was higher using this approach. In our tests, the maximum loading velocity of the dynamic testing device at 1 Hz is an estimated 50% of that from the mechanical testing device. However, due to the sinusoidal loading condition, the scaffolds can only release very limited fluid in between different cycles. This device thus realizes 20 load cycles in 20 seconds. The tests started with 1 Hz and a maximum of 200.000 cycles were applied, as soon as the specimen

did not fail earlier. If the specimens could resist the test duration without failure, the frequency was raised to 2 Hz for the same test duration. If no failure occurs, the next frequencies would be 4 Hz and 8 Hz respectively.
For each testing approach (material testing machine and dynamic testing machine) two ring specimens were used.

A detailed photograph of the chamber set-up, along with an image of the printed ring specimen, is provided in Figure 2.2.

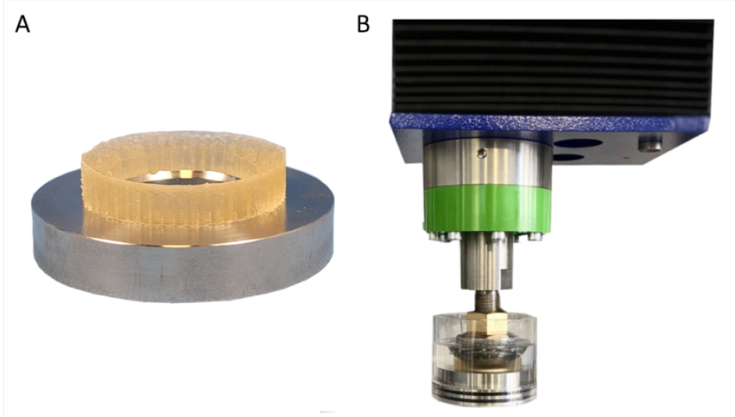

Figure 2.2: A) The metal cylinder on which the ring specimens were placed and B) the relevant parts of the dynamic testing machine with the test chamber.

2.3 Results and discussion

Hydrogels exhibit high water content while providing a specific three-dimensional microenvironment that can be engineered to mimic both the chemical and the topographical nature of the native meniscus. In the meniscus regeneration, various hydrogels, natural as well as synthetic, have been investigated to date to replace and repair the meniscus tissue due to their tuneable properties and biocompatibility. [107,222]

In previous work of our group, we studied so-called AUP based on PEG with various molar masses (1000-8000 g/mol) as potential hydrogel meniscal substitute. [140] Preliminary evaluation of the compressive mechanical properties of the scaffolds revealed that the AUP4K DA variant possesses mechanical properties in the range of the human meniscus. That material was therefore subjected to the present in-depth study.

2.3.1 Hydrogel building block synthesis

The AUP applied in our work was synthesized through a process involving the reaction of PEG with a molar mass of 4000 g/mol with two equivalents of IPDI, followed by the reaction with two equivalents of a monoacrylated oligo(ethylene glycol) spacer. In the rest of this work, the resulting hydrogel (precursor) will be indicated as AUP4K DA.

Figure 2.3 shows the general and the detailed chemical structures of the obtained polymers (panel A) together with the FTIR (panel B) and NMR spectra (panel C).

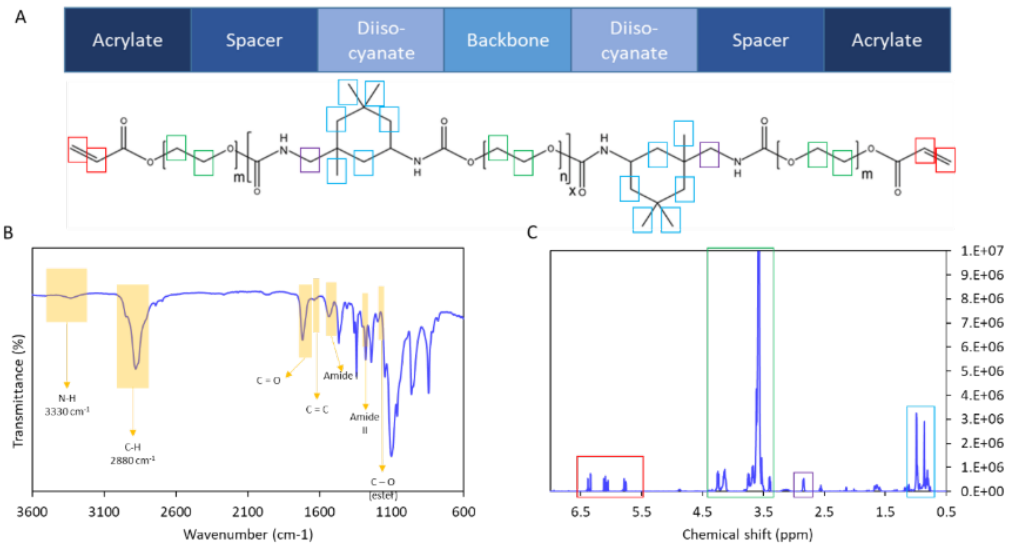

Figure 2.3: Chemical structure, FTIR and NMR spectra of AUP4K DA hydrogel precursor. A) The general (top) and the detailed (bottom) chemical structures of the developed AUP4K DA. B) FTIR spectrum of AUP4K DA. The characteristic IR peaks of the AUP4K DA are indicated. C) ^{1}H-NMR spectrum of AUP4K DA. Peak annotation is performed through the applied colour code in parts A and C of the figure.

The FTIR spectrum reveals the presence of the characteristic absorption bands associated with the acrylate end groups, such as the C=C acrylate stretch (at 1635 cm^{-1}), the C=O stretching at 1720 cm^{-1}, the amide I and II at 1530 and 1300 cm^{-1} respectively, the C-O stretch of the acrylate esters (at 1200 cm^{-1}) and the N-H stretching vibration of the urethane bond (at 3330 cm^{-1}) as reported in literature for other AUP types. [142,148,223]

The collected NMR spectrum enables quantitative structure elucidation/confirmation of the AUP4K DA. The signals between δ=0.7 and δ=2.0 ppm correspond to the methyl and the methylene protons in the cyclic portion of IPDI respectively, while the signals at δ=3.3 and δ=3.8 ppm are attributed to the methylene protons present in the PEG backbone and the spacers. Finally, the signals at δ=5.8, δ=6.1, and δ=6.3 ppm can be ascribed to the acrylate protons.

The acrylate content for the AUP4K DA (0.37 mmol acrylate/g AUP4K DA) was determined using the data obtained from the ^{1}H-NMR spectra using Equation 2.1. This was realized by comparing the signal from the AUP4K DA acrylate groups with the protons in the aromatic ring of dimethyl terephthalate (DMT, used as internal standard). The molar mass of the AUP4K DA was calculated using Equation 2.2 to be 5570 g mol^{-1}. The resulting values reveal that the molar masses of the AUPs are approximately 1.4 times higher than that of the original PEG backbone. This increase can be attributed to the lower selectivity of the bismuth-based catalyst toward the primary isocyanate group of IPDI. Unlike organotin catalysts such as dibutyltin dilaurate (DBTL), the bismuth catalyst may allow both isocyanate groups of IPDI to participate in the first reaction step, promoting unintended repetition of the PEG-IPDI units and therefore extending the chain [224].

2.3.2 Gel fraction, swelling capacity and degree of crosslinking of AUP4K DA

A first important property of hydrogels is their gel fraction which indicates the percentage of the original amount of polymer that is present in the hydrogel network after crosslinking. A high gel fraction indicates that a larger amount of the polymer has formed a crosslinked network, resulting in a more stable and robust hydrogel. The gel fraction affects various hydrogel properties such as the mechanical properties and the swelling behaviour.

In a first step, before studying hydrogel scaffolds, both the swelling degree and the gel fraction were examined on AUP4K DA discs. To potentially enhance the efficiency of hydrogel crosslinking, the study also investigates the incorporation of 2 mol% Irgacure as a photoinitiator (PI).

The data, shown in Figure 2.4 panel A reveal that the addition of 2 mol% PI has a minimal and non-significant ($p > 0.05$) impact on the gel fraction and the swelling degree. The PI amount (2 mol% relative to the number of AUP acrylates) was based on previous research from our group. As the crosslinking efficiency of the discs without PI is already high, PI addition does not affect this property. As aforementioned, one unique characteristic of the AUP family is their photo-crosslink-ability in the absence of a PI. The data for the AUP4K DA applied in this work confirm this.

With the aim to determine the absolute acrylate conversion (i.e. the absolute degree of crosslinking) in the final hydrogels, the reduction of the characteristic acrylate signals (at 5.8, 6.1, and 6.4 ppm) was assessed using HR-MAS ^{1}H NMR. As shown in Figure 4 panel B, a minimum of 99.88% of the double bonds reacted, indicating an almost complete conversion of the acrylates (indicated in the ^{1}H NMR spectra

in the area indicated with the red square). Therefore, it can be concluded that the crosslinking reaction was successful for the AUP4K DA, regardless of the presence of the PI.

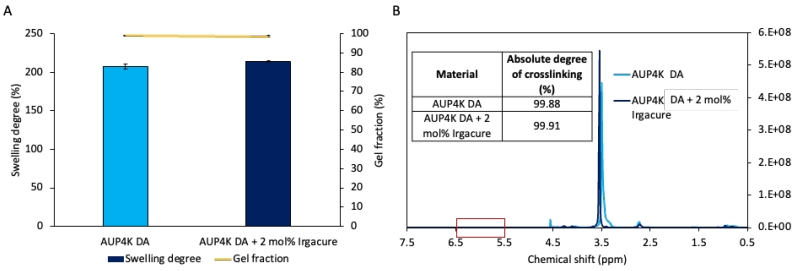

Figure 2.4: Swelling degree, gel fraction and absolute acrylate conversion of AUP4K DA discs. A) Effect of PI on the swelling degree and the gel fraction of AUP4K DA in water. B) The HR-MAS ^{1}H NMR spectrum of AUP4K DA with and without PI. The table shows the values of the absolute degree of crosslinking, while the red box highlights the peaks corresponding to the acrylate protons. Statistical significance between groups was assessed by the paired Student's t-test (n = 6).

2.3.3 Tensile testing of AUP4K DA

Different biomedical researchers previously investigated the load bearing and the stress distribution in the meniscal tissue. [11,13,225,226] Due to its different functions, the meniscus is subjected to a complex combination of compressive, tensile and shear stresses. [33] The human meniscus during flexion and extension has its stretching direction parallel to the meniscal longitudinal axis implying that a tensile force is developed in this direction. Simultaneously, a low tensile force is developed along the other axes. [11,40] Therefore, investigating the tensile properties of any material to be applied is crucial. To this end, tensile tests were performed on double distilled water swollen dog-bone shaped samples as the meniscal tissue can be compared to a hydrogel in swollen condition given the presence of the synovial fluid inside its structure.

It is important to underline that this test aims to test the material performance. Due to the way in which the dogbone is made (casting followed by cutting using a dogbone puncher, see § 2.3.2), the dogbone is isotropic in nature.

The obtained stress-strain curves and the calculated Young's moduli therefrom, the ultimate strengths and the ultimate strains are shown in Figure 2.5.

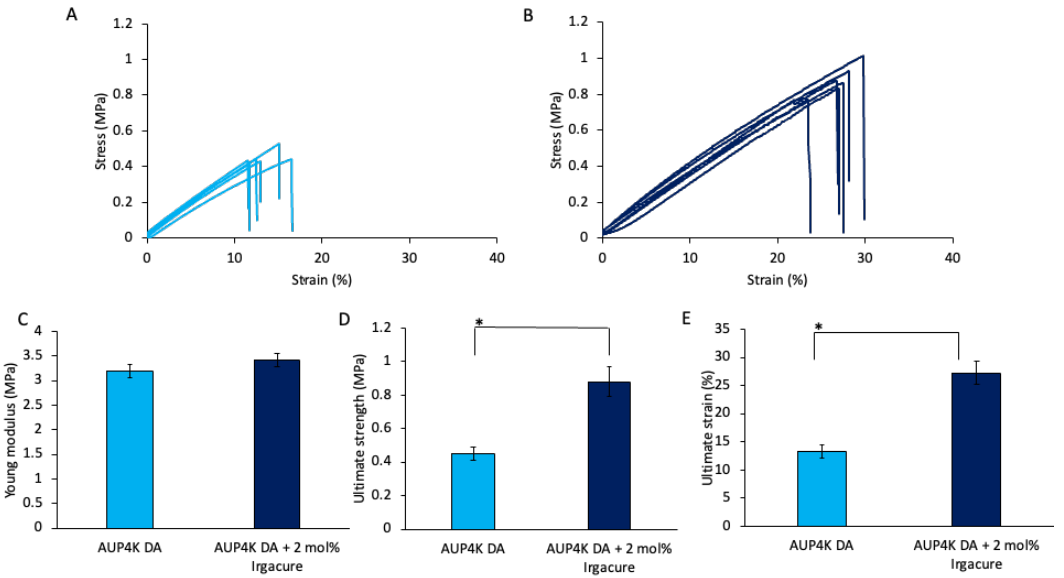

Figure 2.5: Effect of PI on the stress-strain behaviour of water-swollen AUP4K DA dogbones at a tensile speed of 10 mm.min^{-1}, a preload speed of 1 mm.min^{-1} and a preload of 0.2 N. A) Stress-strain curves for AUP4K DA without PI, B) Stress-strain curves for AUP4K DA + 2 mol% PI, C) Young modulus, D) ultimate strength and E) ultimate strain as determined from the tensile curves in parts A and B. The asterisk indicates p values <0.05. Statistical significance between groups was assessed by the paired Student's t-test (n = 6).

The obtained curves reveal similar shapes to curves obtained for swollen hydrogels by other researchers. [227,228] In the crosslinked AUP4K DA hydrogel network, the polymer chains are permanently linked via the crosslinking points, with water in between. Due to the water present, the chains are lubricated and the hydrogel in its crosslinked state is stretched to its maximum level (i.e. the equilibrium swelling), only limited by the presence of the crosslinking points. As the swollen hydrogels can thus not realign upon an applied stress, they will break in a brittle manner. For this reason, the curves tend then to be almost linear. [229,230] A second reason for the linear behaviour is the fact that the tests were conducted in a temperature-controlled room at 20°C. As this is below the crystallization temperature of AUP4K DA (T_c = 25°C as determined by DSC measurement (data shown in Chapter 3).

Based on the data obtained (Figure 2.5), all the values derived from the tensile tests, including the Young's modulus, the ultimate strength and the ultimate strain, demonstrate higher values for the specimens with added PI. The differences are statistically significant ($p < 0.05$) for the ultimate strength and the ultimate strain. This phenomenon, in which more uniform and stronger crosslinked networks are formed in the presence of a PI, was reported earlier in literature. [231–236]

Comparing the obtained results with the literature data, it is noticeable that the results of the tensile Young's modulus of the AUP4K DA dogbones (Figure 2.5 panel C), calculated between 5 and 10% of the strain, are in the lower range of the tensile results of human meniscus samples. Yin et al. reported low elastic moduli for the medial meniscus, with values ranging from 0.11 to 0.18 MPa depending on the studied meniscus region. [37] In contrast, studies from Henderson et al. [36] and Nesbitt et al. [38] showed significantly higher values, with some reaching up to 101.7 MPa and 109.9 MPa, respectively. The variation in the

reported tensile property values can be attributed to several factors. One of the primary reasons is the presence and the orientation of collagen fibres in native menisci. The tensile properties differ significantly when being measured in a direction parallel or perpendicular to these fibres. Additionally, different studies apply samples of varying shapes, sizes, conservation methods and testing conditions (dried versus swollen, ...). Finally, regional variations within the meniscus, including differences in cellular and extracellular matrix composition between inner and outer regions should also be considered. The performed tests are however very relevant as first comparison of the herein developed hydrogel with the *in vivo* situation.

When comparing the ultimate strength (Figure 2.5 panel D) and ultimate strain (Figure 2.5 panel E) results, it is possible to observe the same trend as in the aforementioned studies. The ultimate strength values for AUP4K DA fall within the lower range of reported values for human meniscal samples (0.32–18.63 MPa). [41,48] Similarly, the ultimate strain values align with the human meniscus range, spanning from 2.13% to 94%. [36,38,39,41,48]

2.3.4 Structural characterization of AUP4K DA scaffolds

In the next part of our study, the synthesized AUP4K DA was 3D-printed using the Bioscaffolder as an extrusion-based printing device. As described in Chapter 1, the native meniscus possesses a heterogeneous, zone-dependent architecture in which collagen fibres are organized in distinct orientations, predominantly circumferentially in the deep zone and more radially or randomly in the superficial layers. This structural anisotropy is directly responsible for the directional mechanical behaviour of the tissue, including its ability to resist circumferential tensile hoop stresses under axial compressive loading.

A key objective of the scaffold fabrication strategy pursued in this chapter was therefore to investigate whether variations in printing pattern could be used as a design tool to approximate the heterogeneous mechanical response arising from this native fibre organization. While extrusion-based printing does not allow the direct replication of individual collagen fibre bundles, the orientation of deposited polymer struts across successive layers can be systematically varied to produce scaffolds with different directional stiffness profiles, thereby providing a first-order approximation of the mechanical heterogeneity of the native tissue. Due to the complexity of the meniscal anatomy, the mechanical properties of the native tissue are zone-dependent and thus not homogeneous throughout the meniscus. With the aim of mimicking the mechanical properties of the different zones to the highest extent possible, we varied the pore dimension, the polymer strut size and the printing pattern of the scaffolds.

The effect of printing parameters on scaffold properties was investigated using a one-factor-at-a-time (OFAT) approach, in which one design variable was systematically varied while all others were held constant. The printing pattern was varied first (0°/45°, 0°/90° and 0°/45°/90°/135°) at constant strut and pore dimensions. Based on the superior mechanical performance of the 0°/90° pattern, the strut diameter and pore size were subsequently varied while keeping this pattern fixed.

The pore size and the strut diameter were varied from 200 to 300 µm (± 20 µm) and from 370 to 450 µm (± 20 µm) respectively by design. In all cases, the strand distance (i.e. the distance between the centres of two neighbouring struts) was kept constant at 0.67 mm. A schematic overview of the three different printing patterns selected is shown in Figure 2.6. Furthermore, to obtain optimal scaffold crosslinking, 2

mol% of PI was added to the polymer before printing. Indeed, we demonstrated earlier that the gel fraction of AUP4K DA scaffolds increased with 5-15% when comparing scaffolds without PI (gel fraction ranging from 64%-70%) to scaffolds with PI (gel fraction > 80%). Therefore, 2 mol% of PI was applied as a starting point for crosslinking the printed scaffolds.

Based on previous research in our lab, a scaffold with a 0°/90° printing pattern, strut diameters of 370 µm (± 20 µm) and pore sizes of 300 µm (± 20 µm) was selected as reference.

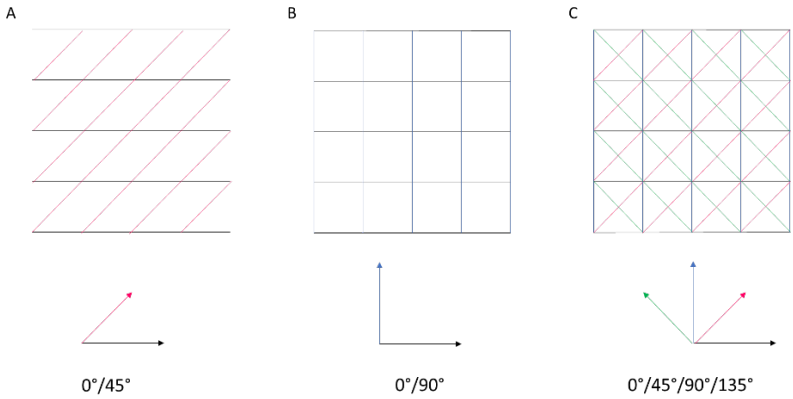

Figure 2.6: Schematic representation of the different printing patterns applied in this study. A) 0°/45°, B) 0°/90° and C) 0°/45°/90°/135° printing pattern.

For each batch of samples, a minimum of three scaffolds were produced and subsequently tested. After visualisation using optical microscopy, different 3D printed cylindrical scaffolds, fabricated on the same day under identical condition using material from the same batch, were subjected to swelling and gel fraction tests, compression tests and dynamic modulus analysis tests.

Optical microscopy images were collected to evaluate the morphological structure of the scaffolds and were used to compare the theoretical scaffold design with the obtained structures.

From the optical microscopy images in Figure 2.7, it is evident that the 0°/90° printing pattern gives rise to scaffolds possessing straight polymer struts. Despite significant efforts to optimize the printing parameters (increasing the spindle speed 250 rpm to 270 rpm while decreasing the plotting speed from 300 mm/min to 280 mm/min) for achieving similar results for the 0°/45° and the 0°/45°/90°/135° printing pattern, these attempts were not successful. This most likely arises from the fact that for both patterns, in contrast to the 0°/90° pattern, a longer distance needs to be bridged to span two polymer struts of an underlying layer. This extended distance causes the polymer strut diameters to fluctuate. [237] In an attempt to mitigate these findings, a reduction in plotting speed could be considered. However, this would result in a substantial increase in strut dimensions. As we wanted to explore the effect of only the printing pattern on the mechanical properties, decreasing the deposition speed was not an option.

Important to note is that both the 0°/45° and the 0°/45°/90°/135° scaffolds possess rhomboidal pores, whereas the 0°/90° scaffolds contain cubic pores. This difference in pore geometry directly influences the mechanical response. The 0°/90° pattern produces a symmetric structure with struts intersecting at right angles, enabling an even load distribution across both principal directions. The 0°/45° pattern, by contrast, introduces asymmetric spanning distances between layers, resulting in unbalanced load transfer and the curved struts observed in Figure 2.3. Although the 0°/45°/90°/135° pattern partially compensates by distributing deposition over four orientations, rhomboidal pores and longer bridging distances still reduce structural regularity. These architectural differences are consistent with the superior and more reproducible compressive performance of the 0°/90° scaffolds.

Unless otherwise specified, all optical microscopy images in this chapter were acquired in top-down view, with the viewing direction perpendicular to the printing plane (along the build direction).

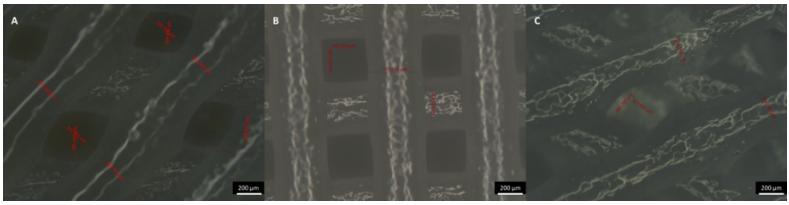

Figure 2.7: Optical microscopy images (5X magnification) of AUP4K DA scaffolds printed using the Bioscaffolder device in a 0°/45° (A), 0°/90° (B) and 0°/45°/90°/135° (C) pattern. For all scaffolds, the strut diameter and the pore size are respectively 370 µm (± 20 µm) and 300 µm (± 20 µm). The scale bars are indicated on each figure.

In the next part of my work, we developed scaffolds with varying combinations of strut diameter and pore size. Based on the above finding that only the 0/90° printing pattern gave rise to straight polymer struts, this pattern was applied. To enable printing these scaffolds, an adaptation of the printing conditions had to be realized. The needle type was changed from 27 gauge to 25 gauge, the pressure was increased from 4 to 5 bar, the screw spindle speed from 270 to 280 rpm and the printing speed decreased from 300 to 250 mm/min. The results shown in Figure 2.8 represent the different scaffolds obtained with different strut diameters and pore sizes.

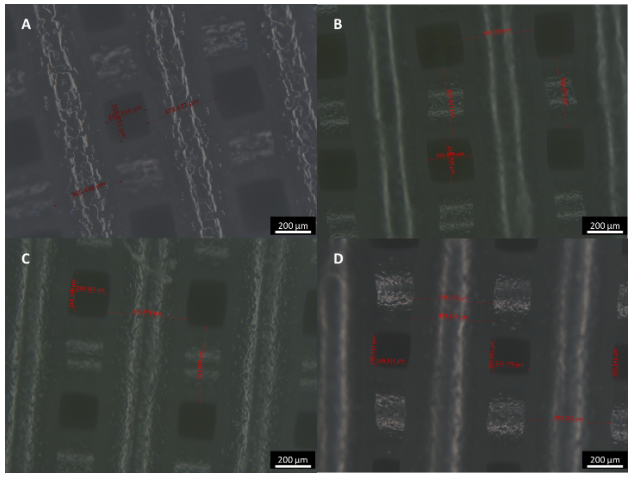

Figure 2.8: Optical microscopy images (5X magnification) of AUP4K DA scaffolds printed using the Bioscaffolder device in a 0°/90° pattern with different strut diameter and pore size. A) Scaffold with strut diameter of 370 µm (± 20 µm) and pores size of 250 µm (± 20 µm); B) Scaffold with strut diameter of 400 µm (± 20 µm) and pores size of 250 µm (± 20 µm); C) Scaffold with strut diameter of 450 µm (± 20 µm) and pores size of 250 µm (± 20 µm); D) Scaffold with strut diameter of 450 µm (± 20 µm) and pores size of 200 µm (± 20 µm). The scale bars are indicated on each figure.

In addition, we also evaluated designs featuring larger pore dimensions and reduced strut diameters to explore the printing limits and geometric versatility of the AUP4K DA. The applied printing parameters are summarized in Table 2.2.

Table 2.2: Summary of printing parameters used for scaffold fabrication. The table provides an overview of the specific printing conditions applied during scaffold production, including the printing temperature, the extrusion speed, the layer height, and the strand spacing. These parameters were optimized to achieve consistent structural integrity and the targeted porosity.

Parameters	**0°/90°** **S: 350 ± 20 µm** **P: 350 ± 20 µm**	**0°/90°** **S: 290 ± 20 µm** **P: 390 ± 20 µm**	**0°/90°** **S: 240 ± 20 µm** **P: 390 ± 20 µm**
Needle type	27 gauge	27 gauge	27 gauge
Temperature	57 C°	57° C	57° C
Layer thickness	0.12 mm	0.12 mm	0.12 mm
Strand distance	0.68 mm	0.70 mm	0.70 mm
Plotting speed	350 mm/min	380 mm/min	400 mm/min
Screw spindle speed (S)	230 rpm	200 rpm	180 rpm
Dispensing pressure	4 bar	4 bar	4 bar

The constructs were fabricated using higher plotting speeds (350–400 mm/min), reduced screw-spindle speeds (180–230 rpm), and slightly increased strand distances (0.68–0.70 mm) compared to the parameters reported in Table 2.1.

Representative optical microscopy images of these alternative constructs are shown in Figure 2.9.

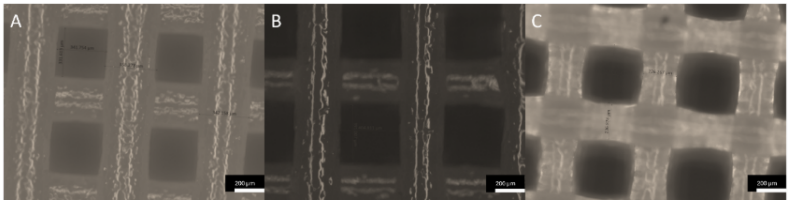

Figure 2.9: Optical microscopy images (5X magnification) of AUP4K DA scaffolds printed using the Bioscaffolder device in a 0°/90° pattern with different strut diameter and pore size. A) Scaffold with strut diameter of 350 µm (± 20 µm) and pores size of 350 µm (± 20 µm); B) Scaffold with strut diameter of 290 µm (± 20 µm) and pores size of 390 µm (± 20 µm); C) Scaffold with strut diameter of 240 µm (± 20 µm) and pores size of 390 µm (± 20 µm). The scale bars are indicated on each figure.

This combination of printing settings resulted in scaffolds featuring larger pore sizes and thinner struts, while still maintaining regular strand deposition and well-defined pore boundaries. These results demonstrate the tunability of the AUP4K DA printing process and the ability to reliably adjust scaffold morphology through controlled modification of the printing parameters.

Before proceeding with any tests, the scaffolds were crosslinked under UV-light as described in § 2.2.2.9.

It could be considered whether in-situ UV curing, that is, crosslinking each layer immediately upon deposition, might improve scaffold structural stability during and after printing, and whether it could introduce additional degrees of freedom in scaffold design. However, several practical and fundamental considerations argue against this approach for the current AUP-based extrusion printing system. First, layer-by-layer crosslinking would significantly compromise interlayer adhesion. When a freshly deposited layer is UV-cured before the next layer is applied, the degree of covalent interlayer bonding depends on the availability of unreacted acrylate groups at the interface. Although the melt state of the deposited AUP allows for some chain interdiffusion and physical entanglement between layers, premature crosslinking of

the lower layer would reduce the number of reactive sites available for covalent bonding with the subsequently deposited material, potentially weakening the interlayer interface compared to the bulk-crosslinking approach, in which all layers remain uncrosslinked and fully interpenetrated prior to a single UV-curing step. Second, the incorporation of a UV-curing step after each deposited layer would substantially increase the total fabrication time. Given the already considerable printing duration required for the precise scaffold architectures developed in this work, with controlled strut diameters, pore sizes, and multi-layered stacking patterns, the addition of a curing step per layer would render the process impractically slow, particularly when multiple scaffolds are needed for systematic characterization. Third, the heat generated during UV exposure at close proximity to the nozzle could alter the rheological behaviour of the AUP melt, potentially affecting extrusion consistency and strand uniformity in subsequent layers. For these reasons, the approach adopted in this thesis, in which the complete scaffold structure is first deposited in its entirety and subsequently crosslinked in a single bulk UV irradiation step, was considered the most appropriate strategy. This post-print crosslinking protocol ensures homogeneous curing throughout the scaffold volume, maintains strong interlayer cohesion through the entanglement and interdiffusion of uncrosslinked polymer chains between adjacent layers during deposition, and allows for a practical and reproducible fabrication workflow. It should be noted, however, that in-situ curing strategies may hold potential for other fabrication techniques, such as DLP-based printing (as explored in Chapter 4), where layer-by-layer photopolymerization is inherent to the process and interlayer bonding is achieved through controlled penetration of light into the previously cured layer.

2.3.5 Gel fraction and swelling degree of AUP4K DA scaffolds

Crosslinking a 3D scaffold is more complex as compared to 2D samples due to potential limitations in UV light penetration within the 3D scaffold structure, given differences in thickness between 3D scaffolds and 2D samples as well as the presence of struts and pores within 3D scaffolds.

The first aspect that was studied included a possible effect of the scaffold printing pattern (0°/45°, 0°/90° versus 0°/45°/90°/135°) on the gel fraction and the swelling degree. Very interestingly, the data in Figure 2.10 panel A reveal that no statistically significant effects of the printing pattern on the scaffold gel fraction ($p > 0.05$) and the swelling degree ($p > 0.05$) were observed. To the best of our knowledge, this has not been reported to date in literature. When comparing the data for 3D scaffolds with those for 2D samples, it can be concluded that the 3D scaffolds reveal lower gel fractions and higher swelling degrees. This confirms that the UV crosslinking is indeed negatively affected by the 3-dimensionality of the scaffolds (cfr. thickness, presence of struts and pores). This leads to a more pronounced swelling of the 3D scaffolds.

The dimensions of both the strut diameter and the pore size represent critical aspects that can potentially influence the swelling degree and the gel fraction. To explore this further, a comparative analysis was carried out on scaffolds with different pore sizes and strut diameters, ranging from 200-300 µm (± 20 µm) and from 370-450 µm (± 20 µm), respectively. The data (Figure 2.10 panel B) reveal that the effect of the pore size and the strut diameter is minimal, at least in the investigated ranges. Moreover, the scaffolds possess similar gel fractions and swelling degrees as those with different printing patterns.

Only the scaffold with the smallest pore size (i.e. 200 µm (± 20 µm)) show a statistically significant decrease ($p < 0.05$) in the gel fraction (89% as compared to the other values exceeding 91%), and a concomitant statistically significant ($p < 0.05$) increase in swelling degree (295% as compared to the second largest swelling degree of 278%. This phenomenon for this scaffold can be attributed to a combined effect of the smaller pore size, hampering the penetration of UV light, and the large strut diameter, causing more pronounced scattering of the UV light. These data are confirmed by other studies.[238,239]

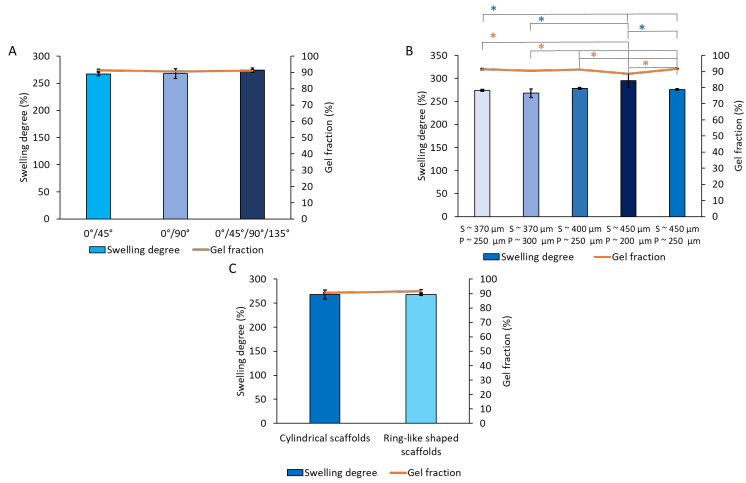

Figure 2.10: Swelling degree (SD) and gel fraction (GF) of various AUP4K DA scaffolds. A) Effect of printing pattern on SD and GF, B) Effect of pore size and strut diameter on SD and GF. C) Effect of scaffold shape (cylinder versus ring-shaped) on SD and GF. All scaffolds were printed in the presence of 2 mol% PI. The scaffolds analysed in parts A and C have strut sizes of 370 µm (± 20 µm) and pore sizes of 300 µm (± 20 µm). Scaffolds analysed in parts B and C were obtained using a 0°/90° printing pattern. The asterisk indicates that the $p < 0.05$. Statistical significance between groups was assessed by the paired Student's t-test (n = 3).

In a final step of this part of our study, we also studied if more complex scaffold geometries, to be applied in the fatigue tests described later, would reveal different gel fractions and swelling degrees. To this end,

ring-like shaped scaffolds (shown in Figure 2.2 left panel) were compared to cylindrical scaffolds. Both types of scaffolds printed with a 0°/90° printing pattern, possessed strut diameters and pore sizes of respectively 370 µm (± 20 µm) and 300 µm (± 20 µm) and contained a PI concentration of 2 mol%. The results (Figure 2.10 panel C) illustrate that the swelling degree and the gel fraction are not statistically different ($p > 0.05$) for these two scaffold shapes. The material can thus be efficiently crosslinked, even if it represents a more complex shape.

When we juxtapose our material with the existing literature on hydrogel scaffolds, we find that the gel fraction and the degree of swelling values are either superior or comparable with the values reported in literature. [240,241] Specifically, the study by Tytgat et al. reported that the 0°/90° Gel-MA and Gel-NB – Gel-SH had a mass swelling ratio ranging from 25 to 52 and a gel fraction between 63 and 65%. [240] In contrast, Lüchow et al. found that the four-armed degradable PEG (MoDPEG) hydrogel had swelling degree ranging from 85 to 100% and a gel fraction between 60 and 85%. [241]

2.3.6 Static compression measurements of AUP4K DA scaffolds

The compression properties of the human meniscus are essential for a proper knee joint function. [226,242] In compression, the meniscus behaves non-linearly. Under low compressive load, the meniscus behaves as an elastic device. However, as the compressive load increases, the meniscus becomes stiffer. Furthermore, the compressive properties of the meniscus also depend on the location within the tissue. Indeed, the inner portion is more fibrocartilaginous, while the outer portion is more fibrous, leading to differences in compressive resistance. [243] The compressibility of the meniscus is due to its chemical nature, its porous structure and the capacity of the

synovial fluid to move internally inside the porous, hierarchical structure of the meniscal tissue (both in the pores and through the fibres). A compression test is thus the first technique that was performed to investigate the mechanical properties of the developed AUP4K DA scaffolds.

At first, we investigated the possible effect of the scaffold printing pattern on the mechanical properties. The tests were performed on water-swollen AUP4K DA scaffolds, printed using 2 mol% of Irgacure 2959, with a strut sizes of 370 μm (± 20 μm) and pore sizes of 300 μm (± 20 μm). The compressive stress-strain curves and the derived mechanical properties for the different printing patterns are shown in Figure 2.11.

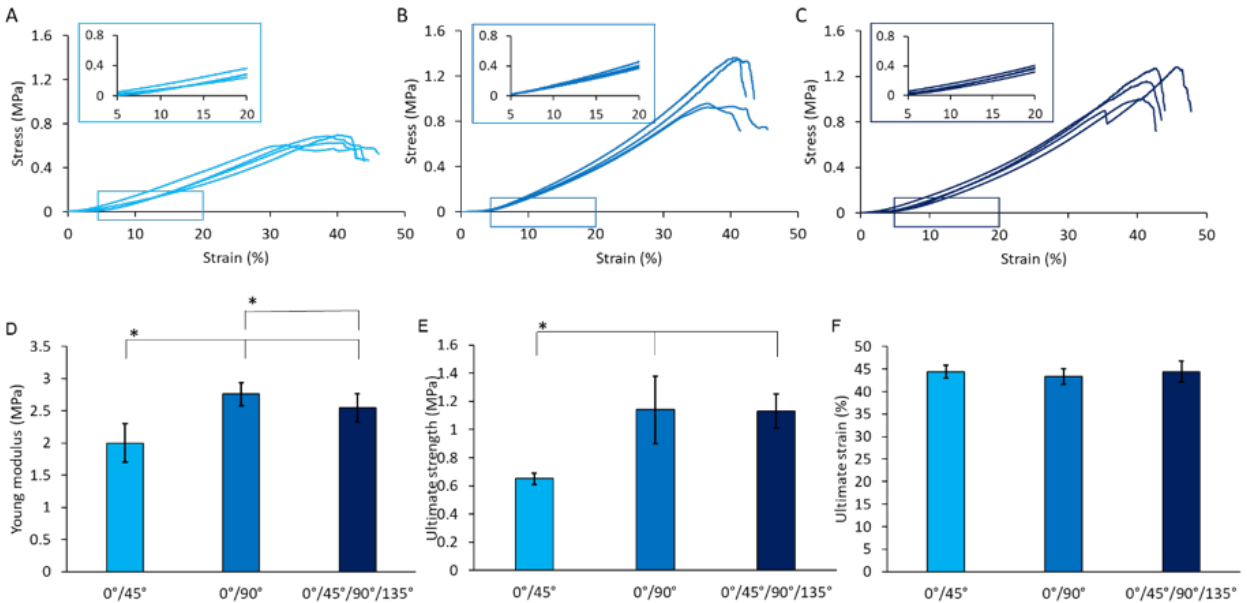

Figure 2.11: Effect of printing pattern on stress-strain compressive properties of AUP scaffolds. The cylindrical water-swollen scaffolds were compressed at a speed of 2 mm.min-1, and a preload speed of 0.5 mm.min-1. Panels A) to C) represent the obtained curves for respectively the 0°/45°, 0°/90° and 0°/45°/90°/135° printing patterns. The data in panels D) to F) represent the Young's moduli, the ultimate strength and the ultimate strain values of the same printing patterns. These values are calculated starting from the obtained stress-strain curves. The Young modulus is calculated as the slope of the curve between 10-20% strain. The asterisk(s) indicate(s) that the p values < 0.05. Statistical significance between groups was assessed by the paired Student's t-test. (n=4).

For all printing patterns, the trends of the curves show that when higher stresses are applied, the scaffold structure is compacted, the porosity is reduced, and the scaffold becomes stiffer.

In the literature, the Young Modulus of swollen hydrogels from static compression tests are calculated from the first part of the curve within a wide range of the strain (between 5-20%). This range is considered the elastic region, where the hydrogel exhibits elastic behaviour. In the curves shown in Figure 2.11, the strain range between 0 and 5% can still be regarded as the preload region. This region is essential for establishing contact between the specimens and the metal plate of the compression apparatus and the samples do not yet exhibit a relevant response to the applied stress. For this reason, this part was excluded from the Young Modulus calculation. Therefore, in our opinion, a reasonable range for calculating the Young's modulus is between 10 and 20% strain, as this portion represents the elastic part of the curve after the preload region.

A detailed analysis of the effect of the printing pattern on the compressive behaviour from Figure 2.11 panel A indicates that the 0°/45° pattern possesses inferior properties as compared to the two other printing patterns studied. The latter two possess a more isotropic character and thus a better-balanced resistance to deformation [244], as reflected by the higher Young's moduli and the ultimate strength values. Very interestingly, the ultimate strain is not affected by the printing pattern, at least not in the investigated range. This can be explained by the fact that while the to be compacted volume is the same for all three printing patterns, the stress level applied to achieve it, is different [245].

The obtained results are in line with literature data in which fused deposition modelling was also applied as 3D printing technique. [245–248] The applied polymer in these studies was mainly PCL. [246–248] The

research showed that polymer scaffolds with a 0°/90° pattern possess a higher Young's modulus and ultimate strength compared to the 0°/45°/90°/135° scaffolds. This is due to the alignment of the struts moving from layers to layer through the scaffold. For the 0°/90° pattern, the struts from subsequent layers cross over at the same position. On the contrary, the 0°/45°/90°/135° scaffolds have struts that cross over at different positions for every layer. Thus, when the latter scaffolds are compressed, the deposited struts are more prone to sliding/deformation. [245–248] The literature data and the data from our study thus clearly highlight the importance of the scaffold printing pattern on its compressive behaviour.

In a next step, we were interested to study possible effects of the polymer strut diameter and the pore size on the scaffold compressive behaviour. In all tests, the 0°/90° printing pattern was selected. More in detail, we sought to quantify the changes in compressive behaviour by variation of the strut dimensions and the pore sizes with respectively 25% and 40%. The minimal selected pore size was 200 µm (± 20 µm). Indeed, lower pore sizes lead to a lower gel fraction as the UV light penetration in the 3D structure is hampered, resulting in gel fractions lower than 90% (see Figure 2.10 panel B). Moreover, printing scaffolds possessing such small pores increases the risk of polymer strut fusion given the smaller strut spacing (data not shown). The results of our tests are shown in Figure 2.12.

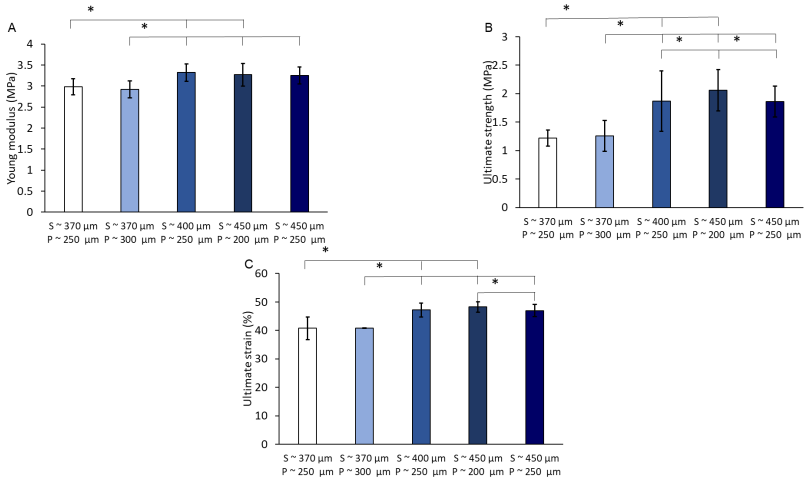

Figure 2.12: Effect of pore size (P) and strut diameter (S) on the stress-strain compressive properties of AUP scaffolds printed in the presence of 2 mol% PI. A) Young's modulus, B) ultimate strength and C) ultimate strain. The Young's modulus is calculated as the value of the slope of the curve between 10-20% of the strain. The asterisks indicates that the p values < 0.05. Statistical significance between groups was assessed by the paired Student's t-test and indicated with an asterisk (n=3).

Reducing the pore size and increasing the strut diameter are anticipated to result in improved overall mechanical properties [247]. Our data confirm this. Indeed, the two scaffolds with the smallest strut diameter (S = 370 µm (± 20 µm)) and the highest pore sizes (P = 250 or 300 µm (± 20 µm)) show significantly lower Young's moduli ($p < 0.05$ for all combinations) compared to those with larger strut diameters and smaller pore sizes. The same trend is observed for both the ultimate strength and the ultimate strain. More in detail, a 13.1 % increase in Young's modulus (from 2.9 MPa to 3.28 MPa), a 71.8 % increase in ultimate strength (from 1.17 MPa to 2.01 MPa) and a 22.9 % increase in ultimate strain (from 39.27% to 48.27%) are observed. Important to note is that the Young's modulus, the ultimate strength and the ultimate strain reach plateau values for scaffolds with strut sizes of 400-450 µm (± 20 µm) and pore sizes of 200-250 µm (± 20 µm).

When we compare the data acquired from compression tests on human menisci, indicating Young's modulus values ranging between 0.97 and 19 MPa (values calculated between 12 and 20% strain), it is evident that our materials fall within the meniscus range [54,58,59]. Specifically, the values for AUP4K DA range respectively from 2 to 3.3 MPa. Again, comparing the obtained results with literature is very challenging as literature values depend on the exact condition of the samples (e.g. dry or hydrated, sliced or intact). Moreover, under physiological conditions, synovial fluid flows through the porous tissue structure. Any attempt to section the meniscus for mechanical testing thus leads to conditions that are completely different from the *in vivo* one.

2.3.7 Dynamic mechanical analysis of AUP4K DA scaffolds

The meniscal tissue has an appreciable viscoelastic mechanical response due to the presence of the interstitial fluid flow and the intrinsic viscoelastic properties of the tissue itself. Viscoelasticity with its dissipative features is essential for the meniscus role to dissipate stresses and act as a shock absorber. Moreover, due to the presence of an interstitial fluid, the meniscus reveals poroelastic behaviour [249]. Poroelasticity is the term used to describe the interaction between fluid flow and solids deformation within a porous medium. Indeed, when a porous material is subjected to an isostatic compression for example, the magnitude of its pore volume is reduced. This mechanical stress induces a pressure change in the fluid occupying the pores, triggering fluid movement. The solid component of the material responds to this alteration in pore volume by undergoing an elastic deformation. [250]

To study these phenomena for the printed AUP4K DA scaffolds, dynamic mechanical analysis (DMA) was performed. The water-swollen cylindrical scaffolds were printed with three different printing

patterns, 0°/45°, 0°/90° and 0°/45°/90°/135° in the presence of 2 mol% Irgacure 2959. Scaffolds with strut and pore sizes of respectively of 370 µm (± 20 µm) and of 300 µm (± 20 µm) were selected as reference material for this study.

The storage and the loss moduli of the scaffolds were compared to examine the impact of the scaffold's geometry on its dynamic response. The device recorded measurements over a frequency spectrum from 2-100 Hz. This range, preset by the device, enables studying the frequency range from walking (1.8 to 2 Hz) to running (3.8 to 4 Hz) [251] and to investigate the presence of any potential resonance peak(s). The absence of resonance peaks at walking and running frequencies is an absolute scaffold requirement.

The results are summarised in Figure 2.13. Panels A-F display the curves of the storage and the loss moduli for the different printing patterns while panels G and H represent the average values as derived from panels A-F.

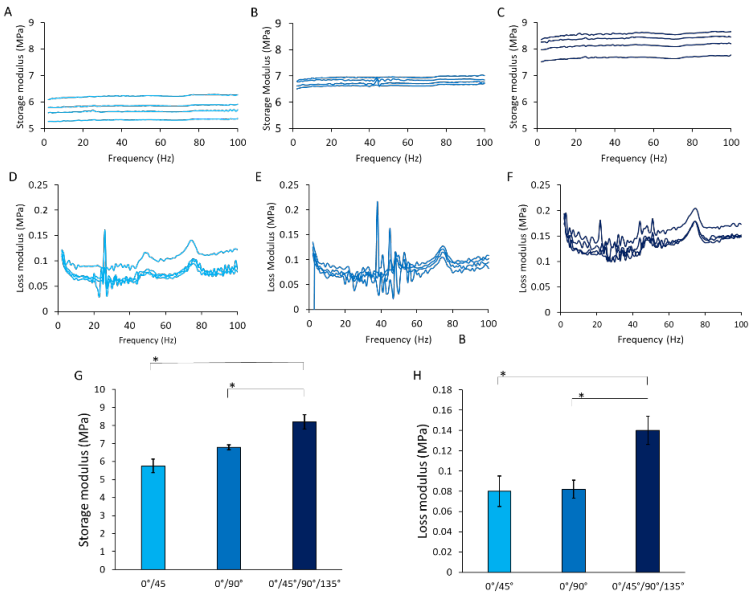

Figure 2.13: Effect of printing pattern on the scaffold storage (panels A-C) and loss modulus (panels D-F) as studied using DMA in the 2 -100 Hz frequency range. Panels A & D, B & E and C & F represent the data of respectively the 0°/45°, 0°/90° and 0°/45°/90°/135° printing patterns. Panels G and H represent the average storage moduli and the average loss moduli as derived from the data in panels A-F. All AUP4K DA scaffolds were printed in the presence of 2 mol% Irgacure and revealed strut and pore sizes of respectively of 370 µm (± 20 µm) and of 300 µm (± 20 µm). Statistical significance between groups was assessed by the paired Student's t-test (n=4). The asterisk indicates $p < 0.05$.

From the obtained data, some important conclusions can be drawn.

First, for both the storage and loss moduli curves, the curves follow similar patterns. Secondly, it is obvious that the scaffolds with the 0°/45°/90°/135° pattern reveal the highest storage and loss modulus values. The differences are statistically significant ($p < 0.05$). This trend deviates from the one obtained in the static compression test. This can most likely be ascribed to the higher mass of the 0°/45°/90°/135° scaffolds. Indeed, scaffolds printed following this pattern possess a 20% higher mass (as obtained by the swelling studies) for the same volume of the cylinder-shaped scaffold. A higher mass can store more energy and thus resist deformation more effectively. Third, the storage modulus curves for the 0°/90° printing pattern (Figure 2.13 panel B versus panels A and C) exhibits less variation as compared to the other two patterns. Looking at this finding in a quantitative fashion, Figure 2.13 panel G confirms this indicating a standard deviation of 0.14 MPa for the 0°/90° printing pattern, as compared to 0.37 MPa and 0.39 MPa for the 0°/45° and the 0°/45°/90°/135° printing patterns respectively. This effect is most likely related to the more regular arrangement for the 0°/90° printing pattern, as evident from Figure 2.7.

Finally, it should be mentioned that two resonance peaks can be observed in the loss moduli plots (Figure 2.13 panels D, E, F): one prominent and well-defined peak at 75 Hz, and a smaller peak at 50 Hz. Both of these two peaks are indicative of the material properties itself. As no resonance peaks are observed in the 2-4 Hz range, the developed scaffolds reveal an adequate dependence between frequency and mechanical properties for the anticipated orthopaedic applications.

Comparison of the herein obtained DMA results to literature is troublesome given the very limited data sets available on human menisci. Some studies indicate values in the range of KPa (for the loss

modulus) up to 9.97 MPa (for the storage modulus). Our AUP4K DA scaffolds are thus in the range of the human menisci for the storage modulus while out of range for the loss modulus. [62,71,72]

2.3.8 Fatigue testing of AUP4K DA scaffolds

The fatigue resistance is an important factor determining the suitability of the material as meniscus replacement. The material should be able to withstand cyclic compression and tensile loads as they occur *in vivo*. Using the applied ring-like shaped specimens and the hemisphere probe from the devices, both of these loading conditions (compression and tensile forces) act on the scaffolds. The fatigue tests in this study were performed at frequencies within the physiological walking range (1–2 Hz) rather than at the elevated frequencies commonly used in accelerated fatigue testing of engineering materials. This choice was deliberate, as the intended application, meniscus replacement, requires mechanical characterization under conditions representative of *in vivo* loading. Accelerated testing at higher frequencies would introduce strain-rate-dependent effects (including increased hydrodynamic pressurization of the interstitial water, elevated viscous dissipation, and altered viscoelastic response) that do not reflect the physiological loading regime of the knee joint, thereby compromising the clinical relevance of the results.

Using two different testing devices for the scaffolds enables studying the possible impact of uniform or non-uniform motions on the fatigue behaviour. The number of cycles until failure, as well as the maximum force acting on the specimens for both devices are summarized in Table 2.3.

Table 2.3: Results of the fatigue tests using the material testing machine and the dynamic testing machine.

Specimen	Testing machine	Applied compression in %	Cycles until failure	Maximum Force (N)
Ring 1	Material testing machine	0 - 75	2,422	111
Ring 2	Material testing machine	0 - 75	2,458	114
Ring 3	Dynamic testing machine	5 - 80	11,989 (1 Hz)	132
Ring 4	Dynamic testing machine	5 - 80	34,949 (1 Hz)	129

The resulting force curves over a time period of 20 seconds is exemplarily shown in Figure 2.14 for both testing devices.

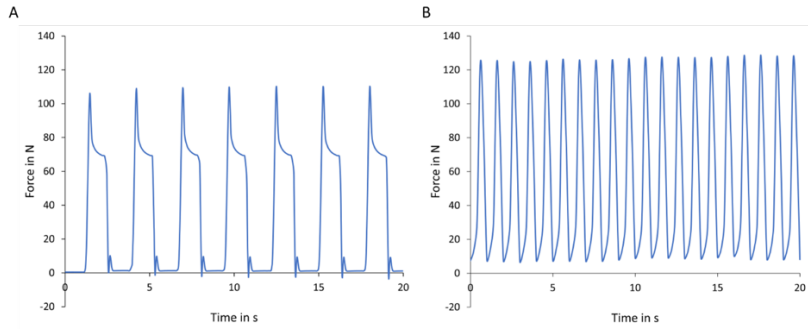

Figure 2.14: Exemplary force curves over time for A) the material testing machine and B) the dynamic testing machine.

The results of the material testing machine indicated a similar fatigue resistance for the two ring samples tested when inducing a compression from approximately 0 to 75% with a speed of 13 mm/s. Indeed, both the number of cycles until failure and the maximum forces

acting on the two specimens were in the same range (respectively 2422 versus 2458 cycles and maximum forces of 111 versus 114 N).

For the dynamic testing machine, a pre-compression of 5% was required, because smaller amounts of pre-compression would lead to a sample lift-off during this sinusoidal fatigue test. To apply the same compression range as for the material testing machine (0-75%), the maximum upper compression was therefore increased to 80%. Using this approach, the maximum force acting on the two samples was again in the same range (129 versus 132 N) while higher than for the material testing device. The cycles until failure differed slightly between both specimens (11,989 versus 34,949) and were again higher as compared to the material testing machine.

The observed higher maximum forces acting on the specimens is due to the higher maximum compression applied. Indeed, every load cycle started with a compression of 5%, which corresponds to a preload of approximately 10 N (see Figure 2.14 right).

For the observed higher number of cycles until failure, the higher velocity of the load application for the material testing machine may lead to an earlier fracture of the scaffolds, despite the higher loads applied using the dynamic testing machine.

Comparing the obtained data with literature is not possible given the fact that the herein developed approach has not been applied to date for hydrogel material analysis.

Finally, and irrespective of the applied loading regime, it is important to indicate that none of the specimens could successfully support the pre-set number of 200.000 cycles. For this reason, no testing at higher frequencies was performed.

2.4 Conclusion

In this chapter, AUP4K DA scaffolds were developed and evaluated for their potential in meniscus replacement, with a focus on cross-linking efficiency, mechanical performance and fatigue resistance.

The material exhibited high cross-linking efficiency and a broad range of mechanical properties, with static compression tests revealing the 0°/45°/90°/135° and 0°/90° printing patterns to be superior compared to the 0°/45° counterpart. More specifically, the 0°/90° printing pattern showed superior mechanical properties, achieving compressive Young's moduli between 2.9 MPa and 3.3 MPa, ultimate strength values ranging from 1.17 MPa to 2.01 MPa and ultimate strains between 39.27% and 48.27%. The best mechanical performance was obtained for strut diameters of 400-450 µm (± 20 µm) and pore sizes of 200-250 µm (± 20 µm), as these dimensions ensured plateau values for the Young's modulus, the ultimate strength and the ultimate strain.

Dynamic Mechanical Analysis (DMA) indicated that the material possesses mechanical properties suitable for meniscus applications, with the 0°/45°/90°/135° pattern demonstrating a higher storage and loss modulus due to its 20% higher mass, which enhanced energy storage and deformation resistance. The absence of resonance peaks at walking and running frequencies indicates its suitability for orthopaedic applications.

Although the AUP4K DA scaffolds developed in this chapter showed promising static compressive and dynamic mechanical properties, the fatigue tests revealed that long-term resistance to cyclic loading remained a major limitation (failure before 200.000 cycles). Since the meniscus is continuously exposed to repetitive mechanical *loading in vivo*, improving the durability and structural stability of the scaffold became a key objective for the following chapters. Therefore, the next

step of this work focused on modifying both the scaffold fabrication strategy and the AUP chemistry, with the aim of increasing network density and mechanical performance. More specifically, Chapter 3 investigates an injection-based indirect 3D printing approach and compares di-acrylated AUP4K DA with hexa-acrylated AUP4K HA to evaluate whether increased acrylate functionality can improve scaffold stiffness and strength.

Further investigations are thus necessary to optimize the fatigue resistance of the herein developed AUP4K DA scaffolds, particularly by evaluating the impact of different testing velocities and loading conditions relevant for specific orthopaedic applications like meniscus replacements.

Chapter 3:

PEG-based Hydrogels for Meniscus Replacement: Advancing Scaffold Fabrication Flexibility through a Customized Injection Moulding Setup

This chapter describes the development of an injection moulding set-up to fabricate hydrogel scaffolds for meniscal tissue engineering application. The work described in this chapter was performed by M. Meazzo and A. Ramezani. M. Meazzo performed the synthesis and characterization of the material and scaffolds, while A. Ramezani fabricated the injection-moulding set-up and carried out the optical microscopy analysis of the fabricated scaffolds. This chapter has been published as:

Meazzo, M., Ramezani, A., Barberis, F., Van Der Straeten, C., & Dubruel, P. (2026). *PEG-Based Hydrogels for Meniscus Replacement: Advancing Scaffold Fabrication Flexibility through a Customized Injection Molding Setup*. ACS Biomaterials Science & Engineering.

Doi: https://doi.org/10.1021/acsbiomaterials.5c02110

3.1 Introduction

As mentioned in Chapter 1, traditional treatments for meniscus injuries, such as meniscectomy or meniscus repair have limitations and do not always provide a long-term solution. This has led to a growing interest in polymeric scaffolds as a promising alternative [162].

When it comes to shaping a polymer into a 3D scaffold, Solid Freeform Fabrication (SFF) techniques, including direct and indirect 3D printing, are considered the most promising methods for fabricating hydrogel scaffolds, as already described in Chapter 1 [7]. At present, direct 3D printing is viewed as superior to traditional methods like solvent casting, particularly for the creation of custom-made scaffolds. By utilizing a Computer-Aided Design (CAD), the structure of the scaffold can be changed, enabling the design of more complex, tailored scaffolds. This enables the creation of intricate and customized scaffolds that traditional methods struggle to replicate [171,252]. Despite its many advantages, direct 3D printing suffers from a limited diversity of available materials as main drawback. While 3D printing is compatible with a broad spectrum of materials, the available materials are still not as extensive as those available in conventional manufacturing Indeed, most commonly used 3D printing materials such as ABS, PLA, PETG, nylon, PC, PVA, and PCL either lack the necessary mechanical properties for soft tissue engineering and/or they are not biocompatible [171]. Additionally, 3D printing may not be as time-efficient as traditional manufacturing techniques, particularly when it comes to fabricating large or intricate items [253].

Indirect Rapid Prototyping (iRP) offers several advantages over other fabrication methods for meniscal replacement scaffolds [144]. Indeed, this technique allows to address the limitations of conventional SFF techniques. In addition to the above-mentioned limited material

availability, the obtained scaffolds often suffer from brittleness, require post-treatment and lengthy optimization processes when applying new materials [176,198,201]. The method utilizes a construct created through a 3D printing technique as a temporary (negative) mould or template for the final product. Consequently, this method is known as the 'lost-mould technique', indirect Solid Freeform Fabrication (iSFF), iRP, indirect additive manufacturing, or indirect 3D printing [202–204]. Utilizing high-resolution techniques for template fabrication, such as stereolithography (SLA) or digital light printing (DLP), allows for the creation of scaffolds with pore and strut sizes as small as 50 and 65 µm, respectively. This is particularly beneficial for materials that are not suitable for direct fabrication using high-resolution manufacturing methods [206]. As a result, well-defined 3D scaffolds can be easily produced from materials that were previously considered 'unprintable' due to their thermomechanical properties, which do not meet the stringent temperature and pressure requirements of direct rapid prototyping [144,201,205,207,208]. After creating the negative mould, a hydrogel building block solution is injected in the pores of the negative mould. After crosslinking and subsequent negative mould removal using an appropriate solvent, the desired scaffold is obtained. The investment in injection moulds is amortized by the manufacturing of large volumes of pieces [252,254].

Almost 20 years ago, Lee et al. demonstrated the effectiveness of the iRP method for creating complex structures on both micro and macro scales. They successfully fabricated porous PLGA scaffolds using a water-soluble negative mould (sieved plaster powder, ZP100 Zcorp, printed and then infiltrated with PEG), which supported cell growth effectively [255]. In another study from 2013, the same research group reported on a PCL/chitosan human mandibular condyle implant using gelatin as negative mould. The scaffolds were coated with bioactive

apatite to enhance their osteo-inductive properties. The *in vitro* biological evaluation showed good cell viability, with the apatite coating promoting cell spreading and – proliferation [256]. More recently, Costa et al. produced hierarchical and multilayered patient-specific meniscus implants using silk fibroin through an indirect printing approach (acrylonitrile butadiene styrene mould). *In vitro* biological tests showed that both the top and bottom layers of the scaffolds facilitated the survival and growth of human meniscus cells (hMCs) and human primary osteoblasts, respectively, for a period of up to 7 days. Furthermore, these scaffolds triggered a minimal inflammatory response when implanted subcutaneously in mice [257]. More studies documented a variety of successfully fabricated 3D scaffolds through indirect 3D printing biopolymers (collagen, silk fibroin, gelatin), synthetic polymers (PLLA, PCL, PPF), ceramics, and composites [144].

The extrusion-based 3D printing approach explored in Chapter 2 demonstrated that AUP4K DA scaffolds can achieve compressive properties within the range of the native meniscus and confirmed the importance of scaffold architecture as a tuning parameter. However, the fatigue experiments also showed that these scaffolds did not yet provide sufficient resistance to prolonged cyclic loading, indicating that architectural optimisation alone was not enough and that further improvement of the material network was required.

Beyond this material limitation, the extrusion-based fabrication method itself revealed several practical constraints. First, extrusion printing is restricted to processing AUP melts, which prevents the fabrication of scaffolds at varying polymer concentrations, a parameter that, as will be shown in this chapter, has a pronounced effect on mechanical properties. Second, the layer-by-layer filament deposition inherent to extrusion printing produces scaffolds with porosity only in the vertical

build direction. The native meniscus, however, requires nutrient diffusion and cellular infiltration from multiple directions, making lateral porosity, that is, interconnected pore channels running parallel to the printing plane, a highly desirable architectural feature that conventional extrusion printing cannot easily achieve. Third, varying the scaffold pore geometry and dimensions in extrusion printing requires extensive re-optimisation of printing parameters for each new configuration, making the process labour-intensive when exploring a broad design space.

To address both the material and the fabrication limitations identified in Chapter 2, this chapter proposes two combined strategies. On the material side, the AUP chemistry was expanded from a di-acrylated precursor (AUP4K DA) to a hexa-acrylated precursor (AUP4K HA), increasing the number of reactive acrylate groups to promote a higher crosslinking density and ultimately obtain scaffolds with improved mechanical performance. On the fabrication side, an indirect rapid prototyping approach based on a custom designed injection moulding setup was developed, enabling the fabrication of AUP scaffolds with lateral porosity, tunable polymer concentration, and reproducible architecture using a single mould design.

3.2 Materials and methods

3.2.1 Materials

The materials applied in this study included Bisomer PEA-6 from Geo Specialty Chemicals, ethoxylated and propoxylated pentaerythritol triacrylate (EPPETA) from Allnex, and butylated hydroxytoluene (BHT) from Innochem GmbH. Additionally, dimethyl terephthalate (DMT) and isophorone diisocyanate (IPDI) were sourced from Sigma-Aldrich, along with lithium bromide (LiBr) butanone, petroleum eher,poly(ethylene glycol) (PEG) with a molar mass of 4 000 g mol^{-1}, phenothiazine (PTZ), triphenylphosphite (TPP), and phosphoric acid. Chloroform, deuterated chloroform ($CDCl_3$) was obtained from Euristop, Poly(lactic acid) (PLA) with the product code 1612 was obtained from Ultimaker Material in Gerldermalsen, the Netherlands. Other materials used included Valikat Bi (bismuth neodecanoate), 2,4,6-trimethylbenzoyl)-phenyl-phosphinic acid ethyl ester (commercially known as Speedcure TPO-L) from Lambson, and the filter paper 424 from VWR Europe (pore size: 125 mm).

3.2.2 Methods

3.2.2.1 Synthesis of acrylate-endcapped urethane-based poly(ethylene glycol) precursors

The synthesis of AUP4K DA was thoroughly described in Chapter 2. In this chapter, the use of AUP4K HA is also documented. The synthesis of AUP4K HA follows the same procedure as that of AUP4K DA, with the exception of the final step, where propoxylated pentaerythritol triacrylate (EPPETA) is utilized as the end-capping agent instead of Bisomer PEA 6 (Figure 3.1).

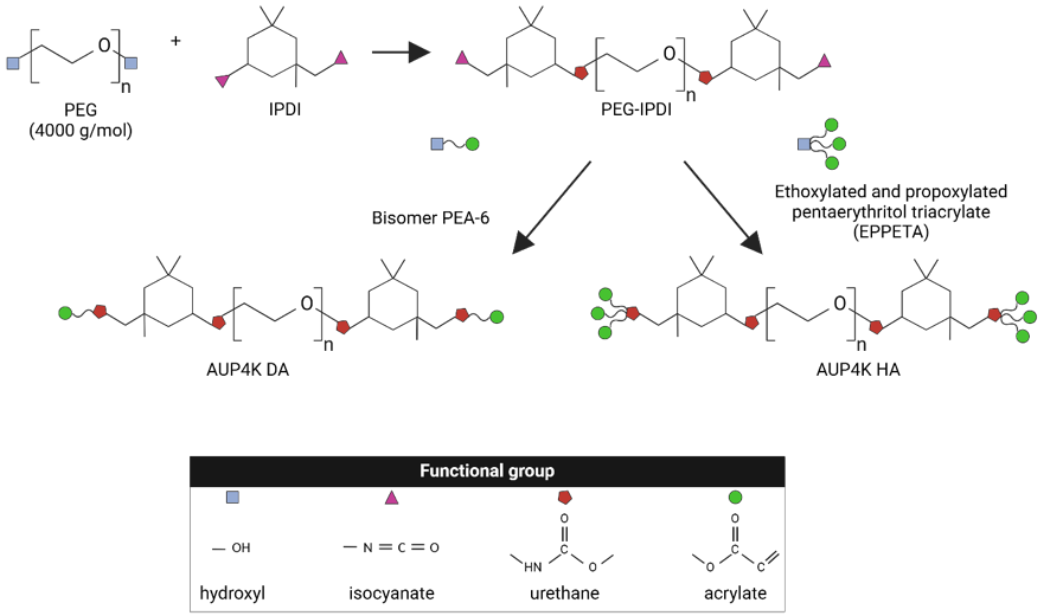

Figure 3.1: Reaction scheme for the AUP4K DA and HA syntheses.

This adjustment led to an increase in the number of acrylate groups from one to three between a polymer chain and its neighboring polymer chains at each end of a polymer chain.

3.2.2.2 Chemical structure of AUP hydrogel building blocks via FTIR spectroscopy

The molecular structures of the synthesized AUP were analysed using Fourier transform infrared (FTIR) spectroscopy, facilitated by the PerkinElmer Frontier FTIR mid-IR as described in Chapter 2.

3.2.2.3 AUP acrylate content determination via ^{1}H-NMR spectroscopy

The chemical structures of AUP4K DA and HA were confirmed through ^{1}H-NMR spectroscopy using a Bruker Avance II Ultrashield 400 MHz spectrometer with deuterated chloroform as the solvent as described in Chapter 2.

3.2.2.4 Photo-initiator synthesis

In Chapter 2, Irgacure was used as the photo-initiator for the UV-induced crosslinking of AUP4K DA scaffolds. However, for the injection-based indirect 3D printing approach applied in the present chapter, the AUP precursors had to be processed as aqueous solutions before crosslinking. Therefore, Li-TPO-L was selected as an alternative photo-initiator due to its improved water solubility compared to Irgacure, which shows limited solubility in aqueous systems. This improved solubility allowed a more homogeneous distribution of the photo-initiator throughout the AUP solution prior to mould injection and crosslinking. In addition, Li-TPO-L has been reported to exhibit a more favourable cytocompatibility profile compared to commonly used Irgacure-type initiators, making it more suitable for hydrogel systems intended for biomedical applications.

The synthesis of Li-TPO-L was performed analogous to patent literature: Lithium Bromide (9.45 g, 109 mmol) was dissolved in 150 mL of butanone. Subsequently, 8.60 g (7.5 mL, 27.2 mmol) of TPO-L was introduced to the reaction mixture, which was then stirred for 24 hours at 65° C using a magnetic stirrer. The resulting precipitate was gathered through suction filtration (using filter paper 424) and rinsed with petroleum ether. The precipitate was then dried under vacuum at room temperature, shielded from light [258].

Previously unpublished data suggested to combine Li-TPO-L with AUP at a concentration of 2 mol% relative to the acrylate content as it is the optimal concentration to achieve a high gel fraction.

3.2.2.5 Rheology analysis of AUP building blocks

For the viscosity measurements of the different AUP solutions, an Anton Paar Physica MCR 301 rheometer was used. The results were analysed using the Rheoplus software. A setup involving parallel plates was employed, where the top plate had a diameter of 25 mm and the gap was set at 0.3 mm. The viscosity of the AUP and of the two end-capping agents was observed by applying the molten precursors between these plates. Initially, sweeps of strain and frequency were recorded to determine the materials' linear viscoelastic range. This was done by increasing the strain from 0.01% to 100% at a frequency of 1 Hz. Subsequently, the mechanical spectrum of the precursors was captured by raising the frequency from 0.01 to 10 Hz, while maintaining a constant strain of 0.1%. Upon assessing the viscoelastic range characteristic for the molten AUP precursors, a strain of 0.1% and an oscillation frequency of 1 Hz were chosen. Finally, the viscosity of the molten precursors was recorded for 1 minute at a temperature of 60 °C and shear rate of 10 s^{-1}.

3.2.2.6 Thermogravimetric analysis

Thermogravimetric Analysis (TGA) was conducted using a Q50 TGA from TA Instruments on dry AUP scaffolds. After removing the PLA mould with chloroform, following the procedure described above, the samples were dried in a vacuum desiccator to ensure complete removal of both water and solvent before testing. The purpose of the TGA analyses was twofold. On the one hand, we wanted to determine the window of thermal stability for subsequent DSC analysis. On the other hand, we wanted to confirm that no substantial PLA was left within the pores of the AUP scaffolds (see § 2.2.10 on sacrificial mould removal). The Q50 TGA was operated using TA Universal Analysis software, and the data gathered was analysed using TA Universal Analysis software. The test parameters were set as follows: an equilibrium temperature of 35° C, a final temperature of 750˚ C, a temperature ramp of 10° C/min, an equilibration temperature of 350° C, and the tests were carried out under a nitrogen flow of 50 mL/min.

The detection limit of the device, as specified in the device manual, is ± 0.01% of weight. This high sensitivity allows TGA to accurately measure small amounts of weight loss or gain, making it a suitable tool for analyzing the presence of PLA in the scaffolds.

3.2.2.7 Differential scanning calorimetry (DSC) analysis of AUP solutions

Differential Scanning Calorimetry (DSC) is employed to identify phase transition temperatures, such as melting (T_m) and crystallization (T_c), by measuring heat fluctuations during temperature cycles ranging from -80°C to 100°C. A sample weighing 5-10 mg is placed in a sealed pan and analysed using a DSC calorimeter (Q2000 DSC, TA Instruments). The thermal cycling protocol began with an equilibration step at 45 °C to stabilize the sample. This was followed by a controlled heating ramp

at 10.00 °C/min up to 100.00 °C, where the sample was held isothermally for 3.00 minutes to complete cycle 0. Subsequently, the temperature was decreased at the same rate to -80 °C, followed by a 4-minute isothermal hold, marking the end of cycle 1. The final cycle involved reheating the sample at 10 °C/min back to 100 °C, with a concluding isothermal step of 3 minutes to complete cycle 2.

3.2.2.8 3D printing setup

The approach utilized a combination of 3D printing and injection moulding. All components (sacrificial mould and injection moulding setup) were printed using PLA using an Ultimaker S3 (Ultimaker B.V., Utrecht, The Netherlands) 3D printer, operating at a nozzle temperature of 200 °C with 100% infill to ensure structural integrity and dimensional stability

The AUP materials were introduced into the mould through this technique. Several injection moulding configurations were developed and evaluated during an iterative optimization process. Ultimately, a setup comprising nine key components was devised. Given the novelty of this developed system, its details and performance will be presented in the Results and Discussion section.

3.2.2.9 Injection-based indirect 3D printing

The moulding process consisted of pouring the materials inside the hollow cylindrical structure, and pressing with the plunger into the mould. The sacrificial mould and injected AUP4k were delicately removed from the middle plate. Subsequently, these components underwent immediate Ultraviolet (UV) light exposure from both sides and from top to bottom for a duration of one hour (lamp intensity 10 mW/cm^2).

3.2.2.10 Sacrificial PLA mould removal

To remove the PLA mould, the mould and the crosslinked AUP were immersed in 20 ml of chloroform for a period of five days, with daily chloroform replacement. After PLA removal, the scaffolds were placed in a vacuum desiccator for 48 hours. Finally, they were subjected to a 48 hours incubation in water, with daily water changes.

3.2.2.11 Microstructure analysis of AUP hydrogel scaffolds

In our study to analyse the microstructure and integrity of the fabricated scaffolds, two devices of imaging were applied: the Axiotech light microscope from Zeiss with a 5x magnification and the JEOL desktop SEM. Several critical tasks were performed:

- Strut and Pore Size Measurement: assessed the dimensions of the struts and pores within the scaffolds.
- PLA Removal Verification: allowed us to verify the successful removal of PLA (polylactic acid) from the scaffolds.
- Chloroform Impact Investigation: investigation whether exposure to chloroform had any adverse effects on the AUP4K struts.

After the removal of the PLA mould, the scaffolds were dried for 48 hours prior the visualization to enable solvent (chloroform) removal. For the microscope pictures, the samples were carefully positioned on a transparent glass slide, directly above the microscope lens. The resulting images were subsequently analysed using the Zen Service software.

For the SEM analyses, the scaffolds were dried using a desiccator after PLA removal and then sputter-coated for a duration of 60 seconds at 20 mA with an automatic Au Sputter Coater K550X from EmiTech,

equipped with a two-stage RV3 rotary vane pump. The samples were secured to the sample holder using double-sided carbon tape.

3.2.2.12 Gel fraction and swelling capacity of AUP hydrogel scaffolds

Gel fraction tests were done in triplicate. The calculations for the degree of swelling and the gel fraction of the scaffolds were performed using Equations 3.1 and 3.2, respectively, based on previous studies [142].

Swelling degree (%) = $\frac{Ws-Wdes}{Wdes} * 100$ (3.1)

Gel fraction (%) = $\frac{Wdes}{Wd} * 100$ (3.2)

The initial weight (W_d) was determined by subtracting the weight of the PLA sacrificial components. The weight after swelling (W_s) was measured after a period of 9 days, which included 5 days in chloroform, 2 days of drying, and 2 days of washing in Milli-Q. To measure W_s, the scaffolds were gently pressed with paper tissues to ensure the removal of any residual water from the pores. After the measurement of W_s, the scaffolds were placed in a desiccator for 72 hours at 20° C for drying, after which the dry weight (W_{des}) was measured.

The test was run in triplicate.

3.2.2.13 Compression testing of AUP hydrogel scaffolds

The compression tests were conducted on samples in their equilibrium water-swollen state. Following the removal of the PLA mould (see § 2.2.10), the scaffolds were left to dry into desiccator for two days to eliminate potential remnants of chloroform. Subsequently, they were submerged in double distilled water at 20°C for a period of two days to allow for swelling and to evaluate them in their swollen state. The tests were performed using a Tinius Olsen 5ST testing machine equipped

with a 500 N load cell. Due to the viscoelastic nature of the polymer, the testing speed was set relatively low at 2 mm/min. The preload was established following our internal lab protocol ranging from 0.1 to 0.3 N. The test was performed on four samples for each condition.

3.2.2.14 Texture profile analysis of AUP hydrogel scaffolds

Texture Profile Analysis (TPA) was performed to evaluate the mechanical properties of the fabricated scaffolds. The variation in hardness between scaffolds made of AUP4K DA and AUP4K HA was investigated starting from solutions of AUP and double-distilled water at concentrations ranging from 30 to 90 wt%. The primary advantage of the TPA test is its non-destructive nature, which allows for repeated testing on the swollen state of scaffolds using the same setup.

The TPA was carried out using a Lloyd TA500 equipped with a 100 N load cell and was done on four different scaffolds for each condition. The TPA was conducted on samples in their water-swollen state. The probe used for the TPA was a standard cylindrical probe with a flat tip and a diameter of 3 mm. This probe compressed the scaffolds at a rate of 5 mm/min for 0.5 mm after reaching a preload of 0.1 N. The experimental parameters were consistent with those outlined in previous research conducted in our lab on indirect moulded scaffolds [209]. In each test, this loading process was repeated twice, and the maximum force in each cycle was considered for TPA calculations using the Nexygen software.

3.3. Results and discussion

In Chapter 2, AUP4K was printed through extrusion printing revealing mechanical properties in the range of the human meniscus [17,140]. The then applied method however revealed some major limitations including (1) the possibility to print melts only, thus not enabling printing hydrogels with varying AUP concentrations, (2) polymer strut delamination after 3D printing and (3) more labour-intensive character when targeting variations in scaffold pore geometry and - size.

To address these challenges, we propose in this chapter the development of a cost-effective injection moulding setup produced using a commercial 3D printer enabling the development of AUP4K scaffolds.

3.3.1 Hydrogel building block synthesis and structural characterisation

The two AUP hydrogel building blocks applied in this work were synthesized through a two-step reaction. In the first step, PEG with a molar mass of 4000 g/mol was reacted with two equivalents of IPDI. In the second step, the obtained product was reacted with two equivalents of Bisomer PEA 6 or EPPETA Acrylate Resin as endcap, yielding AUP with respectively one or three acrylate functionalities at each chain end. The rationale for this selection is based on the anticipated effect of the number of AUP acrylate groups on the properties of the resulting hydrogels including their swelling capacity and mechanical properties. In what follows, these polymers will be denoted as respectively AUP4K DA and AUP4K HA. The chemical structures of the obtained polymers and their structural characterization are shown in Figure 3.2.

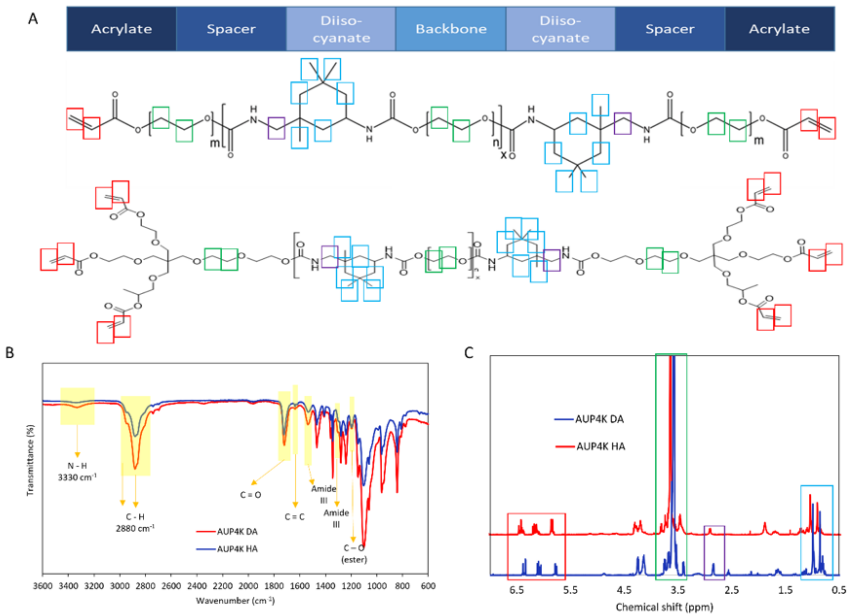

Figure 3.2: Overview of AUP4K chemical structure and the obtained infrared and NMR spectra. A) Chemical structure of the developed AUP (top: di-acrylated AUP, AUP4K DA); bottom: hexa-acrylated AUP, AUP4K HA). B) FTIR spectrum of both AUP4K. The characteristic IR peaks of the AUP4K are indicated. C) ^{1}H-NMR spectrum of both AUP4K. Peak annotation is performed through the applied colour code in parts A and C of the figure.

The FTIR and NMR spectra match those of the AUP4K DA in Chapter 2. The corresponding peaks observed in both tests are also present in these analyses. All the observed peaks confirm data reported earlier in chapter 2 and in literature by our group for other AUP types [142,148,223]. The sole difference between this study and the one referenced in Chapter 2 is the number of acrylates associated with AUP4K HA. By comparing the signals from the AUP4K acrylate groups with the protons in the aromatic ring of dimethyl terephthalate (DMT, used as internal standard [141]), acrylate contents of 0.37 and 1.1 mmol acrylate/g AUP were obtained for respectively AUP4K DA and AUP4K HA using Equation 2.1. As anticipated, the acrylate content increased with a factor 3 when comparing the DA and the HA AUP derivatives.

3.3.2 Melting temperature and viscosity determination

Evaluating the viscosity of hydrogel building block solutions before processing is vital, irrespective of the selected polymer processing technique. For the herein selected injection-based indirect 3D printing, the viscosity determines how easily the polymer solution in water can be injected into the mould. A higher viscosity implies more resistance to flow and thus a higher pressure to fill the mould properly. As we intended to also process the solvent-free formulation (i.e. the AUP melts) into scaffolds, we conducted all measurements at a temperature of 60°C to guarantee the complete melting of both AUP materials. Indeed, AUP4K DA and AUP4K HA melt at a temperature of respectively 47.4°C and 46.2°C, as determined by differential scanning calorimetry (DSC) analysis (Figure 3.3, panel A). The dynamic viscosities of the solutions were determined at a fixed shear rate of 10 s^{-1} as a function of the AUP type and - concentration (Figure 3.3, panel B). The DSC data and the dynamic viscosity data at different

concentrations are shown in Figure 3.3 panel A for both AUP4K materials.

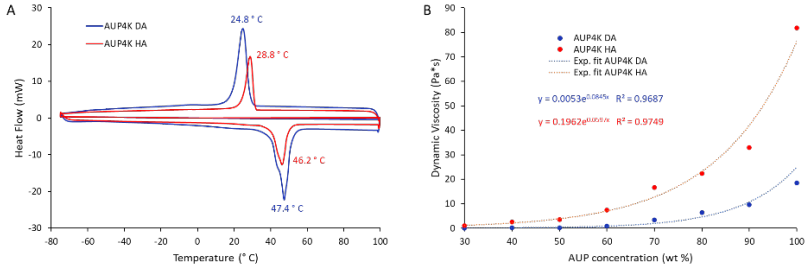

Figure 3.3: A) Differential scanning calorimetry thermograms of AUP4K DA and AUP4K HA. B) Effect of the AUP concentration and end-cap on the dynamic viscosity as measured by rheology.

As anticipated, the dynamic viscosity for both AUP4K solutions increases with an increasing AUP concentration. The more concentrated a polymer solution, the higher the number of chain entanglements, thus leading to a higher viscosity [259]. For both AUP types, the observed trend is exponential in nature, following theoretical expectations [260], with good fits (see Figure 3.3, panel B, R^2 values of 0.97 for both AUP4K types).

A second finding is the fact that the viscosities of the AUP4K HA solutions and melt are higher compared to their AUP4K DA counterparts. This can be explained by the higher molar mass and viscosity (i.e. 533 g/mol and 185 mPa.s) of the EPPETA endcap applied for the synthesis of AUP4K HA, as compared to the PEA6 endcap counterpart that has a molar mass of 336 g/mol and a viscosity of 55 mPa.s. This leads to a higher molar mass for the AUP4K HA and thus a higher viscosity than for the AUP4K DA.

The trends we obtained for our AUP materials are comparable to those reported for other hydrogel precursors including agarose-dextran, chitosan and silk. In all cases, an increase in the hydrogel building block concentration resulted in an increase in viscosity. More specifically, silk solutions with concentrations of 8-12% w/v revealed

viscosities ranging from 1.73-12.69 x 10^{-6} Pa.s while a chitosan solution at a concentration 3% w/v reveals a viscosity of 18.23 x 10^{-6} Pa.s. In another study, aqueous agarose solutions were prepared (1 w/v %) with varying concentrations of dextran (0-5% w/v). The viscosity values ranged from 1-7 mPa.s [259,261,262]. The lower viscosity values obtained as compared to ours can among other be related to the lower hydrogel building block concentrations applied.

3.3.3 Development of injection-based indirect 3D printing set-up

The initial step in the indirect 3D printing of AUP hydrogels involved identifying an appropriate material to serve as a micro-porous sacrificial mould (i.e. the negative mould). Based on existing literature, poly(vinyl alcohol) (PVA), poly(ε-caprolactone) (PCL) and poly(lactic acid) (PLA) are the most commonly applied materials for this purpose [144,252,263]. PVA was initially considered as a candidate mould material due to its water solubility, which would eliminate the need for organic solvents during the mould removal step. However, preliminary experiments revealed that PVA moulds were partially solubilized upon contact with the aqueous AUP precursor solutions during the injection step, leading to contamination of the AUP hydrogel network with dissolved PVA. This issue persisted even at higher AUP concentrations (and thus lower water content), indicating a fundamental incompatibility between PVA as a sacrificial material and the aqueous processing route required for AUP hydrogels. Therefore, PLA was selected due to its high melting temperature (170°C) and solubility in chloroform [264]. The high melting temperature is crucial as the AUP solution is heated to 60°C before being injected into the mould without affecting the integrity of the PLA mould. A high solubility in chloroform is essential for a straightforward PLA removal after AUP

crosslinking. An extra advantage of chloroform is its high volatility, enabling easy removal from the crosslinked AUP scaffolds.

The sacrificial PLA mould was designed using SolidWorks software (Student Edition 2021). The mould was designed to have outer dimensions of 11.66 mm × 11.66 mm × 7.3 mm, pore sizes of 0.430-0.445 mm and strut sizes of 0.300-0.330 mm. Next, the STL file of the designed mould was imported in Cura software connected to an Ultimaker S3 3D printer, equipped with a standard nozzle with a 0.250 mm diameter.

The scaffold architecture applied in this chapter was limited to the 0°/90° cross-hatched printing pattern. This decision was informed by the findings of Chapter 2, where three printing patterns (0°/45°, 0°/90° and 0°/45°/90°/135°) were systematically compared. As described in section 2.3.4, the 0°/45° and 0°/45°/90°/135° patterns resulted in curved struts and rhomboidal pore geometries due to the longer unsupported bridging distances between struts in successive layers, despite significant efforts to optimize the printing parameters. Only the 0°/90° pattern consistently produced scaffolds with straight struts and well-defined cubic pores. Given that the indirect printing approach developed in this chapter relies on a PLA sacrificial mould whose geometric fidelity directly determines the quality of the resulting AUP scaffold, achieving the highest possible mould accuracy was essential. The 0°/90° pattern was therefore selected as the only architecture capable of guaranteeing the structural regularity required for reproducible scaffold fabrication and reliable mechanical characterization.

In the next step, the development of the injection moulding setup was tackled. Several injection moulding set-ups were designed and tested through an iterative optimization process, ultimately leading to the set-

up shown in Figure 3.4. The outer dimensions of the mould were 60 mm x 60 mm x 38 mm.

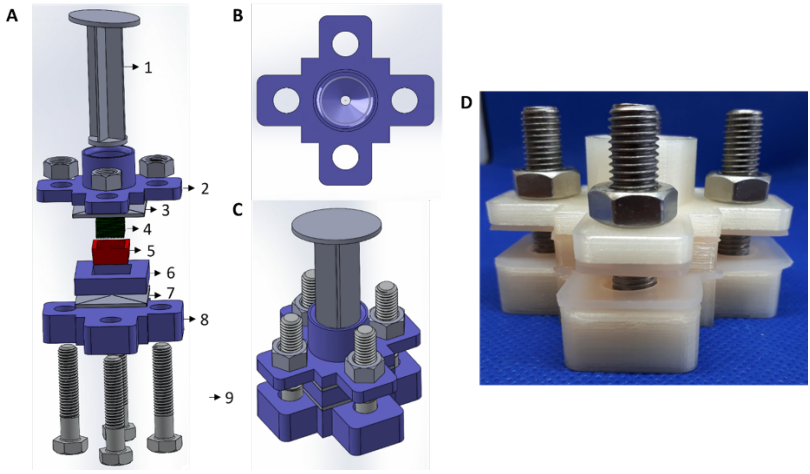

Figure 3.4: Injection moulding set-up applied for AUP injection-based indirect 3D printing. A) Overview of all the components of the designed non-assembled set-up, B) top view of the upper runner system, C) view of the designed assembled set-up, and D) image of the fabricated assembled set-up.

In what follows, the different designed and fabricated components are shortly described.

1) The plunger is used to apply pressure on the AUP solution or melt to enable injection in the mould through the runner system.
2) The upper plate (thickness: 19 mm) covers the top surface of the sacrificial mould via the upper sealing system. This plate features a hollow conical structure with an inner diameter of 16 mm, serving as the runner system for AUP injection. It terminates in a gate with a diameter of 2.5 mm, directing the

AUP solution or melt into the mould. A top view of the upper plate is shown in panel B of Figure 3.4.

3) The upper sealing and air bubble escape system (thickness: 1.5 mm) is a silicon plate placed between the upper and the middle plates. The system is designed to have four grooves with a thickness of 0.3 mm, extended toward its four angles, preventing the presence of air bubbles in the mould.
4) The 3D printed PLA micro-porous sacrificial mould has outer dimensions of 11.66 mm × 11.66 mm × 7.3 mm, pore sizes of 0.430 – 0.445 mm and strut sizes of 0.300 – 0.330 mm.
5) The sacrificial mould cover is a hollow cubic construct functioning as a lateral cover for the sacrificial mould. Its dimensions are intentionally designed to secure the sacrificial mould tightly while allowing it to be positioned more loosely within the middle plate. This deliberate choice of tolerance simplifies the removal of the sacrificial cover from the middle plate after the moulding process. Importantly, this design ensures an intimate contact between the sacrificial PLA mould and the injected AUP. Not only does it prevent AUP from leaching out, but it also maintains an optimal scaffold surface by avoiding excessive AUP buildup on the side, thus keeping the lateral pores unobstructed.
6) The middle plate (thickness: 6.95 mm) is placed between the upper and lower plates with the sealing systems in between, creating a cavity for accommodating the micro-porous sacrificial mould and its cover. Notably, the inner hole of this plate is intentionally designed with a 4° slope, facilitating its removal from the sacrificial mould cover.
7) The bottom sealing and air bubble escape system has an identical design as the upper sealing (see 3), and it is positioned between the middle and lower plates.

8) The lower plate (thickness: 12 mm) covers the lower plane of the sacrificial mould through the bottom sealing system.
9) The clamping system is made out of four M8 bolts that clamp all mould components together, preventing leaching of the AUP solution or melt from the setup.

3.3.4 Development of AUP scaffolds through injection-based indirect 3D printing

After being heated to 60° C, the AUP4K solutions and melts were injected into the runner system within the upper section of the moulding setup (as depicted in Figure 3.4 panel A). Subsequently, the solution or melt was compressed using the plunger and injected into the PLA mould. The entire moulding process takes approximately one minute, comprising of twenty seconds for moulding and forty seconds for maintaining the plunger at its lowest position to ensure proper filling of the mould with the AUP material.

Following several initial moulding attempts, both AUP4K melts were excluded from further study. This was due to their high viscosity (especially for the AUP4K HA melt, see Figure 3.3, panel B) and the quick temperature drop during the moulding process. The latter resulted in difficulties to reproducibly inject the hydrogel building blocks in the PLA mould, given the viscosity increase during the temperature drop. A similar issue was observed with the 90 wt% AUP solution, although to a smaller extent. Therefore, the validation of the mould design was conducted using the 80 wt% AUP solution. This selection was based on a viscosity value that does not pose major challenges in the moulding process, thus providing straightforward processing conditions yielding relevant and reliable data.

The optical microscopy data, proving the success of the different steps in the AUP scaffold production process, are shown in Figure 3.5. In the

first column (panels A and E), the obtained PLA mould is depicted. The second column (panels B and F) shows the PLA mould after AUP4K DA injection and crosslinking. The third and fourth columns show respectively the crosslinked AUP4K DA (panels C and G) and AUP4K HA (panels D and H) scaffolds following PLA mould removal in chloroform.

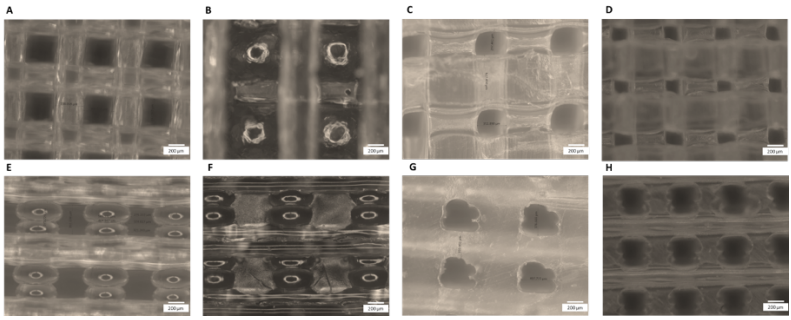

Figure 3.5: Visualisation of the different steps of the production process of the 80 wt% AUP4K DA and AUP4K HA scaffolds using optical microscopy. Panels A-D and E-H represent respectively vertical and lateral views of the scaffolds A&E) PLA sacrificial mould, B&F) PLA sacrificial mould after AUP4K DA injection and crosslinking; C&G) AUP4K DA 80 wt% scaffold after PLA removal D&H) AUP4K HA 80 wt% scaffold after PLA removal. The scale bars are indicated on each figure (5X magnification). Vertical views (top row) are taken along the build direction, perpendicular to the printing plane. Lateral views (bottom row) are taken perpendicular to the build direction, showing the scaffold cross-section.

As an important conclusion, it can be safely stated that the developed injection moulding set-up enables the successful construction of 3D porous hydrogel scaffolds with porosity on all six faces for both types of AUP4K studied. For the anticipated meniscus replacement application and beyond, a highly porous and interconnected scaffold is required as it facilitates various cellular processes as well as nutrient supply and waste product removal [265].

3.3.5 PLA sacrificial mould removal

Successful fabrication of AUP4K scaffolds through the sacrificial mould approach requires the complete removal of the applied PLA mould.

Much to our surprise, there is a lack of literature describing experiments confirming PLA mould removal. Moreover, the applied procedures vary greatly when looking at the scaffold immersion times (ranging from 2 to 7 days), the frequency of solvent changes (once to twice a day), the PLA type, and the absence/application of stirring [144,252].

To address this gap, we performed TGA analyses to assess PLA removal after AUP4K injection and subsequent crosslinking. We anticipated that possible PLA remains on the AUP4K scaffold after PLA dissolution, thus leading to a multi-material scaffold, could be detected through TGA as distinct mass-loss events if the two materials possess varying decomposition temperatures [266,267].

From the data in Figure 3.6 panel A, it can be observed that the thermal degradation of PLA occurs in a single step, with the degradation process taking place between 300°C and 400°C, confirming literature data [268]. The degradation of the dried crosslinked AUP4K scaffold also occurs in a single step but over a broader temperature range (see Figure 3.6 panel A and B). For the PLA mould containing the crosslinked AUP4K, two separate degradation steps can be clearly distinguished.

The temperature at which the mass loss starts, is determined by an extrapolated onset temperature (T_0) which is a property proposed to be used by both ASTM and ISO to enable comparison of the thermal stability of polymers [269]. The T_0 values for PLA, the AUP4K DA and AUP4K HA scaffolds are respectively 343°C, 371°C and 358°C. The data indicate that PLA and the developed AUP show distinct degradation temperatures thus enabling TGA analysis as a PLA mould removal confirmation technique. The data are confirmed by comparing the weight loss derivative peaks of the materials under study (see Figure 3.6 panel C and D). In particular, when looking to the PLA mould

containing the crosslinked AUP4K (DA or HA), two distinct peaks are observed: a first around 358°C (corresponding to the PLA mould) and a second around 400°C or 404° C (corresponding to respectively the AUP4K DA and AUP4K HA).

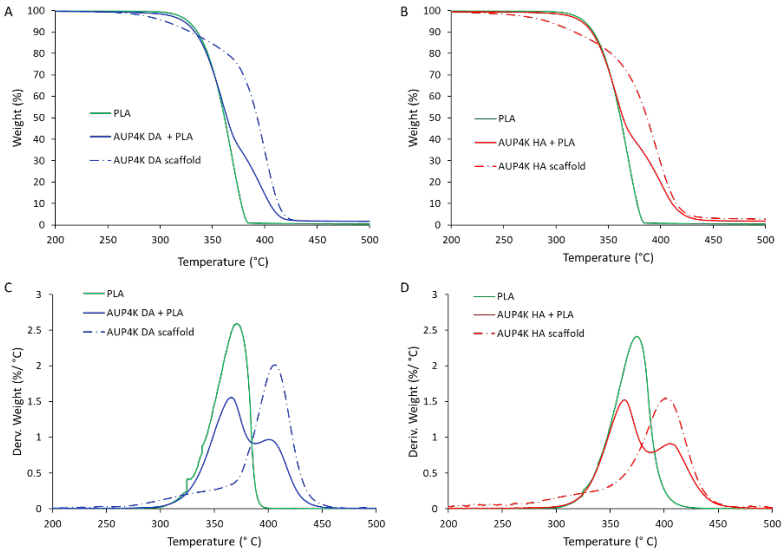

Figure 3.6: Application of TGA to assess the removal of the PLA sacrificial mould after AUP4K crosslinking. A) & B) Thermal degradation curves of PLA, a dried 80 wt% AUP4K with PLA mould and a dried 80 wt% AUP4K scaffold after removal of the PLA mould; C) & D) Peaks of the first derivative of the weight loss as a function of temperature of respectively panels A and B.

The data from both the TGA thermograms and the first derivative plots indicate that no PLA traces were detected in the final AUP scaffolds, suggesting that the mould removal process can be deemed successful taking into account the device accuracy being ≥1%, based upon ASTM-norm E1131−20 and the specifications of the supplier [270,271].

3.3.6 AUP scaffold characterization

3.3.6.1 Scaffold microstructure analysis

In a next part of our work, microstructure analysis of the obtained AUP scaffolds was conducted using optical microscopy enabling the

investigation of relationships between the pore and strut dimensions of the original PLA mould and those from the AUP scaffolds for the applied AUP concentrations (30-90 wt%) and AUP types (AUP4K DA and AUP4K HA). Additionally, we also aimed to visualize potential local scaffold defects and/or residual PLA after sacrificial mould dissolution. The selected values for pore and strut sizes are based on previous research that identified this range as optimal to mimic the mechanical properties of human meniscal tissue [140].

The data of the obtained dry AUP scaffolds are shown in Figure 3.7 for both AUP types studied and for the different applied AUP concentrations (30-90 wt %).

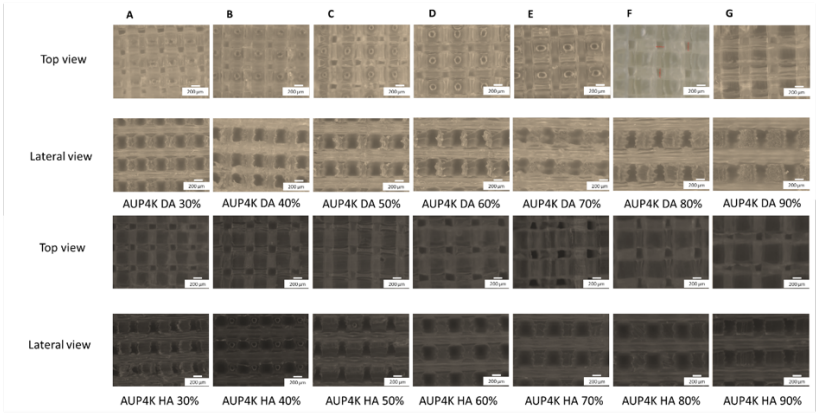

Figure 3.7: Effect of AUP concentration and endcap on the scaffold microstructure after injection-based indirect 3D printing, as visualized using optical microscopy. From top to bottom, images represent vertical and lateral porosities for both AUP4K types at one concentration. Panels A to G represent scaffolds at different concentrations (from 30-90 wt %). The scale bars are indicated on each figure (5X magnification).

The regular and well-defined structure of the scaffolds proves the capabilities of the developed scaffold production technique. The AUP scaffolds showed no signs of damage attributable to the PLA removal. Even more, no visible indications of cracked struts, air bubbles,

collapsed pores and/or PLA traces were observed for the AUP scaffolds.

Interestingly, despite the high viscosity of the AUP4K 90 wt % solutions, especially the AUP4K HA (see § 3.2), a very careful injection enabled the successful production of AUP4K scaffolds.

Scaffolds produced using this concentration were subjected to SEM analysis, enabling confirmation of the obtained optical microscopy data (Figure 3.7) related to scaffold morphology as well as the TGA data (Figure 3.6) related to PLA mould removal, as obtained for the AUP4K 80 wt % hydrogels.

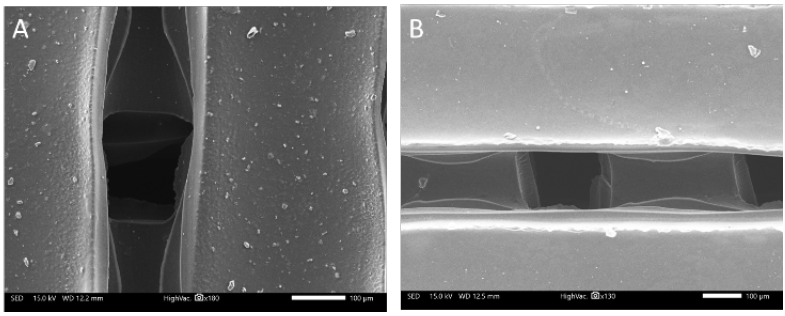

Figure 3.8: SEM images of 90 wt % AUP4K DA (panel A) and AUP4K HA (panel B) scaffolds.

The scale bars are indicated on each figure. The images were acquired with the viewing direction perpendicular to the strut surface / perpendicular to the printing plane

As evidenced from Figure 3.8, the scaffolds possess well-defined pores and struts without visible indications of damage and/or the presence of air bubbles or PLA traces.

3.3.6.2 Scaffold gel fraction and swelling degree

The gel fraction serves as a valuable indicator for the efficiency of the network formation. It indicates the amount of the original polymer that

is present in the hydrogel after crosslinking. The gel fraction affects various hydrogel properties such as the swelling behaviour and the mechanical properties [272]. The swelling degree not only affects the mechanical characteristics but also dictates the scaffold area and -volume available for cells. The latter influences various cellular processes such as cell adhesion, - proliferation, - migration and - differentiation, as well as nutrient supply and waste product removal [265].

From the data in Figure 3.9, it can be concluded that in all cases, the gel fraction meets or exceeds the acceptable threshold of 90%, suggesting that the AUP scaffolds are effectively crosslinked, even in the presence of the PLA mould.

When looking at the swelling degrees, both the AUP concentration and the - type affect this property. The reduction in swelling capacity with an increasing polymer concentration (for both AUP4K DA and HA) is related to the denser crosslinking as more material is present. The lower swelling degree of AUP4K HA hydrogels as compared to AUP4K DA is anticipated due to their higher crosslinking density based on the higher number of acrylates in the photocrosslinkable endgroups.

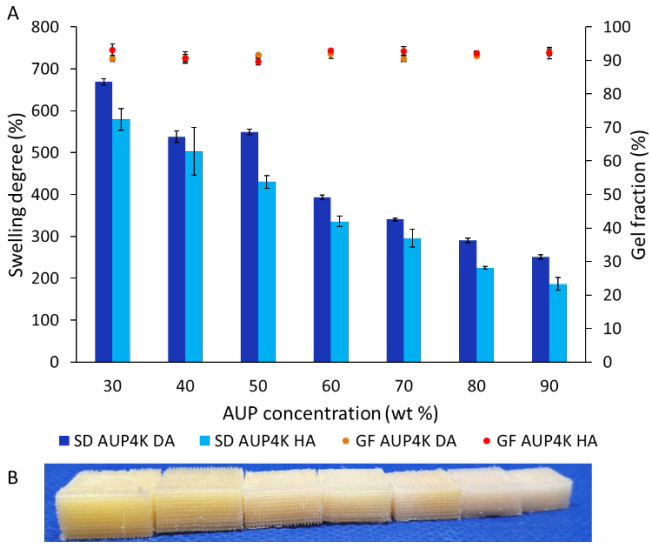

Figure 3.9: Swelling degree (SD) and gel fraction (GF) of AUP scaffolds. A) Effect of AUP concentration and endcap on the SD and the GF. B) Images of the swollen AUP4K DA scaffolds. The swollen scaffolds from left to right are those with an increasing AUP4K DA concentration (from 30-90 wt %).

3.3.6.3 Scaffold mechanical characterization

Developing scaffolds revealing adequate mechanical properties is one of the most important challenges while engineering an artificial meniscus [11,242]. The compression characteristics of the human meniscus are crucial for the correct functioning of the knee joint. Therefore, static compression testing was the first mechanical test performed for assessing the E-modulus, the ultimate strength and -strain of the developed hydrogel scaffolds. The tests were performed on equilibrium water-swollen AUP scaffolds to mimic the *in vivo* hydrated state in which these materials will find application.

As can be seen from Figure 3.10 panel A, B and insets, the strain range of 0-5% is classified as the preload region as there is a very low stress response upon applying the initial deformation. Consequently, this

segment was omitted from the evaluation of the Young's modulus. As for some of the herein developed AUP scaffolds, the 5-10% strain range still yields a low stress response (see again Figure 3.10 panel A, B and insets), we believe that a suitable range for determining the Young's modulus is situated between 10 and 20% strain. This section represents for our hydrogels the elastic portion of the curve following the preload region.

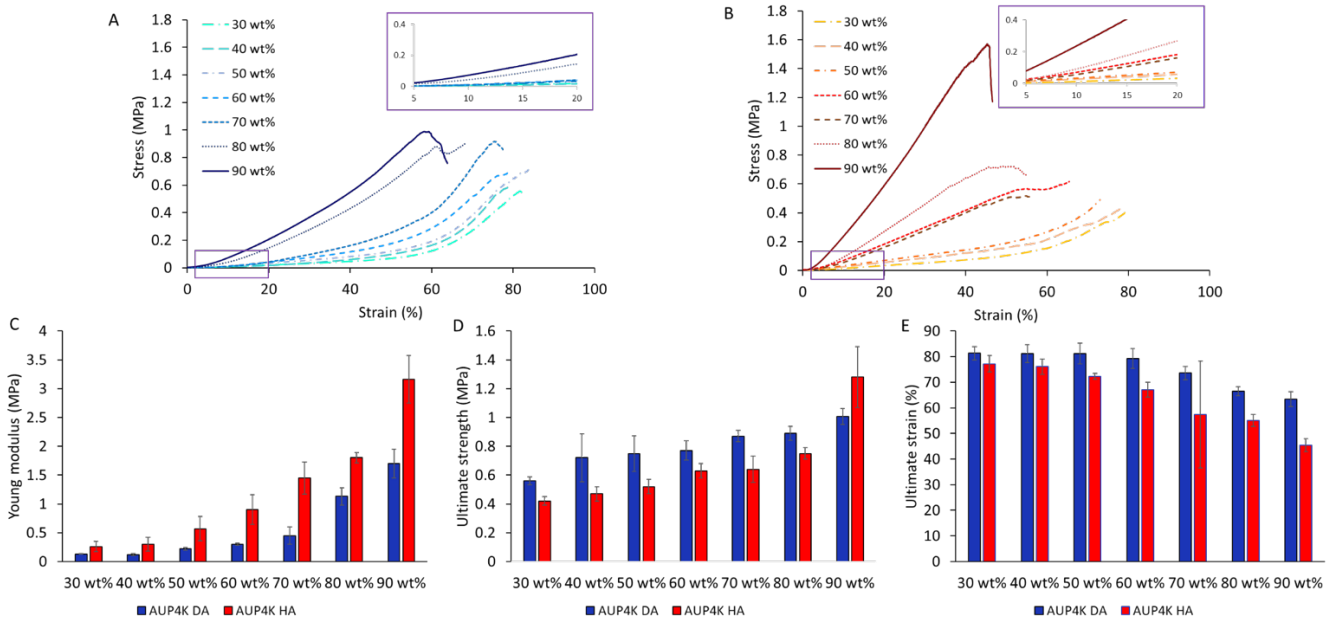

Figure 3.10: Effect of the AUP concentration and - endcap on the compressive properties of equilibrium water-swollen scaffolds. The scaffolds were compressed at a speed of 2 mm.min^{-1}. Panels A and B represent the obtained test curves for respectively AUP4K DA and AUP4K HA. Panels C to E represent respectively the Young moduli, the ultimate strength and the ultimate strain values for AUP4K DA and AUP4K HA, as derived from panels A and B.

Interestingly, for both AUP types, the observed evolution in the stress strain curves is AUP concentration dependent. For AUP4K DA, two patterns can be distinguished: one from 30-70 wt % and one from 80-90 wt%. Both patterns can be considered as soft interconnected scaffolds [273,274], while the second pattern represents scaffolds with more rigid properties as compared to those at lower concentrations. For AUP4K HA, three patterns can be distinguished: one from 30-50 wt %, a second one from 60-80 wt % and a third one for the 90 wt%. The first two patterns show similar evolutions as the AUP4K DA. Interestingly, the AUP4K HA with the highest concentration (90 wt%) reveals an alternative evolution, with the material being the most rigid one under evaluation.

The evolution of the curves at lower concentrations mirrors the typical compressive stress-strain curves observed in a soft interconnected scaffold due to presence of porosity in all directions of the scaffolds [273,274]. However, at higher concentrations, the inherent properties of the hydrogel become more influential than the effect of the pores. Indeed, both materials exhibit increased stiffness due to a higher crosslinking density, which compensates the stretchability of the interconnected scaffolds. This results in stress-strain curves like those seen in materials with only vertical porosity as reported in the literature [274,275].

From the data (Figure 3.10 panels C-E), it can be concluded that both types of AUP4K scaffolds show an increase in mechanical properties with an increase in hydrogel building block concentration. Indeed, both the Young's modulus and the ultimate strength follow this trend, while the ultimate strain follows the anticipated inverse trend. The findings are linked to an increasing crosslinking density and a decrease in swelling degree with an increasing AUP concentration and confirm previous literature reports using other polymers [276–278].

When comparing AUP4K DA and the AUP4K HA counterpart, the Young's modulus data (Figure 3.10 panel C) highlight that AUP4K HA outperforms AUP4K DA across all concentrations. This can be explained by the higher crosslinking density for the AUP4K HA (cfr. more crosslinkable groups per macromonomer). For the ultimate strain, the anticipated opposite trend is observed. Given the lower number of photocrosslinkable groups, AUP4K DA outperforms the HA-derivative as higher ultimate strains can be reached at all concentrations.

For the ultimate compressive strength (UCS) (panel D), the picture becomes more complex. The UCS measures the final load at which the material breaks. This can occur either in the elastic phase, as seen in brittle materials with no plastic deformation, or after an elastic phase followed by plastic deformation, which is typical for most polymers. It is hypothesized that the AUP4K DA scaffolds exhibit limited plastic deformation, allowing it to achieve a higher UCS compared to the more densily interconnected and thus structurally reinforced HA. This trend persists up to the 80 wt% composition. Above that concentration, the extensive chain interconnections and morphology of the AUP4K HA scaffolds surpass those of the DA counterpart, resulting in a higher fracture resistance. The data for AUP4K HA in panel B from Figure 3.10 indicate a slight increase in stress beyond the yielding point for materials with mass percentages lower than 90 wt%. In contrast, the 90 wt% AUP4K HA is the only material that lacks a yielding point and fractures in a fragile manner.

To study the effect of the porosity on the mechanical properties, we compared a porous and non-porous 90 wt% AUP4K DA and AUP4K HA material. The data (Figure 3.11 and table 3.1) reveal that, as anticipated, porosity leads to scaffolds with inferior mechanical properties.

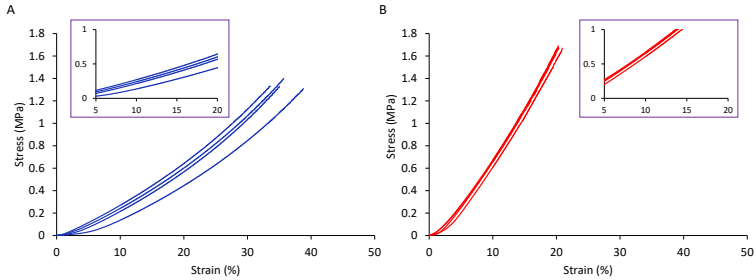

Figure 3.11: Effect of the AUP endcap on the compressive properties of non-porous equilibrium water-swollen scaffolds at a 90 wt % AUP concentration. The scaffolds were compressed at a speed of 2 mm.min-1. Panels A and B represent the obtained test curves for respectively AUP4K DA and AUP4K HA (n = 4).

Figure 3.11 shows the data of the compressive testing on non-porous 90 wt % AUP4K DA and AUP4K HA scaffolds. The Young's Modulus (YM) as derived from Figure 3.11 A and B are shown in Table 3.1.

Table 3.1: Comparison of compressive Young Modulus (MPa) for porous and non-porous scaffolds. The table presents Young modulus values for two types of scaffolds, AUP4K DA and AUP4K HA, in both porous and non-porous forms.

	Young modulus values (MPa) Porous scaffold	Young modulus values (MPa) Non-porous scaffold
AUP4K DA	1.7 ± 0.25	2.76 ± 0.43
AUP4K HA	3.16 ± 0.41	8.61 ± 0.12

Both for the porous and the non-porous samples, the AUP4K HA outperforms AUP4K DA in YM. This is linked to the higher number of photo-crosslinkable groups for the AUP4K HA as compared to the AUP4K DA counterpart. When comparing the YM data from the porous and the non-porous samples, the non-porous samples reveal, as anticipated, the best mechanical properties.

The trend for both curves indicates that both AUP exhibit behavior similar to that of a rigid material. Indeed, both AUP can be categorized as tough hydrogels.

When we compare the herein obtained data with compression tests on human menisci, indicating Young's modulus values ranging between 0.97 and 19 MPa (values calculated between 12 and 20% strain), it is evident that our materials fall within the meniscus range, although at the low end [54,58–60]. Specifically, the values for AUP4K DA and AUP4K HA range respectively from 0.13-1.7 MPa and from 0.26-3.16 MPa. However, drawing definite conclusions from this comparison should be done with care. Indeed, the data of the reported mechanical properties of human menisci depend both on the test specimen and the testing conditions (dry versus hydrated, sliced or intact, specimen shape, specimen dimensions). Important to note is also that *in vivo*, the synovial fluid permeates the porous meniscal tissue structure. This makes comparison even more troublesome. However, the performed tests give a very good first indication of the potential of the developed materials in terms of their mechanical properties.

In a final part of our work, we performed TPA of the scaffolds. While the obtained Young modulus, ultimate strength and ultimate strain values offer insight into the scaffold's overall stiffness and elastic behaviour, the scaffold hardness provides information about its resistance to deformation and wear [279]. This information is crucial for ensuring that the scaffold can withstand physiological loads, provide the necessary support for tissue growth and match the biomechanical properties of the different meniscus zones [18,61]. Indeed, the biomechanical properties of the meniscus vary between its anterior and posterior regions, contributing to its overall functionality within the knee joint. The anterior region of the meniscus is typically stiffer than the posterior part making it crucial to develop scaffolds that achieve a

range of mechanical properties [280]. The TPA test was conducted on samples in their equilibrium water-swollen state, again with the aim to mimic the *in vivo* conditions. The data are shown in 3.12.

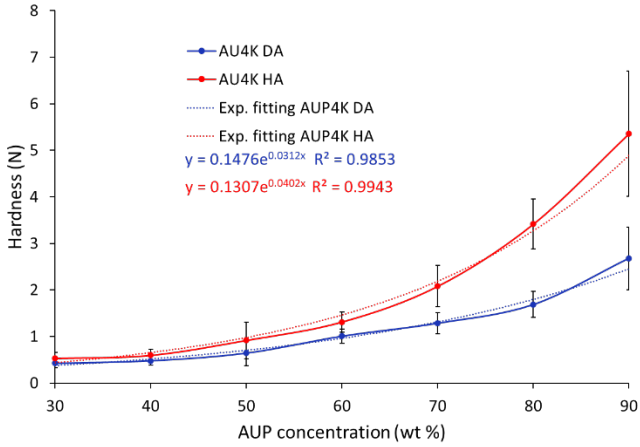

Figure 3.12: Effect of the AUP concentration and endcap on the hardness of equilibrium water-swollen scaffolds as studied using texturometry.

Consistent with the obtained compression test results, an increasing AUP concentration leads to an increase in scaffold hardness for both AUP types. For both AUP4K, an exponential relation is observed, similar to the above-described viscosity data (see § 3.2). Irrespective of the AUP concentration, the hardness of AUP4K HA scaffolds is higher than their AUP4K DA counterparts. The former effect is again related to the higher amount of polymer present in the scaffolds at higher AUP concentrations while the latter effect is linked to a higher crosslinking density for AUP4K HA as compared to AUP4K DA.

To the best of our knowledge, there is no research available on the application of TPA tests on human menisci, disabling a direct comparison with the herein obtained data. A comparison of our material with other hydrogels is however feasible. In one study, calcium Alg-HA gels (30-50-70% w/v Alg and 70-50-30% w/v of HA) exhibited

hardness values below 0.981 N, while cross-linking lead to a six-fold increase [279]. Another study on GelMod at concentrations of 5 and 10% w/v revealed hardness values ranging from 0.04-0.07 N [144]. The herein developed AUP scaffolds appear to be significantly harder than GelMod while comparable with Alg-HA.

3.4 Conclusions

In this chapter AUP4K scaffolds using hydrogel building blocks with either 1 or 3 crosslinkable groups at each chain end, denoted as respectively AUP4K DA and AUP4K HA, were developed through an indirect printing approach using an in-house developed injection moulding setup making use of a commercial 3D printer. A porous PLA scaffold was applied as sacrificial mould enabling the injection of the AUP4K solutions at various concentrations (30-90 wt%) and subsequent UV-crosslinking. Despite the presence of the PLA mould during the crosslinking process, the achieved gel fractions exceeded 90% for all hydrogel compositions. After successful PLA mould removal through dissolution in chloroform, as evidenced using TGA and scaffold visualisation, the scaffolds obtained were porous at all sides, crack - and air bubble free, indicating the applied methodology to be both efficient and reproducible. In addition, the approach is fast (the moulding takes around 1 minute), enables moulding materials with low and high viscosity and does not require a vacuum to be applied. Leaving the scaffold pore and strut sizes constant, the compression test and the TPA performed indicate that the mechanical properties can be varied by the AUP type and its concentration. For both AUP4K types, the mechanical properties increase with an increasing AUP4K concentration. The AUP4K HA scaffolds outperform their AUP4K DA counterparts in terms of E-modulus and hardness while revealing a lower maximum strain. AUP4K DA scaffolds show higher UCS values than AUP4K HA up to a concentration of 80 wt%, whereas AUP4K HA demonstrates higher UCS values at 90 wt%. The compressive properties obtained are in the range of the human meniscus, confirming the potential of the proposed hydrogels as meniscal substitutes.

In conclusion, the comparison between AUP4K DA and AUP4K HA confirmed that precursor functionality plays an important role in determining scaffold performance. However, although fatigue resistance had been identified as a key limitation in Chapter 2, fatigue testing was not performed on the injection-moulded scaffolds developed in this chapter. This was due to practical limitations related to specimen geometry and fabrication. Producing fatigue ring specimens with this method would have required the design and validation of a new dedicated mould and injection set-up, which was not feasible within the available timeframe. Therefore, the present chapter focused on evaluating the influence of precursor functionality and scaffold architecture through swelling, gel fraction, static compression, and texture profile analysis. Based on these findings, Chapter 4 further explores the influence of AUP chemistry by changing the PEG backbone molar mass, while also introducing DLP printing as a more precise additive manufacturing technique compatible with the fabrication of defined test geometries, including ring specimens for fatigue evaluation.

Chapter 4:

Synthetic PEG-based Hydrogel Scaffolds for Meniscus Replacement via Digital Light Processing

This chapter describes the formulation and DLP printing of PEG-based urethane–acrylate (AUP2K DA/AUP4K DA) hydrogel meniscus scaffolds and their structural and physicochemical characterization. It then assesses mechanical performance under compression and cyclic loading and confirms cytocompatibility, supporting their use as a tunable platform for meniscus scaffolds. The work described in this chapter was performed by M. Meazzo, S. Schroeder, S. Vereecken, and M. Minsart. M. Meazzo performed the synthesis, printing, and characterization of the scaffolds. S. Schroeder performed the fatigue tests, S. Vereecken performed the cytotoxicity tests, and M. Minsart carried out the photorheology analysis.

This chapter is almost finalized for submission

4.1 Introduction

As outlined in Chapter 1, meniscal injuries represent a major clinical burden and, when irreparable, current surgical options (repair or partial meniscectomy) can compromise long-term joint homeostasis and accelerate degenerative changes [74,281–284]. Chapter 1 also detailed the key anatomical and compositional features of the meniscus (high water content, low vascularity in the inner zone, and strong structure–function relationships), which together explain both the limited intrinsic healing capacity and the stringent requirements for a functional replacement scaffold [107,285].

As already seen in previous chapters, the advent of 3D printing in scaffold development represented a significant breakthrough, enabling the creation of intricate, customized implants for regenerative medicine, which also holds potential for the production of artificial meniscal implants [286,287]. The ASTM/F2921 standard identifies seven 3D printing methods: material extrusion, binder jetting, material jetting, powder bed fusion, directed energy deposition, sheet lamination, and vat photopolymerization [8]. Currently, the use of light-based additive manufacturing techniques has been increasingly recognized for its potential in creating scaffolds for tissue engineering. Stereolithography-based techniques, including SLA and digital light processing (DLP), are among the leading fabrication methods, providing resolutions as low as 0.6 up to 90 µm [288,289]. Both extrusion-based and DLP-based bioprinting methods have successfully been used to 3D print a variety of tissues, including heart tissue, blood vessels, bone, cartilage, liver, lung, eye, neuronal tissue, and pancreatic tissue [290]. Although the versatility of DLP printing enables the production of scaffolds with highly tuneable structural and/or mechanical properties, its broader implementation remains constrained by the limited availability of suitable photo-polymerizable

inks. Consequently, as DLP remains a relatively recent addition to the field of 3D printing, further investigation is required to explore and refine material formulations and rigorously assess its suitability for future clinical translation.

Building on the findings of Chapters 2 and 3, the next step of this work focused on further increasing the mechanical performance and reproducibility of AUP-based scaffolds. Chapter 2 showed that AUP4K DA could be processed by extrusion-based printing, but that fatigue resistance remained insufficient. Chapter 3 demonstrated that increasing the acrylate functionality from di-acrylated AUP4K DA to hexa-acrylated AUP4K HA could increase scaffold stiffness, confirming the importance of crosslinking density. In the present chapter, a different strategy was investigated: reducing the PEG backbone molar mass from 4K to 2K. This change was expected to increase the concentration of reactive acrylate groups per unit mass, resulting in a denser and mechanically stronger network after photo-crosslinking. At the same time, digital light processing was introduced to improve control over scaffold geometry and pore fidelity compared to extrusion-based fabrication. [291] The produced scaffolds were consecutively subjected to an in-depth characterization including the determination of the crosslinking efficiency, the swelling behaviour and the mechanical properties (via compression and fatigue testing) and the preliminary evaluation of the biocompatibility.

The complete workflow from AUP synthesis over DLP printing to scaffold evaluation is summarized schematically in Figure 4.1.

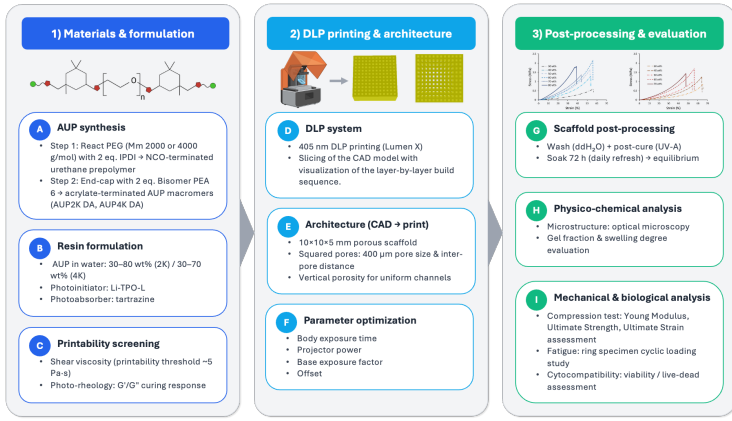

Figure 4.1: Schematic overview of the digital light processing (DLP) workflow for the fabrication and evaluation of acrylate-terminated urethane-PEG (AUP) scaffolds. The process includes (1) AUP synthesis and resin formulation, (2) DLP printing and architectural design, and (3) post-processing and physico-chemical, mechanical, and biological characterization.

4.2 Materials and Methods

4.2.1 Materials

Bisomer PEA-6 (Geo Specialty Chemicals), butylated hydroxytoluene (BHT, Innochem GmbH), dimethyl terephthalate (DMT, Sigma-Aldrich), isophorone diisocyanate (IPDI, Sigma-Aldrich), deuterated chloroform ($CDCl_3$, Euriso-Top), poly(ethylene glycol) 2 000 g/mol (PEG, Merck), poly(ethylene glycol) 4 000 g/mol (PEG, Merck), phenothiazine (PTZ, Merck), triphenylphosphite (TPP, Merck), phosphoric acid (Sigma-Aldrich), Valikat Bi (bismuth neodecanoate, Umicore), 2,4,6-trimethylbenzoyl)-phenyl-phosphinic acid ethyl ester (commercial Speedcure TPO-L, Lambson), butan-2-one (Sigma-Aldrich), lithium bromide (LiBr, Sigma-Aldrich), tartrazine (Sigma-Aldrich), phosphate buffered saline (PBS, Sigma-Aldrich), penicillin/streptomycin (P/S, Sigma-Aldrich), Dulbecco's modified eagle medium (DMEM, Sigma-Aldrich), fetal bovine serum (FBS) and calcein acetoxymethyl/propidium iodide (Ca-AM/PI) (Sigma-Aldrich), 3-(4,5-dimethylthiazol-2-yl)-5-(3-carboxymethoxyphenyl)-2-(4-sulfophenyl)-2H-tetrazolium (MTS, Abcam), commercial human foreskin fibroblasts (HFF) (ATCC) and 70% ethanol in water (Chem-Lab) were used as received.

4.2.2 Methods

4.2.2.1 Synthesis of acrylate-endcapped urethane-based poly(ethylene glycol) precursors

The AUP2K DA and AUP4K DA were synthesized as previously published in literature, and described in the previous chapters [143,148,150]. In this chapter, we used PEG with molar masses of 2 000 g/mol (PEG2K) and 4 000 g/mol (PEG4K) as the primary building blocks for developing the AUP hydrogel precursors, named AUP2K DA and AUP4K DA.

4.2.2.2 Chemical structure via FTIR spectroscopy

The molecular structures of the synthesized AUP were analysed using Fourier transform infrared (FTIR) spectroscopy, facilitated by the PerkinElmer Frontier FTIR mid-IR as described in Chapter 2.

4.2.2.3 Acrylate content and molar mass determination via 1H-NMR spectroscopy

The chemical structures of AUP4K DA and AUP2K DA were confirmed through ^{1}H-NMR spectroscopy using a Bruker Avance II Ultrashield 400 MHz spectrometer with deuterated chloroform as the solvent as described in Chapter 2.

4.2.2.4 Photo-initiator synthesis

The synthesis of Li-TPO-L was carried out similarly to the method described in patent literature [258] and as described in Chapter 3.

4.2.2.5 Analysis of the viscosity and the crosslinking kinetics of the AUP building block via in situ rheology

For the rheological analysis of various AUP solutions, an Anton Paar Physica MCR 302 rheometer was utilized, using the Rheoplus software for data processing. The experimental set-up featured parallel plates, with the top plate measuring 25 mm in diameter and a gap of 0.3 mm. The viscosity of the AUPs was measured by placing the aqueous precursors (30 wt% to 90 wt%; 300 µL) containing 5 mol% of Li-TPO-L (photo-initiator, PI) and 0.5 mol% of tartrazine (photoabsorber, PA) between these plates. The Li-TPO-L concentration was increased from 2 mol%, as used in the extrusion-based and injection-moulding approaches, to 5 mol% for the DLP process. This adjustment was necessary because the DLP printer relies on an internal 405 nm light source with a lower effective intensity and a wavelength range slightly shifted compared to the external UV crosslinking setup used in the

other chapters. In addition, Tartrazine (E102) was selected as the photoabsorber for the DLP printing process based on several considerations. First, tartrazine exhibits strong absorption in the near-UV to blue-violet range (λ_max ≈ 425 nm), which overlaps effectively with the emission wavelength of the DLP projector (405 nm), making it a suitable candidate for controlling light penetration depth during layer-by-layer photopolymerization. Second, tartrazine is a water-soluble, FDA-approved food-grade dye that has been widely used as a photoabsorber in hydrogel-based DLP printing, including in GelMA and PEGDA systems, due to its established biocompatibility profile and its ability to limit overcuring without compromising cell viability [292]. Third, tartrazine does not participate in the radical polymerization reaction and is progressively washed out during the post-printing swelling steps, avoiding its long-term presence in the final scaffold. The suitability of tartrazine as a photoabsorber for the AUP system was confirmed empirically within our laboratory, where it demonstrated effective control over the curing depth at the applied concentration of 0.5 mol%, enabling the fabrication of scaffolds with well-defined layer resolution and minimal interlayer overcuring. Initially, strain and frequency sweeps were conducted to identify the materials' linear viscoelastic range, by varying the strain from 0.01% to 100% at a frequency of 1 Hz. Following this, the mechanical spectrum of the precursors was recorded by increasing the frequency from 0.01 to 10 Hz, while keeping the strain constant at 0.1%.

The cross-linking kinetics of the AUPs were also investigated using parallel-plate rheology. Indeed, rheology is a useful tool for determining the curing kinetics of a material. This can be qualitatively estimated by combining rheological measurements with in *situ* curing experiments (photo-rheology) [293].

The storage and loss moduli as a function of time of aqueous AUP precursor solutions were recorded before, during and after VISBG irradiation (400-500 nm, 20 mW/cm^2, OmniCure 1500 light source) at 1 Hz frequency and 0.1% strain.

4.2.2.6 Digital Light Processing of AUPs ink toward meniscal tissue engineering applications

The scaffolds were fabricated using DLP (Lumen X, Cellink), which utilizes 405 nm visible light to cure a photo-crosslinkable polymer. The technical specifications include an XYZ resolution of 50 µm, and an intensity range of 10-30 mW/cm². The print bed temperature is adjustable up to 50°C; however, for this application, a temperature of 35°C was selected to reduce the viscosity of the highest concentration solutions, which exhibit the highest viscosity. Three scaffold designs were utilized: the first design is a cubic scaffold (10 mm x 10 mm x 5 mm) with a pore size of 0.40 mm and an interpore distance of 0.40 mm, used to evaluate the overall properties of the 3D printed AUP scaffold. The second design is a disk (7.5 mm in diameter and 1 mm in thickness) for cytotoxicity evaluation. The third design is a symmetric ring-shaped specimen, following the geometry reported in a previous study for fatigue behaviour analysis [17]. The detailed dimensions of the ring specimens are provided in Figure 2.1 in Chapter 2.

The print solutions were prepared by melting AUP at 40 °C and mixing it with double-distilled water and a solution containing 5 mol% of photo-initiator (Li-TPO-L) and 0.5 mol% photo-absorber (tartrazine) with respect to the acrylate content in the synthesized AUPs.

The scaffolds were washed with double distilled water to remove any excess solution and unclog the pores. They were then crosslinked under two-sided UV-A light (λ = 365 nm, 10 mW/cm^2 from bottom and top) for 10 minutes to ensure complete reaction of all acrylate groups.

4.2.2.7 Studying the thermal properties of the AUPs pre- and post-crosslinking

Thermogravimetric analysis (TGA) and differential scanning calorimetry (DSC) were used to evaluate the thermal properties of both crosslinked and uncrosslinked AUP samples. For TGA, samples weighing 10-25 mg were placed on a platinum pan and heated from 35°C to 750°C at a rate of 10°C/min under a nitrogen atmosphere. Specifically, $T_{99\%}$, temperature at which 99% of the material's original mass remains, $T_{95\%}$, temperature at which 95% of the material's original mass remains, and T_D, temperature at which the material begins to decompose significantly, are assessed.

DSC was used to identify phase transition temperatures such as melting and crystallization (T_m and T_c, respectively) by measuring heat fluctuations during temperature cycling between -90°C and 120°C with a heating rate of 10°C/min and a cooling rate of 5°C/min. A sample weighing 5-10 mg was placed in a sealed pan and analyzed using a DSC calorimeter (Q2000 DSC, TA Instruments). These two techniques combined offer insights into material stability and behaviour at application-specific temperatures. Both analysis techniques were conducted on crosslinked (after washing and post-curing) and uncrosslinked samples of AUP2K DA and AUP4K DA.

The various temperatures were calculated using the TA Universal Analysis 2000 software, version 4.5A (build 4.5.0.5) (TA Instruments, New Castle, DE, USA).

4.2.2.8 Evaluation of gel fraction and swelling capacity of the AUP digital light processing scaffolds

To calculate the gel fraction and the swelling capacity of the scaffolds, dry samples were weighed (Wd) and placed in double distilled water for 72 hours according to internal protocol. The medium was refreshed

every 24 hours to promote the leaching of uncrosslinked parts and allow equilibrium swelling. After recording the swollen weight (Ws), the samples were placed inside a desiccator filled with silica gel and then transferred to a drying chamber (FD 23, Binder) at 40°C overnight. Finally, the samples were weighed again (Wdes).

The swelling degree was calculated using Equation (4.1) and the gel fraction using Equation (4.2).

Swelling degree (%) = $\frac{Ws-Wdes}{Wdes} * 100$ (4.1)

Gel fraction (%) = $\frac{Wdes}{Wd} * 100$ (4.2)

4.2.2.9 Evaluation of the mechanical properties of AUP scaffolds.

4.2.2.9.1 Evaluation of the compressive properties of AUP scaffolds.

The compression tests were performed on samples in their swollen state under ambient conditions, without the use of any lubricant, after having been immersed in double distilled water for 72 hours. A Tinius Olsen 5ST testing machine with a 500 N load cell was used for the tests. Given the viscoelastic properties of the polymer, the testing speed was set to a relatively low value of 2 mm/min. The preload, as per our internal lab protocol, ranged from 0.1 to 0.3 N. Four samples were tested for each formulation.

4.2.2.9.2 Evaluation of the fatigue behaviour of AUP scaffolds

Dynamic compression tests were conducted to evaluate the fatigue resistance of the two AUP formulations. All samples were produced using the DLP printing process described in Section 2.2.6 with a concentration of 80 wt% and 70 wt% for AUP2K DA and AUP4K DA respectively.

Two groups of fatigue-ring specimen were compared in a fatigue test. The first group consisted of eight AUP2K DA and the second group consisted of eight AUP4K DA specimens. All fatigue-ring specimens (see Figure 2.1) were immersed in double distilled water for 24 hours before testing. Before and after pre-soaking, the fatigue-ring specimens were inspected for material defects using a digital microscope (VHX, Keyence, Japan).

A novel fatigue test setup was developed to induce a compression as well as a stretching in the fatigue-ring specimen. Using this setup, two specimens could be tested simultaneously as shown in Figure 4.2. The setup was integrated into a pneumatic testing machine (DYNA-MESS Prüfsysteme GmbH, Stolberg, Germany).

Figure 4.2: Developed test setup to simultaneously induce a compression and a stretching in two fatigue-ring specimens.

A load (L) is applied to a seesaw, which transfers the load evenly to both test stations. The test stations are placed on axial groove ball bearings which act as shear force compensations. The test stations are filled with ultrapure water to test the fatigue-ring specimen in a

swollen condition. The functionality of the individual test stations is shown in a sectional drawing in Figure 4.3.

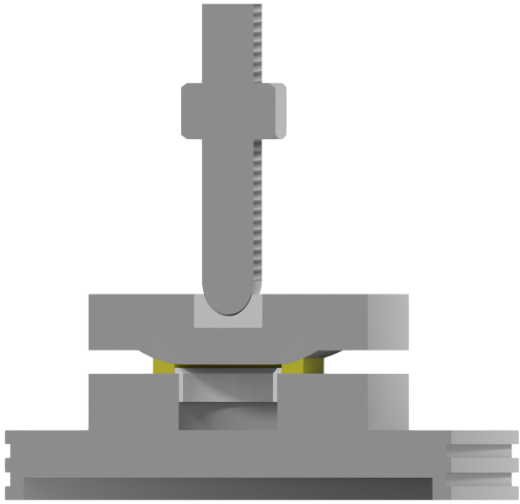

Figure 4.3: Test station with the fatigue-ring specimen (sectional view) receiving a compression as well as a stretching.

The fatigue-ring specimen (yellow) is placed on the bottom plate around a plastic ring, which is holding the fatigue-ring specimen in the right place. An upper plate with a curvature on the downside is placed on the fatigue-ring specimen. A threaded rod with a polished round end induces the force into the upper plate. By inducing the force into the upper plate, the fatigue-ring specimen is getting compressed and stretched at the same time.

For testing, two fatigue-ring specimens were placed into two test stations and each was filled with 250 ml ultrapure water. The two test stations were then placed into the test setup. A sinusoidal load was applied to both test stations and thus to both fatigue-ring specimens simultaneously with a frequency of 3 Hz. For loading, a locati test (Figure 4.4) was used by increasing the force after a specific number of cycles, when no failures of the fatigue-ring specimens occurred.

Indeed, the Locati method provides an accelerated alternative to the conventional step (up–down) procedure. By applying progressively increasing loading levels, it enables faster fatigue assessment while maintaining reliable accuracy, thereby improving testing efficiency and reducing both experimental duration and the number of specimens required [294]. The cyclic loading was performed in stepwise increasing load levels at a constant load ratio (R = 0.1), with 50,000 cycles per level, until failure occurred. After failure of one specimen, the second specimen was tested further using a TPU dummy. The load level and total number of cycles to failure were recorded, and groups were compared using an independent-samples t-test ($p \leq 0.05$).

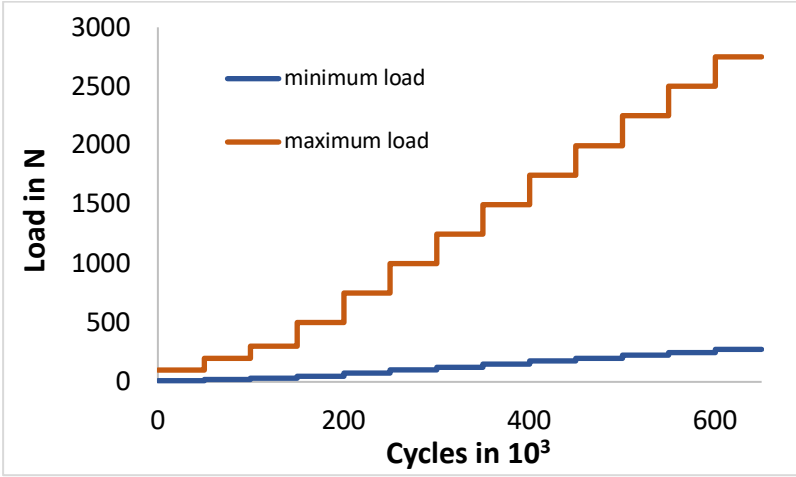

Figure 4.4: Minimum and maximum load acting on the test setup for each load level of 50.000 cycles (locati test).

In the first load level, a maximum force of 100 N and a minimum force of 10 N was applied to the test setup for 50 000 cycles. Due to the seesaw, the force on each fatigue-ring specimen was halved leading to a maximum load of 50 N and a minimum load of 5 N acting on the fatigue-ring specimens. The quotient between maximum and minimum load corresponds to a ratio of 0.1. If no failure occurred, the maximum load to the test setup was raised to 200 N and the minimum load was

increased to 20 N, which leads to the same ratio of 0.1. If no failure occurred after 50 000 cycles of this load level, the maximum and minimum loads increased to 300 N and 30 N for another 50 000 cycles and after that the maximum and minimum loads increased to 500 N and 50 N. If still no failure occurs, the maximum load increased by 250 N and the minimum load by 25 N for every following load level, until failure occurs.

If one specimen failed, the machine stops automatically. Afterwards, the test of the remaining fatigue-ring specimen will be continued with a dummy made of TPU on the contrarily side until the second fatigue-ring specimen failed as well. The load level and the total number of cycles until failure are recorded. A t-test for independent samples is used to compare the total number of cycles between the two groups. A p-value of ≤0.05 was considered being significant. All statistical calculations were carried out using the statistical evaluation software SPSS 28 (IBM, Amonk, NY, USA).

4.2.2.10 Cytotoxicity evaluation of AUPs printed disks.

The cytotoxicity of the 3D printed disks was evaluated via indirect cell tests. First the materials were sterilized by incubation in 70v/v% ethanol for 24 h (refreshed after 12 h), followed by 48h of incubation in PBS (refreshed after 24h) and subsequent UV-C irradiation (100–250 nm, 15 mW cm^{-2}) for 2 h.

HFFs were cultured at 37°C in 5% CO_2 in culture medium until the desired number of cells was obtained. The culture medium, consisting of Dulbecco's Modified Eagle Medium (DMEM) high glucose, 10 v% nutritional fetal bovine serum (FBS) and 1 v% antibacterial penicillin/streptomycin (P/S), was refreshed every 2–3 days, and cells were split when 80–90% confluency was reached. In these experiments, HFFs with a passage number of 8 were used. 7.5 mm

disks were leached in 1 mL cell medium for 1, 3 or 7 days at 37 °C in 5% CO_2. Meanwhile, 10 000 HFF cells were seeded in a 96-well plate and allowed to attach for 24 hours. Afterwards, the medium was replaced with 300 µL of the leached medium and the metabolic activity and the cell viability were assessed after 24h. As a positive control, fresh cell medium that had not been in contact with the materials was used. All experiments were performed in triplicate (n = 3).

The metabolic activity of the HFFs was evaluated using an 3-(4,5-dimethylthiazol-2-yl)-5-(3-carboxy-methoxyphenyl)-2-(4-sulfophenyl)-2H-tetrazolium (MTS) assay. The cell medium on the HFF cells was replaced with 120 µL of a mixture of 16 v/v% of MTS in culture medium. Subsequently, the plate was incubated in the dark (wrapped with aluminium foil) for 2h at 37 °C in 5% CO_2 allowing the bioreduction of MTS into the brown-colored formazan. Finally, the absorbance of the formazan was measured at 490 nm using a spectrophotometer (Tecan Inifinite M200 Pro, with Tecan i-control software). The viability and cytotoxicity were evaluated to the absorbance of the control cells.

A live-dead viability assay was performed using a mixture of 0.2 v/v% calcein-acetoxymethyl (CaAM) and 0.2 v/v% propidium iodide (PI) in PBS. After incubation of 15 min in the dark, live (green, CaAM) and dead (red, PI) cells were visualized using an Olympus IX 81 fluorescence microscope with Xcellence Pro software and equipped with a green fluorescent protein (GFP) filter and a Texas Red (TxRed) filter, allowing to distinguish live (green) and dead (red) cells. The obtained images were analyzed using ImageJ software (v 1.54g, Wayne Rasband, National Institutes of Health, Bethesda, MD, USA) and allowed determination of the cell viability by taking the ratio of living cells to the sum of living and dead cells.

All results are shown as a mean ± standard deviation (SD). Statistical analysis was performed using one-way analysis of variance (ANOVA)

using GraphPad Prism 10.3.1 and a significance of $p < 0.05$ was used. Statistically significant differences ($p^* < 0.05$ and $p^{**} < 0.01$) are indicated in the figures.

4.3. Results and discussion

The present work aims to contribute to studying the suitability of AUPs, photo-crosslinkable hydrogels with a PEG backbone, as meniscal replacement. Specifically, two variants, AUP2K DA and AUP4K DA, with PEG backbones of 2 000 and 4 000 g/mol molar mass respectively, were investigated. These materials were synthesized and the uncrosslinked materials were analyzed through NMR, IR, viscosity determination, thermal analyses and (photo)rheology.

The printability of these materials was evaluated using DLP. Starting with an initial concentration of 30 wt%, the concentration was systematically increased in 10% increments until the viscosity became too high to allow successful printing. After defining the precise printability range through rheological measurements, the next step was to ensure consistent scaffold fabrication. Printing parameters were carefully fine-tuned for each concentration and specific PEG backbone molar mass. Once optimized, scaffolds were printed to assess their compressive and fatigue properties as a function of the AUP type and - concentration.

Finally, as the goal of the constructs is application in the human body, the biocompatibility of the printed scaffolds was evaluated using preliminary *in vitro* biological assays.

4.3.1 Hydrogel building block synthesis and structural characterisation

The AUP hydrogel building blocks utilized in this study were synthesized through a two-step reaction, as described earlier [141,143,144,148]. In short, in the first step, PEG with molar masses of either 2000 or 4000 g/mol was reacted with two equivalents of IPDI. In the second step, the resulting intermediate was reacted with two equivalents of Bisomer PEA 6 as an end-capping agent, yielding two

AUP variants with distinct molar masses, referred to as AUP2K DA and AUP4K DA. The rationale for this selection lies in the expected influence of the molar mass on the hydrogel's swelling behaviour and mechanical properties.

Figure 4.5 shows the general and the detailed chemical structures of the obtained polymers (panel A) together with the FTIR (panel B) and NMR spectra (panel C).

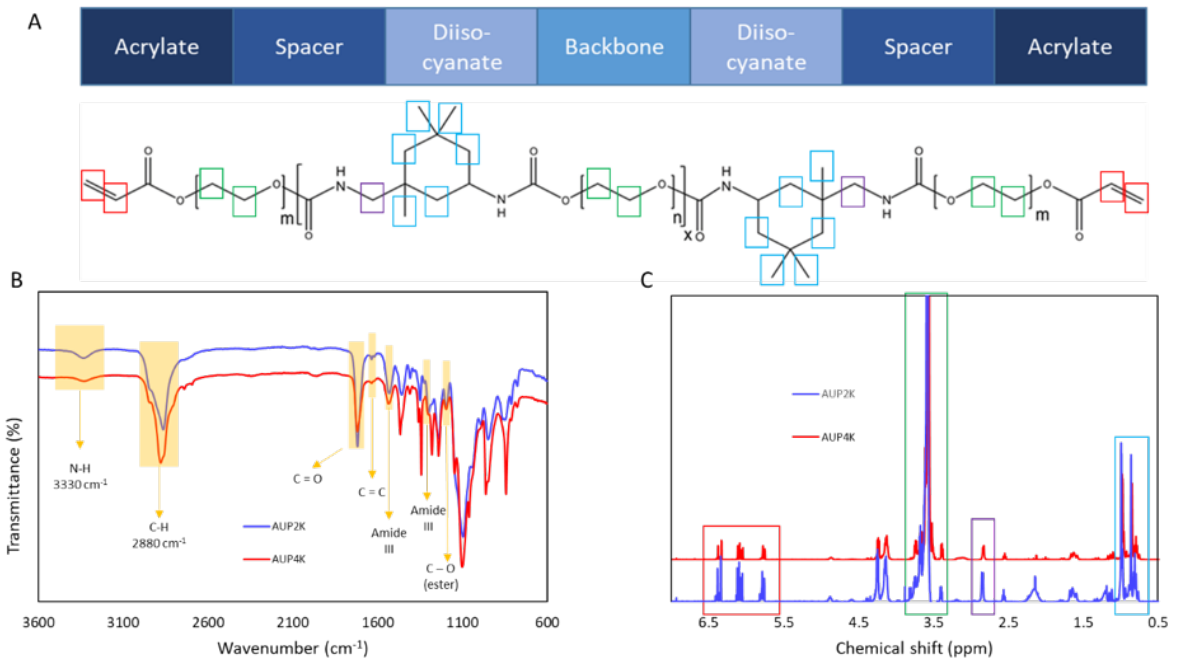

Figure 4.5: Overview of AUP chemical structure and obtained infrared and NMR spectra. A) The chemical structure of the synthesized AUPs. B) The FTIR spectrum of AUP2K DA and 4K DA, highlighting its characteristic IR peaks. C) The ^{1}H-NMR spectrum of AUP2K DA and 4K DA, with peak annotations indicated using the color code applied in parts A and C of the figure.

The acrylate content of the developed AUP materials, very important for the anticipated DLP printing, was determined using ^{1}H-NMR spectroscopy. By comparing the signals of the acrylate groups in AUP2K and AUP4K DA with those of the aromatic protons of dimethyl terephthalate (DMT), which served as an internal standard, the acrylate contents for AUP2K DA and AUP4K DA were, using Equation 2.1, calculated to be 0.37 and 0.55 mmol acrylate/g AUP, respectively. As anticipated, the acrylate content decreased with the PEG molar mass, which is expected to influence the mechanical and swelling properties of the resulting hydrogels [141].

By applying Equations 2.2 and 2.3, the molar masses of the synthesized AUP materials were determined. Similarly to what obtained in §2.3.1, the molar masses of the AUPs are approximately 1.4 times higher than that of the original PEG backbone, due to the lower selectivity of the bismuth-based catalyst toward the primary isocyanate group of IPDI. [224] Based on these calculations, the estimated molar masses are 2812 g·mol^{-1} for AUP2K DA and 5572 g·mol^{-1} for AUP4K DA.

4.3.2 Evaluation of the hydrogel building block properties via (photo)-rheology

The rheological properties of AUP solutions, as reflected by among other the viscosities measured at various concentrations, play a crucial role in assessing the printability and overall print quality of the scaffold. Figure 4.6 illustrates an exponential increase in viscosity with increasing AUP concentrations for both AUP2K DA and AUP4K DA. The test was performed at 35°C, the vat printing temperature, to reduce the high viscosity of the highest concentration solutions, while preventing the solvent (double-distilled water) from evaporating during the printing process.

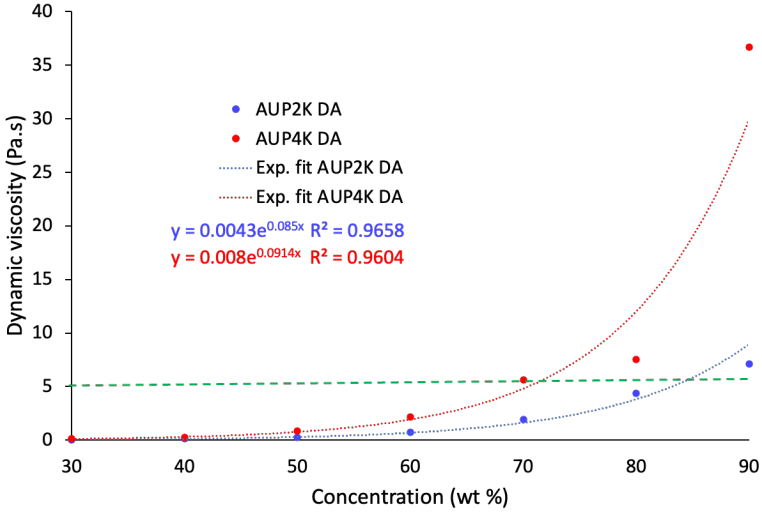

Figure 4.6: Effect of AUP concentration and - molar mass on dynamic viscosity, measured by rheology at 35 °C. The green line marks the printability threshold, defining the viscosity range considered compatible with the LumenX system's operating capabilities.

As anticipated, the dynamic viscosity of solutions of both AUP increases at higher polymer concentrations. Indeed, higher polymer concentrations result in more chain entanglements, which contribute to a higher viscosity [259]. For both types of AUP, the pattern observed is exponential with R^2 values of 0.96 for both AUP types (Figure 4.6). The exponential trend aligns well with theoretical predictions [259].

From the obtained data, is also evident that the viscosity of AUP4K DA solutions is higher than AUP2K DA. This is explained by the larger backbone molar mass for AUP4K DA that leads to an increase of the intermolecular interactions and entanglements of polymer chains, which impede the relative movement of the chains and result in a more viscous behaviour [295].

Printability issues, such as printer misalignment, air bubble entrapment in scaffolds, and layer delamination, are commonly observed in scaffolds printed from solutions with viscosities of 5 Pa·s or higher [296].

For AUP2K DA, the viscosity remains well below this printability threshold at concentrations up to 80 wt%, reaching 4.4 Pa·s. However, for AUP4K DA, the viscosity surpasses the threshold at a concentration of 80 wt%, reaching 7.56 Pa·s, and further increases to 36.7 Pa·s at 90 wt%, which may present significant printability challenges. Consequently, two different concentration ranges were selected for printing: 30 to 80 wt% for AUP2K DA and 30 to 70 wt% for AUP4K DA.

To assess whether the photo-crosslinkability of the AUP solutions is favourable for the selected light-based additive manufacturing technique, *in situ* UV curing experiments were conducted using photo-rheology determining the evolution of the storage modulus (G') and the loss modulus (G''), two critical properties when designing hydrogels that aim to mimic the intricate mechanical conditions of the meniscus [62,297]. The evolution of the storage and loss moduli of aqueous AUP solutions at different concentrations and for the two AUP types is plotted in Figure 4.7.

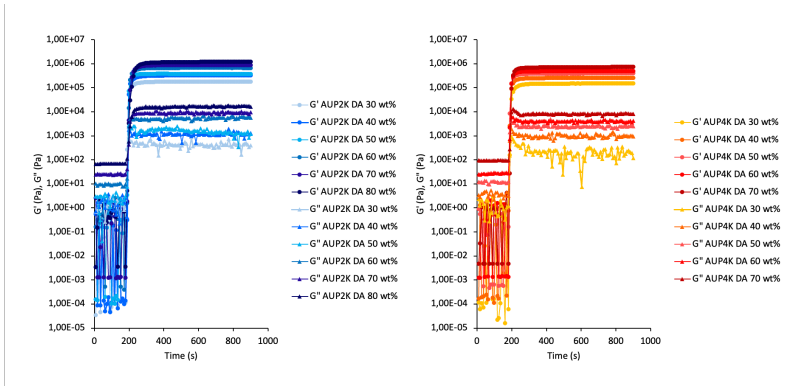

Figure 4.7: Effect of AUP type and - concentration on the crosslinking behaviour as determined by photo-rheological analysis of AUP solutions: A) AUP2K DA at a concentration of 30 wt% to 80 wt%; B) AUP4K DA at a concentration of 30 wt% to 70 wt%. All solutions contain 5 mol% Li-TPO-L and 0.5 mol% Tartrazine as respectively photo-initiator and photo-absorber.

All the solutions were proven to be photo-cross-linkable in the presence of 5 mol% Li-TPO-L (as photo-initiator) and 0.5 mol%

Tartrazine (as photo-absorber) (T = 35 °C, λ = 400−500 nm) as shown in Figure 4.7.

Initially, prior to irradiation, both G' and G" were below 100 Pa for all hydrogel precursors. Upon irradiation, the crosslinking reaction started, resulting in a significant increase in both moduli as the network formed. As the network formation reaches completion, the storage moduli reach a plateau value, summarized in Table 4.1.

Table 4.1: Effect of AUP type and - concentration on the storage modulus (G') and loss modulus (G") of hydrogels as studied by photo-rheology.

Material	G' (Pa)	G" (Pa)
AUP2K DA 30 wt%	162 070 ± 18 220	352 ± 43
AUP2K DA 40 wt%	329 515 ± 2 015	1 199 ± 90
AUP2K DA 50 wt%	375 640 ± 5 800	1 956 ± 12
AUP2K DA 60 wt%	657 615 ± 12 755	5 381 ± 280
AUP2K DA 70 wt%	857 585 ± 22 955	9 007 ± 642
AUP2K DA 80 wt%	1 149 300 ± 61 500	14 464 ± 2 088
AUP4K DA 30 wt%	148 730 ± 1 400	225 ± 107
AUP4K DA 40 wt%	235 205 ± 22 215	938 ± 16
AUP4K DA 50 wt%	386 325 ± 11 745	2 381 ± 132
AUP4K DA 60 wt%	452 265 ± 39 775	3 685 ± 524
AUP4K DA 70 wt%	709 440 ± 23 200	7 746 ± 403

The values in Table 4.1 align with those previously reported in literature for other hydrogels, as polymers with lower molar masses typically exhibit higher G' and G'' values [298,299]. Previous studies on poly(ether urethane)-based hydrogels have shown that the molecular characteristics of the hydrogel precursor strongly influence the viscoelastic properties of the resulting network. For instance, systems with a denser or more tightly packed network structure exhibited a stronger elastic contribution, reflected by higher G′ values and a shift in the G′/G″ crossover towards more elastic behaviour.[300]

Our data reveal that AUP2K DA outperforms the AUP4K DA counterpart for both G' and G''. Given the lower molar mass of AUP2K DA, the number of crosslinkable end groups per mass unit is larger as compared to AUP4K DA. This enables the formation of a denser covalent network upon photo-polymerisation, leading to a polymer network with smaller mesh sizes and thus being stiffer. This higher crosslink density restricts chain mobility more effectively, resulting in increased elastic and viscous moduli. In contrast, AUP4K DA forms networks with longer chain segments between crosslinks, leading to a more flexible and compliant structure [301].

Directly comparing the storage (G') and loss moduli (G") of our hydrogels, with the G' and G" values of the native meniscus tissue reported in the literature is challenging due to differences in the applied methodology. As an example, the native meniscus tissue data is often obtained using techniques such as Dynamic Mechanical Analysis (DMA), which operates under distinct testing conditions and protocols as compared to photo-rheology. These differences in factors like strain, frequency, and material state (e.g. hydrogel building block solution versus solid tissue) can lead to variations in the measured properties, making direct comparison complex.

4.3.3 Development of AUP scaffolds through DLP

Optimal printing parameters are crucial to limit scaffold defects such as delamination, the presence of air bubbles and poor shape fidelity. Balancing both overcuring and undercuring ensures that the printed designs align with CAD models, particularly regarding pore sizes and inter-pore distance. For the envisaged meniscal application of our scaffolds, the desired pore sizes range from 300-450 µm to enable chondrogenic cell attachment, growth and differentiation [302]. In this study, a regular squared-pore architecture was designed with both the pore size and the inter-pore distance set to 400 µm, featuring only

vertical porosity to better match the targeted mechanical properties, while ensuring a uniform structure favourable for future studies on cell growth and nutrient diffusion. The CAD model used for scaffold fabrication is presented in Figure 4.8. The scaffold architecture applied in this chapter was based on a rectilinear 0°/90° cross-hatched pattern, consistent with the approach adopted in Chapters 2 and 3. Alternative layer orientations (e.g. 0°/45° or 0°/45°/90°/135°) were not attempted for the DLP-printed scaffolds due to an increased risk of pore occlusion due to partial overcuring of the resin in narrow, obliquely oriented channels.

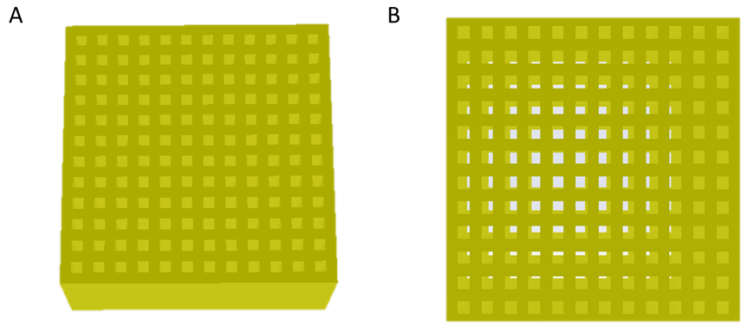

*Figure 4.8: Computer-aided design (CAD) model of the porous scaffolds (10*10*5 mm) used for digital light processing (DLP) printing. The design features a regular cubic lattice with uniform pore geometry and a nominal pore size of 400 µm. The left image shows the oblique view of the scaffold, while the right image depicts the top view.*

To fabricate the scaffolds, we tested and optimized four printing parameters that are often investigated in scaffold fabrication [303]: the body exposure time (i.e. the duration of light exposure for each layer), the projector power (i.e. the intensity of light projected onto the resin vat), the base exposure time (i.e. the light exposure duration for the initial few layers adhering to the build plate) and the offset (i.e. the vertical distance between the build plate and the resin vat during layer formation). In addition, the photo-initiator and photo-absorber contents were optimized, and 5 mol% of Li-TPOL and 0.5 mol% of tartrazine were

selected because these concentrations provided the most reliable curing behaviour during printing and consistently yielded scaffolds with the target porosity and strut definition.

As the polymer concentration increased (from 30 to 80 wt% for AUP2K DA and from 30 to 70 wt% for AUP4K DA), both the body exposure time and the projector power had to be decreased (see Table 4.2) to avoid overcuring. At higher AUP concentrations, the resin contains a larger fraction of reactive acrylate groups per volume unit and exhibits a higher viscosity (see Figure 4.6), which limits resin refresh between layers. Together, these effects make the formulation more sensitive to the applied light dose: excessive exposure or intensity can drive polymerization beyond the intended layer thickness, causing light bleed-through and uncontrolled crosslinking into adjacent regions. This leads to loss of pore definition, thickened or fused struts, and partial closure of the designed architecture. Reducing the exposure time and the projector power therefore helped confine curing to the targeted voxel volume and preserve the scaffold's intended porosity and strut geometry.

Table 4.2: Effect of AUP concentration and - molar mass on DLP printing parameters.

Material	Concentration [wt%]	Body Exposure Time [s]	Projector Power [%]	Base Exposure Factor	Offset [um]
AUP2K DA	30	8	35%	2	150
AUP2K DA	40	8	30%	2	150
AUP2K DA	50	8	30%	2	150
AUP2K DA	60	6	30%	3	150
AUP2K DA	70	6	30%	3	150
AUP2K DA	80	6	30%	3	150
AUP4K DA	30	9	40%	2	150
AUP4K DA	40	8	40%	2	150
AUP4K DA	50	7	40%	3	150
AUP4K DA	60	6.5	40%	3	150
AUP4K DA	70	6	35%	3	150

In detail, for respectively AUP2K DA and AUP4K DA, the body exposure times decreased from 8 to 6 s and from 9 to 6 s while the projector powers decreased from 35 to 30% and from 40 to 35% when increasing the AUP concentration. These trends in printing parameters reflect the enhanced photopolymerization kinetics at higher concentrations, which require less energy for effective crosslinking. Increasing the AUP concentration produced a similar effect as comparing AUP4K DA to AUP2K DA: the larger density of reactive groups for AUP2K DA as compared to AUP4K DA accelerated network formation, requiring shorter exposure durations to achieve complete

layer curing.

The observed dependence of the body exposure time and the projector power on the polymer concentration is consistent with literature findings [232]. In a visible-light thiol–ene PEG system, Wiley et al. reported that increasing the macromer concentration accelerated network formation such that the G' modulus stopped increasing (i.e. reached a plateau) after ~4 min at 6 wt% while after ~3 min at 14 wt% under otherwise comparable visible-light curing conditions. These data indicate that a higher density of reactive groups requires a shorter irradiation time to achieve network formation completion [232].

Moreover, the influence of the AUP molar mass on the curing behavior of AUP2K DA and AUP4K DA also mirrors the trends reported in literature [304]. In a study on PEGDMA–PLA systems, the authors demonstrated that higher molar mass species exhibit reduced chain mobility, leading to slower radical diffusion and lower crosslinking efficiency, whereas low molar mass analogues polymerize more rapidly and form more homogeneous networks. Analogously, in our work AUP2K DA, characterized by a lower molar mass and viscosity, required shorter body exposure times and lower light intensities to achieve complete layer curing, while AUP4K DA - owing to its longer chains and increased entanglement density - displayed more limited mobility and thus smaller variations in curing response across concentrations.

Interestingly, higher AUP concentrations necessitated an increase in base exposure factor, attributed to the unique rheological properties of the solutions. Indeed, solutions revealing a higher viscosity can cause the first layer to stick to the resin vat rather than the build plate, often resulting in detachment and print failure. To counteract this, the base exposure factor was increased from 2 to 3 for more concentrated formulations, irrespective of the AUP type, as shown in Table 2.

Increasing the base exposure factor allows the first layers to crosslink more effectively and adhere better to the build plate.

Offsets, ranging from 300 µm down to 100 µm were tested in increments of 50 µm, with 150 µm yielding the most successful prints across all concentrations for both AUP.

The scaffolds fabricated using AUP2K DA and AUP4K DA, at varying concentrations ranging from 30 wt% to 70 or 80 wt% (for respectively AUP2K DA and AUP4K DA) are shown in Figure 4.9. Despite the variation in hydrogel building block concentrations, all scaffolds exhibit a uniform pore size and inter-pore distance of 400 microns, closely mimicking the CAD file with a tolerance of ± 10 µm (Figure 4.8). This observation highlights the consistency in pore size achieved, regardless of the hydrogel composition, which is a critical feature for the intended biomedical application.

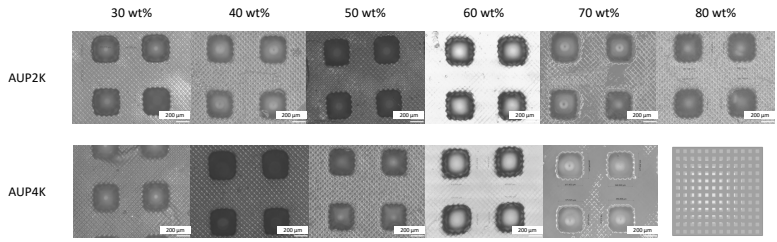

Figure 4.9: Effect of AUP concentration and - molar mass on the scaffold microstructure, as visualized using optical microscopy. Images represent vertical porosities for both AUP2K DA and AUP4K DA at different concentrations (30 wt% to 80 wt% for AUP2K DA and 30 wt% to 70 wt% for AUP4K DA). At the bottom right, the CAD model of the porous scaffold is shown. The scale bars are indicated on each figure (5X magnification).

To proof the formation of well-defined pores in the scaffold after DLP printing, this aspect was studied for both AUP at the highest concentration enabling printing (80 and 70 wt% for respectively AUP2K DA and AUP4K DA). Optical microscopy images (Figure 4.10) show that well defined pores extend from top to bottom of the scaffolds and

are free of residual crosslinked material.

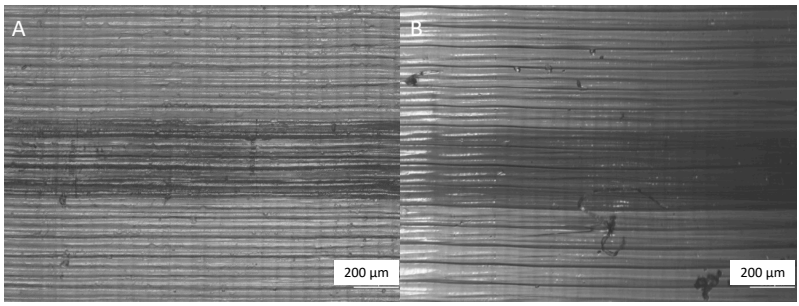

Figure 4.10: Optical microscopy images of AUP scaffolds cross-section showing a side-view (viewing direction perpendicular to the build direction) indicating the vertical porosity in the scaffolds. A) AUP2K DA 80 wt%, B) AUP4K DA 70 wt%.

4.3.4 Thermal properties of uncrosslinked AUP and crosslinked AUP scaffolds

To evaluate the thermal properties of both AUP materials, TGA and DSC were conducted on the uncrosslinked AUP and on the corresponding crosslinked scaffolds printed at their highest processable concentrations (70 wt% for AUP4K DA and 80 wt% for AUP2K DA), each containing 5 mol% of Li-TPOL as photo-initiator and 0.5 mol% of Tartrazine as photoabsorber. These concentrations were selected based on the viscosity measurements reported in Section 3.2, which confirmed compatibility with the operating range of the DLP printing system. TGA was performed first to evaluate the post-curing properties of the DLP-printed scaffolds, with a focus on their thermal stability. The data (Figure 4.11, panels A and B) reveal onset degradation temperatures exceeding 340 °C for all AUP samples, as summarized in Table 3. Both AUP thus demonstrated excellent thermal stability, with all samples exhibiting a single major degradation step above 300 °C. In line with literature, cross-linking does not affect the overall shape of the degradation curves [305,306]. As shown in Table 3,

the T_d values increased when comparing the uncrosslinked polymers to the corresponding crosslinked scaffolds for both AUP. This shift reflects the enhanced structural integrity and higher resistance to thermal decomposition resulting from the covalent network formed during photo-crosslinking. Notably, the presence of a single, sharp degradation step at higher temperatures (typically above 300 °C) reflects a homogeneous and stable crosslinked network [307]. The results indicate that crosslinking during DLP printing, together with the post-processing steps, yields highly efficient curing of the printed constructs.

Following TGA analysis, the melting and crystallization behaviours of the two different AUP were evaluated using DSC (Figure 4.11 panel C and D). After photo-crosslinking, both materials exhibited an increase in melting and crystallisation temperatures (Table 4.3), indicating reduced polymer chain mobility and enhanced network rigidity. This upward shift was more pronounced for the lower molar mass AUP2K DA, which contains a higher concentration of reactive acrylate end groups per mass unit, leading to a denser crosslinked structure. Similar trends have been reported for urethane-acrylate and hyperbranched acrylate systems, where lower molar mass precursors have thermal transitions at higher temperature, after curing due to increased crosslink density and more constrained segmental motion [308].

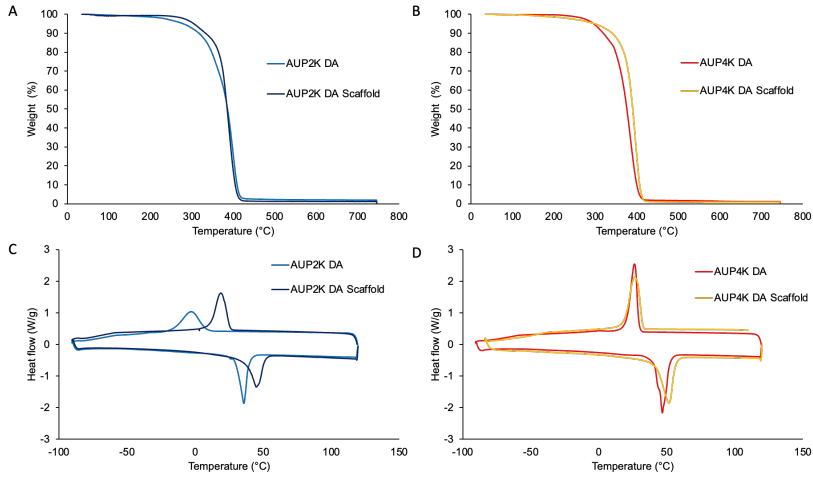

Figure 4.11: Effect of crosslinking on the thermal properties of AUP2K DA and AUP4K DA. A) TGA curve of AUP2K DA (uncrosslinked) and the crosslinked scaffold printed at 80 wt% with 5 mol% Li-TPOL and 0.5 mol% Tartrazine, B) TGA curve of AUP4K DA (uncrosslinked) and the crosslinked scaffold printed at 70 wt% with 5 mol% Li-TPOL and 0.5 mol% Tartrazine; C) and D) DSC thermograms of (un)crosslinked AUP2K DA (panel C) and (un)crosslinked AUP4K DA (panel D.)

Table 4.3: Effect of crosslinking on the thermal stability and transition temperatures of AUP as studied using TGA and DSC analyses.

Material	T_d (° C)	T_c (° C)	T_m (° C)
AUP2K DA	347	-3	36
AUP2K DA scaffold	356	19	45
AUP4K DA	343	26	47
AUP4K DA scaffold	370	27	52

4.3.5 Physico-chemical characterization of printed AUP scaffolds

4.3.5.1 Swelling degree and gel fraction of printed AUP scaffolds

An essential property of hydrogels is the gel fraction, which denotes the amount of the polymer that is incorporated within the network after crosslinking. A high gel fraction indicates that a large fraction of the original hydrogel building block has formed a crosslinked network, leading to a more stable and robust hydrogel. This gel fraction influences several hydrogel characteristics, including the mechanical properties and the swelling behaviour [309].

The gel fraction and the swelling degree were calculated using respectively equations (4.1) and (4.2).

From the data in Figure 4.12, it can be concluded that gel fractions for both AUP types exceed values of 95%, indicating that all AUP scaffolds are effectively crosslinked and that network formation was highly efficient, regardless of the applied concentration. In detail, the gel fraction for AUP2K DA ranges from 95.5% (30 wt%) to 98.5% (80 wt%), while for AUP4K DA it ranges from 96.2% (30 wt%) to 98% (70 wt%). The small while statistically significant ($p = 0.032$ for AUP4K DA and $p = 0.0316$) increase in gel fraction going from lower to higher concentration for both AUP is due to the presence of more AUP, leading to a higher crosslinking density. Although no individual pairwise comparisons reached statistical significance after Tukey correction, a trend toward increasing gel fraction with concentration was observed, suggesting near-complete network formation across the tested range.

When looking at the swelling degree, both the AUP concentration and the AUP molar mass affect this property. The swelling degree decreased with an increasing polymer concentration due to a higher

crosslinking density. The lower swelling observed for AUP2K DA hydrogels compared to their AUP4K DA counterparts is again related to the higher crosslinking density for the lower molar mass AUP2K DA.[306] One-way ANOVA revealed a significant effect of material concentration on swelling degree for both AUP2K DA and AUP4K DA formulations ($p < 0.001$). Tukey HSD post-hoc analysis confirmed a concentration-dependent reduction in swelling, with statistically significant differences between concentrations indicated in Figure 4.12 by different letters above the bars. Overall, the most pronounced changes occurred between low (30–40 wt%) and higher (≥50 wt%) concentrations, while higher solid contents showed a plateauing behaviour.

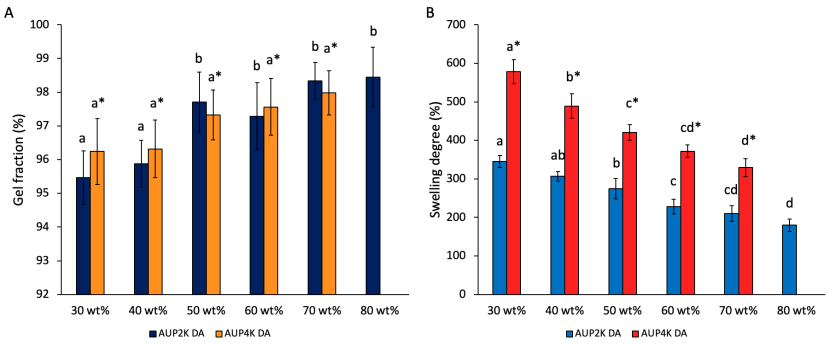

Figure 4.12: Effect of AUP concentration and molar mass on: (A) gel fraction and (B) swelling degree of AUP scaffolds. Data are presented as mean ± SD. Letters indicate significant differences between concentrations within the same material type; bars sharing at least one common letter are not significantly different ($p > 0.05$) according to one-way ANOVA followed by Tukey's HSD post-hoc test ($n = 4$). Non-asterisked and asterisked letters denote separate comparison groups (i.e., different material types) and should not be compared directly.

4.3.5.2 Mechanical properties of AUP printed scaffolds via compression tests

There are specific criteria that scaffold materials must meet for application in the meniscal replacement field. One of the most crucial

scaffold criteria is adequate mechanical properties [310,311]. Indeed, the meniscus experiences various forces, including shear, tensile and compressive forces. All these forces influence the mechanical behaviour of the meniscus, while compression remains particularly vital [11]. We therefore investigated the scaffold properties through compression testing. The test was conducted on hydrated scaffolds to mimic the *in vivo* situation. The results are shown in Figure 4.13.

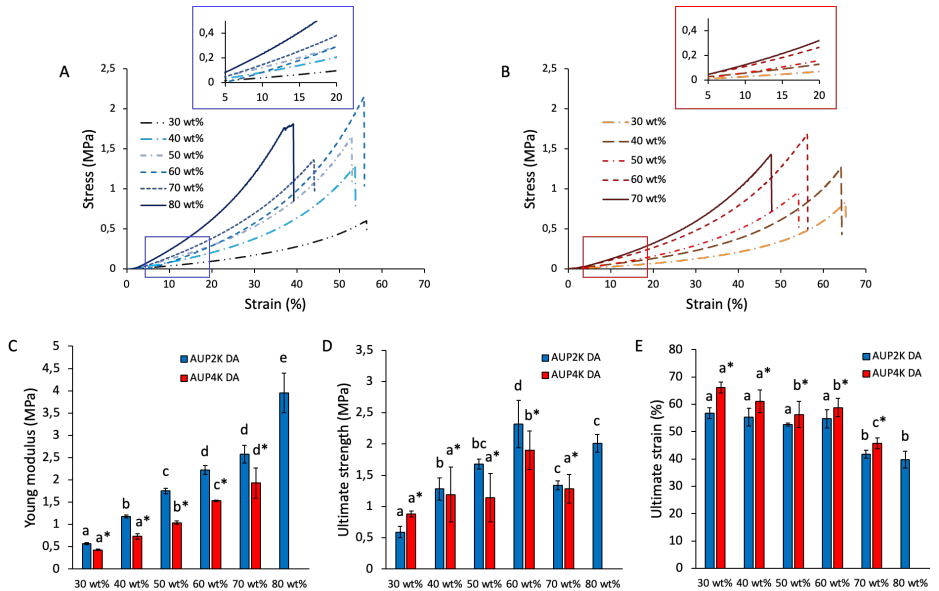

Figure 4.13: Effect of AUP concentration and molar mass on the compressive properties of AUP scaffolds. Scaffolds were compressed at a crosshead speed of 2 mm/min. Panels A and B show the compression curves of AUP2K DA and AUP4K DA, respectively. Panels C–E present the Young's modulus, ultimate strength, and ultimate strain of AUP2K DA and AUP4K DA scaffolds at different concentrations. Data are presented as mean ± SD. Letters indicate significant differences between concentrations within the same material type; bars sharing at least one common letter are not significantly different ($p > 0.05$) according to one-way ANOVA followed by Tukey's HSD post-hoc test ($n = 4$). Non-asterisked and asterisked letters denote separate comparison groups (different material types) and should not be compared directly.

As can be seen from Figure 4.13, panel A and B and insets, the 0-5% strain range can be considered as the preload region and is therefore excluded from the Young's modulus calculation. Considering the AUP scaffolds developed, the 5-10% strain range continues to exhibit a low stress response. We therefore propose that the ideal range for evaluating the Young's modulus is situated between strains of 10 and 20%, as this section corresponds to the elastic region of the curve following the preload region for our hydrogels.

Both AUP exhibited a typical increase in the Young Modulus (Figure 4.13 panel C) with an increasing AUP concentration, and consequently, the crosslinking density, as well as a decrease in the ultimate strain which agrees with results reported in the literature [312,313]. Indeed, similar behaviour was observed for PVA-based hydrogels, where the modulus increased from 1.53 ± 0.16 MPa to 6.66 ± 0.29 MPa depending on the polymer concentration and salt content [313]. Comparable concentration-dependent stiffening was also reported for collagen and fibrin hydrogels, whose compressive modulus ranged from approximately 2 kPa to 9 kPa and 1 kPa to 6 kPa, respectively, as the polymer content increased [312].

Overall, it is evident that the Young's modulus is higher for AUP2K DA as compared to AUP4K DA, as shown in Figure 4.13 panel C. This is again due to the higher crosslinking density for the lower molar mass AUP. Conversely, AUP4K DA hydrogels thus exhibit a larger stretchability than AUP2K DA.

The ultimate strength of the scaffolds showed an increase up to a 60 wt% concentration for both AUPs, followed by a decrease (Figure 4.13 panel D). This trend has previously been observed for other hydrogels and is likely due to an increased brittleness due to the presence of more crosslinking points, which enhances friction between polymer chains [313,314]. According to Liu et al. [313], the tensile strength of the PVA

hydrogels showed a concentration-dependent trend. As the PVA concentration increased from about 3 wt% to 7.5 wt%, the tensile strength rose markedly, from roughly 6.5 ± 0.7 MPa to 26.7 ± 1.0 MPa. Beyond this optimal range, however, further increases in polymer content led to a slight decrease or plateau in tensile strength, attributed to reduced chain mobility and increased internal friction within the more densely crosslinked network. In agreement with our observations on AUP scaffolds, another study reported a similar trend in their zwitterionic double-network hydrogel. As shown in their results, the tensile strength at break first increased, reaching a maximum of 1.05 MPa for the optimal PAC-2 composition. However, further addition of CBMAE led to a gradual decrease in tensile strength (down to ≈ 0.8 MPa), as the network became overly rigid and brittle, reducing chain mobility and extensibility [314]. Indeed, forming a denser polymer network resulted in a reduction in water content (see Figure 4.12) and caused chain stiffening. This produced a brittle polymer network because the highly extended polymer chains lacked the ability to deform before fracturing [315].

Comparing our data with reported compressive properties of soft biological tissues, the measured Young's modulus values of the AUP scaffolds fall within the range of load-bearing soft tissues. Highly compliant tissues such as adipose tissue or muscle typically exhibit Young's moduli below 0.1 MPa, whereas denser connective tissues such as ligaments and tendons show compressive moduli on the order of ~0.1–1 MPa under transverse loading conditions [316,317]. Articular cartilage, which experiences sustained compressive loading in the knee joint, displays compressive (aggregate) moduli typically ranging from ~0.2 to 2 MPa, depending on strain level, loading rate, and hydration state [318,319]. In this context, the AUP materials display mechanical properties that overlap with cartilage and extend toward

the lower range reported for human menisci [59,68]. Compression tests on human menisci have reported Young's modulus values ranging from 0.97 to 19 MPa (calculated between 12 and 20% strain). Here, AUP4K DA values ranged from 0.43 to 1.93 MPa, while AUP2K DA values ranged from 0.57 to 3.95 MPa. Although these values suggest encouraging proximity to cartilage-like behavior and partial overlap with the lower end of meniscal properties, direct comparison with literature remains difficult because mechanical outcomes are highly sensitive to sample preparation, geometry, hydration, and testing protocol. Moreover, meniscal function *in vivo* is governed by a fluid-filled, biphasic environment in which synovial fluid permeates the porous matrix; therefore, testing isolated samples in compression provides only an approximation of physiological behaviour.

A similar caution applies when comparing the present DLP-printed scaffolds to our previously reported AUP scaffolds produced by extrusion-based printing or injection moulding [17,140]. These approaches differ fundamentally in processing and starting material: extrusion and injection moulding typically rely on melt processing, whereas the DLP method prints from an aqueous formulation, where the presence of water effectively dilutes the final polymer network during fabrication and can result in reduced mechanical properties relative to melt-processed constructs [17]. In addition, comparison with injection-moulded AUP4K DA scaffolds is further complicated by differences in porosity: earlier scaffolds exhibited porosity in both the x–y plane and along the z direction, while within the current manuscript, the DLP-printed scaffolds are characterized by vertical porosity only. Despite these architectural differences, the scaffolds produced in this work demonstrate superior mechanical performance compared to the injection-moulded counterparts at equivalent polymer concentrations, highlighting the mechanical advantage achieved through the DLP-

derived structure and curing control [17].

4.3.5.3 Mechanical properties of AUP printed scaffolds via fatigue test

Following the compressive testing, the fatigue properties of the developed scaffolds were evaluated. Representative post-failure images of the fractured fatigue-ring specimens are provided in Figure 4.14 (panel A) alongside the cycles-to-failure data (panel B).

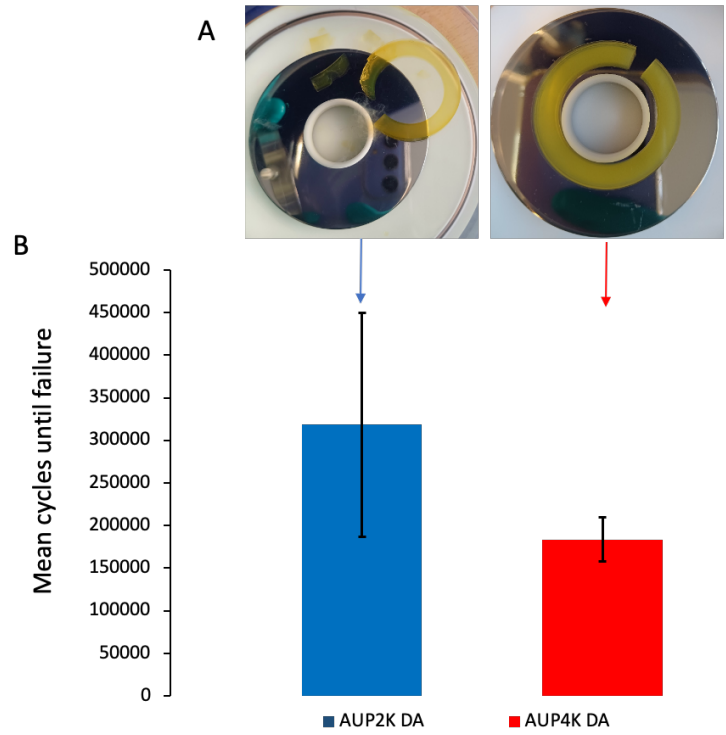

Figure 4.14: Fatigue performance of printed fatigue-ring specimens. A) Representative images of fatigue-ring specimens at failure after cyclic loading. B) Number of cycles to failure obtained from the fatigue test (bars represent mean ± SD).

After increasing the force every 50 000 cycles, the AUP2K DA material

failed after a total number of cycles of 318 396 ± 140 446 cycles while the AUP4K DA material led to a total number of cycles until failure of 183 827 ± 9732. The t-test for independent samples revealed that the AUP2K material leads to significantly more cycles until failure compared to the AUP4K DA material ($p = 0.03$). Thus, on the one hand, the AUP2K DA showed better fatigue results than the AUP4K DA material. On the other hand, the AUP2K DA material showed a much higher standard deviation compared to the AUP4K DA material. This might be due to possible small printing defects in the fatigue-ring specimen leading to broad variation in fatigue results. In both groups the main failure mechanism was a rupture of the fatigue-ring specimen at one or more locations (see Figure 4.14 panel A). The AUP2K DA specimens however, typically broke into more fragments than the AUP4K DA material. This might be due to the higher loading conditions that could be applied until failure occurred.

The higher scatter observed for AUP2K DA compared to AUP4K DA (Figure 4.14) can be attributed to the more densely crosslinked and stiffer network formed by the shorter PEG backbone (2 000 g/mol versus 4 000 g/mol). Materials with a higher crosslinking density exhibit reduced capacity for stress redistribution upon loading, rendering their mechanical response more sensitive to local microstructural variations such as minor differences in pore geometry, strut uniformity, or crosslinking homogeneity between specimens [320,321]. This is a well-documented phenomenon in polymer network mechanics, where more tightly crosslinked and brittle systems show larger specimen-to-specimen variability under mechanical testing compared to their more flexible counterparts, even when fabricated under identical conditions.

The maximum load level that was reached in the AUP2K DA group was 2500 N, which means that a maximum load of 1250 N was applied to one fatigue-ring specimen. In the AUP4K DA group the maximum load

was 1000 N, which means that a maximum load of 500 N was applied to one fatigue-ring specimen.

In an experimental study, loads between 1615 and 2104 N were measured in the medial meniscus compartment during walking [322]. Considering, that the medial meniscus absorbs approximately 58% of the load, [323] the resulting force on the medial meniscus would be between 937 and 1220 N. Therefore, the maximum applied load of 1250 N on the meniscus fatigue-rings in the current fatigue test is in a realistic range for simulating walking levels. However, an artificial meniscus needs to withstand higher loads, which can occur during other daily activities like stair descending or walking downhill [324]. In addition, an artificial meniscus needs to withstand much higher cycle numbers. Schmalzried et al. analyzed the number of gait cycles of patients having an artificial joint [325]. The mean number of gait cycles is estimated at approximately 0.9 million cycles per year, although highly active patients may reach up to 3.2 million cycles per year. Consequently, once the herein developed AUP material is further optimized to withstand higher loads (e.g., by reducing the PEG molar mass and/or implementing alternative crosslinking chemistries), high-cycle fatigue tests in the range of several million cycles will be required to assess its long-term durability under physiologically relevant conditions. In this context, reducing creep deformation is expected to improve fatigue performance, as it limits the accumulation of time-dependent strain during cyclic loading, helps preserve structural stability, and delays microdamage initiation. Increasing network stiffness is one strategy to achieve this, since a stiffer polymer network generally restricts molecular mobility, improves load transfer, and reduces creep; however, the final fatigue response will still depend on the balance between stiffness, toughness, and overall network architecture [326,327].

4.3.6 Assessment of the *in vitro* cytotoxicity of 3D printed scaffolds

The biocompatibility of (3D printed) scaffolds plays an important role in any biomedical application of polymers. Although the gel fraction of 95% is well above the threshold for all materials, we still evaluated if any toxic compounds were leaching out from our developed hydrogels. Therefore, to assess the cytotoxicity of the DLP-printed AUP discs, a live-dead and a MTS assay were performed using HFF cells via indirect contact tests. According to the ISO-10993-5 standard, cell viability should be above 70 % for a material to be considered non-cytotoxic. The hydrogels with the highest concentrations of both AUP-materials were selected for this test: a concentration of 70 and 80 wt% for respectively the AUP4K DA and AUP2K DA. Both samples were prepared using 5 mol% Li-TPOL and 0.5 mol% tartrazine as respectively photo-initiator and photo-absorber.

Evaluation of the metabolic activity of HFF cells when treated with leached medium after 1, 3 and 7 days was performed using the MTS assay, in which MTS is bioreduced to formazan by living and metabolically active cells by means of an NADPH-dependent dehydrogenase [328]. The treated cells were compared to a monolayer of HFFs incubated in non-treated culture medium. As can be seen in Figure 4.15 both AUP2K DA and AUP4K DA showed to be non-cytotoxic with a metabolic activity well over 70 %. When comparing the media of leached scaffolds after 1 day of incubation, the metabolic activity of the HFF cells treated with AUP2K DA extracts (89.13 ± 4.90 %) was significantly ($p = 0.0277$) lower than those treated with AUP4K DA (101.32 ± 4.65 %). In addition, a significant ($p = 0.0084$) decrease in metabolic activity was observed for AUP2K DA (85.68 ± 1.33 %) when compared to the control (100.00 ± 0.04 %) after 3 days of leaching. Finally, the metabolic activity of the HFF cells was

significantly ($p = 0.0401$) decreased upon treating them with 3-day leaching medium of AUP4K DA (89.80 ± 1.44 %) in contrast to 1-day leaching medium (101.32 ± 4.65 %), while recovering when leached for 7 days (96.35 ± 5.40 %). Despite some significant differences, the high metabolic activities obtained for all materials clearly indicate the absence of toxic effects.

Using Ca-AM/PI staining, the HFF cell viability and cell morphology were assessed over the course of 7 days. In this assay, no significant differences ($p > 0.05$) in terms of cell viability and cell morphology were observed between the control, AUP2K DA and AUP4K DA. All cell viabilities were constant over the 7 days, with the lowest observed viability of 96.03 ± 2.93 % for AUP2K DA after 3 days of leaching and the highest viability of 98.43 ± 0.62 % for AUP4K DA after 1 day of leaching. A slight change in cell morphology was observed for AUP4K DA after 3 days with some HFF cells no longer having their elongated shape. At present, the reason for these findings remains unclear. Importantly, this phenomenon did not reflect in a lower cell viability.

Overall, both assays showed that the *in vitro* cytotoxicity was well over 70 %, indicating the non-cytotoxic character of our hydrogels according to the ISO 10993-5:2009 standard. These herein obtained data are in line with previously obtained results on other AUP [141,142,149,154,155]. Pien *et al.* demonstrated that AUPs with short (530 g/mol [154]) and long (70 – 90 kg/mol [149]) PCL backbones are non-cytotoxic in indirect cell assays with cell viabilities well above 70 %. Similarly, AUPs with PCL backbones sizes of 2000 [155,224] and 6000 g/mol [155] were screened by Arslan *et al.* and Greant *et al.*, respectively. Minsart *et al.* investigated the cytotoxicity of AUP-PEG derivatives (2 to 20 kg/mol) after one (2, 8, 10 and 20 kg/mol) or multiple (10 and 20 kg/mol) days of leaching [141,142]. They showed that the materials were non-cytotoxic with cell viabilities over 90 %. Our results extend these observations by showing

that prolonged leaching of the lower molar mass AUP derivatives does not provoke cytotoxicity to HFF cells, further demonstrating the potential of AUP materials in the biomedical field.

Future studies will incorporate a biomimetic coating to better replicate the native meniscal environment, with literature supporting options such as ECM-based hydrogels and or mimics such as chondroitin sulphate, aggrecan or GelMA [6,140,329].

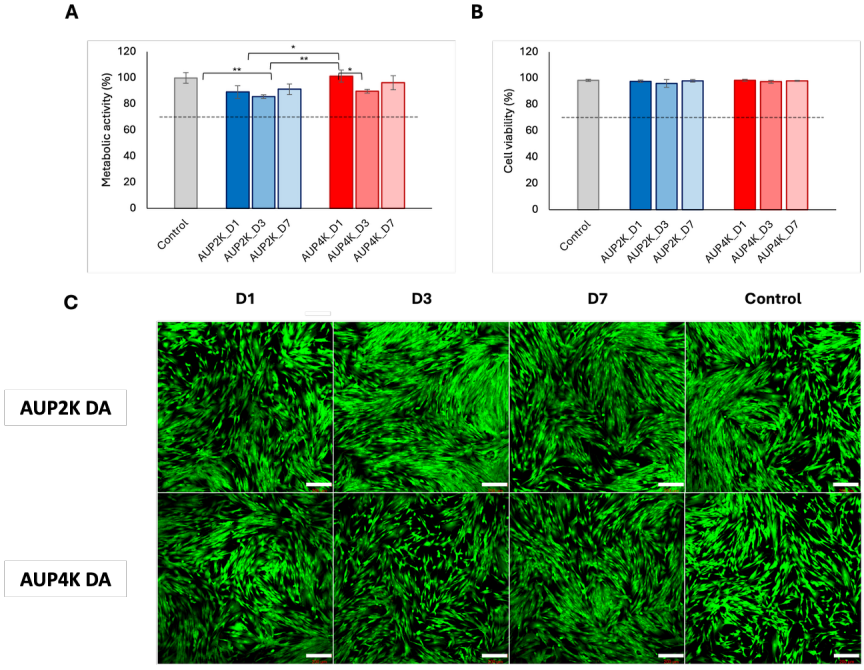

*Figure 4.15: Indirect cell viability tests of DLP-printed AUP materials using HFF cells after 1, 3 and 7 days of leaching in cell culture medium. The metabolic activity as assessed by the MTS assay is represented in panel (A). Cellular viability of HFF cells after 1,3 and 7 days of incubation is quantified in panel (B) and qualitatively presented in panel (C). HFF cells exposed for 1 day to non-treated cell culture medium were used as a positive control. According to the ISO 10993-5 standard, a viability above 70 % (dotted line in panels A and B) is required. The scale bars represent 200 µm. (*p ≤ 0.05; **p ≤ 0.01).*

4.4. Conclusions

This study successfully demonstrated the synthesis, processing, and characterization of two PEG-based acrylate-endcapped urethane prepolymers, AUP2K DA and AUP4K DA, as promising hydrogel building blocks for digital light processing (DLP) fabrication of meniscus replacement scaffolds. Both AUP scaffolds exhibited excellent photo-crosslinking capability revealing high gel fractions (>95%), for both AUP and across a wide concentration range, confirming efficient network formation and structural integrity after printing. Swelling behavior was strongly governed by formulation parameters: swelling degree decreased with increasing polymer concentration (cfr. higher crosslink density), and AUP2K DA showed lower swelling than AUP4K DA, consistent with its higher effective crosslink density at equal concentration.

(Photo-)rheology supported this molar-mass dependence of network formation. Under identical photo-initiator/-absorber conditions, AUP2K DA consistently reached higher plateau viscoelastic values than AUP4K DA (e.g., G′ = 162 070 ± 18 220 Pa at 30 wt% rising to 1 149 300 ± 61 500 Pa at 80 wt% for AUP2K DA; versus 148 730 ± 1 400 Pa at 30 wt% rising to 709 440 ± 23 200 Pa at 70 wt% for AUP4K DA), reflecting the higher density of crosslinkable end groups per mass unit in the lower-molar-mass precursor.

Additionally, mechanical testing of hydrated scaffolds confirmed concentration- and molar-mass-dependent strengthening. Compressive Young's moduli ranged from 0.57–3.95 MPa for AUP2K DA and 0.43–1.93 MPa for AUP4K DA, placing the materials in a meniscus-relevant regime and overlapping with the lower range reported for meniscal tissue. The fatigue tests showed that DLP-printed AUP scaffolds can withstand cyclic loading within a physiologically relevant force range. The AUP2K DA formulation exhibited significantly

higher fatigue resistance than AUP4K DA, sustaining several hundred thousand cycles and tolerating loads comparable to those acting on the native knee meniscus during daily activities. Despite the higher variability observed for AUP2K DA, these results indicate its promising potential for meniscus replacement applications.

Finally, biocompatibility assays validated the non-cytotoxic nature of the developed AUP-based scaffolds, showing metabolic activities and cell viabilities well above the ISO 10993-5 threshold of 70 %. These findings collectively confirm that AUP-based formulations can be reliably processed via DLP printing into robust, cytocompatible, and structurally consistent scaffolds suitable for further preclinical evaluation. Future work should focus on integrating biological functionality by incorporating extracellular-matrix components or bioactive cues to promote cellular infiltration and tissue remodelling. Moreover, designing zonal or gradient scaffolds could bridge the gap between mechanical fidelity and biological performance, advancing the translation of synthetic AUP hydrogels toward clinically relevant meniscal implants.

Together with the findings from Chapters 2 and 3, these chapter results show that scaffold performance can be modulated through both material chemistry, including functionality and backbone molar mass, and fabrication strategy. However, beyond scaffold fabrication itself, practical translation also requires consideration of post-processing steps such as dehydration, storage, and rehydration. Therefore, Chapter 5 focuses on the influence of drying techniques on the morphology and mechanical behaviour of AUP4K DA scaffolds.

Chapter 5:

Influence of Drying Techniques on the Structural and Mechanical Properties of Urethane-Based Poly(ethylene glycol) Scaffolds

This chapter evaluates the impact of four distinct dehydration protocols - desiccation, lyophilization (freeze-drying), vacuum drying, and ventilated oven drying - on the physicochemical and mechanical profile of urethane-PEG scaffolds. Specifically, we investigate how these methods dictate the final pore morphology, gel fraction, and swelling kinetics, and how these structural changes subsequently influence the material's compressive behaviour. This work was entirely conducted by M. Meazzo.

5.1 Introduction

While Chapters 2–4 focused mainly on material chemistry and scaffold fabrication, the practical translation of hydrogel-based meniscus scaffolds also requires attention to post-processing. Chapter 2 identified AUP4K DA as an extrusion-printable hydrogel platform, while Chapters 3 and 4 explored strategies to improve scaffold performance by increasing precursor functionality and decreasing PEG backbone molar mass, respectively. However, even when suitable scaffolds can be fabricated, hydrogels remain highly sensitive to dehydration and rehydration because of their high water content. Therefore, the present chapter returns to the AUP4K DA extrusion-printed scaffold system as a representative and previously characterized platform to isolate the effect of different drying methods on scaffold morphology, swelling behaviour, and compressive mechanical properties.

As discussed in Chapter 1, a functional tissue-engineered scaffold must meet several essential design requirements. Its architecture should support cell adhesion, proliferation, and extracellular matrix deposition, while an interconnected and highly porous structure enables cell infiltration and nutrient transport. Pore size must be optimized to promote tissue regeneration without pore occlusion. Finally, the scaffold should be composed of biocompatible, non-toxic materials with a predictable degradation behaviour suited to the intended application.

However, the transition from a synthesized polymer network to a functional scaffold constitutes a critical bottleneck in the journey from bench-top fabrication to clinical implementation [330]. While the initial chemical synthesis defines the fundamental covalent framework of the urethane-PEG network, the subsequent processing steps determine the material's ultimate viability for sterilization, long-term storage, and surgical handling. A functional scaffold must maintain a delicate

balance: it must be robust enough for long-term shelf stability while retaining the intrinsic capacity to recover its biomimetic, hydrated state upon implantation into the joint space [331].

From a translational perspective, dehydration is essential for extending shelf life, ensuring long-term storage stability, and facilitating sterilization protocols [332]. Based on the exact chemical structure, some hydrogels in their fully hydrated state are prone to hydrolysis, unintended degradation, and microbial growth, which limit their viability for off-the-shelf surgical use [333]. Furthermore, dried scaffolds are significantly easier to handle, transport, and package compared to their "wet" counterparts [334]. Ideally, the hydrogel should be capable of recovering its original structure and functional properties upon rehydration prior to use. From both translational and commercial perspectives, a key challenge lies in extending the shelf life of scaffolds while ensuring that processing do not compromise their intended performance [335].

However, the removal of the liquid phase is a high-energy process that introduces capillary forces, which can lead to significant structural alterations such as pore collapse, surface "skinning," or internal stresses [336]. These morphological changes directly affect the physicochemical response of the scaffolds, particularly the swelling degree and the measured gel fraction, which are relevant to how the scaffolds rehydrate and interact with physiological fluids *in vivo*. Furthermore, the mechanical performance, characterized by among other the compressive Young's modulus, is inextricably linked to the density and porosity resulting from the drying pathway [337].

In the field of tissue engineering, several dehydration strategies have been employed to improve the stability and shelf life of hydrogel-based scaffolds prior to clinical use. Among these, freeze-drying (lyophilization) is the most widely adopted approach, as it enables

efficient water removal while often preserving much of the original scaffold architecture. In addition, freeze-drying is widely used as a pore-forming strategy, since ice crystal formation during freezing can generate a highly porous microstructure with good rehydration capacity, making this method particularly suitable for off-the-shelf applications [335,338]. Oven-based drying methods, including ventilated and vacuum oven drying, have also been explored due to their simplicity and scalability; however, these approaches may induce pore collapse, densification, or changes in mechanical behaviour if temperature and pressure are not carefully controlled [335,339]. Ambient or desiccant drying represents a low-cost alternative; however, these evaporative drying approaches often promote shrinkage and densification of the scaffold structure, which may compromise structural fidelity and make them less suitable for highly porous scaffolds [340]. More advanced techniques, such as supercritical CO_2 drying, have been proposed to minimize capillary stresses during dehydration and better preserve delicate porous networks, although their higher complexity and cost restrict widespread adoption [341].

This chapter investigates four different dehydration strategies: desiccation, lyophilization (freeze-drying), vacuum oven drying, and ventilated oven drying. The structural integrity of the scaffolds following each drying treatment is first assessed using scanning electron microscopy (SEM). These images confirmed that the overall scaffold architecture was preserved across all treatment protocols. However, a systematic quantitative analysis of dimensional accuracy (e.g. strut diameter and pore size measurements before and after treatment) was not performed in this study. The primary objective of this chapter was to evaluate the effect of the post-processing protocols on the mechanical and biological performance of the scaffolds, rather than to conduct a full geometric fidelity assessment. It is acknowledged that

quantifying potential dimensional changes resulting from the dehydration–rehydration cycles and sterilization treatments would provide valuable additional insight, and this is recommended as a direction for future investigation.

Subsequently, the dried scaffolds are evaluated in terms of their structural properties through swelling degree and gel fraction measurements, as well as their mechanical performance via compressive testing. Through this comparative approach, the study aims to identify the drying method that best preserves the mechanical properties and scaffold morphology, thereby maintaining an architecture suitable for meniscus replacement applications.

5.2 Materials and Methods

5.2.1 Materials

Poly(ethylene glycol) (PEG, molar mass of 4000 g/mol), phosphoric acid, isophorone diisocyanate (IPDI), phenothiazine (PTZ) and triphenylphosphite (TPP), lithium bromide (LiBr) butanone, petroleum eher were purchased from Merck. Bismuth neodecanoate (Valikat BI 2021) was purchased from Shepherd. Butylated hydroxytoluene was bought from Innochem GmbH and Bisomer PEA-6 from Geo Specialty Chemicals. Deuterated chloroform (CDCl3) was purchased from Euriso-Top. Printing needle (25 gauge) was purchased from DL technology. Other materials used included 2,4,6-trimethylbenzoyl)-phenyl-phosphinic acid ethyl ester (commercially known as Speedcure TPO-L) from Lambson, and the filter paper 424 from VWR Europe (pore size: 125 mm). All materials were used as received.

5.2.2 Methods

5.2.2.1 Synthesis of acrylate-endcapped urethane-based poly(ethylene glycol) precursors

The AUP-PEG4K-6EO-DA (AUP4K DA) was synthesized as described in literature and in Chapter 2 and further [143,148,150].

5.2.2.2 Photo initiator synthesis

The synthesis of Li-TPO-L was performed analogous to patent literature and described in Chapter 3 [258].

5.2.2.3 Extrusion-based 3D printing

The photo-initiator Li-TPOL (2 mol% relative to the acrylate concentration) was added in the AUP material before the printing process. In this chapter, the Li-TPOL concentration was reduced again to 2 mol%. Unlike the DLP process described in Chapter 4, the scaffolds in this chapter were fabricated by extrusion-based printing

and subsequently crosslinked using the external UV irradiation setup. Under these conditions, the light intensity and exposure conditions were sufficient to obtain photo-crosslinked AUP4K DA scaffolds without requiring the higher photo-initiator concentration used for DLP printing. Therefore, 2 mol% Li-TPO-L was selected to maintain efficient crosslinking while avoiding unnecessary excess of photo-initiator in the hydrogel network.

Porous cylindrical AUP scaffolds (dry dimensions: 5 mm height, 10 mm diameter) were fabricated using a Bioscaffolder® system (Sys-Eng, Germany), following the procedure described in Chapter 2. A strut diameter of 400 ± 20 µm and a pore size of 250 ± 20 µm were selected based on the outcomes of Chapter 2, as this architecture provided an optimal balance between mechanical performance, print fidelity - minimizing strut merging during filament deposition - and high gel fraction. In addition, previous results demonstrated that further increases in strut diameter did not lead to improvements in mechanical properties. [17]

Table 5.1 presents a summary of the printing parameters employed for generating AUP4K DA scaffolds with the aforementioned strut and pore size.

Table 5.1: Overview of the printing conditions employed for scaffold fabrication, including key parameters such as printing temperature, deposition speed, layer height, and strand spacing. These parameters were systematically optimized to achieve the targeted scaffold architecture, ensuring adequate structural stability and controlled porosity.

Scaffold printing pattern	**0°/90°**
Needle type	25 gauge
Temperature	57 C°
Layer thickness	0.12 mm
Strand distance	0.67 mm
Plotting speed	270 mm/min
Screw spindle speed (S)	280 rpm
Dispensing pressure	5 bar

The printed AUP4K DA scaffolds were subsequently crosslinked under UV-A for 30 minutes (lamp intensity of 10 mW/cm^2 at top and bottom).

5.2.2.4 Gel fraction and swelling capacity of AUP scaffolds

The procedure to calculate the gel fraction and swelling capacity were applied as described before in Chapter 2.

5.2.2.5 Drying of AUP scaffolds

Four different drying protocols were investigated in this study: freeze-drying, desiccator drying, ventilated oven drying, and vacuum oven drying. Freeze-drying (lyophilization) was performed using a Christ Alpha 2–4 LSC freeze-dryer at −85 °C and 0.37 mbar for 24 h, after which the samples were removed and weighed. Desiccator drying was carried out following the procedure described in Chapter 2; briefly, the

scaffolds were placed in a silica gel–filled desiccator and subsequently kept overnight in a drying chamber (FD 23, Binder) at 40 °C.

Ventilated oven drying was performed at 40 °C for 24 h under ambient pressure. Vacuum oven drying was carried out at 35 °C under reduced pressure. Since the scaffolds remained visibly wet after 24 h in the vacuum oven, the drying time was extended to 48 h to ensure complete dehydration before final weighing. After completion of each drying protocol, the scaffolds were reweighed in their dry state and the final dry mass was recorded for all batches. As the temperature and drying duration were adjusted to achieve complete drying under each oven condition, the comparison between both methods should be interpreted as a comparison between practical drying protocols rather than as the isolated effect of vacuum alone.

5.2.2.6 Static compression test of AUP scaffolds

Static compression tests were performed on AUP4K DA scaffolds in the swollen state. After printing, the scaffolds were UV-crosslinked for 30 min (lamp intensity 10 $mW \cdot cm^{-2}$ at top and bottom) and subsequently immersed in double-distilled water for 72 h at 19 °C to remove unreacted species, with the medium refreshed every 24 h. The purified scaffolds were then subjected to one of the drying protocols described above. Following dehydration, each batch was rehydrated in double-distilled water for 24 h to ensure complete swelling prior to mechanical testing.

Compression tests were conducted using a Tinius Olsen 5ST equipped with a 500 N load cell. A low crosshead speed of 2 $mm \cdot s^{-1}$ was selected to account for the viscoelastic behaviour of the material, and a preload of 0.3 N was applied in accordance with internal laboratory protocols.

5.3 Results and Discussion

As discussed in Chapter 1, hydrogels provide a highly hydrated three-dimensional environment that can be engineered to replicate key chemical and structural features of native meniscal tissue. Both natural and synthetic hydrogel systems have been extensively explored for meniscus repair due to their biocompatibility and tunable physicochemical properties [107,222].

In previous chapters, PEG-based acrylated urethane prepolymers (AUPs) with varying molar masses were evaluated as potential meniscal substitutes. Among these, the AUP4K DA formulation demonstrated compressive mechanical properties comparable to those of the native human meniscus and was therefore selected for further investigation in the present chapter [17].

5.3.1 Hydrogel building block synthesis

The PEG-based acrylated urethane prepolymer used in this study (AUP4K DA) was synthesized as described in Chapter 2 via the reaction of PEG (M_n = 4000 g·mol^{-1}) with IPDI, followed by chain extension with a monoacrylated oligo(ethylene glycol) spacer. Detailed structural characterization by FTIR and ^{1}H NMR, including polymer structures and spectra, is provided in Chapter 2 and 4 and is not repeated here. Briefly, AUP4K DA exhibited an acrylate content of 0.37 mmol·g^{-1}, as determined by ^{1}H NMR using dimethyl terephthalate as an internal standard, and a calculated molar mass of 5570 g·mol^{-1}.

5.3.2 Structural characterization of AUP4K DA scaffolds

Consistent with the approach described in Chapter 2, scaffolds printed using a 0°/90° laydown pattern with strut diameters of 400 ± 20 µm and pore sizes of 250 ± 20 µm were selected as the reference architecture.

For each experimental batch, at least three scaffolds were fabricated under identical printing conditions using material from the same batch. Following optical microscopy inspection, cylindrical scaffolds printed on the same day were subjected to different drying protocols prior to swelling and gel fraction analyses. The dried samples were subsequently examined by SEM to assess structural integrity. In parallel, separate batches of scaffolds were used for compressive testing to evaluate the influence of the drying methods on mechanical performance.

An example of printed scaffold with the aforementioned strut and pore size is depicted in Figure 5.1. Unless otherwise specified, all images in this chapter were acquired in top-down view, with the viewing direction perpendicular to the printing plane (along the build direction)

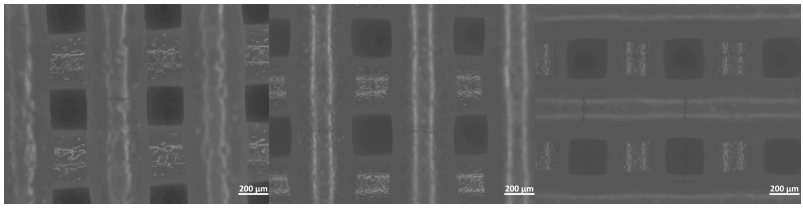

Figure 5.1: Optical microscopy images (5X magnification) of AUP4K DA scaffolds printed using the Bioscaffolder device. For all scaffolds, the strut diameter and the pore size are respectively 400 µm (± 20 µm) and 250 µm (± 20 µm). The scale bars are indicated on each figure.

5.3.3 Comparative SEM Visualization: The Impact of Drying on Scaffold Architecture.

After 3D printing the scaffolds, as described in § 5.2.2.3 and subsequent UV crosslinking, the scaffolds were subjected to a 72-hour washing protocol in double-distilled water to remove unreacted species, as described in § 5.2.2.5. During this purification step, the washing medium was refreshed every 24 hours. The purified scaffolds were then dried using four different dehydration strategies - desiccation, lyophilization, vacuum oven drying, and ventilated oven drying - to evaluate their influence on the final scaffold architecture.

As shown in Figure 5.2, scanning electron microscopy (SEM) demonstrates that the selected drying method plays a decisive role in defining both surface morphology and internal strut morphology of the 3D-printed scaffolds.

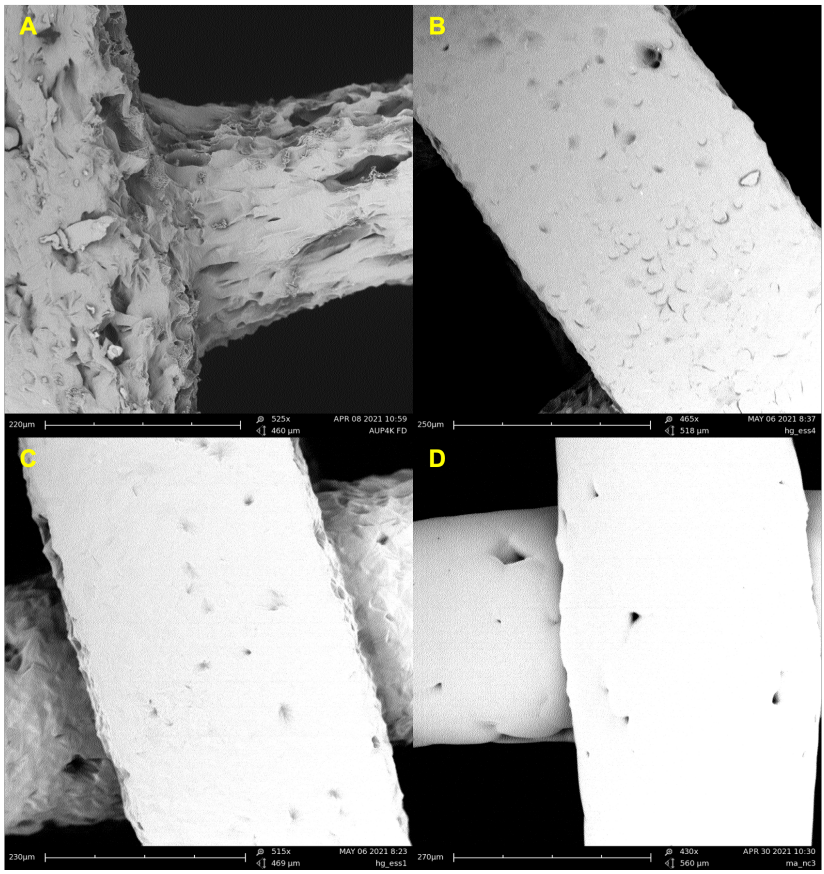

Figure 5.2: Scanning electron microscopy (SEM) images of AUP4K DA scaffold struts after dehydration using different drying protocols: (A) freeze-drying, (B) desiccator drying, (C) ventilated oven drying, and (D) vacuum oven drying. Distinct differences in surface morphology and strut integrity are observed depending on the drying method, highlighting the strong influence of dehydration strategy on the final scaffold microarchitecture.

For freeze-dried scaffolds (Figure 5.2 panel A), the strut surface appears highly rough, irregular, and porous, with visible lamellar features, i.e. thin plate-like layered structures, and microvoids distributed throughout the strut surface. This morphology is characteristic of lyophilization, and is consistent with the known pore-forming effect of this dehydration method, in which ice crystals formed during freezing act as porogens and their subsequent sublimation

generates an open, textured network [342–344]. From a tissue engineering perspective, this roughened surface may also be advantageous for cell attachment and integration, as increased surface area and topographical cues are known to promote cell–material interactions [345–348].

In contrast, the desiccator (Figure 5.2 panel B), ventilated oven–dried (Figure 5.2 panel C) and vacuum oven–dried samples (Figure 5.2 panel D) scaffolds display smoother, denser strut surfaces with fewer visible pores than the freeze-dried scaffolds. The absence of the pore-forming ice templating effect associated with freeze-drying, resulting in a less textured and less visibly porous surface morphology.

Overall, Figure 5.2 shows that the dehydration method strongly affects scaffold morphology. Freeze-drying generated a rough, highly porous, and lamellar strut surface due to its pore-forming mechanism, but this also indicates that the original printed structure was altered during processing. Such structural modification may be detrimental to the mechanical integrity of the scaffolds and could increase the risk of mechanical failure. In contrast, the other drying methods resulted in smoother and more uniform strut surfaces. Together, these observations highlight the important role of the dehydration strategy in determining the final structural and functional properties of hydrogel-based scaffolds.

5.3.4 Gel fraction and swelling degree of dried AUP4K DA scaffolds

The swelling degree and gel fraction of the AUP4K DA scaffolds were calculated with the formula present in Chapter 2. The results are displayed in Figure 5.3.

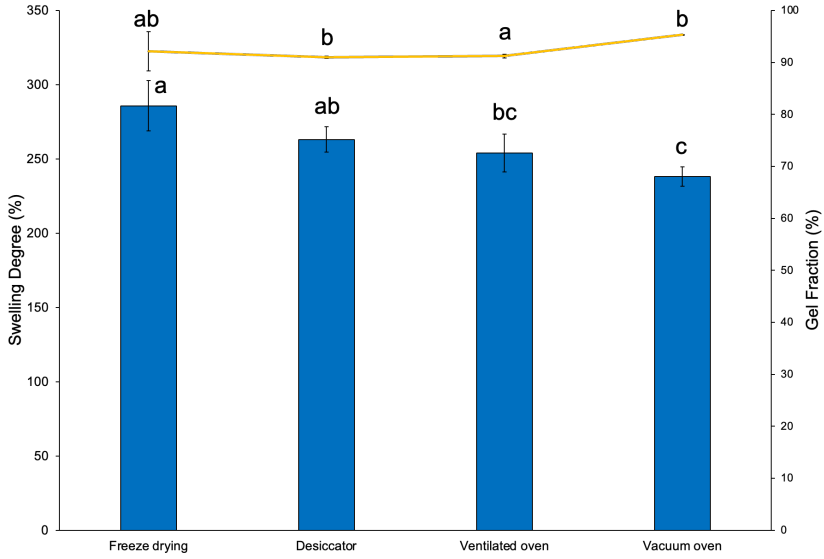

Figure 5.3: Swelling degree (SD) and gel fraction (GF) of AUP4K DA scaffolds dried using different drying methods (n = 4). Data are presented as mean ± SD. Different letters indicate significant differences between groups; bars sharing at least one common letter are not significantly different (p > 0.05) according to one-way ANOVA followed by Tukey's HSD post-hoc test.

The swelling degree of the AUP4K DA scaffolds were influenced by the applied drying protocol, whereas the gel fraction remained high for all conditions. Statistical analysis confirmed that the drying protocol significantly affected both swelling degree and gel fraction; however, the effect was much more pronounced for swelling degree, while only limited pairwise differences were observed for gel fraction. After 72 h of swelling, freeze-dried scaffolds exhibited the highest swelling degree, which can be attributed to the increased internal porosity generated by ice crystal formation during freezing and subsequent sublimation, as shown in Figure 5.2. In lyophilized hydrogels, ice crystals act as porogens, producing voids within the polymer network and effectively reducing the solid fraction of the scaffold, thereby amplifying the apparent swelling ratio when normalized to dry mass. This effect has been widely reported for freeze-dried hydrogel systems

and does not necessarily reflect increased chemical swelling, but rather a combination of enhanced pore volume and reduced polymer density [342,349].

In contrast, scaffolds dried in a desiccator, ventilated oven, or vacuum oven exhibited lower swelling degrees, consistent with their smoother and less visibly porous strut morphology. Despite these differences in swelling behaviour, all samples displayed high gel fraction values (>91%), confirming effective network formation in all cases. Since the drying step was performed after UV crosslinking, the gel fraction was not expected to be affected by the drying protocol. Overall, these results indicate that the dehydration strategy mainly influences the measured swelling behaviour of the scaffolds through changes in dry-state morphology and porosity, while the underlying crosslinked network remains preserved. The slightly higher gel fraction measured for vacuum oven–dried scaffolds should not be interpreted as a true change in network formation, since the drying step was performed after UV-induced crosslinking and was therefore not expected to affect the true covalent gel fraction of the polymer network. In the present study, gel fraction was determined gravimetrically from the mass retained after swelling and re-drying. Consequently, the small differences observed between groups are regarded as apparent differences in mass retention after the swelling procedure, rather than as changes in the underlying crosslinked network.

5.3.5 Static compression measurements of AUP4K DA scaffolds

As discussed in Chapter 1, the compressive properties of the human meniscus are critical for proper knee joint function [11]. Moreover, numerous studies on hydrogel systems have demonstrated that the chosen drying method can significantly influence the mechanical

properties, underscoring the importance of systematically evaluating these effects [344,350,351].

Therefore, in addition to swelling and gel fraction analyses, compressive mechanical testing was performed to evaluate how the different drying protocols influence the mechanical behavior of the scaffolds after hydration. Following dehydration, the scaffolds were rehydrated in double-distilled water for 24 h prior to testing to ensure equilibrium swelling of the hydrogel network. Compression tests were then conducted on the rehydrated samples to directly compare the mechanical response of scaffolds subjected to desiccation, freeze-drying, ventilated oven drying, and vacuum oven drying. This approach enabled assessment of the extent to which drying-induced structural differences persist after hydration and affect the mechanical performance of the scaffolds.

The results are shown in Figure 5.4.

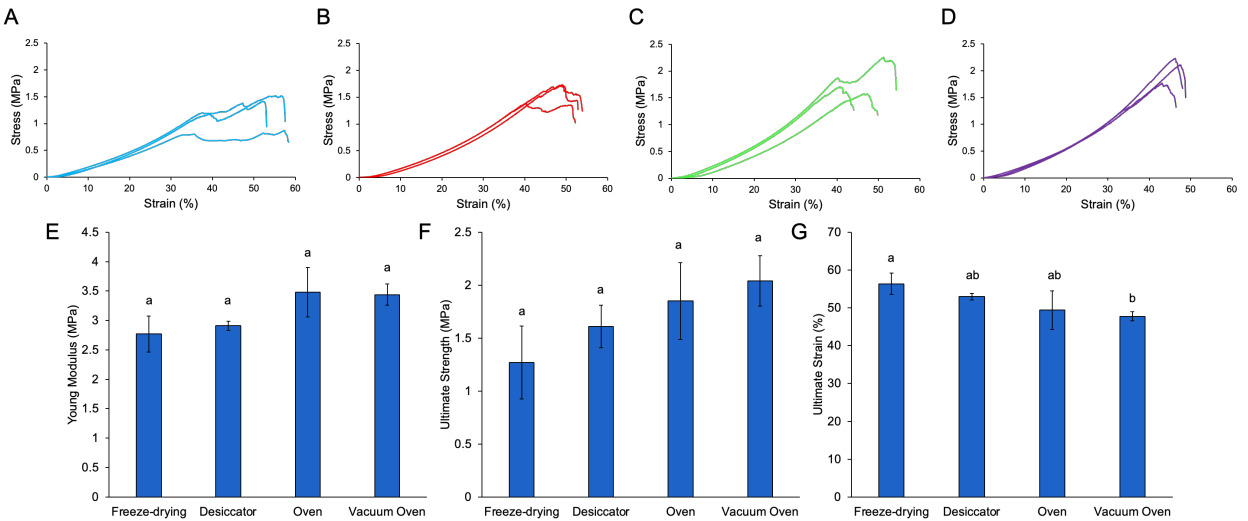

Figure 5.4: Compressive mechanical behaviour of AUP4K DA scaffolds after dehydration using different drying protocols and subsequent rehydration in double-distilled water for 24 h. The water-swollen scaffolds were compressed at a speed of 2 mm.min-1, and a preload speed of 0.5 mm.min-1. A) Freeze-dried, B) desiccator-dried, C) ventilated oven-dried, and D) vacuum oven-dried scaffolds. The data in panels E) to G) represent the Young's moduli, the ultimate strength and the ultimate strain values. These values are calculated starting from the obtained stress-strain curves. The Young modulus is calculated as the slope of the curve between 10-20% strain (n=3) Different letters indicate significant differences between groups; bars sharing at least one common letter are not significantly different ($p > 0.05$) according to one-way ANOVA followed by Tukey's HSD post-hoc test.

The compressive stress–strain curves reveal clear differences in mechanical behaviour as a function of the applied drying protocol, which closely correlate with the SEM observations. In particular, freeze-dried (FD) scaffolds showed reduced resistance to compressive loading and earlier deviation from linear elastic behaviour, indicating mechanically weaker structures compared to the oven-dried counterparts [332,352]. This reduced mechanical resistance is consistent with the highly porous, irregular strut morphology observed by SEM, where ice-templating during freeze-drying generates internal voids and surface roughness that reduce the effective load-bearing cross-section. Although this open microstructure enhances swelling capacity, it compromises mechanical integrity under compression [352,353]. In contrast, oven-dried scaffolds displayed higher compressive moduli than the freeze-dried and desiccator scaffolds, although no significant pairwise differences were detected for Young's modulus in the Tukey post-hoc analysis. Vacuum oven–dried scaffolds showed the highest compressive resistance, with a significantly higher ultimate compressive strength than the freeze-dried scaffolds [352]. For ultimate compressive strength, however, vacuum oven–dried scaffolds were significantly stronger than freeze-dried scaffolds, while desiccator- and ventilated oven–dried scaffolds showed intermediate values that were not significantly different from either group.

Overall, these results demonstrate that while freeze-drying preserves and induces porosity and swelling capacity, it yields mechanically weaker scaffolds, underscoring the trade-off between microstructural openness and load-bearing performance governed by the dehydration strategy.

As a reference, scaffolds fabricated with the same porosity and strut size but not subjected to any drying step—printed, UV-crosslinked, and swollen in double-distilled water for 72 h—exhibited a Young's modulus

of 3.32 MPa, an ultimate compressive strength of 1.87 MPa, and an ultimate strain of 47.2%, as described in Chapter 2. When compared to these baseline values, freeze-dried scaffolds displayed a lower Young's modulus, consistent with the reduced stiffness observed in the stress–strain curves. This decrease can be attributed to the highly porous, ice-templated microstructure identified by SEM, which reduces the effective load-bearing cross-section despite full rehydration. In contrast, scaffolds dried using desiccator, ventilated oven, or vacuum oven methods exhibited Young's modulus values closer to, or in some cases exceeding, those of the reference hydrated scaffolds. Regarding the statistical relevance of the post-processing treatments on mechanical performance (Figure 5.4), the results present a nuanced picture. For the Young's modulus, the one-way ANOVA indicated overall statistical significance across drying conditions; however, the subsequent Tukey post-hoc analysis did not resolve pairwise differences between individual treatment groups. This outcome indicates that while a global effect of the drying protocol on scaffold stiffness exists, the magnitude of the pairwise differences is small relative to the within-group variability, placing them below the detection threshold of the post-hoc test. For the ultimate strain, no statistically significant differences were identified. From a practical standpoint, this finding carries a positive implication for the clinical translation of these scaffolds: the mechanical performance of the AUP hydrogels is largely preserved across the investigated post-processing protocols, suggesting that the material is tolerant to different dehydration–rehydration and sterilization conditions without substantial loss of mechanical integrity. This robustness is a desirable property for a scaffold intended for surgical application, where storage, transport, and handling conditions may vary between clinical settings. To be more specific, the Young's modulus changed from 3.32 MPa for the hydrated reference to 2.91 MPa, 3.49 MPa, and 3.44 MPa for the desiccator-,

ventilated oven–, and vacuum oven–dried scaffolds, respectively. Similarly, the ultimate compressive strength changed from 1.87 MPa for the hydrated reference to 1.61 MPa, 1.85 MPa, and 2.04 MPa, while the ultimate strain shifted from 47.2% to 52.97%, 49.4%, and 47.77%, respectively. In particular, ventilated oven–dried scaffolds exhibited the highest Young's modulus, while vacuum oven–dried scaffolds showed the highest ultimate compressive strength. Only the increase in ultimate compressive strength for vacuum oven–dried scaffolds relative to freeze-dried scaffolds was statistically significant, whereas the remaining groups were not significantly different from one another. Overall, these findings indicate that, compared with freeze-drying, the non-freeze-dried scaffolds better retained the compressive performance of the hydrated reference after rehydration.

Consistent with previous results, the rehydrated scaffolds display mechanical properties within the reported meniscal range [54,58,59].

5.4 Conclusion

In conclusion, this chapter demonstrates that the dehydration pathway constitutes a critical processing parameter governing the structural, physicochemical, and mechanical performance of urethane-based PEG scaffolds. While freeze-drying effectively preserves a highly porous microarchitecture and maximizes swelling capacity through ice-templated porosity, it also leads to a reduction in compressive stiffness due to decreased effective load-bearing capacity. In contrast, oven-based drying methods resulted in lower swelling degrees while better preserving the compressive performance of the scaffolds after rehydration. Although small differences in measured gel fraction were observed between groups, all values remained high, confirming effective network formation irrespective of the drying protocol. Importantly, despite the morphological and physicochemical differences introduced by dehydration, all scaffold variants retained compressive properties within the range reported for native meniscal tissue after rehydration, underscoring the robustness of the AUP4K DA material platform. Collectively, these findings highlight a trade-off between porosity-driven hydration behaviour and mechanical performance, emphasizing that the choice of drying strategy must be carefully tailored according to the intended balance between swelling behaviour, and functional scaffold integrity for meniscus scaffold applications.

Chapter 6:

General conclusion and future perspectives

This chapter will consolidate the main findings of this thesis and provide an integrated conclusion on the development of hydrogel-based, 3D printed AUP scaffolds for full meniscus replacement. It will synthesize how polymer design (PEG molar mass and functionality), formulation parameters (concentration and crosslinking conditions), and manufacturing route (extrusion printing, indirect injection moulding, and DLP) collectively govern scaffold architecture, crosslinking efficiency, swelling behavior, and mechanical performance. Finally, this chapter will discuss the key remaining limitations - particularly cyclic durability - and outline concrete perspectives for future research aimed at improving fatigue resistance, introducing meniscus-mimicking anisotropy, and advancing translational steps such as storage/sterilization and biological validation.

Meniscal tears remain among the most frequent orthopaedic injuries and, when irreparable, are commonly treated by partial or total meniscectomy. Although this approach can provide short-term symptom relief, it disrupts load distribution within the knee joint and is strongly associated with the onset and progression of osteoarthritis. Consequently, there is a clear clinical need for off-the-shelf meniscus substitutes that can restore load transfer, shock absorption, and joint stability while remaining compatible with surgical handling and long-term function.

This doctoral research aimed to develop a tunable, synthetic, hydrogel-based scaffold platform for full meniscus replacement, relying on photo-crosslinkable acrylate-endcapped urethane PEG (AUP) macromers and additive-manufacturing-enabled architecture control. The central hypothesis of this thesis was that the combination of (i) controllable polymer network chemistry (via PEG molar mass, end-group functionality, and concentration), (ii) controllable scaffold microarchitecture (via strand/pore dimensions and printing pattern), and (iii) controllable processing routes (direct extrusion printing, indirect injection moulding, and vat photopolymerization) would enable the fabrication of meniscus-mimicking scaffolds with high crosslinking efficiency, reproducible porosity, and mechanical properties within (or approaching) the relevant range for meniscal tissue.

To this end, the following objectives were accomplished in the scope of this work:

- Developed a synthetic, photo-crosslinkable hydrogel material platform suitable for meniscus-oriented scaffold fabrication.

    - Acrylate-endcapped urethane PEG (AUP) macromers were used to build stable hydrogel networks, with formulation knobs that allow systematic tuning.
- Established structure–processing–property relationships to tune hydrogel/scaffold performance.
    - The effects of PEG molar mass (AUP2K DA vs AUP4K DA), polymer concentration, and end-group functionality (DA vs higher functionality) were explored and linked to swelling, gel fraction, crosslinking behavior, and mechanics.
- Demonstrated manufacturability of porous scaffolds via multiple fabrication routes.
    - The work validated AUP scaffold production by (i) direct extrusion-based printing, (ii) an indirect injection-moulding strategy enabling lateral porosity, and (iii) DLP printing enabling high-resolution lattices and improved geometric fidelity.
- Achieved controlled and reproducible scaffold architectures relevant for meniscus replacement.
    - Printing patterns, strand/pore dimensions, and lattice designs (including vertical porosity in DLP and lateral porosity via moulding) were used to control pore connectivity and structural reproducibility.
- Performed a comprehensive physicochemical and thermal characterization of printed scaffolds.
    - Gel fraction and swelling were used to assess network formation and water uptake, while TGA/DSC provided thermal stability/transition insights across formulations and processing routes.
- Quantified mechanical performance under conditions relevant to meniscal loading and identified the key limitation.

    - Static compression testing and cyclic/fatigue screening were implemented to benchmark performance and reveal fatigue resistance as the primary remaining bottleneck for translation.
- Addressed a practical translational need: dehydration of hydrogel scaffolds.
    - Multiple drying methods were compared, demonstrating that the dehydration route strongly affects morphology, swelling/gel fraction, and post-rehydration compressive behaviour.
- Provided initial biocompatibility screening to support future biological validation.
    - Preliminary cytocompatibility was assessed (indirect assays), supporting further development toward meniscus tissue engineering studies.

Indeed, across Chapters 2–5, the work established structure–processing–property relationships for urethane-PEG AUP hydrogels and demonstrated that these materials can be shaped into porous scaffolds using multiple manufacturing strategies. The main outcomes are summarized below, followed by an integrated conclusion and perspectives for future research.

Chapter 1 provided the clinical and biomechanical context for meniscus replacement and reviewed biomaterials and additive manufacturing strategies suitable for soft load-bearing tissues. It highlighted the anisotropic and viscoelastic nature of the native meniscus, the broad variability in reported mechanical properties due to test methodology and sample preparation, and the importance of combining appropriate chemistry with an architecture capable of supporting fluid-mediated load transfer and long-term cyclic loading.

Chapter 2 demonstrated that AUP4K can be processed via extrusion-based 3D printing into scaffolds with high crosslinking efficiency and a broad tunability of mechanical properties through architectural parameters. Importantly, the printing pattern and the strut/pore dimensions were shown to be decisive levers: (i) more isotropic patterns (0°/90° and 0°/45°/90°/135°) outperformed the 0°/45° pattern under compression, and (ii) reducing pore size and increasing strut diameter improved compressive properties up to plateau values. In the optimized 0°/90° configuration, compressive Young's moduli of approximately 2.9–3.3 MPa were obtained, with ultimate strength values of about 1.17–2.01 MPa and ultimate strains of ~39–48%. Dynamic mechanical analysis further indicated a viscoelastic response compatible with orthopaedic loading frequencies. However, the fatigue assessment revealed premature failure (before 200,000 cycles), identifying cyclic durability as the key bottleneck for clinical translation and motivating subsequent material/process exploration.

Chapter 3 expanded fabrication flexibility by developing a customized indirect rapid prototyping route (injection moulding into a sacrificial 3D-printed mould) to obtain scaffolds with lateral porosity - an architectural feature that is difficult to access by conventional direct extrusion printing. Two AUP4K variants were compared: a diacrylate end-capped version (AUP4K DA) and a higher-functionality analogue (AUP4K HA) with an increased number of photocrosslinkable groups. Both scaffold types showed concentration-dependent stiffening (increasing Young's modulus and ultimate strength with increasing AUP concentration, and decreasing ultimate strain), consistent with an increasing crosslinking density and reduced swelling. Across concentrations, AUP4K HA generally provided higher stiffness than AUP4K DA, while AUP4K DA retained higher extensibility. Overall, the indirect method validated that AUP hydrogels can be processed into

interconnected architectures beyond the constraints of direct printing, while preserving the ability to tune mechanics through both polymer chemistry and - concentration.

Chapter 4 translated the AUP platform to high-resolution vat photopolymerization (digital light processing, DLP) by formulating visible-light-curable resins and printing regular lattice scaffolds with controlled, reproducible porosity. Two PEG molar masses (AUP2K DA and AUP4K DA) were compared. The results confirmed that decreasing the PEG molar mass increases crosslinking density and stiffness: AUP2K DA scaffolds exhibited higher compressive moduli than AUP4K at comparable conditions. In the reported concentration range, AUP4K compressive Young's moduli ranged from ~0.43 to 1.93 MPa, while AUP2K ranged from ~0.57 to 3.95 MPa. For both materials, the moduli increased with concentration, while the ultimate strain decreased; the ultimate strength increased up to an intermediate concentration (~60 wt%) and then decreased at higher concentrations, consistent with the emergence of brittleness in more densely crosslinked networks. In this Chapter, a dedicated cyclic-loading approach using ring specimens revealed that the AUP2K DA material failed after 318,396 ± 140.446 cycles, whereas the AUP4K DA material reached failure after 183,827 ± 9.732 cycles, whereas the previously developed AUP4K DA formulation failed before reaching 2,500 cycles. In addition, preliminary indirect cytocompatibility assays supported the potential of these synthetic materials as a tunable platform for meniscus-oriented scaffold optimization.

Chapter 5 addressed a translationally critical step: the dehydration of hydrogel scaffolds. Four drying routes (freeze-drying, desiccator drying, ventilated oven drying, and vacuum oven drying) were compared for AUP4K scaffolds produced by extrusion printing. The dehydration pathway strongly affected strut morphology, swelling

degree, gel fraction, and post-rehydration compression behavior. Freeze-drying best preserved the porous microarchitecture and maximized swelling capacity, but resulted in lower compressive stiffness. In contrast, oven-based methods show compressive properties closer or even higher than the hydrated references. Importantly, all rehydrated scaffold variants maintained compressive properties within the reported meniscal range, highlighting the robustness of the AUP4K DA network and demonstrating that drying is not merely a logistical step but a design parameter that can be exploited to balance handling requirements with functional performance.

Taken together, this thesis establishes that urethane-PEG AUP hydrogels constitute a versatile synthetic platform for meniscus scaffold fabrication. First, the work demonstrates that AUP networks can be efficiently crosslinked into stable hydrogels with consistently high gel fractions across processing routes and that their swelling and mechanical behavior can be tuned by polymer concentration and molecular design (PEG molar mass and end-group functionality). Second, it shows that architecture control -printing pattern, strand/pore dimensions, and connectivity - provides an additional, independent lever to tune mechanical response. Third, it highlights that processing route selection (extrusion printing vs. indirect moulding vs. DLP) is not only a manufacturing choice but influences achievable architecture, resolution, and ultimately the structure–property relationships of the final scaffold.

Several aspects of this work represent original contributions to the field. First, this thesis provides the first comprehensive, multi-modal mechanical characterization of AUP-based hydrogel scaffolds, encompassing static compression, tensile testing, dynamic mechanical analysis, texture profile analysis, and, critically, cyclic fatigue testing.

Prior studies on AUP materials had been limited to basic mechanical screening; the systematic fatigue assessment conducted here identified cyclic durability as the dominant limitation for meniscal application, a finding that had not been previously reported for this material class and that fundamentally redirects future optimization efforts. Second, the indirect rapid prototyping approach developed in Chapter 3, combining a custom-designed injection moulding setup with sacrificial hot melt extrusion-printed PLA moulds, represents a novel fabrication strategy that enables the production of hydrogel scaffolds with lateral porosity. This architectural feature, which is inaccessible via conventional layer-by-layer direct printing, is of particular relevance for meniscus scaffolds, where nutrient transport from the vascularized peripheral zone toward the avascular inner region requires interconnected pore channels oriented parallel to the meniscal rim. Third, the translation of AUP materials to DLP printing, including the identification of suitable photoabsorber and photoinitiator systems for visible-light curing of AUP resins, had not been received major focus prior to this work and opens the door to high-resolution scaffold architectures with improved geometric fidelity compared to extrusion-based approaches. Finally, the systematic comparison of four dehydration protocols and their effects on scaffold microstructure, swelling, and post-rehydration mechanical performance (Chapter 5) addresses a practical translational question that is frequently overlooked in the scaffold development literature but is essential for clinical implementation.

From a meniscus-replacement perspective, the most important insight is that matching meniscal properties is multi-factorial and cannot be achieved through material chemistry alone. The compressive moduli obtained in the optimized extrusion-printed AUP4K DA scaffolds (on the order of a few MPa) and in selected DLP-printed AUP2K DA

scaffolds (up to ~4 MPa) overlap with the lower range reported for human menisci under comparable strain windows. Importantly, the dedicated cyclic-loading approach in Chapter 2 demonstrated a substantial improvement in fatigue resistance compared to the previously developed AUP4K DA formulation, which failed before reaching 2,500 cycles. In contrast, the AUP2K DA and AUP4K DA materials investigated here reached 300,000 cycles and 180,000 cycles before failure, respectively. In other words, the key challenge is to reconcile meniscus-like hydration and porosity (needed for biomimetic behavior and potential cell/tissue integration) with long-term cyclic stability under complex, multiaxial joint loading.

Overall, this work provides a clear roadmap for future optimization: (i) tailor crosslink density and chain mobility to improve resistance to cyclic deformation and damage accumulation under compression, (ii) engineer scaffold architecture to distribute stresses more uniformly and limit local strut bending or sliding, and (iii) integrate processing-aware steps (including drying) that preserve pore fidelity while maintaining mechanical integrity and manufacturability.

Future research should therefore focus on enhancing fatigue resistance and functional anisotropy through three complementary strategies, each grounded in the structure–property relationships established in this thesis. The first strategy is chemistry-driven: lowering PEG molar mass increases crosslink density and stiffness (as demonstrated by the AUP2K vs AUP4K comparison in Chapter 4), but at the cost of increased brittleness and defect sensitivity. Future formulations should therefore explore intermediate molar masses, increased end-group multifunctionality (building on the HA concept introduced in Chapter 3), and the introduction of secondary energy-dissipating mechanisms, such as interpenetrating network (IPN) formation or reversible non-covalent crosslinks (e.g. hydrogen bonding

or hydrophobic associations), to decouple stiffness from brittleness. The rationale is that toughening requires the ability to dissipate energy ahead of a propagating crack, which single-network covalently crosslinked hydrogels inherently lack; dual-network or composite-network strategies have been shown in the broader hydrogel literature to increase fracture energies by orders of magnitude while maintaining high stiffness. The second strategy is architecture-driven: the mechanical data from Chapters 2–4 consistently show that scaffold geometry (printing pattern, pore size, strut dimensions, porosity orientation) is at least as influential as material chemistry in determining the macroscopic mechanical response. Future designs should exploit this by implementing zonal or gradient architectures that emulate the native meniscus, for example, denser outer regions for circumferential hoop-stress resistance and more compliant inner regions for compressive damping, and by incorporating circumferential deposition paths that promote load transfer along the principal stress direction rather than relying on vertical strut compression alone. The feasibility of such directional architectures has been enhanced by the DLP platform established in Chapter 4, which offers the resolution necessary for fine-scale gradient control. The third strategy is composite-driven: introducing reinforcing elements such as electrospun fibre mats, aligned short fibres, or interpenetrating fibre networks into the AUP hydrogel matrix could provide the tensile reinforcement and crack-bridging mechanisms that are currently absent from the homogeneous hydrogel network. This approach would more closely replicate the structural principle of the native meniscus, in which the collagen fibre network provides tensile resistance while the proteoglycan-rich matrix provides compressive resilience.

Beyond mechanics, the translational pathway requires systematic evaluation of sterilization compatibility, storage stability, and

rehydration reproducibility at clinically relevant timescales. The results of Chapter 5 indicate that drying can be tuned to balance swelling and stiffness; future work should extend this by including sterilization modalities (e.g., gamma irradiation, ethylene oxide, or alternative methods suitable for hydrogels), and by defining acceptance criteria for pore fidelity, gel fraction, swelling kinetics, and mechanical performance after rehydration.

The biological validation of AUP-based meniscus scaffolds should progress through a structured, stepwise programme. As a first priority, the preliminary cytocompatibility screening reported in Chapter 4 (indirect contact assays) should be extended to direct-contact cell culture studies using meniscus-relevant cell types, including primary meniscal fibrochondrocytes isolated from the inner (avascular) and outer (vascular) zones, as well as mesenchymal stem cells (MSCs) as a clinically accessible cell source. These studies should evaluate not only cell viability but also cell attachment, proliferation, migration into the scaffold pore network, and, importantly, the phenotypic response of seeded cells, including the expression of meniscus-specific extracellular matrix markers such as collagen types I and II, aggrecan, and glycosaminoglycans. Given the known mechanosensitivity of meniscal cells, future *in vitro* studies should incorporate mechanical stimulation (e.g. cyclic compression in a bioreactor) to assess whether AUP scaffold architecture and stiffness can support or guide the formation of organized, load-bearing tissue.

A second phase of biological evaluation should address the degradation behaviour of AUP scaffolds under physiological conditions. Although the high gel fractions consistently observed across all chapters (≥90%) indicate stable network formation, the long-term hydrolytic and enzymatic stability of urethane-PEG networks in a

synovial fluid environment remains to be characterized. This is particularly relevant given the non-degradable design intent of the scaffold: unlike resorbable implants, where controlled degradation is desired, a meniscal substitute must maintain its structural and mechanical integrity over years of cyclic loading. Accelerated ageing studies in simulated synovial fluid, combined with periodic mechanical testing, would provide essential data on long-term scaffold stability.

Once fatigue performance has been sufficiently improved to withstand physiologically relevant cycle counts, *ex vivo* biomechanical evaluation using whole-joint knee simulators should be pursued. Such studies would enable assessment of the scaffold's ability to restore tibiofemoral contact mechanics, distribute compressive loads, and resist extrusion under realistic multi-axial loading conditions, functional parameters that cannot be captured by isolated scaffold testing alone. Subsequently, *in vivo* evaluation in an appropriate large-animal model (e.g. ovine or caprine total meniscectomy model) would be required to assess biological integration, chondroprotective efficacy, and long-term mechanical survival under physiological loading.

Parallel to biological validation, regulatory and manufacturing considerations, including batch-to-batch consistency of macromer synthesis, resin formulation stability, sterilization compatibility (e.g. gamma irradiation, ethylene oxide), and scalable printing and post-processing workflows, should be addressed early to enable translation of the most promising scaffold configurations toward clinical application.

In conclusion, this thesis demonstrates that AUP-based synthetic hydrogels can be manufactured into porous, mechanically tunable 3D scaffolds using multiple printing strategies and can achieve

compressive properties overlapping with the lower end of the reported meniscus range. It further identifies fatigue resistance as the primary limitation for immediate meniscus replacement application and establishes dehydration as a key processing parameter for translation. The combined insights into chemistry, architecture and processing provide a strong foundation for the next development cycle toward a clinically viable, full meniscus replacement scaffold.

Appendix: Curriculum Vitae

Education

- **Ph.D.** **July 2020 – July 2026**
  Ghent University, Department of Organic and Macromolecular Chemistry, Ghent, Belgium
- **MSc** **September 2017 – October 2019**
  Genova University, Dipartimento di Informatica, Bioingegneria, Robotica e Ingegneria dei Sistemi, Genova, Italy
- **BA** **September 2014 – October 2017**
  Genova University, Dipartimento di Informatica, Bioingegneria, Robotica e Ingegneria dei Sistemi, Genova, Italy

Work experience

- **Application Scientist** at Sustanix (January 2026 - …)

  Geleen, Netherlands

Publications in peer reviewed journals

- Meazzo, M., Schroeder, S., Kretzer, J. P., Barberis, F., Van Der Straeten, C., & Dubruel, P. (2026). *Customizable 3D-printed scaffolds for meniscal replacement: Mechanical insights into urethane-based poly(ethylene glycol) polymer*. **European Polymer Journal, 242**, 114451. https://doi.org/10.1016/j.eurpolymj.2025.114451

- Meazzo, M., Ramezani, A., Barberis, F., Van Der Straeten, C., & Dubruel, P. (2026). *PEG-Based Hydrogels for Meniscus Replacement: Advancing Scaffold Fabrication Flexibility through a Customized Injection Molding Setup*. **ACS Biomaterials Science & Engineering**. https://doi.org/10.1021/acsbiomaterials.5c02110

Presentation in international conferences

- Meazzo, M., Barberis, F., Van Der Straeten, C., & Dubruel, P. 3D printed hydrogel scaffolds for tissue engineering applications: an in-depth mechanical analysis as the key to success. Oral presentation, ESB 2021, European Society for Biomaterials
- Meazzo, M., Barberis, F., Van Der Straeten, C., & Dubruel, P. Printing versatility of a novel hydrogel material as a key to tissue engineering applications. Conference abstract / poster presentation.

References

(1) Twomey-Kozak, J.; Jayasuriya, C. T. Meniscus Repair and Regeneration: A Systematic Review from a Basic and Translational Science Perspective. *Clin. Sports Med.* **2020**, *39* (1), 125. https://doi.org/10.1016/J.CSM.2019.08.003.

(2) McDermott, I. D.; Amis, A. A. The Consequences of Meniscectomy. *J. Bone Joint Surg. Br.* **2006**, *88* (12), 1549–1556. https://doi.org/10.1302/0301-620X.88B12.18140.

(3) Ikada, Y. Challenges in Tissue Engineering. *J. R. Soc. Interface* **2006**, *3* (10), 589. https://doi.org/10.1098/RSIF.2006.0124.

(4) Pereira, H.; Cengiz, I. F.; Silva-Correia, J.; Oliveira, J. M.; Reis, R. L.; Espregueira-Mendes, J. Human Meniscus: From Biology to Tissue Engineering Strategies. *Sports Inj.* **2015**, 1089–1102. https://doi.org/10.1007/978-3-642-36569-0_73.

(5) Rey-Rico, A.; Cucchiarini, M.; Madry, H. Hydrogels for Precision Meniscus Tissue Engineering: A Comprehensive Review. *Connect. Tissue Res.* **2017**, *58* (3–4), 317–328. https://doi.org/10.1080/03008207.2016.1276576.

(6) Zhou, Z.; Wang, J.; Jiang, C.; Xu, K.; Xu, T.; Yu, X.; Fang, J.; Yang, Y.; Dai, X. Advances in Hydrogels for Meniscus Tissue Engineering: A Focus on Biomaterials, Crosslinking, Therapeutic Additives. *Gels* **2024**, *10* (2), 114. https://doi.org/10.3390/gels10020114.

(7) Billiet, T.; Vandenhaute, M.; Schelfhout, J.; Van Vlierberghe, S.; Dubruel, P. A Review of Trends and Limitations in Hydrogel-Rapid Prototyping for Tissue Engineering. *Biomaterials* **2012**, *33* (26), 6020–6041. https://doi.org/10.1016/J.BIOMATERIALS.2012.04.050.

(8) Jadhav, A.; Jadhav, V. S. A Review on 3D Printing: An Additive Manufacturing Technology. In *Materials Today: Proceedings*; Elsevier Ltd, 2022; Vol. 62, pp 2094–2099. https://doi.org/10.1016/j.matpr.2022.02.558.

(9) Lee, J. M.; Fu, F. H. The Meniscus: Basic Science and Clinical Applications. *Oper. Tech. Orthop.* **2000**, *10* (3), 162–168. https://doi.org/10.1016/S1048-6666(00)80002-6.

(10) Grassi, A.; Dal Fabbro, G.; Di Paolo, S.; Stefanelli, F.; Macchiarola, L.; Lucidi, G. A.; Zaffagnini, S. Medial and Lateral Meniscus Have a Different Role in Kinematics of the ACL-Deficient Knee: A Systematic Review. *J. ISAKOS* **2019**, *4* (5), 233–241. https://doi.org/10.1136/JISAKOS-2019-000293.

(11) Fox, A. J. S.; Wanivenhaus, F.; Burge, A. J.; Warren, R. F.; Rodeo, S. A. The Human Meniscus: A Review of Anatomy, Function, Injury, and Advances in Treatment. *Clin. Anat.* **2015**, *28* (2), 269–287. https://doi.org/10.1002/ca.22456.

(12) Allen, A. A.; Caldwell, G. L.; Fu, F. H. *ANATOMY AND BIOMECHANICS OF THE MENISCUS*; 1995.

(13) Fox, A. J. S.; Bedi, A.; Rodeo, S. A. The Basic Science of Human Knee Menisci: Structure, Composition, and Function. *Sports Health* **2012**, *4* (4), 340. https://doi.org/10.1177/1941738111429419.

(14) Makris, E. A.; Hadidi, P.; Athanasiou, K. A. The Knee Meniscus: Structure–Function, Pathophysiology, Current Repair Techniques, and Prospects for Regeneration. *Biomaterials* **2011**, *32* (30), 7411–7431. https://doi.org/10.1016/j.biomaterials.2011.06.037.

(15) Yan, W.; Dai, W.; Cheng, J.; Fan, Y.; Wu, T.; Zhao, F.; Zhang, J.; Hu, X.; Ao, Y. Advances in the Mechanisms Affecting Meniscal Avascular Zone Repair and Therapies. *Front. Cell Dev. Biol.* **2021**, *9*, 758217. https://doi.org/10.3389/FCELL.2021.758217/BIBTEX.

(16) McNally, E. G.; Lin, K.; Sherman, S. L.; Stevens, K. J. Meniscus. *Knee Arthrosc. Knee Preserv. Surg.* **2024**, 1–24. https://doi.org/10.1007/978-3-030-82869-1_1-1.

(17) Meazzo, M.; Schroeder, S.; Kretzer, J. P.; Barberis, F.; Der Straeten, C. V.; Dubruel, P. Customizable 3D-Printed Scaffolds for Meniscal Replacement: Mechanical Insights into Urethane-Based

Poly(Ethylene Glycol) Polymer. *Eur. Polym. J.* **2026**, *242*, 114451. https://doi.org/10.1016/J.EURPOLYMJ.2025.114451.

(18) Mameri, E. S.; Dasari, S. P.; Fortier, L. M.; Verdejo, F. G.; Gursoy, S.; Yanke, A. B.; Chahla, J. Review of Meniscus Anatomy and Biomechanics. *Curr. Rev. Musculoskelet. Med.* **2022**, *15* (5), 323–335. https://doi.org/10.1007/S12178-022-09768-1/FIGURES/5.

(19) Giancamillo, A. D. I.; Mangiavini, L.; Tessaro, I.; Marmotti, A.; Scurati, R.; Peretti, G. M. The Meniscus Vascularization: The Direct Correlation with Tissue Composition for Tissue Engineering Purposes. *J. Biol. Regul. Homeost. Agents* **2016**, *30* (4 Suppl 1), 85–90.

(20) Petersen, W.; Tillmann, B. Collagenous Fibril Texture of the Human Knee Joint Menisci. *Anat. Embryol. (Berl.)* **1998**, *197* (4), 317–324. https://doi.org/10.1007/S004290050141.

(21) Biçer, E. K.; Aydoğdu, S.; Sur, H. The Structure, Function, and Healing of the Meniscus. *Musculoskelet. Res. Basic Sci.* **2015**, 405–427. https://doi.org/10.1007/978-3-319-20777-3_24/FIGURES/11.

(22) Stärke, C. Form Und Funktion von Menisken. *Arthroskopie* **2008**, *21* (4), 223–228. https://doi.org/10.1007/S00142-008-0469-8/FIGURES/4.

(23) Markes, A. R.; Hodax, J. D.; Ma, C. B. Meniscus Form and Function. *Clin. Sports Med.* **2020**, *39* (1), 1–12. https://doi.org/10.1016/J.CSM.2019.08.007/ASSET/CBC12F08-20F5-4507-95EB-236C35F25866/MAIN.ASSETS/GR6.JPG.

(24) Verdonk, P. C. M.; Forsyth, R. G.; Wang, J.; Almqvist, K. F.; Verdonk, R.; Veys, E. M.; Verbruggen, G. Characterisation of Human Knee Meniscus Cell Phenotype. *Osteoarthritis Cartilage* **2005**, *13* (7), 548–560. https://doi.org/10.1016/J.JOCA.2005.01.010.

(25) de Caro, F.; Grammens, J.; Van Genechten, W.; Verdonk, R.; Verdonk, P. Meniscus Substitution. *Adv. Knee Ligament Knee Preserv. Surg.* **2022**, 333–339. https://doi.org/10.1007/978-3-030-84748-7_27.

(26) Brindle, T.; Nyland, J.; Johnson, D. L. The Meniscus: Review of Basic Principles With Application to Surgery and Rehabilitation. *J. Athl. Train.* **2001**, *36* (2), 160.

(27) Caterine, S.; Hourigan, M.; Getgood, A. The Biomechanical Function of the Menisci. *Menisci Compr. Rev. Their Anat. Biomech. Funct. Surg. Treat.* **2017**, 9–20. https://doi.org/10.1007/978-3-662-53792-3_2/TABLES/1.

(28) Adib, M. A. H. M.; Jaafar, M. F. Review: Modelling of Meniscus of Knee Joint during Soccer Kicking. In *IOP Conference Series: Materials Science and Engineering*; 2013; Vol. 50. https://doi.org/10.1088/1757-899X/50/1/012027.

(29) McDermott, I. D.; Masouros, S. D.; Amis, A. A. Biomechanics of the Menisci of the Knee. *Curr. Orthop.* **2008**, *22* (3), 193–201. https://doi.org/10.1016/J.CUOR.2008.04.005.

(30) Bedi, A.; Kelly, N.; Baad, M.; Fox, A. J. S.; Ma, Y.; Warren, R. F.; Maher, S. A. Dynamic Contact Mechanics of Radial Tears of the Lateral Meniscus: Implications for Treatment. *Arthrosc. J. Arthrosc. Relat. Surg. Off. Publ. Arthrosc. Assoc. N. Am. Int. Arthrosc. Assoc.* **2012**, *28* (3), 372–381. https://doi.org/10.1016/J.ARTHRO.2011.08.287.

(31) Henning, C. E.; Lynch, M. A.; Clark, J. R. Vascularity for Healing of Meniscus Repairs. *Arthrosc. J. Arthrosc. Relat. Surg.* **2010**, *26* (10), 1368–1369. https://doi.org/10.1016/J.ARTHRO.2010.07.014.

(32) Baratz, M. E.; Fu, F. H.; Mengato, R. Meniscal Tears: The Effect of Meniscectomy and of Repair on Intraarticular Contact Areas and Stress in the Human Knee. A Preliminary Report. *Am. J. Sports Med.* **1986**, *14* (4), 270–275. https://doi.org/10.1177/036354658601400405.

(33) McNulty, A. L.; Guilak, F. Mechanobiology of the Meniscus. *J. Biomech.* **2015**, *48* (8), 1469–1478. https://doi.org/10.1016/j.jbiomech.2015.02.008.

(34) Fayard, J. M.; Pereira, H.; Servien, E.; Lustig, S.; Neyret, P. Meniscectomy: Global Results-Complications. *The Meniscus* **2010**, 177–190. https://doi.org/10.1007/978-3-642-02450-4_23.

(35) Peloquin, J. M.; Santare, M. H.; Elliott, D. M. Advances in Quantification of Meniscus Tensile Mechanics Including Nonlinearity, Yield, and Failure. *J. Biomech. Eng.* **2016**, *138* (2). https://doi.org/10.1115/1.4032354.

(36) Henderson, B. S.; Cudworth, K. F.; Wale, M. E.; Siegel, D. N.; Lujan, T. J. Tensile Fatigue Strength and Endurance Limit of Human Meniscus. *J. Mech. Behav. Biomed. Mater.* **2022**, *127*. https://doi.org/10.1016/j.jmbbm.2021.105057.

(37) Yin, X. Y.; Chung, J. Y.; Park, D. Y.; Song, H. K.; Kim, B. K.; Bae, H. W.; Park, K. H.; Min, B. H. The Perimensical Capsule: Potential Supporting Structure Surrounding Meniscus. *Cartilage* **2021**, *13* (1_suppl), 208S-215S. https://doi.org/10.1177/1947603519892316/ASSET/IMAGES/LARGE/10.1177_1947603519892316-FIG7.JPEG.

(38) Nesbitt, D. Q.; Siegel, D. N.; Nelson, S. J.; Lujan, T. J. Effect of Age on the Failure Properties of Human Meniscus: High-Speed Strain Mapping of Tissue Tears. *J. Biomech.* **2021**, *115*, 110126. https://doi.org/10.1016/J.JBIOMECH.2020.110126.

(39) Ahmad, S.; Singh, V. A.; Hussein, S. I. Cryopreservation versus Fresh Frozen Meniscal Allograft: A Biomechanical Comparative Analysis. *J. Orthop. Surg.* **2017**, *25* (3). https://doi.org/10.1177/2309499017727946/ASSET/IMAGES/LARGE/10.1177_2309499017727946-FIG3.JPEG.

(40) Yan, S. H.; Ou-Yang, H. K.; Shan, Y. L.; Luo, D. Z.; Wang, H.; Zhang, K. Tensile Biomechanical Characteristics of Human Meniscus. *Emerg. Mater. Res.* **2016**, *5* (1), 44–49. https://doi.org/10.1680/jemmr.15.00031.

(41) Freutel, M.; Scholz, N. B.; Seitz, A. M.; Ignatius, A.; Dürselen, L. Mechanical Properties and Morphological Analysis of the Transitional Zone between Meniscal Body and Ligamentous Meniscal Attachments. *J. Biomech.* **2015**, *48* (8), 1350–1355. https://doi.org/10.1016/j.jbiomech.2015.03.003.

(42) Tanaka, M. L.; Vest, N.; Ferguson, C. M.; Gatenholm, P. Comparison of Biomechanical Properties of Native Menisci and Bacterial Cellulose Implant. *Int. J. Polym. Mater. Polym. Biomater.* **2014**, *63* (17), 891–897. https://doi.org/10.1080/00914037.2014.886226.

(43) Párraga Quiroga, J. M.; Emans, P.; Wilson, W.; Ito, K.; van Donkelaar, C. C. Should a Native Depth-Dependent Distribution of Human Meniscus Constitutive Components Be Considered in FEA-Models of the Knee Joint? *J. Mech. Behav. Biomed. Mater.* **2014**, *38*, 242–250. https://doi.org/10.1016/J.JMBBM.2014.03.005.

(44) Abraham, A. C.; Moyer, J. T.; Villegas, D. F.; Odegard, G. M.; Haut Donahue, T. L. Hyperelastic Properties of Human Meniscal Attachments. *J. Biomech.* **2011**, *44* (3), 413–418. https://doi.org/10.1016/J.JBIOMECH.2010.10.001.

(45) Hauch, K. N.; Villegas, D. F.; Haut Donahue, T. L. Geometry, Time-Dependent and Failure Properties of Human Meniscal Attachments. *J. Biomech.* **2010**, *43* (3), 463–468. https://doi.org/10.1016/J.JBIOMECH.2009.09.043.

(46) Bursac, P.; York, A.; Kuznia, P.; Brown, L. M.; Arnoczky, S. P. Influence of Donor Age on the Biomechanical and Biochemical Properties of Human Meniscal Allografts. *https://doi.org/10.1177/0363546508330140* **2009**, *37* (5), 884–889. https://doi.org/10.1177/0363546508330140.

(47) Lechner, K.; Hull, M. L.; Howell, S. M. Is the Circumferential Tensile Modulus within a Human Medial Meniscus Affected by the Test Sample Location and Cross-Sectional Area? *J. Orthop. Res. Off. Publ.*

Orthop. Res. Soc. **2000**, *18* (6), 945–951. https://doi.org/10.1002/JOR.1100180614.

(48) Tissakht, M.; Ahmed, A. M. Tensile Stress-Strain Characteristics of the Human Meniscal Material. *J. Biomech.* **1995**, *28* (4), 411–422. https://doi.org/10.1016/0021-9290(94)00081-E.

(49) Fithian, D. C.; Kelly, M. A.; Mow, V. C. Material Properties and Structure-Function Relationships in the Menisci. *Clin. Orthop.* **1990**, *252* (252), 19–31. https://doi.org/10.1097/00003086-199003000-00004.

(50) Bullough, P. G.; Munuera, L.; Murphy, J.; Weinstein, A. M. The Strength of the Menisci of the Knee as It Relates to Their Fine Structure. *J. Bone Joint Surg. Br.* **1970**, *52* (3), 564–567. https://doi.org/10.1302/0301-620X.52B3.564/LETTERTOEDITOR.

(51) Warnecke, D.; Balko, J.; Haas, J.; Bieger, R.; Leucht, F.; Wolf, N.; Schild, N. B.; Stein, S. E. C.; Seitz, A. M.; Ignatius, A.; Reichel, H.; Mizaikoff, B.; Dürselen, L. Degeneration Alters the Biomechanical Properties and Structural Composition of Lateral Human Menisci. *Osteoarthritis Cartilage* **2020**, *28* (11), 1482–1491. https://doi.org/10.1016/J.JOCA.2020.07.004.

(52) Jacquet, C.; Erivan, R.; Sharma, A.; Pithioux, M.; Parratte, S.; Argenson, J. N.; Ollivier, M. Preservation Methods Influence the Biomechanical Properties of Human Lateral Menisci: An Ex Vivo Comparative Study of 3 Methods. *Orthop. J. Sports Med.* **2019**, *7* (4). https://doi.org/10.1177/2325967119841622/ASSET/IMAGES/LARGE/10.1177_2325967119841622-FIG5.JPEG.

(53) Fischenich, K. M.; Lewis, J.; Kindsfater, K. A.; Bailey, T. S.; Haut Donahue, T. L. Effects of Degeneration on the Compressive and Tensile Properties of Human Meniscus. *J. Biomech.* **2015**, *48* (8), 1407–1411. https://doi.org/10.1016/J.JBIOMECH.2015.02.042.

(54) Truhn, D.; Brill, N.; Braun, B.; Merhof, D.; Kuhl, C.; Knobe, M.; Thüring, J.; Nebelung, S. A Multi-Purpose Force-Controlled Loading

Device for Cartilage and Meniscus Functionality Assessment Using Advanced MRI Techniques. *J. Mech. Behav. Biomed. Mater.* **2020**, *101*, 103428. https://doi.org/10.1016/J.JMBBM.2019.103428.

(55) Seitz, A. M.; Osthaus, F.; Schwer, J.; Warnecke, D.; Faschingbauer, M.; Sgroi, M.; Ignatius, A.; Dürselen, L. Osteoarthritis-Related Degeneration Alters the Biomechanical Properties of Human Menisci Before the Articular Cartilage. *Front. Bioeng. Biotechnol.* **2021**, *9*, 659989. https://doi.org/10.3389/FBIOE.2021.659989/BIBTEX.

(56) Berni, M.; Marchiori, G.; Cassiolas, G.; Grassi, A.; Zaffagnini, S.; Fini, M.; Lopomo, N. F.; Maglio, M. Anisotropy and Inhomogeneity of Permeability and Fibrous Network Response in the Pars Intermedia of the Human Lateral Meniscus. *Acta Biomater.* **2021**, *135*, 393–402. https://doi.org/10.1016/J.ACTBIO.2021.08.020.

(57) Pordzik, J.; Bernstein, A.; Watrinet, J.; Mayr, H. O.; Latorre, S. H.; Schmal, H.; Seidenstuecker, M. Correlation of Biomechanical Alterations under Gonarthritis between Overlying Menisci and Articular Cartilage. *Appl. Sci. 2020 Vol 10 Page 8673* **2020**, *10* (23), 8673. https://doi.org/10.3390/APP10238673.

(58) Nebelung, S.; Dötsch, L.; Shah, D.; Abrar, D. B.; Linka, K.; Knobe, M.; Sewerin, P.; Thüring, J.; Kuhl, C.; Truhn, D. Functional MRI Mapping of Human Meniscus Functionality and Its Relation to Degeneration. *Sci. Rep. 2020 101* **2020**, *10* (1), 1–14. https://doi.org/10.1038/s41598-020-59573-4.

(59) Chia, H. N.; Hull, M. L. Compressive Moduli of the Human Medial Meniscus in the Axial and Radial Directions at Equilibrium and at a Physiological Strain Rate. *J. Orthop. Res.* **2008**, *26* (7), 951–956. https://doi.org/10.1002/jor.20573.

(60) Leslie, B. W.; Gardner, D. L.; McGeough, J. A.; Moran, R. S. Anisotropic Response of the Human Knee Joint Meniscus to Unconfined Compression. *Proc. Inst. Mech. Eng. [H]* **2000**, *214* (6), 631–635. https://doi.org/10.1243/0954411001535651.

(61) Sweigart, M. A.; Zhu, C. F.; Burt, D. M.; Deholl, P. D.; Agrawal, C. M.; Clanton, T. O.; Athanasiou, K. A. Intraspecies and Interspecies Comparison of the Compressive Properties of the Medial Meniscus. *Ann. Biomed. Eng.* **2004**, *32* (11), 1569–1579. https://doi.org/10.1114/B:ABME.0000049040.70767.5C.

(62) Norberg, C.; Filippone, G.; Andreopoulos, F.; Best, T. M.; Baraga, M.; Jackson, A. R.; Travascio, F. Viscoelastic and Equilibrium Shear Properties of Human Meniscus: Relationships with Tissue Structure and Composition. *J. Biomech.* **2021**, *120*, 110343. https://doi.org/10.1016/J.JBIOMECH.2021.110343.

(63) Zin, M. H.; Abdan, K.; Norizan, M. N. The Effect of Different Fiber Loading on Flexural and Thermal Properties of Banana/Pineapple Leaf (PALF)/Glass Hybrid Composite. *Struct. Health Monit. Biocomposites Fibre-Reinf. Compos. Hybrid Compos.* **2019**, 1–17. https://doi.org/10.1016/B978-0-08-102291-7.00001-0.

(64) Liu, Q.; Donner, E.; Tarn, R.; Singh, J.; Chung, H.-J. Advanced Analytical Techniques to Evaluate the Quality of Potato and Potato Starch. *Adv. Potato Chem. Technol.* **2009**, 221–248. https://doi.org/10.1016/B978-0-12-374349-7.00008-8.

(65) Ala-Myllymäki, J.; Danso, E. K.; Honkanen, J. T. J.; Korhonen, R. K.; Töyräs, J.; Afara, I. O. Optical Spectroscopic Characterization of Human Meniscus Biomechanical Properties. *https://doi.org/10.1117/1.JBO.22.12.125008* **2017**, *22* (12), 125008. https://doi.org/10.1117/1.JBO.22.12.125008.

(66) Nordberg, R. C.; Charoenpanich, A.; Vaughn, C. E.; Griffith, E. H.; Fisher, M. B.; Cole, J. H.; Spang, J. T.; Loboa, E. G. Enhanced Cellular Infiltration of Human Adipose-Derived Stem Cells in Allograft Menisci Using a Needle-Punch Method. *J. Orthop. Surg.* **2016**, *11* (1), 1–10. https://doi.org/10.1186/S13018-016-0467-X/FIGURES/7.

(67) Gaugler, M.; Wirz, D.; Ronken, S.; Hafner, M.; Göpfert, B.; Friederich, N. F.; Elke, R. Fibrous Cartilage of Human Menisci Is Less

Shock-Absorbing and Energy-Dissipating than Hyaline Cartilage. *Knee Surg. Sports Traumatol. Arthrosc.* **2015**, *23* (4), 1141–1146. https://doi.org/10.1007/S00167-014-2926-4/FIGURES/5.

(68) Schwer, J.; Ignatius, A.; Seitz, A. M. The Biomechanical Properties of Human Menisci: A Systematic Review. *Acta Biomater.* **2024**, *175*, 1–26. https://doi.org/10.1016/J.ACTBIO.2023.12.010.

(69) Danso, E. K.; Mäkelä, J. T. A.; Tanska, P.; Mononen, M. E.; Honkanen, J. T. J.; Jurvelin, J. S.; Töyräs, J.; Julkunen, P.; Korhonen, R. K. Characterization of Site-Specific Biomechanical Properties of Human Meniscus-Importance of Collagen and Fluid on Mechanical Nonlinearities. *J. Biomech.* **2015**, *48* (8), 1499–1507. https://doi.org/10.1016/j.jbiomech.2015.01.048.

(70) Pereira, H.; Caridade, S. G.; Frias, A. M.; Silva-Correia, J.; Pereira, D. R.; Cengiz, I. F.; Mano, J. F.; Oliveira, J. M.; Espregueira-Mendes, J.; Reis, R. L. Biomechanical and Cellular Segmental Characterization of Human Meniscus: Building the Basis for Tissue Engineering Therapies. *Osteoarthritis Cartilage* **2014**, *22* (9), 1271–1281. https://doi.org/10.1016/J.JOCA.2014.07.001.

(71) Pillai, M. M.; Gopinathan, J.; Selvakumar, R.; Bhattacharyya, A. Human Knee Meniscus Regeneration Strategies: A Review on Recent Advances. *Curr. Osteoporos. Rep.* **2018**, *16* (3), 224–235. https://doi.org/10.1007/S11914-018-0436-X.

(72) Bursac, P.; Arnoczky, S.; York, A. Dynamic Compressive Behavior of Human Meniscus Correlates with Its Extra-Cellular Matrix Composition. *Biorheology* **2009**, *46* (3), 227–237. https://doi.org/10.3233/BIR-2009-0537.

(73) *American Academy of Orthopaedic Surgeons - AAOS*. https://www.aaos.org/ (accessed 2024-09-12).

(74) Allied Market Research. *Meniscus Repair System Market Size & Share | Report - 2031*; 2023; p 386.

https://www.alliedmarketresearch.com/meniscus-repair-system-market-A47390 (accessed 2024-10-09).

(75) Doral, M. N.; Bilge, O.; Huri, G.; Turhan, E.; Verdonk, R. Modern Treatment of Meniscal Tears. *EFORT Open Rev.* **2018**, *3* (5), 260. https://doi.org/10.1302/2058-5241.3.170067.

(76) Mulry, T. J.; McIntyre, L. F. The Classification of Knee Meniscal Cartilage Tears. *Oper. Tech. Sports Med.* **2018**, *26* (4), 228–232. https://doi.org/10.1053/J.OTSM.2018.10.002.

(77) Snoeker, B. A. M.; Bakker, E. W. P.; Kegel, C. A. T.; Lucas, C. Risk Factors for Meniscal Tears: A Systematic Review Including Meta-Analysis. *J. Orthop. Sports Phys. Ther.* **2013**, *43* (6), 352–367. https://doi.org/10.2519/JOSPT.2013.4295/ASSET/IMAGES/LARGE/JOSPT-352-FIG008.JPEG.

(78) Mordecai, S. C.; Al-Hadithy, N.; Ware, H. E.; Gupte, C. M. Treatment of Meniscal Tears: An Evidence Based Approach. *World J. Orthop.* **2014**, *5* (3), 233–241. https://doi.org/10.5312/wjo.v5.i3.233.

(79) Trivedi, J.; Jayasuriya, C. T. Meniscus Tissue Engineering and Repair. *Musculoskelet. Tissue Eng.* **2022**, 107–132. https://doi.org/10.1016/B978-0-12-823893-6.00006-1.

(80) Rongen, J. J.; van Tienen, T. G.; van Bochove, B.; Grijpma, D. W.; Buma, P. Biomaterials in Search of a Meniscus Substitute. *Biomaterials* **2014**, *35* (11), 3527–3540. https://doi.org/10.1016/J.BIOMATERIALS.2014.01.017.

(81) Liu, C.; Toma, I. C.; Mastrogiacomo, M.; Krettek, C.; Von Lewinski, G.; Jagodzinski, M. Meniscus Reconstruction: Today's Achievements and Premises for the Future. *Arch. Orthop. Trauma Surg.* **2013**, *133* (1), 95–109. https://doi.org/10.1007/S00402-012-1624-2.

(82) Scotti, C.; Hirschmann, M. T.; Antinolfi, P.; Martin, I.; Peretti, G. M. Meniscus Repair and Regeneration: Review on Current Methods

and Research Potential. *Eur. Cell. Mater.* **2013**, *26*, 150–170. https://doi.org/10.22203/eCM.v026a11.

(83) Abram, S. G. F.; Judge, A.; Beard, D. J.; Price, A. J. Adverse Outcomes after Arthroscopic Partial Meniscectomy: A Study of 700 000 Procedures in the National Hospital Episode Statistics Database for England. *The Lancet* **2018**, *392* (10160), 2194–2202. https://doi.org/10.1016/S0140-6736(18)31771-9.

(84) Bhan, K. Meniscal Tears: Current Understanding, Diagnosis, and Management. *Cureus* **2020**. https://doi.org/10.7759/cureus.8590.

(85) Sihvonen, R.; Paavola, M.; Malmivaara, A.; Itälä, A.; Joukainen, A.; Nurmi, H.; Kalske, J.; Ikonen, A.; Järvelä, T.; Järvinen, T. A. H.; Kanto, K.; Karhunen, J.; Knifsund, J.; Kröger, H.; Kääriäinen, T.; Lehtinen, J.; Nyrhinen, J.; Paloneva, J.; Päiväniemi, O.; Raivio, M.; Sahlman, J.; Sarvilinna, R.; Tukiainen, S.; Välimäki, V. V.; Äärimaa, V.; Toivonen, P.; Järvinen, T. L. N. Arthroscopic Partial Meniscectomy versus Placebo Surgery for a Degenerative Meniscus Tear: A 2-Year Follow-up of the Randomised Controlled Trial. *Ann. Rheum. Dis.* **2018**, *77* (2), 188–195. https://doi.org/10.1136/annrheumdis-2017-211172.

(86) Cucchiarini, M.; McNulty, A. L.; Mauck, R. L.; Setton, L. A.; Guilak, F.; Madry, H. Advances in Combining Gene Therapy with Cell and Tissue Engineering-Based Approaches to Enhance Healing of the Meniscus. *Osteoarthritis Cartilage* **2016**, *24* (8), 1330. https://doi.org/10.1016/J.JOCA.2016.03.018.

(87) Shen, W.; Chen, J.; Zhu, T.; Chen, L.; Zhang, W.; Fang, Z.; Heng, B. C.; Yin, Z.; Chen, X.; Ji, J.; Chen, W.; Ouyang, H.-W. Intra-Articular Injection of Human Meniscus Stem/Progenitor Cells Promotes Meniscus Regeneration and Ameliorates Osteoarthritis Through Stromal Cell-Derived Factor-1/CXCR4-Mediated Homing. *Stem Cells Transl. Med.* **2014**, *3* (3), 387–394. https://doi.org/10.5966/SCTM.2012-0170/-/DC1.

(88) Figueroa, F.; Figueroa, D.; Calvo, R.; Vaisman, A.; Espregueira-Mendes, J. Meniscus Allograft Transplantation: Indications, Techniques and Outcomes. *EFORT Open Rev.* **2019**, *4* (4), 115. https://doi.org/10.1302/2058-5241.4.180052.

(89) Lee, S. R.; Kim, J. G.; Nam, S. W. The Tips and Pitfalls of Meniscus Allograft Transplantation. *Knee Surg. Relat. Res.* **2012**, *24* (3), 137. https://doi.org/10.5792/KSRR.2012.24.3.137.

(90) Visser, J.; Levett, P. A.; Te Moller, N. C. R.; Besems, J.; Boere, K. W. M.; Van Rijen, M. H. P.; De Grauw, J. C.; Dhert, W. J. A.; Van Weeren, P. R.; Malda, J. Crosslinkable Hydrogels Derived from Cartilage, Meniscus, and Tendon Tissue. *Tissue Eng. Part A* **2015**, *21* (7–8), 1195–1206. https://doi.org/10.1089/TEN.TEA.2014.0362.

(91) Gelber, P. E.; Verdonk, P.; Getgood, A. M.; Monllau, J. C. Meniscal Transplantation: State of the Art. *J. ISAKOS* **2017**, *2* (6), 339–349. https://doi.org/10.1136/JISAKOS-2017-000138.

(92) Ibarra, C.; Koski, J. A.; Warren, R. F. Tissue Engineering Meniscus: Cells and Matrix. *Orthop. Clin. North Am.* **2000**, *31* (3), 411–418. https://doi.org/10.1016/S0030-5898(05)70160-7.

(93) Abbadessa, A.; Crecente-Campo, J.; Alonso, M. J. Engineering Anisotropic Meniscus: Zonal Functionality and Spatiotemporal Drug Delivery. *Tissue Eng. Part B Rev.* **2021**, *27* (2), 133–154. https://doi.org/10.1089/TEN.TEB.2020.0096.

(94) Nerem, R. M.; Schutte, S. C. The Challenge of Imitating Nature. *Princ. Tissue Eng. Fourth Ed.* **2014**, 9–24. https://doi.org/10.1016/B978-0-12-398358-9.00002-1.

(95) Hasnain, M. S.; Ahmad, S. A.; Chaudhary, N.; Hoda, M. N.; Nayak, A. K. Biodegradable Polymer Matrix Nanocomposites for Bone Tissue Engineering. *Appl. Nanocomposite Mater. Orthop.* **2019**, 1–37. https://doi.org/10.1016/B978-0-12-813740-6.00001-6.

(96) Donati, D.; Zolezzi, C.; Tomba, P.; Viganò, A. Bone Grafting: Historical and Conceptual Review, Starting with an Old Manuscript by

Vittorio Putti. *Acta Orthop.* **2007**, *78* (1), 19–25. https://doi.org/10.1080/17453670610013376.

(97) Kaul, H.; Ventikos, Y. On the Genealogy of Tissue Engineering and Regenerative Medicine. *Tissue Eng. Part B Rev.* **2014**, *21* (2), 203. https://doi.org/10.1089/TEN.TEB.2014.0285.

(98) Chan, B. P.; Leong, K. W. Scaffolding in Tissue Engineering: General Approaches and Tissue-Specific Considerations. *Eur. Spine J.* **2008**, *17* (Suppl 4), 467. https://doi.org/10.1007/S00586-008-0745-3.

(99) Almouemen, N.; Kelly, H. M.; O'Leary, C. Tissue Engineering: Understanding the Role of Biomaterials and Biophysical Forces on Cell Functionality Through Computational and Structural Biotechnology Analytical Methods. *Comput. Struct. Biotechnol. J.* **2019**, *17*, 591–598. https://doi.org/10.1016/j.csbj.2019.04.008.

(100) Ghisa, C.; Zaslav, K. R. Current State of off the Shelf Scaffolds and Implants for Meniscal Replacement. *J. Cartil. Jt. Preserv.* **2022**, *2* (1), 100040. https://doi.org/10.1016/J.JCJP.2022.100040.

(101) Bilgen, B.; Jayasuriya, C. T.; Owens, B. D. Current Concepts in Meniscus Tissue Engineering and Repair. *Adv. Healthc. Mater.* **2018**, *7* (11). https://doi.org/10.1002/ADHM.201701407.

(102) Zheng, R.; Song, D.; Ding, Y.; Sun, B.; Lu, C.; Mo, X.; Xu, H.; Liu, Y.; Wu, J. A Comparative Study on Various Cell Sources for Constructing Tissue-Engineered Meniscus. *Front. Bioeng. Biotechnol.* **2023**, *11*, 1128762. https://doi.org/10.3389/FBIOE.2023.1128762/BIBTEX.

(103) Patil, S. V.; Shelake, S. S.; Patil, S. S. Polymeric Materials for Targeted Delivery of Bioactive Agents and Drugs. *Fundam. Biomater. Polym.* **2018**, 249–266. https://doi.org/10.1016/B978-0-08-102194-1.00011-6.

(104) Chundawat, N. S.; Rathore, B. S.; Meghwal, K. Phenolic and Epoxy-Based Copolymers and Terpolymers. *Adv. Funct. Polym.*

Biomed. Appl. **2019**, 143–165. https://doi.org/10.1016/B978-0-12-816349-8.00008-4.

(105) Brinson, H. F.; Brinson, L. C. Characteristics, Applications and Properties of Polymers. *Polym. Eng. Sci. Viscoelasticity* **2008**, 55–97. https://doi.org/10.1007/978-0-387-73861-1_3.

(106) Kahar, N. N. F. N. M. N.; Osman, A. F.; Alosime, E.; Arsat, N.; Azman, N. A. M.; Syamsir, A.; Itam, Z.; Hamid, Z. A. A. The Versatility of Polymeric Materials as Self-Healing Agents for Various Types of Applications: A Review. *Polym. 2021 Vol 13 Page 1194* **2021**, *13* (8), 1194. https://doi.org/10.3390/POLYM13081194.

(107) Jin, P.; Liu, L.; Chen, X.; Cheng, L.; Zhang, W.; Zhong, G. Applications and Prospects of Different Functional Hydrogels in Meniscus Repair. *Front. Bioeng. Biotechnol.* **2022**, *10*. https://doi.org/10.3389/fbioe.2022.1082499.

(108) Rey-Rico, A.; Klich, A.; Cucchiarini, M.; Madry, H. Biomedical-Grade, High Mannuronic Acid Content (BioMVM) Alginate Enhances the Proteoglycan Production of Primary Human Meniscal Fibrochondrocytes in a 3-D Microenvironment. *Sci. Rep. 2016 61* **2016**, *6* (1), 1–13. https://doi.org/10.1038/srep28170.

(109) Yuan, X.; Wei, Y.; Villasante, A.; Ng, J. J. D.; Arkonac, D. E.; Chao, P. hsiu G.; Vunjak-Novakovic, G. Stem Cell Delivery in Tissue-Specific Hydrogel Enabled Meniscal Repair in an Orthotopic Rat Model. *Biomaterials* **2017**, *132*, 59–71. https://doi.org/10.1016/J.BIOMATERIALS.2017.04.004.

(110) Ruprecht, J. C.; Waanders, T. D.; Rowland, C. R.; Nishimuta, J. F.; Glass, K. A.; Stencel, J.; DeFrate, L. E.; Guilak, F.; Weinberg, J. B.; McNulty, A. L. Meniscus-Derived Matrix Scaffolds Promote the Integrative Repair of Meniscal Defects. *Sci. Rep.* **2019**, *9* (1). https://doi.org/10.1038/S41598-019-44855-3.

(111) Marrella, A.; Lagazzo, A.; Dellacasa, E.; Pasquini, C.; Finocchio, E.; Barberis, F.; Pastorino, L.; Giannoni, P.; Scaglione, S.

3D Porous Gelatin/PVA Hydrogel as Meniscus Substitute Using Alginate Micro-Particles as Porogens. *Polymers* **2018**, *10* (4). https://doi.org/10.3390/polym10040380.

(112) Joshi, A.; Fussell, G.; Thomas, J.; Hsuan, A.; Lowman, A.; Karduna, A.; Vresilovic, E.; Marcolongo, M. Functional Compressive Mechanics of a PVA/PVP Nucleus Pulposus Replacement. *Biomaterials* **2006**, *27* (2), 176–184. https://doi.org/10.1016/J.BIOMATERIALS.2005.06.003.

(113) Kobayashi, M.; Toguchida, J.; Oka, M. Preliminary Study of Polyvinyl Alcohol-Hydrogel (PVA-H) Artificial Meniscus. *Biomaterials* **2003**, *24* (4), 639–647. https://doi.org/10.1016/S0142-9612(02)00378-2.

(114) Holloway, J. L.; Lowman, A. M.; Palmese, G. R. Mechanical Evaluation of Poly(Vinyl Alcohol)-Based Fibrous Composites as Biomaterials for Meniscal Tissue Replacement. *Acta Biomater.* **2010**, *6* (12), 4716–4724. https://doi.org/10.1016/J.ACTBIO.2010.06.025.

(115) Kobayashi, M.; Chang, Y. S.; Oka, M. A Two Year in Vivo Study of Polyvinyl Alcohol-Hydrogel (PVA-H) Artificial Meniscus. *Biomaterials* **2005**, *26* (16), 3243–3248. https://doi.org/10.1016/J.BIOMATERIALS.2004.08.028.

(116) Hayes, J. C.; Curley, C.; Tierney, P.; Kennedy, J. E. Biomechanical Analysis of a Salt-Modified Polyvinyl Alcohol Hydrogel for Knee Meniscus Applications, Including Comparison with Human Donor Samples. *J. Mech. Behav. Biomed. Mater.* **2016**, *56*, 156–164. https://doi.org/10.1016/J.JMBBM.2015.11.011.

(117) Hayes, J. C.; Kennedy, J. E. An Evaluation of the Biocompatibility Properties of a Salt-Modified Polyvinyl Alcohol Hydrogel for a Knee Meniscus Application. *Mater. Sci. Eng. C* **2016**, *59*, 894–900. https://doi.org/10.1016/J.MSEC.2015.10.052.

(118) Duan, W. L.; Zhang, L. N.; Bohara, R.; Martin-Saldaña, S.; Yang, F.; Zhao, Y. Y.; Xie, Y.; Bu, Y. Z.; Pandit, A. Adhesive Hydrogels

in Osteoarthritis: From Design to Application. *Mil. Med. Res. 2023 101* **2023**, *10* (1), 1–26. https://doi.org/10.1186/S40779-022-00439-3.

(119) Shimomura, K.; Rothrauff, B. B.; Tuan, R. S. Region-Specific Effect of the Decellularized Meniscus Extracellular Matrix on Mesenchymal Stem Cell-Based Meniscus Tissue Engineering. *Am. J. Sports Med.* **2017**, *45* (3), 604–611. https://doi.org/10.1177/0363546516674184/ASSET/IMAGES/LARGE/10.1177_0363546516674184-FIG4.JPEG.

(120) Sasaki, H.; Rothrauff, B. B.; Alexander, P. G.; Lin, H.; Gottardi, R.; Fu, F. H.; Tuan, R. S. In Vitro Repair of Meniscal Radial Tear With Hydrogels Seeded With Adipose Stem Cells and TGF-B3. *Am. J. Sports Med.* **2018**, *46* (10), 2402–2413. https://doi.org/10.1177/0363546518782973/ASSET/IMAGES/LARGE/10.1177_0363546518782973-FIG8.JPEG.

(121) Bupphathong, S.; Quiroz, C.; Huang, W.; Chung, P. F.; Tao, H. Y.; Lin, C. H. Gelatin Methacrylate Hydrogel for Tissue Engineering Applications—A Review on Material Modifications. *Pharm. 2022 Vol 15 Page 171* **2022**, *15* (2), 171. https://doi.org/10.3390/PH15020171.

(122) Jian, Z.; Zhuang, T.; Qinyu, T.; Liqing, P.; Kun, L.; Xujiang, L.; Diaodiao, W.; Zhen, Y.; Shuangpeng, J.; Xiang, S.; Jingxiang, H.; Shuyun, L.; Libo, H.; Peifu, T.; Qi, Y.; Quanyi, G. 3D Bioprinting of a Biomimetic Meniscal Scaffold for Application in Tissue Engineering. *Bioact. Mater.* **2020**, *6* (6), 1711. https://doi.org/10.1016/J.BIOACTMAT.2020.11.027.

(123) Bahcecioglu, G.; Bilgen, B.; Hasirci, N.; Hasirci, V. Anatomical Meniscus Construct with Zone Specific Biochemical Composition and Structural Organization. *Biomaterials* **2019**, *218*, 119361. https://doi.org/10.1016/J.BIOMATERIALS.2019.119361.

(124) Pawelec, K. M.; White, A. A.; Best, S. M. Properties and Characterization of Bone Repair Materials. *Bone Repair Biomater.*

Regen. Clin. Appl. Second Ed. **2019**, 65–102. https://doi.org/10.1016/B978-0-08-102451-5.00004-4.

(125) Veth, R. P. H.; Jansen, H. W. B.; Leenslag, J. W.; Pennings, A. J.; Hartel, R. M.; Nielsen, H. K. Experimental Meniscal Lesions Reconstructed with a Carbon Fiber-Polyurethane-Poly(L-Lactide) Graft. *Clin. Orthop.* **1986**, *202*, 286–293. https://doi.org/10.1097/00003086-198601000-00041.

(126) Klompmaker, J.; Jansen, H. W. B.; Veth, R. P. H.; de Groot, J. H.; Nijenhuis, A. J.; Pennings, A. J. Porous Polymer Implant for Repair of Meniscal Lesions: A Preliminary Study in Dogs. *Biomaterials* **1991**, *12* (9), 810–816. https://doi.org/10.1016/0142-9612(91)90066-J.

(127) Pezzin, A. P. T.; Cardoso, T. P.; Rincón, M. D. C. A.; De Carvalho Zavaglia, C. A.; Duek, E. A. D. R. Bioreabsorbable Polymer Scaffold as Temporary Meniscal Prosthesis. *Artif. Organs* **2003**, *27* (5), 428–431. https://doi.org/10.1046/J.1525-1594.2003.07251.X.

(128) Murakami, T.; Otsuki, S.; Nakagawa, K.; Okamoto, Y.; Inoue, T.; Sakamoto, Y.; Sato, H.; Neo, M. Establishment of Novel Meniscal Scaffold Structures Using Polyglycolic and Poly- l -Lactic Acids. *J. Biomater. Appl.* **2017**, *32* (2), 150–161. https://doi.org/10.1177/0885328217713631.

(129) Elsner, J. J.; Portnoy, S.; Zur, G.; Guilak, F.; Shterling, A.; Linder-Ganz, E. Design of a Free-Floating Polycarbonate-Urethane Meniscal Implant Using Finite Element Modeling and Experimental Validation. *J. Biomech. Eng.* **2010**, *132* (9). https://doi.org/10.1115/1.4001892.

(130) Linder-Ganz, E.; Elsner, J. J.; Zur, G.; Shani, J.; Brenner, O.; Hershman, E.; Shterling, A.; Guilak, F. Chondroprotective Effects of a Polycarbonate-Urethane Meniscal Implant: Semi-Quantitative Results in a Sheep Model. *ASME 2010 Summer Bioeng. Conf. SBC 2010* **2013**, No. PARTS A AND B, 761–762. https://doi.org/10.1115/SBC2010-19048.

(131) Kohli, S.; Schwenck, J.; Barlow, I. Failure Rates and Clinical Outcomes of Synthetic Meniscal Implants Following Partial Meniscectomy: A Systematic Review. *Knee Surg. Relat. Res.* **2022**, *34* (1), 1–9. https://doi.org/10.1186/S43019-022-00155-1/TABLES/5.

(132) Straeten, C. V. D.; Doyen, B.; Dutordoir, C.; Goedertier, W.; Pirard, S.; Victor, J. SHORT- AND MEDIUM-TERM RESULTS OF ARTIFICIAL MENISCAL IMPLANTS. *Orthop. Proc.* **2016**, *98-B* (SUPP_4), 91–91. https://doi.org/10.1302/1358-992X.98BSUPP_4.ISTA2014-091.

(133) Koller, U.; Nehrer, S.; Vavken, P.; Kapeller, B.; Windhager, R.; Chiari, C. Polyethylene Terephthalate (PET) Enhances Chondrogenic Differentiation of Ovine Meniscocytes in a Hyaluronic Acid/Polycaprolactone Scaffold in Vitro. *Int. Orthop.* **2012**, *36* (9), 1953. https://doi.org/10.1007/S00264-012-1534-5.

(134) Fisher, M. B.; Henning, E. A.; Söegaard, N.; Bostrom, M.; Esterhai, J. L.; Mauck, R. L. Engineering Meniscus Structure and Function via Multi-Layered Mesenchymal Stem Cell-Seeded Nanofibrous Scaffolds. *J. Biomech.* **2015**, *48* (8), 1412–1419. https://doi.org/10.1016/J.JBIOMECH.2015.02.036.

(135) Leroy, A.; Beaufils, P.; Faivre, B.; Steltzlen, C.; Boisrenoult, P.; Pujol, N. Actifit® Polyurethane Meniscal Scaffold: MRI and Functional Outcomes after a Minimum Follow-up of 5 Years. *Orthop. Traumatol. Surg. Res.* **2017**, *103* (4), 609–614. https://doi.org/10.1016/J.OTSR.2017.02.012.

(136) Vadodaria, K.; Kulkarni, A.; Santhini, E.; Vasudevan, P. Materials and Structures Used in Meniscus Repair and Regeneration: A Review. *BioMedicine* **2019**, *9* (1), 2. https://doi.org/10.1051/BMDCN/2019090102.

(137) Welsing, R. T. C.; Van Tienen, T. G.; Ramrattan, N.; Heijkants, R.; Schouten, A. J.; Veth, R. P. H.; Buma, P. Effect on Tissue Differentiation and Articular Cartilage Degradation of a Polymer

Meniscus Implant: A 2-Year Follow-up Study in Dogs. *Am. J. Sports Med.* **2008**, *36* (10), 1978–1989. https://doi.org/10.1177/0363546508319900.

(138) Yan, L. P.; Oliveira, J. M.; Oliveira, A. L.; Caridade, S. G.; Mano, J. F.; Reis, R. L. Macro/Microporous Silk Fibroin Scaffolds with Potential for Articular Cartilage and Meniscus Tissue Engineering Applications. *Acta Biomater.* **2012**, *8* (1), 289–301. https://doi.org/10.1016/J.ACTBIO.2011.09.037.

(139) Ahmed, E. M. Hydrogel: Preparation, Characterization, and Applications: A Review. *J. Adv. Res.* **2015**, *6* (2), 105–121. https://doi.org/10.1016/J.JARE.2013.07.006.

(140) Akalin, O. B.; Serafim, A.; Stancu, I. C.; Van Der Straeten, C.; Dubruel, P. 3D Printed Hydrogel Scaffolds for Meniscal Implant Application: Photo-Crosslinkable Urethane-Based Poly(Ethylene Glycol) as a Case Study. *Biomater. Sci.* **2026**. https://doi.org/10.1039/D4BM01730G.

(141) Minsart, M.; Deroose, N.; Parmentier, L.; Van Vlierberghe, S.; Mignon, A.; Dubruel, P. Fine-Tuning the Endcap Chemistry of Acrylated Poly(Ethylene Glycol)-Based Hydrogels for Efficient Burn Wound Exudate Management. *Macromol. Biosci.* **2023**, *23* (3). https://doi.org/10.1002/mabi.202200341.

(142) Minsart, M.; Mignon, A.; Arslan, A.; Allan, I. U.; Van Vlierberghe, S.; Dubruel, P. Activated Carbon Containing PEG-Based Hydrogels as Novel Candidate Dressings for the Treatment of Malodorous Wounds. *Macromol. Mater. Eng.* **2021**, *306* (1). https://doi.org/10.1002/mame.202000529.

(143) Houben, A.; Roose, P.; Van den Bergen, H.; Declercq, H.; Van Hoorick, J.; Gruber, P.; Ovsianikov, A.; Bontinck, D.; Van Vlierberghe, S.; Dubruel, P. Flexible Oligomer Spacers as the Key to Solid-State Photopolymerization of Hydrogel Precursors. *Mater. Today Chem.* **2017**, *4*, 84–89. https://doi.org/10.1016/j.mtchem.2017.01.005.

(144) Houben, A.; Van Hoorick, J.; Van Erps, J.; Thienpont, H.; Van Vlierberghe, S.; Dubruel, P. Indirect Rapid Prototyping: Opening Up Unprecedented Opportunities in Scaffold Design and Applications. *Ann. Biomed. Eng.* **2017**, *45* (1), 58–83. https://doi.org/10.1007/S10439-016-1610-X.

(145) Thijssen, Q.; Vlierberghe, S. V. Thiol-Mediated Chain Transfer as a Tool to Improve the Toughness of Acrylate Photo-Crosslinked Poly(ε-Caprolactone). *Macromol. Mater. Eng.* **2022**, *307* (3), 2100754. https://doi.org/10.1002/MAME.202100754.

(146) Thijssen, Q.; Parmentier, L.; Augustyniak, E.; Mouthuy, P. A.; Van Vlierberghe, S. From Chain Growth to Step Growth Polymerization of Photoreactive Poly-ε-Caprolactone: The Network Topology of Bioresorbable Networks as Tool in Tissue Engineering. *Adv. Funct. Mater.* **2022**, *32* (20), 2108869. https://doi.org/10.1002/ADFM.202108869.

(147) Sahranavard, M.; Zamanian, A.; Ghorbani, F.; Shahrezaee, M. H. A Critical Review on Three Dimensional-Printed Chitosan Hydrogels for Development of Tissue Engineering. *Bioprinting* **2020**, *17*, e00063. https://doi.org/10.1016/J.BPRINT.2019.E00063.

(148) Ionescu, O. M.; Mignon, A.; Minsart, M.; Caruntu, I. D.; Giusca, S. E.; Gardikiotis, I.; Van Vlierberghe, S.; Profire, L. Acrylate-Endcapped Urethane-Based Hydrogels: An in Vivo Study on Wound Healing Potential. *Mater. Sci. Eng. C* **2021**, *130*. https://doi.org/10.1016/j.msec.2021.112436.

(149) Pien, N.; Van de Maele, Y.; Parmentier, L.; Meeremans, M.; Mignon, A.; De Schauwer, C.; Peeters, I.; De Wilde, L.; Martens, A.; Mantovani, D.; Van Vlierberghe, S.; Dubruel, P. Design of an Electrospun Tubular Construct Combining a Mechanical and Biological Approach to Improve Tendon Repair. *J. Mater. Sci. Mater. Med.* **2022**, *33* (6). https://doi.org/10.1007/S10856-022-06673-4.

(150) Mignon, A.; Pezzoli, D.; Prouvé, E.; Lévesque, L.; Arslan, A.; Pien, N.; Schaubroeck, D.; Van Hoorick, J.; Mantovani, D.; Van Vlierberghe, S.; Dubruel, P. Combined Effect of Laponite and Polymer Molecular Weight on the Cell-Interactive Properties of Synthetic PEO-Based Hydrogels. *React. Funct. Polym.* **2019**, *136*, 95–106. https://doi.org/10.1016/j.reactfunctpolym.2018.12.017.

(151) Pien, N.; Pokholenko, I.; Deroose, N.; Perneel, C.; Vinturelle, R.; Meeremans, M.; Mantovani, D.; Van Vlierberghe, S.; De Schauwer, C. Toward In Vitro Vascular Wall Models: Digital Light Processing of Acrylate-Endcapped Urethane-Based Polymers into Tubular Constructs. *Macromol. Chem. Phys.* **2024**, *225* (24), 2400277. https://doi.org/10.1002/macp.202400277.

(152) Arslan, A.; Roose, P.; Houben, A.; Declercq, H.; Van Vlierberghe, S.; Dubruel, P. Printability Evaluation of UV-Curable Aqueous Laponite/Urethane-Based PEG Inks. *ACS Appl. Polym. Mater.* **2023**, *5* (4), 2345–2358. https://doi.org/10.1021/acsapm.2c02013.

(153) Galindo, J. M.; Deroose, N.; García-Béjar, B.; Damme, L. V.; Arévalo-Villena, M.; Merino, S.; Vázquez, E.; Herrero, M. A.; Dubruel, P. Graphene-Assisted Porosity in Acrylate-Endcapped Urethane-Based Hydrogels for Biomedical Applications. *Mater. Adv.* **2026**, *7* (8), 4266–4279. https://doi.org/10.1039/D6MA00095A.

(154) Pien, N.; Peeters, I.; Deconinck, L.; Van Damme, L.; De Wilde, L.; Martens, A.; Van Vlierberghe, S.; Dubruel, P.; Mignon, A. Design and Development of a Reinforced Tubular Electrospun Construct for the Repair of Ruptures of Deep Flexor Tendons. *Mater. Sci. Eng. C* **2021**, *119*, 111504. https://doi.org/10.1016/J.MSEC.2020.111504.

(155) Greant, C.; Van Durme, B.; Van Damme, L.; Brancart, J.; Van Hoorick, J.; Van Vlierberghe, S. Digital Light Processing of Poly(ε-Caprolactone)-Based Resins into Porous Shape Memory Scaffolds.

Eur. Polym. J. **2023**, *195*, 112225. https://doi.org/10.1016/J.EURPOLYMJ.2023.112225.

(156) Bandyopadhyay, A.; Mandal, B. B. A Three-Dimensional Printed Silk-Based Biomimetic Tri-Layered Meniscus for Potential Patient-Specific Implantation. *Biofabrication* **2020**, *12* (1). https://doi.org/10.1088/1758-5090/AB40FA.

(157) Yan, R.; Chen, Y.; Gu, Y.; Tang, C.; Huang, J.; Hu, Y.; Zheng, Z.; Ran, J.; Heng, B.; Chen, X.; Yin, Z.; Chen, W.; Shen, W.; Ouyang, H. A Collagen-Coated Sponge Silk Scaffold for Functional Meniscus Regeneration. *J. Tissue Eng. Regen. Med.* **2019**, *13* (2), 156–173. https://doi.org/10.1002/TERM.2777.

(158) Stein, S. E. C.; von Luebken, F.; Warnecke, D.; Gentilini, C.; Skaer, N.; Walker, R.; Kessler, O.; Ignatius, A.; Duerselen, L. The Challenge of Implant Integration in Partial Meniscal Replacement: An Experimental Study on a Silk Fibroin Scaffold in Sheep. *Knee Surg. Sports Traumatol. Arthrosc.* **2019**, *27* (2), 369–380. https://doi.org/10.1007/S00167-018-5160-7.

(159) Gruchenberg, K.; Ignatius, A.; Friemert, B.; von Lübken, F.; Skaer, N.; Gellynck, K.; Kessler, O.; Dürselen, L. In Vivo Performance of a Novel Silk Fibroin Scaffold for Partial Meniscal Replacement in a Sheep Model. *Knee Surg. Sports Traumatol. Arthrosc.* **2015**, *23* (8), 2218–2229. https://doi.org/10.1007/S00167-014-3009-2.

(160) Melrose, J. The Importance of the Knee Joint Meniscal Fibrocartilages as Stabilizing Weight Bearing Structures Providing Global Protection to Human Knee-Joint Tissues. *Cells 2019 Vol 8 Page 324* **2019**, *8* (4), 324. https://doi.org/10.3390/CELLS8040324.

(161) Bodin, A.; Concaro, S.; Brittberg, M.; Gatenholm, P. Bacterial Cellulose as a Potential Meniscus Implant. *J. Tissue Eng. Regen. Med.* **2007**, *1* (5), 406–408. https://doi.org/10.1002/TERM.51.

(162) Buma, P.; Ramrattan, N. N.; Van Tienen, T. G.; Veth, R. P. H. Tissue Engineering of the Meniscus. *Biomaterials* **2004**, *25* (9), 1523–1532. https://doi.org/10.1016/S0142-9612(03)00499-X.

(163) Rodkey, W. G.; DeHaven, K. E.; Montgomery, W. H.; Baker, C. L.; Beck, C. L.; Hormel, S. E.; Steadman, J. R.; Cole, B. J.; Briggs, K. K. Comparison of the Collagen Meniscus Implant with Partial Meniscectomy. A Prospective Randomized Trial. *J. Bone Joint Surg. Am.* **2008**, *90* (7), 1413–1426. https://doi.org/10.2106/JBJS.G.00656.

(164) Lombardo, M. D. M.; Mangiavini, L.; Peretti, G. M. Biomaterials and Meniscal Lesions: Current Concepts and Future Perspective. *Pharmaceutics* **2021**, *13* (11), 1886. https://doi.org/10.3390/PHARMACEUTICS13111886.

(165) Zaffagnini, S.; Marcheggiani Muccioli, G. M.; Lopomo, N.; Bruni, D.; Giordano, G.; Ravazzolo, G.; Molinari, M.; Marcacci, M. Prospective Long-Term Outcomes of the Medial Collagen Meniscus Implant Versus Partial Medial Meniscectomy. *https://doi.org/10.1177/0363546510391179* **2011**, *39* (5), 977–985. https://doi.org/10.1177/0363546510391179.

(166) Vrancken, A. C. T.; Buma, P.; Van Tienen, T. G. Synthetic Meniscus Replacement: A Review. *Int. Orthop.* **2012**, *37* (2), 291. https://doi.org/10.1007/S00264-012-1682-7.

(167) van Minnen, B. S.; van Tienen, T. G. The Current State of Meniscus Replacements. *Curr. Rev. Musculoskelet. Med.* **2024**, *17* (8), 293–302. https://doi.org/10.1007/S12178-024-09902-1/TABLES/2.

(168) Ho, T. C.; Chang, C. C.; Chan, H. P.; Chung, T. W.; Shu, C. W.; Chuang, K. P.; Duh, T. H.; Yang, M. H.; Tyan, Y. C. Hydrogels: Properties and Applications in Biomedicine. *Molecules* **2022**, *27* (9). https://doi.org/10.3390/MOLECULES27092902.

(169) Sachlos, E.; Czernuszka, J. T.; Gogolewski, S.; Dalby, M. Making Tissue Engineering Scaffolds Work. Review on the Application Ofsolid Freeform Fabrication Technology to the Production of Tissue

Engineeringscaffolds. *Eur. Cell. Mater.* **2003**, *5*, 29–40. https://doi.org/10.22203/ECM.V005A03.

(170) Hutmacher, D. W.; Sittinger, M.; Risbud, M. V. Scaffold-Based Tissue Engineering: Rationale for Computer-Aided Design and Solid Free-Form Fabrication Systems. *Trends Biotechnol.* **2004**, *22* (7), 354–362. https://doi.org/10.1016/J.TIBTECH.2004.05.005.

(171) Peltola, S. M.; Melchels, F. P. W.; Grijpma, D. W.; Kellomäki, M. A Review of Rapid Prototyping Techniques for Tissue Engineering Purposes. *Ann. Med.* **2008**, *40* (4), 268–280. https://doi.org/10.1080/07853890701881788.

(172) Vasiliadis, A. V.; Koukoulias, N.; Katakalos, K. Three-Dimensional-Printed Scaffolds for Meniscus Tissue Engineering: Opportunity for the Future in the Orthopaedic World. *J. Funct. Biomater. 2021 Vol 12 Page 69* **2021**, *12* (4), 69. https://doi.org/10.3390/JFB12040069.

(173) Betancourt, N.; Chen, X. Review of Extrusion-Based Multi-Material Bioprinting Processes. *Bioprinting* **2022**, *25*, e00189. https://doi.org/10.1016/J.BPRINT.2021.E00189.

(174) Hutmacher, D. W. Scaffolds in Tissue Engineering Bone and Cartilage. *Biomaterials* **2000**, *21* (24), 2529–2543. https://doi.org/10.1016/S0142-9612(00)00121-6.

(175) Hollister, S. J. Porous Scaffold Design for Tissue Engineering. *Nat. Mater.* **2005**, *4* (7), 518–524. https://doi.org/10.1038/nmat1421.

(176) Gleadall, A.; Visscher, D.; Yang, J.; Thomas, D.; Segal, J. Review of Additive Manufactured Tissue Engineering Scaffolds: Relationship between Geometry and Performance. *Burns Trauma* **2018**, *6* (1), 1–16. https://doi.org/10.1186/S41038-018-0121-4/FIGURES/11.

(177) Pfister, A.; Landers, R.; Laib, A.; Hübner, U.; Schmelzeisen, R.; Mülhaupt, R. Biofunctional Rapid Prototyping for Tissue-Engineering Applications: 3D Bioplotting versus 3D Printing. *J. Polym.*

Sci. Part Polym. Chem. **2004**, *42* (3), 624–638. https://doi.org/10.1002/POLA.10807.

(178) Yang, S.; Leong, K. F.; Du, Z.; Chua, C. K. The Design of Scaffolds for Use in Tissue Engineering. Part II. Rapid Prototyping Techniques. *Tissue Eng.* **2002**, *8* (1), 1–11. https://doi.org/10.1089/107632702753503009.

(179) Parulski, C.; Jennotte, O.; Lechanteur, A.; Evrard, B. Challenges of Fused Deposition Modeling 3D Printing in Pharmaceutical Applications: Where Are We Now? *Adv. Drug Deliv. Rev.* **2021**, *175*, 113810. https://doi.org/10.1016/J.ADDR.2021.05.020.

(180) Esposito Corcione, C.; Gervaso, F.; Scalera, F.; Padmanabhan, S. K.; Madaghiele, M.; Montagna, F.; Sannino, A.; Licciulli, A.; Maffezzoli, A. Highly Loaded Hydroxyapatite Microsphere/ PLA Porous Scaffolds Obtained by Fused Deposition Modelling. *Ceram. Int.* **2019**, *45* (2), 2803–2810. https://doi.org/10.1016/J.CERAMINT.2018.07.297.

(181) Lobo, D. A.; Ginestra, P. Cell Bioprinting: The 3D-Bioplotter™ Case. *Materials* **2019**, *12* (23), 4005. https://doi.org/10.3390/MA12234005.

(182) Landers, R.; Hübner, U.; Schmelzeisen, R.; Mülhaupt, R. Rapid Prototyping of Scaffolds Derived from Thermoreversible Hydrogels and Tailored for Applications in Tissue Engineering. *Biomaterials* **2002**, *23* (23), 4437–4447. https://doi.org/10.1016/S0142-9612(02)00139-4.

(183) Woods, P.; Smith, C.; Clark, S.; Habib, A. Integrating Pneumatic and Thermal Control in 3D Bioprinting for Improved Bio-Ink Handling. *Des. 2024 Vol 8 Page 83* **2024**, *8* (4), 83. https://doi.org/10.3390/DESIGNS8040083.

(184) Zhang, Y. S.; Haghiashtiani, G.; Hübscher, T.; Kelly, D. J.; Lee, J. M.; Lutolf, M.; McAlpine, M. C.; Yeong, W. Y.; Zenobi-Wong, M.;

Malda, J. 3D Extrusion Bioprinting. *Nat. Rev. Methods Primer* **2021**, *1* (1), 75. https://doi.org/10.1038/s43586-021-00073-8.

(185) Ozbolat, I. T. Bioprinting Scale-up Tissue and Organ Constructs for Transplantation. *Trends Biotechnol.* **2015**, *33* (7), 395–400. https://doi.org/10.1016/J.TIBTECH.2015.04.005.

(186) Willson, K.; Ke, D.; Kengla, C.; Atala, A.; Murphy, S. V. Extrusion-Based Bioprinting: Current Standards and Relevancy for Human-Sized Tissue Fabrication. *Methods Mol. Biol.* **2020**, *2140*, 65–92. https://doi.org/10.1007/978-1-0716-0520-2_5/FIGURES/3.

(187) Ravanbakhsh, H.; Karamzadeh, V.; Bao, G.; Mongeau, L.; Juncker, D.; Zhang, Y. S.; Ravanbakhsh, H.; Zhang, Y. S.; Bao, G.; Mongeau, L.; Karamzadeh, V.; Juncker, D. Emerging Technologies in Multi-Material Bioprinting. *Adv. Mater.* **2021**, *33* (49), 2104730. https://doi.org/10.1002/ADMA.202104730.

(188) Chekkaramkodi, D.; Jacob, L.; C, M. S.; Umer, R.; Butt, H. Review of Vat Photopolymerization 3D Printing of Photonic Devices. *Addit. Manuf.* **2024**, *86*, 104189. https://doi.org/10.1016/J.ADDMA.2024.104189.

(189) Zhang, Z.-Z.; Wang, S.-J.; Zhang, J.-Y.; Jiang, W.-B.; Huang, A.-B.; Qi, Y.-S.; Ding, J.-X.; Chen, X.-S.; Jiang, D.; Yu, J.-K. 3D-Printed Poly(ε-Caprolactone) Scaffold Augmented With Mesenchymal Stem Cells for Total Meniscal Substitution: A 12- and 24-Week Animal Study in a Rabbit Model. *Am. J. Sports Med.* **2017**, *45* (7), 1497–1511. https://doi.org/10.1177/0363546517691513.

(190) Zhang, Z.-Z.; Chen, Y.-R.; Wang, S.-J.; Zhao, F.; Wang, X.-G.; Yang, F.; Shi, J.-J.; Ge, Z.-G.; Ding, W.-Y.; Yang, Y.-C.; Zou, T.-Q.; Zhang, J.-Y.; Yu, J.-K.; Jiang, D. Orchestrated Biomechanical, Structural, and Biochemical Stimuli for Engineering Anisotropic Meniscus. *Sci. Transl. Med.* **2019**, *11* (487), eaao0750. https://doi.org/10.1126/scitranslmed.aao0750.

(191) Deng, X.; Chen, X.; Geng, F.; Tang, X.; Li, Z.; Zhang, J.; Wang, Y.; Wang, F.; Zheng, N.; Wang, P.; Yu, X.; Hou, S.; Zhang, W. Precision 3D Printed Meniscus Scaffolds to Facilitate hMSCs Proliferation and Chondrogenic Differentiation for Tissue Regeneration. *J. Nanobiotechnology* **2021**, *19* (1), 400. https://doi.org/10.1186/s12951-021-01141-7.

(192) Kalossaka, L. M.; Sena, G.; Barter, L. M. C.; Myant, C. Review: 3D Printing Hydrogels for the Fabrication of Soilless Cultivation Substrates. *Appl. Mater. Today* **2021**, *24*, 101088. https://doi.org/10.1016/J.APMT.2021.101088.

(193) Ho, C. M. B.; Ng, S. H.; Yoon, Y. J. A Review on 3D Printed Bioimplants. *Int. J. Precis. Eng. Manuf.* **2015**, *16* (5), 1035–1046. https://doi.org/10.1007/S12541-015-0134-X/METRICS.

(194) Yang, Y.; Wang, G.; Liang, H.; Gao, C.; Peng, S.; Shen, L.; Shuai, C. Additive Manufacturing of Bone Scaffolds. *Int. J. Bioprinting* **2018**, *5* (1), 148. https://doi.org/10.18063/IJB.V5I1.148.

(195) Román, A. J.; Dibisa, O.; Perilla, J.; Lendvai, L.; Osswald, T. A. Additive Manufacturing of Rubbers: A New Frontier in Polymer Science. *Rubber Mater.* **2025**, 601–640. https://doi.org/10.1016/B978-0-443-28989-7.00024-9.

(196) Kalsoom, U.; Nesterenko, P. N.; Paull, B. Current and Future Impact of 3D Printing on the Separation Sciences. *TrAC Trends Anal. Chem.* **2018**, *105*, 492–502. https://doi.org/10.1016/J.TRAC.2018.06.006.

(197) Ho, C. M. B.; Mishra, A.; Hu, K.; An, J.; Kim, Y. J.; Yoon, Y. J. Femtosecond-Laser-Based 3D Printing for Tissue Engineering and Cell Biology Applications. *ACS Biomater. Sci. Eng.* **2017**, *3* (10), 2198–2214.
https://doi.org/10.1021/ACSBIOMATERIALS.7B00438/ASSET/IMAGES/LARGE/AB-2017-00438Z_0018.JPEG.

(198) Li, H.; Dai, J.; Wang, Z.; Zheng, H.; Li, W.; Wang, M.; Cheng, F. Digital Light Processing (DLP)-Based (Bio)Printing Strategies for Tissue Modeling and Regeneration. *Aggregate* **2023**, *4* (2), e270. https://doi.org/10.1002/AGT2.270.

(199) Chaudhary, R.; Fabbri, P.; Leoni, E.; Mazzanti, F.; Akbari, R.; Antonini, C. Additive Manufacturing by Digital Light Processing: A Review. *Prog. Addit. Manuf. 2022 82* **2022**, *8* (2), 331–351. https://doi.org/10.1007/S40964-022-00336-0.

(200) Mondschein, R. J.; Kanitkar, A.; Williams, C. B.; Verbridge, S. S.; Long, T. E. Polymer Structure-Property Requirements for Stereolithographic 3D Printing of Soft Tissue Engineering Scaffolds. *Biomaterials* **2017**, *140*, 170–188. https://doi.org/10.1016/J.BIOMATERIALS.2017.06.005.

(201) Mondrinos, M. J.; Dembzynski, R.; Lu, L.; Byrapogu, V. K. C.; Wootton, D. M.; Lelkes, P. I.; Zhou, J. Porogen-Based Solid Freeform Fabrication of Polycaprolactone–Calcium Phosphate Scaffolds for Tissue Engineering. *Biomaterials* **2006**, *27* (25), 4399–4408. https://doi.org/10.1016/J.BIOMATERIALS.2006.03.049.

(202) Grogan, S. P.; Chung, P. H.; Soman, P.; Chen, P.; Lotz, M. K.; Chen, S.; D'Lima, D. D. Digital Micromirror Device Projection Printing System for Meniscus Tissue Engineering. *Acta Biomater.* **2013**, *9* (7), 7218–7226. https://doi.org/10.1016/J.ACTBIO.2013.03.020.

(203) Yang, Y.; Chen, Z.; Song, X.; Zhang, Z.; Zhang, J.; Shung, K. K.; Zhou, Q.; Chen, Y. Biomimetic Anisotropic Reinforcement Architectures by Electrically Assisted Nanocomposite 3D Printing. *Adv. Mater.* **2017**, *29* (11). https://doi.org/10.1002/adma.201605750.

(204) Taboas, J. M.; Maddox, R. D.; Krebsbach, P. H.; Hollister, S. J. Indirect Solid Free Form Fabrication of Local and Global Porous, Biomimetic and Composite 3D Polymer-Ceramic Scaffolds. *Biomaterials* **2003**, *24* (1), 181–194. https://doi.org/10.1016/S0142-9612(02)00276-4.

(205) Lee, M.; Wu, B. M.; Dunn, J. C. Y. Effect of Scaffold Architecture and Pore Size on Smooth Muscle Cell Growth. *J. Biomed. Mater. Res. A* **2008**, *87* (4), 1010–1016. https://doi.org/10.1002/JBM.A.31816.

(206) Chu, T. M. G.; Halloran, J. W.; Hollister, S. J.; Feinberg, S. E. Hydroxyapatite Implants with Designed Internal Architecture. *J. Mater. Sci. Mater. Med.* **2001**, *12* (6), 471–478. https://doi.org/10.1023/A:1011203226053.

(207) Schumacher, M.; Uhl, F.; Detsch, R.; Deisinger, U.; Ziegler, G. Static and Dynamic Cultivation of Bone Marrow Stromal Cells on Biphasic Calcium Phosphate Scaffolds Derived from an Indirect Rapid Prototyping Technique. *J. Mater. Sci. Mater. Med.* **2010**, *21* (11), 3039–3048. https://doi.org/10.1007/S10856-010-4153-Y.

(208) Schumacher, M.; Deisinger, U.; Ziegler, G.; Detsch, R. Indirect Rapid Prototyping of Biphasic Calcium Phosphate Scaffolds as Bone Substitutes: Influence of Phase Composition, Macroporosity and Pore Geometry on Mechanical Properties. *J. Mater. Sci. Mater. Med.* **2010**, *21* (12), 3119–3127. https://doi.org/10.1007/S10856-010-4166-6/TABLES/2.

(209) Burdick, J. A.; Mason, M. N.; Hinman, A. D.; Thorne, K.; Anseth, K. S. Delivery of Osteoinductive Growth Factors from Degradable PEG Hydrogels Influences Osteoblast Differentiation and Mineralization. *J. Controlled Release* **2002**, *83* (1), 53–63. https://doi.org/10.1016/S0168-3659(02)00181-5.

(210) De Maria, C.; De Acutis, A.; Vozzi, G. Indirect Rapid Prototyping for Tissue Engineering. *Essent. 3D Biofabrication Transl.* **2015**, 153–164. https://doi.org/10.1016/B978-0-12-800972-7.00008-6.

(211) Chen, Z.; Li, D.; Lu, B.; Tang, Y.; Sun, M.; Wang, Z. Fabrication of Artificial Bioactive Bone Using Rapid Prototyping. *Rapid Prototyp. J.* **2004**, *10* (5), 327–333. https://doi.org/10.1108/13552540410562368/FULL/XML.

(212) Van Hoorick, J.; Declercq, H.; De Muynck, A.; Houben, A.; Van Hoorebeke, L.; Cornelissen, R.; Van Erps, J.; Thienpont, H.; Dubruel, P.; Van Vlierberghe, S. Indirect Additive Manufacturing as an Elegant Tool for the Production of Self-Supporting Low Density Gelatin Scaffolds. *J. Mater. Sci. Mater. Med.* **2015**, *26* (10). https://doi.org/10.1007/S10856-015-5566-4.

(213) Chen, X. B.; Fazel Anvari-Yazdi, A.; Duan, X.; Zimmerling, A.; Gharraei, R.; Sharma, N. K.; Sweilem, S.; Ning, L. Biomaterials / Bioinks and Extrusion Bioprinting. *Bioact. Mater.* **2023**, *28*, 511–536. https://doi.org/10.1016/J.BIOACTMAT.2023.06.006.

(214) P.b., S.; S., G.; J., P.; Muthusamy, S.; R., N.; Krishnakumar, G. S.; R., S. Tricomposite Gelatin-Carboxymethylcellulose-Alginate Bioink for Direct and Indirect 3D Printing of Human Knee Meniscal Scaffold. *Int. J. Biol. Macromol.* **2022**, *195*, 179–189. https://doi.org/10.1016/j.ijbiomac.2021.11.184.

(215) El Kommos, A.; Magesh, P.; Lattanze, S.; Perros, A.; Andreopoulos, F.; Travascio, F.; Jackson, A. Hybrid Hydrogels Augmented via Additive Network Integration (HANI) for Meniscal Tissue Engineering Applications. *Gels* **2025**, *11* (4), 223. https://doi.org/10.3390/gels11040223.

(216) Van Der Straeten, C.; Byttebier, P.; Eeckhoudt, A.; Victor, J. Meniscal Allograft Transplantation Does Not Prevent or Delay Progression of Knee Osteoarthritis. *PLoS ONE* **2016**, *11* (5). https://doi.org/10.1371/JOURNAL.PONE.0156183.

(217) Murphy, C. A.; Costa, J. B.; Silva-Correia, J.; Oliveira, J. M.; Reis, R. L.; Collins, M. N. Biopolymers and Polymers in the Search of Alternative Treatments for Meniscal Regeneration: State of the Art and Future Trends. *Appl. Mater. Today* **2018**, *12*, 51–71. https://doi.org/10.1016/J.APMT.2018.04.002.

(218) Grabner, M.; Wolf, A.; Schwabl, E.; Schickhofer, G. Methods of Forming Veneer Structures, 2016, 1027_a.

https://graz.elsevierpure.com/en/publications/methods-of-forming-veneer-structures-2 (accessed 2024-09-16).

(219) Declercq, H. A.; Desmet, T.; Berneel, E. E. M.; Dubruel, P.; Cornelissen, M. J. Synergistic Effect of Surface Modification and Scaffold Design of Bioplotted 3-D Poly-ε-Caprolactone Scaffolds in Osteogenic Tissue Engineering. *Acta Biomater.* **2013**, *9* (8), 7699–7708. https://doi.org/10.1016/j.actbio.2013.05.003.

(220) Ragaert, K.; De Somer, F.; Van De Velde, S.; Degrieck, J.; Cardon, L. *Methods for Improved Flexural Mechanical Properties of 3D-Plotted PCL-Based Scaffolds for Heart Valve Tissue Engineering*.

(221) Ragaert, K.; Cardon, L.; Dekeyser, A.; Degrieck, J. Machine Design and Processing Considerations for the 3D Plotting of Thermoplastic Scaffolds. *Biofabrication* **2010**, *2* (1). https://doi.org/10.1088/1758-5082/2/1/014107.

(222) Dabiri, S. M. H.; Lagazzo, A.; Barberis, F.; Shayganpour, A.; Finocchio, E.; Pastorino, L. New In-Situ Synthetized Hydrogel Composite Based on Alginate and Brushite as a Potential pH Sensitive Drug Delivery System. *Carbohydr. Polym.* **2017**, *177*, 324–333. https://doi.org/10.1016/j.carbpol.2017.08.046.

(223) Heller, R. A. Mechanics of Structures. *Encycl. Phys. Sci. Technol.* **2003**, 259–278. https://doi.org/10.1016/B0-12-227410-5/00415-4.

(224) Billah, K. Y.; Scanlan, R. H. Resonance, Tacoma Narrows Bridge Failure, and Undergraduate Physics Textbooks. *Am. J. Phys.* **1991**, *59* (2), 118–124. https://doi.org/10.1119/1.16590.

(225) Mantha, S.; Pillai, S.; Khayambashi, P.; Upadhyay, A.; Zhang, Y.; Tao, O.; Pham, H. M.; Tran, S. D. Smart Hydrogels in Tissue Engineering and Regenerative Medicine. *Materials* **2019**, *12* (20). https://doi.org/10.3390/MA12203323.

(226) Pien, N.; Deroose, N.; Meeremans, M.; Perneel, C.; Popovici, C. Ş.; Dubruel, P.; De Schauwer, C.; Van Vlierberghe, S. Tailorable

Acrylate-Endcapped Urethane-Based Polymers for Precision in Digital Light Processing: Versatile Solutions for Biomedical Applications. *Biomater. Adv.* **2024**, *162*, 213923. https://doi.org/10.1016/J.BIOADV.2024.213923.

(227) Arslan, A.; Steiger, W.; Roose, P.; Van den Bergen, H.; Gruber, P.; Zerobin, E.; Gantner, F.; Guillaume, O.; Ovsianikov, A.; Van Vlierberghe, S.; Dubruel, P. Polymer Architecture as Key to Unprecedented High-Resolution 3D-Printing Performance: The Case of Biodegradable Hexa-Functional Telechelic Urethane-Based Poly-ε-Caprolactone. *Mater. Today* **2021**, *44*, 25–39. https://doi.org/10.1016/J.MATTOD.2020.10.005.

(228) Aagaard, H.; Verdonk, R. Function of the Normal Meniscus and Consequences of Meniscal Resection. *Scand. J. Med. Sci. Sports* **1999**, *9* (3), 134–140. https://doi.org/10.1111/J.1600-0838.1999.TB00443.X.

(229) Wang, S.; Hase, K.; Kita, S.; Ogaya, S. Biomechanical Effects of Medial Meniscus Radial Tears on the Knee Joint during Gait: A Concurrent Finite Element Musculoskeletal Framework Investigation. *Front. Bioeng. Biotechnol.* **2022**, *10*. https://doi.org/10.3389/FBIOE.2022.957435.

(230) Cao, H.; Chang, X.; Mao, H.; Zhou, J.; Wu, Z. L.; Shan, G.; Bao, Y.; Pan, P. Stereocomplexed Physical Hydrogels with High Strength and Tunable Crystallizability. *Soft Matter* **2017**, *13* (45), 8502–8510. https://doi.org/10.1039/C7SM01491K.

(231) Jiang, P.; Yan, C.; Guo, Y.; Zhang, X.; Cai, M.; Jia, X.; Wang, X.; Zhou, F. Direct Ink Writing with High-Strength and Swelling-Resistant Biocompatible Physically Crosslinked Hydrogels. *Biomater. Sci.* **2019**, *7* (5), 1805–1814. https://doi.org/10.1039/C9BM00081J.

(232) ALEXANDER, H.; BRUNSKI, J. B.; COOPER, S. L.; HENCH, L. L.; HERGENROTHER, R. W.; HOFFMAN, A. S.; KOHN, J.; LANGER, R.; PEPPAS, N. A.; RATNER, B. D.; SHALABY, S. W.;

VISSER, S. A.; YANNAS, I. V. Classes of Materials Used in Medicine. *Biomater. Sci.* **1996**, 37–130. https://doi.org/10.1016/B978-0-08-050014-0.50007-9.

(233) De Souza, F. M.; Kahol, P. K.; Gupta, R. K. Introduction to Polyurethane Chemistry. *ACS Symp. Ser.* **2021**, *1380*, 1–24. https://doi.org/10.1021/BK-2021-1380.CH001/ASSET/IMAGES/LARGE/BK-2020-00517M_G020.JPEG.

(234) Kędzierska, M.; Bańkosz, M.; Potemski, P. Studies on the Impact of the Photoinitiator Amount Used during the PVP-Based Hydrogels' Synthesis on Their Physicochemical Properties. *Materials* **2022**, *15* (17). https://doi.org/10.3390/ma15176089.

(235) Wiley, K. L.; Ovadia, E. M.; Calo, C. J.; Huber, R. E.; Kloxin, A. M. Rate-Based Approach for Controlling the Mechanical Properties of 'Thiol-Ene' Hydrogels Formed with Visible Light. *Polym. Chem.* **2019**, *10* (32), 4428. https://doi.org/10.1039/c9py00447e.

(236) Lebedevaite, M.; Ostrauskaite, J. Influence of Photoinitiator and Temperature on Photocross-Linking Kinetics of Acrylated Epoxidized Soybean Oil and Properties of the Resulting Polymers. *Ind. Crops Prod.* **2021**, *161*, 113210. https://doi.org/10.1016/J.INDCROP.2020.113210.

(237) Ma, S.; Jiang, Y.; Liu, X.; Fan, L.; Zhu, J. Bio-Based Tetrafunctional Crosslink Agent from Gallic Acid and Its Enhanced Soybean Oil-Based UV-Cured Coatings with High Performance. *RSC Adv.* **2014**, *4* (44), 23036–23042. https://doi.org/10.1039/C4RA01311E.

(238) Steyrer, B.; Neubauer, P.; Liska, R.; Stampfl, J. Visible Light Photoinitiator for 3D-Printing of Tough Methacrylate Resins. *Mater. Basel Switz.* **2017**, *10* (12). https://doi.org/10.3390/MA10121445.

(239) Maziz, A.; Leprette, O.; Boyer, L.; Blatché, C.; Bergaud, C. Tuning the Properties of Silk Fibroin Biomaterial via Chemical Cross-

Linking. *Biomed. Phys. Eng. Express* **2018**, *4* (6), 065012. https://doi.org/10.1088/2057-1976/AAE3B2.

(240) Olubamiji, A. D.; Izadifar, Z.; Si, J. L.; Cooper, D. M. L.; Eames, B. F.; Chen, D. X. B. Modulating Mechanical Behaviour of 3D-Printed Cartilage-Mimetic PCL Scaffolds: Influence of Molecular Weight and Pore Geometry. *Biofabrication* **2016**, *8* (2), 025020. https://doi.org/10.1088/1758-5090/8/2/025020.

(241) Khan, M. A.; Azad, A. K.; Safdar, M.; Nawaz, A.; Akhlaq, M.; Paul, P.; Hossain, M. K.; Rahman, M. H.; Baty, R. S.; El-Kott, A. F.; Kamel, M.; Bungau, S. G.; Abdel-Daim, M. M. Synthesis and Characterization of Acrylamide/Acrylic Acid Co-Polymers and Glutaraldehyde Crosslinked pH-Sensitive Hydrogels. *Gels 2022 Vol 8 Page 47* **2022**, *8* (1), 47. https://doi.org/10.3390/GELS8010047.

(242) Ali, M.; Hussain, Z.; Basit, H. M.; Mahmood, S.; Ullah, N. Novel Composite pH Controlled Drug Release Hydrogel Containing Dexibuprofen. *RADS J. Pharm. Pharm. Sci.* **2018**, *6* (4), 223–235.

(243) Tytgat, L.; Van Damme, L.; Van Hoorick, J.; Declercq, H.; Thienpont, H.; Ottevaere, H.; Blondeel, P.; Dubruel, P.; Van Vlierberghe, S. Additive Manufacturing of Photo-Crosslinked Gelatin Scaffolds for Adipose Tissue Engineering. *Acta Biomater.* **2019**, *94*, 340–350. https://doi.org/10.1016/J.ACTBIO.2019.05.062.

(244) Lüchow, M.; Fortuin, L.; Malkoch, M. Modular, Synthetic, Thiol-Ene Mediated Hydrogel Networks as Potential Scaffolds for 3D Cell Cultures and Tissue Regeneration. *J. Polym. Sci.* **2020**, *58* (22), 3153–3164. https://doi.org/10.1002/POL.20200530.

(245) Morejon, A.; Norberg, C. D.; De Rosa, M.; Best, T. M.; Jackson, A. R.; Travascio, F. Compressive Properties and Hydraulic Permeability of Human Meniscus: Relationships With Tissue Structure and Composition. *Front. Bioeng. Biotechnol.* **2021**, *8*, 622552. https://doi.org/10.3389/FBIOE.2020.622552/BIBTEX.

(246) Grassi, A.; Dal Fabbro, G.; Di Paolo, S.; Lucidi, G. A.; Macchiarola, L.; Al-Khelaifi, K.; Zaffagnini, S. Meniscus Biomechanics. *Orthop. Biomech. Sports Med.* **2021**, 345–360. https://doi.org/10.1007/978-3-030-81549-3_27.

(247) Tsai, S. W. A i THEORY OF COMPOSITES DESIGN 2008.

(248) Tellis, B. C.; Szivek, J. A.; Bliss, C. L.; Margolis, D. S.; Vaidyanathan, R. K.; Calvert, P. Trabecular Scaffolds Created Using Micro CT Guided Fused Deposition Modeling. *Mater. Sci. Eng. C Mater. Biol. Appl.* **2009**, *28* (1), 171. https://doi.org/10.1016/J.MSEC.2006.11.010.

(249) Domingos, M.; Intranuovo, F.; Russo, T.; Santis, R. D.; Gloria, A.; Ambrosio, L.; Ciurana, J.; Bartolo, P. The First Systematic Analysis of 3D Rapid Prototyped Poly(ε-Caprolactone) Scaffolds Manufactured through BioCell Printing: The Effect of Pore Size and Geometry on Compressive Mechanical Behaviour and in Vitro hMSC Viability. *Biofabrication* **2013**, *5* (4). https://doi.org/10.1088/1758-5082/5/4/045004.

(250) Ruiz-Cantu, L.; Gleadall, A.; Faris, C.; Segal, J.; Shakesheff, K.; Yang, J. Characterisation of the Surface Structure of 3D Printed Scaffolds for Cell Infiltration and Surgical Suturing. *Biofabrication* **2016**, *8* (1). https://doi.org/10.1088/1758-5090/8/1/015016.

(251) Wheatley, B. B.; Fischenich, K. M.; Button, K. D.; Haut, R. C.; Haut Donahue, T. L. An Optimized Transversely Isotropic, Hyper-Poro-Viscoelastic Finite Element Model of the Meniscus to Evaluate Mechanical Degradation Following Traumatic Loading. *J. Biomech.* **2015**, *48* (8), 1454. https://doi.org/10.1016/J.JBIOMECH.2015.02.028.

(252) Merxhani, A. An Introduction to Linear Poroelasticity. **2016**.

(253) Heinemann, P.; Kasperski, M. Damping Induced by Walking and Running. *Procedia Eng.* **2017**, *199*, 2826–2831. https://doi.org/10.1016/J.PROENG.2017.09.537.

(254) Damme, L. V.; Briant, E.; Blondeel, P.; Van Vlierberghe, S. *Indirect versus Direct 3D Printing of Hydrogel Scaffolds for Adipose Tissue Regeneration*.

(255) Xie, Z.; Gao, M.; Lobo, A. O.; Webster, T. J. 3D Bioprinting in Tissue Engineering for Medical Applications: The Classic and the Hybrid. *Polymers* **2020**, *12* (8), 1717. https://doi.org/10.3390/POLYM12081717.

(256) Melcher, R.; Martins, S.; Travitzky, N.; Greil, P. Fabrication of Al2O3-Based Composites by Indirect 3D-Printing. *Mater. Lett.* **2006**, *60* (4), 572–575. https://doi.org/10.1016/J.MATLET.2005.09.059.

(257) Lee, M.; Dunn, J. C. Y.; Wu, B. M. Scaffold Fabrication by Indirect Three-Dimensional Printing. *Biomaterials* **2005**, *26* (20), 4281–4289. https://doi.org/10.1016/J.BIOMATERIALS.2004.10.040.

(258) Lee, J. Y.; Choi, B.; Wu, B.; Lee, M. Customized Biomimetic Scaffolds Created by Indirect Three-Dimensional Printing for Tissue Engineering. *Biofabrication* **2013**, *5* (4). https://doi.org/10.1088/1758-5082/5/4/045003.

(259) Costa, J. B.; Silva-Correia, J.; Pina, S.; da Silva Morais, A.; Vieira, S.; Pereira, H.; Espregueira-Mendes, J.; Reis, R. L.; Oliveira, J. M. Indirect Printing of Hierarchical Patient-Specific Scaffolds for Meniscus Tissue Engineering. *Bio-Des. Manuf.* **2019**, *2* (4), 225–241. https://doi.org/10.1007/s42242-019-00050-x.

(260) Noe Ralf; Henne Andreas; Maase Matthias. Acyl- and Bisacylphosphine Derivatives (WO2003068784A2).

(261) Schaller, C. *POLYMER CHEMISTRY*. https://chem.libretexts.org/Bookshelves/Organic_Chemistry/Polymer_Chemistry_(Schaller) (accessed 2025-12-04).

(262) Huggins, M. L. The Viscosity of Dilute Solutions of Long-Chain Molecules. IV. Dependence on Concentration. *J. Am. Chem. Soc.* **1942**, *64* (11), 2716–2718.

https://doi.org/10.1021/JA01263A056/ASSET/JA01263A056.FP.PNG_V03.

(263) Cacopardo, L.; Guazzelli, N.; Nossa, R.; Mattei, G.; Ahluwalia, A. Engineering Hydrogel Viscoelasticity. *J. Mech. Behav. Biomed. Mater.* **2019**, *89*, 162–167. https://doi.org/10.1016/J.JMBBM.2018.09.031.

(264) Fang, J. Y.; Chen, J. P.; Leu, Y. L.; Wang, H. Y. Characterization and Evaluation of Silk Protein Hydrogels for Drug Delivery. *Chem. Pharm. Bull. (Tokyo)* **2006**, *54* (2), 156–162. https://doi.org/10.1248/CPB.54.156.

(265) Doyle, S. E.; Duchi, S.; Onofrillo, C.; Quigley, A.; Di Bella, C.; Pirogova, E.; O'Connell, C. D. Printing between the Lines: Intricate Biomaterial Structures Fabricated via Negative Embodied Sacrificial Template 3D (NEST3D) Printing. *Adv. Mater. Technol.* **2021**, *6* (7), 2100189. https://doi.org/10.1002/ADMT.202100189.

(266) Darwis, D.; Mitomo, H.; Enjoji, T.; Yoshii, F.; Makuuchi, K. Heat Resistance of Radiation Crosslinked Poly (ε-Caprolactone). *J. Appl. Polym. Sci.* **1998**, *68* (4), 581–588. https://doi.org/10.1002/(SICI)1097-4628(19980425)68:4%3C581::AID-APP9%3E3.0.CO;2-I.

(267) Declercq, H. A.; Desmet, T.; Dubruel, P.; Cornelissen, M. J. The Role of Scaffold Architecture and Composition on the Bone Formation by Adipose-Derived Stem Cells. *Tissue Eng. Part A* **2013**, *20* (1–2), 434. https://doi.org/10.1089/TEN.TEA.2013.0179.

(268) Singh, M. K.; Singh, A. Thermogravimetric Analyzer. *Charact. Polym. Fibres* **2022**, 223–240. https://doi.org/10.1016/B978-0-12-823986-5.00015-4.

(269) Ratna, D. Characterization, Performance Evaluation and Lifetime Analysis of Thermoset Resin. *Recent Adv. Appl. Thermoset Resins* **2022**, 503–582. https://doi.org/10.1016/B978-0-323-85664-5.00004-1.

(270) Zou, H.; Yi, C.; Wang, L.; Liu, H.; Xu, W. Thermal Degradation of Poly(Lactic Acid) Measured by Thermogravimetry Coupled to Fourier Transform Infrared Spectroscopy. *J. Therm. Anal. Calorim.* **2009**, *97* (3), 929–935. https://doi.org/10.1007/S10973-009-0121-5/METRICS.

(271) Menczel, J. D.; Prime, R. B. Thermal Analysis of Polymers: Fundamentals and Applications. *Therm. Anal. Polym. Fundam. Appl.* **2008**, 1–688. https://doi.org/10.1002/9780470423837.

(272) Test Method for Compositional Analysis by Thermogravimetry, 2020. https://doi.org/10.1520/E1131-20.

(273) *TA Instruments, Thermal Analysis, TGA Q500 Specifications 20212 TA Instruments. Available on Tainstruments.Com*. tainstruments.com (accessed 2025-02-18).

(274) Halligan, E.; Tie, B. S. H.; Colbert, D. M.; Alsaadi, M.; Zhuo, S.; Keane, G.; Geever, L. M. Synthesis and Characterisation of Hydrogels Based on Poly (N-Vinylcaprolactam) with Diethylene Glycol Diacrylate. *Gels 2023 Vol 9 Page 439* **2023**, *9* (6), 439. https://doi.org/10.3390/GELS9060439.

(275) Song, X.; Zhu, C.; Fan, D.; Mi, Y.; Li, X.; Fu, R. Z.; Duan, Z.; Wang, Y.; Feng, R. R. A Novel Human-Like Collagen Hydrogel Scaffold with Porous Structure and Sponge-Like Properties. *Polymers* **2017**, *9* (12), 638. https://doi.org/10.3390/POLYM9120638.

(276) Naghieh, S.; Karamooz-Ravari, M. R.; Sarker, M. D.; Karki, E.; Chen, X. Influence of Crosslinking on the Mechanical Behavior of 3D Printed Alginate Scaffolds: Experimental and Numerical Approaches. *J. Mech. Behav. Biomed. Mater.* **2018**, *80*, 111–118. https://doi.org/10.1016/j.jmbbm.2018.01.034.

(277) Polez, R. T.; Morits, M.; Jonkergouw, C.; Phiri, J.; Valle-Delgado, J. J.; Linder, M. B.; Maloney, T.; Rojas, O. J.; Österberg, M. Biological Activity of Multicomponent Bio-Hydrogels Loaded with

Tragacanth Gum. *Int. J. Biol. Macromol.* **2022**, *215*, 691–704. https://doi.org/10.1016/j.ijbiomac.2022.06.153.

(278) Zhang, X.; Kim, G. J.; Kang, M. G.; Lee, J. K.; Seo, J. W.; Do, J. T.; Hong, K.; Cha, J. M.; Shin, S. R.; Bae, H. Marine Biomaterial-Based Bioinks for Generating 3D Printed Tissue Constructs. *Mar. Drugs* **2018**, *16* (12). https://doi.org/10.3390/MD16120484.

(279) Yoon, H. J.; Shin, S. R.; Cha, J. M.; Lee, S. H.; Kim, J. H.; Do, J. T.; Song, H.; Bae, H. Cold Water Fish Gelatin Methacryloyl Hydrogel for Tissue Engineering Application. *PLoS ONE* **2016**, *11* (10), e0163902. https://doi.org/10.1371/JOURNAL.PONE.0163902.

(280) Nichol, J. W.; Koshy, S. T.; Bae, H.; Hwang, C. M.; Yamanlar, S.; Khademhosseini, A. Cell-Laden Microengineered Gelatin Methacrylate Hydrogels. *Biomaterials* **2010**, *31* (21), 5536–5544. https://doi.org/10.1016/J.BIOMATERIALS.2010.03.064.

(281) Janarthanan, G.; Kim, J. H.; Kim, I.; Lee, C.; Chung, E. J.; Noh, I. Manufacturing of Self-Standing Multi-Layered 3D-Bioprinted Alginate-Hyaluronate Constructs by Controlling the Cross-Linking Mechanisms for Tissue Engineering Applications. *Biofabrication* **2022**, *14* (3), 035013. https://doi.org/10.1088/1758-5090/AC6C4C.

(282) Danso, E. K.; Oinas, J. M. T.; Saarakkala, S.; Mikkonen, S.; Töyräs, J.; Korhonen, R. K. Structure-Function Relationships of Human Meniscus. *J. Mech. Behav. Biomed. Mater.* **2017**, *67*, 51–60. https://doi.org/10.1016/J.JMBBM.2016.12.002.

(283) Bergstein, V. E.; Ahiarakwe, U.; Haft, M.; Mikula, J. D.; Best, M. J. Decreasing Incidence of Partial Meniscectomy and Increasing Incidence of Meniscus Preservation Surgery From 2010 to 2020 in the United States. *Arthrosc. J. Arthrosc. Relat. Surg.* **2025**, *41* (6), 1919-1927.e1. https://doi.org/10.1016/j.arthro.2024.07.030.

(284) Rongen, J. J.; van Tienen, T. G.; Buma, P.; Hannink, G. Meniscus Surgery Is Still Widely Performed in the Treatment of Degenerative Meniscus Tears in The Netherlands. *Knee Surg. Sports*

Traumatol. Arthrosc. 2017 264 **2017**, *26* (4), 1123–1129. https://doi.org/10.1007/s00167-017-4473-2.

(285) Longo, U. G.; Mazzola, A.; Cardinale, M. E.; De Salvatore, S.; Piergentili, I.; Marx, R.; Papalia, R. Halving of the Meniscectomy Rate and Their Costs in Italy: A 15-Years Period Analysis. *Knee Surg. Sports Traumatol. Arthrosc.* **2025**, *33* (2), 534–543. https://doi.org/10.1002/ksa.12407.

(286) Karia, M.; Ghaly, Y.; Al-Hadithy, N.; Mordecai, S.; Gupte, C. Current Concepts in the Techniques, Indications and Outcomes of Meniscal Repairs. *Eur. J. Orthop. Surg. Traumatol.* **2019**, *29* (3), 509–520. https://doi.org/10.1007/s00590-018-2317-5.

(287) Jacob, G.; Shimomura, K.; Krych, A. J.; Nakamura, N. The Meniscus Tear: A Review of Stem Cell Therapies. *Cells* **2019**, *9* (1), 92. https://doi.org/10.3390/cells9010092.

(288) Bishop, E. S.; Mostafa, S.; Pakvasa, M.; Luu, H. H.; Lee, M. J.; Wolf, J. M.; Ameer, G. A.; He, T. C.; Reid, R. R. 3-D Bioprinting Technologies in Tissue Engineering and Regenerative Medicine: Current and Future Trends. *Genes Dis.* **2017**, *4* (4), 185–195. https://doi.org/10.1016/j.gendis.2017.10.002.

(289) Stocco, E.; Porzionato, A.; De Rose, E.; Barbon, S.; De Caro, R.; Macchi, V. Meniscus Regeneration by 3D Printing Technologies: Current Advances and Future Perspectives. *J. Tissue Eng.* **2022**, *13*. https://doi.org/10.1177/20417314211065860.

(290) Szabó, A.; De Vlieghere, E.; Costa, P. F.; Geurs, I.; Dewettinck, K.; Maes, L.; Laukens, D.; Van Vlierberghe, S. Effect of Porosity on the Colonization of Digital Light-Processed 3D Hydrogel Constructs toward the Development of a Functional Intestinal Model. *Biomacromolecules* **2024**, *25* (5), 2863–2874. https://doi.org/10.1021/acs.biomac.4c00019.

(291) Ge, Q.; Jian, B.; Li, H. Shaping Soft Materials via Digital Light Processing-Based 3D Printing: A Review. *Forces Mech.* **2022**, *6*, 100074. https://doi.org/10.1016/j.finmec.2022.100074.

(292) Gong, J.; Qian, Y.; Lu, K.; Zhu, Z.; Siow, L.; Zhang, C.; Zhou, S.; Gu, T.; Yin, J.; Yu, M.; Wang, H.; Yang, H. Digital Light Processing (DLP) in Tissue Engineering: From Promise to Reality, and Perspectives. *Biomed. Mater.* **2022**, *17* (6), 062004. https://doi.org/10.1080/03008207.2016.1276576.

(293) Verisqa, F.; Cha, J.-R.; Nguyen, L.; Kim, H.-W.; Knowles, J. C. Digital Light Processing 3D Printing of Gyroid Scaffold with Isosorbide-Based Photopolymer for Bone Tissue Engineering. *Biomolecules* **2022**, *12* (11), 1692. https://doi.org/10.3390/biom12111692.

(294) Grigoryan, B.; Paulsen, S. J.; Corbett, D. C.; Sazer, D. W.; Fortin, C. L.; Zaita, A. J.; Greenfield, P. T.; Calafat, N. J.; Gounley, J. P.; Ta, A. H.; Johansson, F.; Randles, A.; Rosenkrantz, J. E.; Louis-Rosenberg, J. D.; Galie, P. A.; Stevens, K. R.; Miller, J. S. Multivascular Networks and Functional Intravascular Topologies within Biocompatible Hydrogels. *Science* **2019**, *364* (6439), 458–464. https://doi.org/10.1126/science.aav9750.

(295) Chiou, B.-S.; English, R. J.; Khan, S. A. *Rheology and Photo-Cross-Linking of Thiol-Ene Polymers*. https://pubs.acs.org/sharingguidelines.

(296) Wang, Y.; Serra, R.; Argoul, E. P. Adapted Locati Method Used for Accelerated Fatigue Test under Random Vibrations. *Procedia Struct. Integr.* **2019**, *19*, 674–681. https://doi.org/10.1016/j.prostr.2019.12.073.

(297) Peters, J. T.; Wechsler, M. E.; Peppas, N. A. Advanced Biomedical Hydrogels: Molecular Architecture and Its Impact on Medical Applications. *Regen. Biomater.* **2021**, *8* (6), 1–21. https://doi.org/10.1093/RB/RBAB060.

(298) Bagheri Saed, A.; Behravesh, A. H.; Hasannia, S.; Akhoundi, B.; Hedayati, S. K.; Gashtasbi, F. An in Vitro Study on the Key Features of Poly L-Lactic Acid/Biphasic Calcium Phosphate Scaffolds Fabricated via DLP 3D Printing for Bone Grafting. *Eur. Polym. J.* **2020**, *141*. https://doi.org/10.1016/j.eurpolymj.2020.110057.

(299) Schwartz, G.; Morejon, A.; Gracia, J.; Best, T. M.; Jackson, A. R.; Travascio, F. Heterogeneity of Dynamic Shear Properties of the Meniscus: A Comparison between Tissue Core and Surface Layers. *J. Orthop. Res.* **2023**, *41* (7), 1607–1617. https://doi.org/10.1002/JOR.25495.

(300) Bernreitner, K.; Neil31, W.; Gahleitner, M. *Correlation between Molecular Structure and Rheological Behaviour of Polypropylene*; 1992; Vol. 11, pp 89–100.

(301) Steinman, N. Y.; Bentolila, N. Y.; Domb, A. J. Effect of Molecular Weight on Gelling and Viscoelastic Properties of Poly(Caprolactone)–b-Poly(Ethylene Glycol)–b-Poly(Caprolactone) (PCL–PEG–PCL) Hydrogels. *Polymers* **2020**, *12* (10), 2372. https://doi.org/10.3390/POLYM12102372.

(302) Laurano, R.; Abrami, M.; Grassi, M.; Ciardelli, G.; Boffito, M.; Chiono, V. Using Poloxamer® 407 as Building Block of Amphiphilic Poly(Ether Urethane)s: Effect of Its Molecular Weight Distribution on Thermo-Sensitive Hydrogel Performances in the Perspective of Their Biomedical Application. *Front. Mater.* **2020**, *7*. https://doi.org/10.3389/fmats.2020.594515.

(303) Solbu, A. A.; Caballero, D.; Damigos, S.; Kundu, S. C.; Reis, R. L.; Halaas, Ø.; Chahal, A. S.; Strand, B. L. Assessing Cell Migration in Hydrogels: An Overview of Relevant Materials and Methods. *Mater. Today Bio* **2023**, *18*. https://doi.org/10.1016/j.mtbio.2022.100537.

(304) Zhao, Y.; Tan, K.; Zhou, Y.; Ye, Z.; Tan, W. S. A Combinatorial Variation in Surface Chemistry and Pore Size of Three-Dimensional Porous Poly(ε-Caprolactone) Scaffolds Modulates the Behaviors of

Mesenchymal Stem Cells. *Mater. Sci. Eng. C Mater. Biol. Appl.* **2016**, *59*, 193–202. https://doi.org/10.1016/J.MSEC.2015.10.017.

(305) Huang, J.; Cai, J.; Huangfu, C.; Li, S.; Chen, G.; Yun, H.; Xiao, J. A Scalable Digital Light Processing 3D Printing Method. *Micromachines 2024 Vol 15 Page 1298* **2024**, *15* (11), 1298. https://doi.org/10.3390/MI15111298.

(306) Zhang, K.; Wu, J.; Zhang, W.; Yan, S.; Ding, J.; Chen, X.; Cui, L.; Yin, J. In Situ Formation of Hydrophobic Clusters to Enhance Mechanical Performance of Biodegradable Poly(L-Glutamic Acid)/Poly(ε-Caprolactone) Hydrogel towards Meniscus Tissue Engineering. *J. Mater. Chem. B* **2018**, *6* (47), 7822–7833. https://doi.org/10.1039/C8TB01453A.

(307) Oh, K. H.; Kim, H.; Seo, Y. A Facile Synthetic Route to Novel Thermotropic Liquid Crystalline Polymers and Characterization of Their Mesophases. *RSC Adv.* **2017**, *7* (47), 29772–29778. https://doi.org/10.1039/C7RA02809A.

(308) Hlangothi, S. P.; Krupa, I.; Djoković, V.; Luyt, A. S. Thermal and Mechanical Properties of Cross-Linked and Uncross-Linked Linear Low-Density Polyethylene–Wax Blends. *Polym. Degrad. Stab.* **2003**, *79* (1), 53–59. https://doi.org/10.1016/S0141-3910(02)00238-0.

(309) Pitzanti, G.; Mohylyuk, V.; Corduas, F.; Byrne, N. M.; Coulter, J. A.; Lamprou, D. A. Urethane Dimethacrylate-Based Photopolymerizable Resins for Stereolithography 3D Printing: A Physicochemical Characterisation and Biocompatibility Evaluation. *Drug Deliv. Transl. Res. 2023 141* **2023**, *14* (1), 177–190. https://doi.org/10.1007/S13346-023-01391-Y.

(310) Delaey, J.; Parmentier, L.; Pyl, L.; Brancart, J.; Adriaensens, P.; Dobos, A.; Dubruel, P.; Van Vlierberghe, S. Solid-State Crosslinkable, Shape-Memory Polyesters Serving Tissue Engineering. *Macromol. Rapid Commun.* **2023**, *44* (8), 2200955.

https://doi.org/10.1002/MARC.202200955;JOURNAL:JOURNAL:01732803;WGROUP:STRING:PUBLICATION.

(311) Capanema, N. S. V.; Mansur, A. A. P.; Carvalho, I. C.; Carvalho, S. M.; Mansur, H. S. Bioengineered Water-Responsive Carboxymethyl Cellulose/Poly(Vinyl Alcohol) Hydrogel Hybrids for Wound Dressing and Skin Tissue Engineering Applications. *Gels Basel Switz.* **2023**, *9* (2). https://doi.org/10.3390/GELS9020166.

(312) Liu, M.; Zeng, X.; Ma, C.; Yi, H.; Ali, Z.; Mou, X.; Li, S.; Deng, Y.; He, N. Injectable Hydrogels for Cartilage and Bone Tissue Engineering. *Bone Res. 2017 51* **2017**, *5* (1), 17014-. https://doi.org/10.1038/boneres.2017.14.

(313) Simon, J. C.; Sapozhnikov, O. A.; Khokhlova, V. A. A Review of Mechanical Properties of Scaffold in Tissue Engineering: Aloe Vera Composites. https://doi.org/10.1088/1742-6596/1082/1/012080.

(314) Lee, J.; Song, B.; Subbiah, R.; Chung, J. J.; Choi, U. H.; Park, K.; Kim, S. H.; Oh, S. J. Effect of Chain Flexibility on Cell Adhesion: Semi-Flexible Model-Based Analysis of Cell Adhesion to Hydrogels. *Sci. Rep.* **2019**, *9* (1). https://doi.org/10.1038/S41598-019-38951-7.

(315) Liu, D.; Cao, Y.; Jiang, P.; Wang, Y.; Lu, Y.; Ji, Z.; Wang, X.; Liu, W. Tough, Transparent, and Slippery PVA Hydrogel Led by Syneresis. *Small* **2023**, *19* (14). https://doi.org/10.1002/smll.202206819.

(316) Ding, H.; Xu, S.; Wang, J.; Fan, Z.; Huang, Z.; Wu, H.; Pi, P.; Cheng, J.; Wen, X. A Conductive, Antibacterial, and Antifouling Hydrogel Based on Zwitterion. *J. Appl. Polym. Sci.* **2022**, *139* (7). https://doi.org/10.1002/app.51648.

(317) Means, A. K.; Grunlan, M. A. Modern Strategies To Achieve Tissue-Mimetic, Mechanically Robust Hydrogels. **2019**. https://doi.org/10.1021/acsmacrolett.9b00276.

(318) Screen, H. R. C.; Chhaya, V. H.; Greenwald, S. E.; Bader, D. L.; Lee, D. A.; Shelton, J. C. The Influence of Swelling and Matrix

Degradation on the Microstructural Integrity of Tendon. *Acta Biomater.* **2006**, *2* (5), 505–513. https://doi.org/10.1016/j.actbio.2006.05.008.
(319) Salisbury, S. T. S.; Buckley, C. P.; Zavatsky, A. B. Transverse Compression of Tendons. *J. Biomech. Eng.* **2016**, *138* (4), 041002. https://doi.org/10.1115/1.4032627.
(320) Mow, V. C.; Kuei, S. C.; Lai, W. M.; Armstrong, C. G. Biphasic Creep and Stress Relaxation of Articular Cartilage in Compression? Theory and Experiments. *J. Biomech. Eng.* **1980**, *102* (1), 73–84. https://doi.org/10.1115/1.3138202.
(321) Setton, L. A.; Zhu, W.; Mow, V. C. The Biphasic Poroviscoelastic Behavior of Articular Cartilage: Role of the Surface Zone in Governing the Compressive Behavior. *J. Biomech.* **1993**, *26* (4–5), 581–592. https://doi.org/10.1016/0021-9290(93)90019-B.
(322) Keya, K. N.; Li, Z.; Xu, L.; Xia, W. Exploring Cross-Link Density and Additive Effects on Mechanical and Morphological Behaviors of Cross-Linked Polymers. *Macromol. Mater. Eng.* **2025**, *310* (5), 2400383. https://doi.org/10.1002/mame.202400383.
(323) Creton, C.; Ciccotti, M. Fracture and Adhesion of Soft Materials: A Review. *Rep. Prog. Phys. Phys. Soc.* **2016**, *79* (4), 046601. https://doi.org/10.1088/0034-4885/79/4/046601.
(324) Kumar, D.; Manal, K. T.; Rudolph, K. S. Knee Joint Loading during Gait in Healthy Controls and Individuals with Knee Osteoarthritis. *Osteoarthritis Cartilage* **2013**, *21* (2), 298–305. https://doi.org/10.1016/j.joca.2012.11.008.
(325) Walker, P. S.; Arno, S.; Bell, C.; Salvadore, G.; Borukhov, I.; Oh, C. Function of the Medial Meniscus in Force Transmission and Stability. *J. Biomech.* **2015**, *48* (8), 1383–1388. https://doi.org/10.1016/J.JBIOMECH.2015.02.055.
(326) Dreyer, M. J.; Trepczynski, A.; Hosseini Nasab, S. H.; Kutzner, I.; Schütz, P.; Weisse, B.; Dymke, J.; Postolka, B.; Moewis, P.; Bergmann, G.; Duda, G. N.; Taylor, W. R.; Damm, P.; Smith, C. R.

European Society of Biomechanics S.M. Perren Award 2022: Standardized Tibio-Femoral Implant Loads and Kinematics. *J. Biomech.* **2022**, *141*, 111171. https://doi.org/10.1016/J.JBIOMECH.2022.111171.

(327) Schmalzried, T. P.; Szuszczewicz, E. S.; Northfield, M. R.; Akizuki, K. H.; Frankel, R. E.; Belcher, G.; Amstutz, H. C. Quantitative Assessment of Walking Activity after Total Hip or Knee Replacement*. *J. Bone Joint Surg. Am.* **1998**, *80* (1), 54–59. https://doi.org/10.2106/00004623-199801000-00010.

(328) Zwain, I. M. H.; Alithari, A. S. Improving the Fatigue Life of Composite by Using Multiwall Carbon Nanotubes. *Open Eng.* **2023**, *13* (1). https://doi.org/10.1515/eng-2022-0490.

(329) Panin, S. V.; Bogdanov, A. A.; Eremin, A. V.; Buslovich, D. G.; Shilko, I. S. Effect of Polymer Matrix on Inelastic Strain Development in PI- and PEI-Based Composites Reinforced with Short Carbon Fibers under Low-Cyclic Fatigue. *Polymers* **2023**, *15* (5), 1228. https://doi.org/10.3390/polym15051228.

(330) Martin, F.; Neubert, A.; Lutter, A. H.; Scholka, J.; Hentschel, E.; Richter, H.; Anderer, U. MTS, WST-8, and ATP Viability Assays in 2D and 3D Cultures: Comparison of Methodologically Different Assays in Primary Human Chondrocytes. *Clin. Hemorheol. Microcirc.* **2024**, *88* (Suppl 1), S3. https://doi.org/10.3233/CH-248101.

(331) Asgarpour, R.; Masaeli, E.; Kermani, S. Development of Meniscus-Inspired 3D-Printed PCL Scaffolds Engineered with Chitosan/Extracellular Matrix Hydrogel. *Polym. Adv. Technol.* **2021**, *32* (12), 4721–4732. https://doi.org/10.1002/pat.5465.

(332) Liu, Y.; Zhao, M.; Zhang, M.; Yang, B.; Qi, Y. K.; Fu, Q. Mesoporous Silica Nanoparticle-Based Nanomedicine: Preparation, Functional Modification, and Theranostic Applications. *Mater. Today Bio* **2025**, *34*, 102223. https://doi.org/10.1016/J.MTBIO.2025.102223.

(333) Yeong, W. Y.; Chua, C. K.; Leong, K. F.; Chandrasekaran, M.; Lee, M. W. Comparison of Drying Methods in the Fabrication of Collagen Scaffold via Indirect Rapid Prototyping. *J. Biomed. Mater. Res. - Part B Appl. Biomater.* **2007**, *82* (1), 260–266. https://doi.org/10.1002/JBM.B.30729;JOURNAL:JOURNAL:15524981;WGROUP:STRING:PUBLICATION.

(334) Odziomek, K.; Drabczyk, A. K.; Kościelniak, P.; Konieczny, P.; Barczewski, M.; Bialik-Wąs, K.; Odziomek, K.; Drabczyk, A. K.; Kościelniak, P.; Konieczny, P.; Barczewski, M.; Bialik-Wąs, K. The Role of Freeze-Drying as a Multifunctional Process in Improving the Properties of Hydrogels for Medical Use. *Pharm. 2024 Vol 17* **2024**, *17* (11). https://doi.org/10.3390/PH17111512.

(335) Segneanu, A. E.; Bejenaru, L. E.; Bejenaru, C.; Blendea, A.; Mogoşanu, G. D.; Biţă, A.; Boia, E. R. Advancements in Hydrogels: A Comprehensive Review of Natural and Synthetic Innovations for Biomedical Applications. *Polymers* **2025**, *17* (15), 2026. https://doi.org/10.3390/POLYM17152026.

(336) Xu, F.; Dawson, C.; Lamb, M.; Mueller, E.; Stefanek, E.; Akbari, M.; Hoare, T. Hydrogels for Tissue Engineering: Addressing Key Design Needs Toward Clinical Translation. *Front. Bioeng. Biotechnol.* **2022**, *10*, 849831. https://doi.org/10.3389/FBIOE.2022.849831/FULL.

(337) Luong, P. T.; Browning, M. B.; Bixler, R. S.; Cosgriff-Hernandez, E. Drying and Storage Effects on Poly(Ethylene Glycol) Hydrogel Mechanical Properties and Bioactivity. *J. Biomed. Mater. Res. A* **2013**, *102* (9), 3066. https://doi.org/10.1002/JBM.A.34977.

(338) Scherer, G. W. Theory of Drying. *J. Am. Ceram. Soc.* **1990**, *73* (1), 3–14. https://doi.org/10.1111/J.1151-2916.1990.TB05082.X;WGROUP:STRING:PUBLICATION.

(339) Gaharwar, A. K.; Avery, R. K.; Assmann, A.; Paul, A.; McKinley, G. H.; Khademhosseini, A.; Olsen, B. D. Shear-Thinning

Nanocomposite Hydrogels for the Treatment of Hemorrhage. *ACS Nano* **2014**, *8* (10), 9833–9842. https://doi.org/10.1021/NN503719N.

(340) Balsters, J. M.; Bäumchen, A.; Roland, M.; Diebels, S.; Neubauer, J. C.; Gepp, M. M.; Zimmermann, H. Drying of Functional Hydrogels: Development of a Workflow for Bioreactor-Integrated Freeze-Drying of Protein-Coated Alginate Microcarriers for iPS Cell-Based Screenings. *Gels 2025 Vol 11 Page 439* **2025**, *11* (6), 439. https://doi.org/10.3390/GELS11060439.

(341) Arthus, L.; Ramos Estevam, B.; Jova Aguila, Z.; Regina Wolf Maciel, M.; Vasconcelos Fregolente, L. Facile Tuning of Hydrogel Properties for Efficient Water Removal from Biodiesel: An Assessment of Alkaline Hydrolysis and Drying Techniques. *Chem. Eng. Sci.* **2023**, *282*, 119224. https://doi.org/10.1016/J.CES.2023.119224.

(342) Heimbuck, A. M.; Priddy-Arrington, T. R.; Sawyer, B. J.; Caldorera-Moore, M. E. Effects of Post-Processing Methods on Chitosan-Genipin Hydrogel Properties. *Mater. Sci. Eng. C Mater. Biol. Appl.* **2019**, *98*, 612–618. https://doi.org/10.1016/j.msec.2018.12.119.

(343) Cardea, S.; Baldino, L.; Marco, I. D.; Pisanti, P.; Reverchon, E. Supercritical Gel Drying of Polymeric Hydrogels for Tissue Engineering Applications. *Chem. Eng. Trans.* **2013**, *32*, 1123–1128. https://doi.org/10.3303/CET1332188.

(344) Annabi, N.; Nichol, J. W.; Zhong, X.; Ji, C.; Koshy, S.; Khademhosseini, A.; Dehghani, F. Controlling the Porosity and Microarchitecture of Hydrogels for Tissue Engineering. *Tissue Eng. Part B Rev.* **2010**, *16* (4), 371. https://doi.org/10.1089/TEN.TEB.2009.0639.

(345) Sornkamnerd, S.; Okajima, M. K.; Kaneko, T. Tough and Porous Hydrogels Prepared by Simple Lyophilization of LC Gels. *ACS Omega* **2017**, *2* (8), 5304. https://doi.org/10.1021/ACSOMEGA.7B00602.

(346) Simoni, R. C.; Lemes, G. F.; Fialho, S.; Gonçalves, O. H.; Gozzo, A. M.; Chiaradia, V.; Sayer, C.; Shirai, M. A.; Leimann, F. V. Effect of Drying Method on Mechanical, Thermal and Water Absorption Properties of Enzymatically Crosslinked Gelatin Hydrogels. *An. Acad. Bras. Cienc.* **2017**, *89* (1 Suppl 0), 745–755. https://doi.org/10.1590/0001-3765201720160241.

(347) Degobert, G.; Aydin, D. Lyophilization of Nanocapsules: Instability Sources, Formulation and Process Parameters. *Pharmaceutics* **2021**, *13* (8), 1112. https://doi.org/10.3390/PHARMACEUTICS13081112.

(348) Fadzil, A. F. bin A.; Pramanik, A.; Basak, A. K.; Prakash, C.; Shankar, S. Role of Surface Quality on Biocompatibility of Implants - A Review. *Ann. 3D Print. Med.* **2022**, *8*, 100082. https://doi.org/10.1016/J.STLM.2022.100082.

(349) Damiati, L.; Eales, M. G.; Nobbs, A. H.; Su, B.; Tsimbouri, P. M.; Salmeron-Sanchez, M.; Dalby, M. J. Impact of Surface Topography and Coating on Osteogenesis and Bacterial Attachment on Titanium Implants. *J. Tissue Eng.* **2018**, *9*, 2041731418790694. https://doi.org/10.1177/2041731418790694.

(350) Liu, F.; Xu, J.; Wu, L.; Zheng, T.; Han, Q.; Liang, Y.; Zhang, L.; Li, G.; Yang, Y. The Influence of the Surface Topographical Cues of Biomaterials on Nerve Cells in Peripheral Nerve Regeneration: A Review. *Stem Cells Int.* **2021**, *2021*, 8124444. https://doi.org/10.1155/2021/8124444.

(351) Hoffman, A. S. Hydrogels for Biomedical Applications. *Adv. Drug Deliv. Rev.* **2012**, *64* (SUPPL.), 18–23. https://doi.org/10.1016/J.ADDR.2012.09.010.

(352) Sozcu, S.; Frajova, J.; Wiener, J.; Venkataraman, M.; Tomkova, B.; Militky, J.; Sozcu, S.; Frajova, J.; Wiener, J.; Venkataraman, M.; Tomkova, B.; Militky, J. Effect of Drying Methods on the Thermal and Mechanical Behavior of Bacterial Cellulose

Aerogel. *Gels 2024 Vol 10* **2024**, *10* (7). https://doi.org/10.3390/GELS10070474.

(353) Genevro, G. M.; de Moraes, M. A.; Beppu, M. M. Freezing Influence on Physical Properties of Glucomannan Hydrogels. *Int. J. Biol. Macromol.* **2019**, *128*, 401–405. https://doi.org/10.1016/J.IJBIOMAC.2019.01.112.

(354) Jaya, S.; Durance, T. D. Compressive Characteristics of Cellular Solids Produced Using Vacuum-Microwave, Freeze, Vacuum and Hot Air Dehydration Methods. *J. Porous Mater. 2007 161* **2007**, *16* (1), 47–58. https://doi.org/10.1007/S10934-007-9167-6.

(355) Walker, R. C.; Potochniak, A. E.; Hyer, A. P.; Ferri, J. K. Zirconia Aerogels for Thermal Management: Review of Synthesis, Processing, and Properties Information Architecture. *Adv. Colloid Interface Sci.* **2021**, *295*, 102464. https://doi.org/10.1016/J.CIS.2021.102464.